Master of Science Thesis

Design of a crash energy absorber for a composite aircraft fuselage using a combined analytical-numerical approach

V.K. Poorte

Faculty of Aerospace Engineering · Delft University of Technology

TU Delft Delft University of Technology

Design of a crash energy absorber for a composite aircraft fuselage using a combined analytical-numerical approach

Master of Science Thesis

For obtaining the degree of Master of Science in Aerospace Engineering
at Delft University of Technology

V.K. Poorte

15/04/2020

Faculty of Aerospace Engineering · Delft University of Technology

The work in this thesis was supported by Clean Sky 2 STUNNING project. Their cooperation is gratefully acknowledged.

Delft University of Technology
Faculty of Aerospace Engineering
Department of Aerospace Structures and Materials

GRADUATION COMMITTEE

Dated: 15/04/2020

Chair holder:

Prof.dr.ir. C. Bisagni

Committee members:

Dr.ir. I. Fernandez-Villegas

Dr.ir. C.L. Walters

Dr.ir. S.L. Veldman

Acknowledgments

After a long year filled with governmental measures trying to contain the coronavirus, and many days spent in my room working on my thesis, I can say that I have gotten the better of one of the two. While the virus is still spreading, and we are hoping for better days, I can proudly say that in the meantime, I have managed to complete my master thesis, and thereby wrap up my beautiful years in Delft.

First of all, I would like to thank my supervisor Prof. Chiara Bisagni for her time during this year. Even though we were only able to meet once face to face outside the faculty, I appreciate the time you have dedicated to my work, be it to provide feedback on my thesis or get back in touch with my Italian roots. I would like to thank the STUNNING project for letting me use their fuselage section as part of my research. Furthermore, I would like to thank my friends, especially my room-mates and Bente, who have kept me sane in this insane time by keeping my mind from crashing every now and then. Finally, and most importantly, I would like to thank my parents for supporting me during my studies and for all the undertakings that I have done aside. You have helped shape me into the person I am today.

Delft, University of Technology V.K. Poorte
15/04/2020

Abstract

This thesis aims to provide more insight into the crashworthiness behaviour of a composite aircraft fuselage. This is achieved by studying both analytically and numerically the crushing behaviour of composite energy absorbers. The analytical model, which is based on energy dissipation rates, generalises previously derived analytical models to study a wider variety of structural components. It is found that the analytical model can give an estimation of the mean crushing load of square, C-shaped, and corrugated specimens. Next to the analytical study, numerical models are created to gain insight into the behaviour of the studied shapes when subjected to crash loading.

Another part of the numerical study investigates the effectiveness of different material models to capture the complex failure mechanism of the composite crash absorber. In LS-Dyna, the MAT054, MAT058, and MAR262 material models are used, which are all able to reproduce the results obtained from reference tests. The ability of the material models to recreate the crushing phenomenon is thought to originate from the opportunity LS-Dyna offers to degrade material properties in the crush frond, which incorporates the formation of cracks and delaminations.

In the final stage of this research, a case study is performed, where different absorbers are introduced into a simplified digital twin of the Next Generation Multifunctional Fuselage Demonstration as developed by the STUNNING project. Here, it is found that the fuselage's energy absorption can be increased by introducing energy absorbers. All the simulated fuselage sections show similar behaviour in the first crash stages, characterised by the flattening of the lower section of the frame. Subsequently, the behaviour of the absorber and the surrounding structure highly depends on the absorber's integration. Finally, it is found that by combining the numerical results of a baseline fuselage section and the analytical model for the energy absorbers, one can estimate the energy absorption of the augmented structure with a discrepancy of less than 20%. This proves that the suggested analytical-numerical method can aid engineers during the preliminary design for crashworthiness of a thermoplastic composite aircraft fuselage.

Table of Contents

List of Figures

List of Tables

Chapter 1

Introduction

Over the years, aircraft may not have changed significantly to the untrained eye. Ever since the introduction of the Boeing 707 back in the 1950s, almost all commercial airliners have had the same shape, characterised by a long fuselage with wings and a tail formed by a duo of stabilisers, commonly referred to as the cigar with wings. Even though the outer looks have remained largely the same, many technological improvements have been implemented. For example, over the last 50 years, an increase in efficiency between 30 and 50% has been achieved by engine manufacturers [19]. A perhaps more unnoticed change is the introduction of new materials. Over the past 100 years of aviation, aircraft have been made initially from wood and textile, after which a switch to aluminium alloys was made, while the modern standard is considered to be the use of fibre reinforced polymers. Figure 1.1 depicts an overview of which materials are used in a Boeing 787, along with the corresponding percentages. In the same figure, a comparison is provided with a Boeing 777. To have more context, to accompany the provided percentages, which indicate an increase in the use of composite materials, the Boeing 777 entered service in 1995, while the 787 has been introduced in 2011.

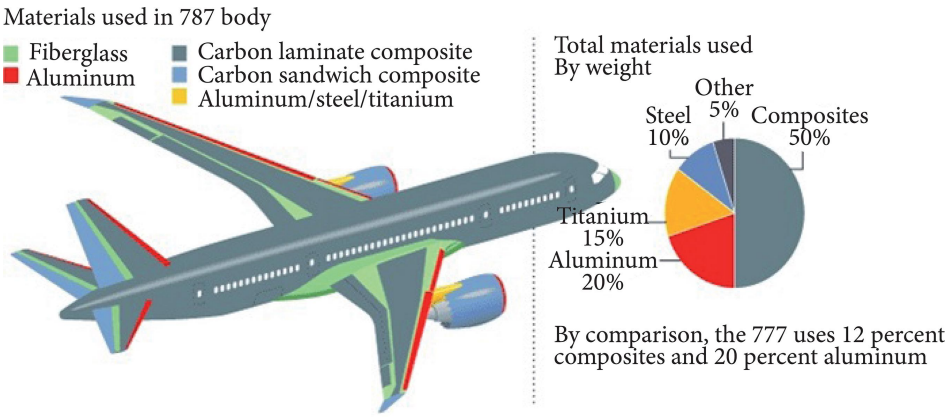

Figure 1.1: Materials used in a Boeing 787 [1].

Fibre-reinforced polymers have been introduced in aircraft structures for two reasons: specific properties and design freedom. When a material has high specific properties, it indicates a high stiffness modulus or failure stress for low weight. As weight is of paramount importance in an aircraft, high specific properties is an extremely desired feature from a material. The design freedom, on the other hand, originates from the way composite materials are manufactured. Fibre-reinforced materials are fabricated by stacking layers of material with directional properties. Therefore, by orienting the different layers, one can tailor the properties of the final product as one desires.

While implementing innovation into an aircraft, one key aspect has always been kept in mind by the engineers: "Safety is not an option". From this, it becomes clear that in the aviation industry, one does not perform a trade-off on safety. Thanks to these high standards, air-travel is considered one of the safest means of transport, and with the ever-increasing demand, the industry is driven to maintain this status. To ensure this, the Federal Aviation Association (FAA) and the European Aviation Safety Agency (EASA), the largest governing bodies for aviation, set-up regulations that aircraft manufacturers have to respect. These rules contain requirements for the aircraft's nominal operation and more extreme conditions such as a crash event, which are the subject of this study.

With the introduction of composite materials into the aircraft structure, engineers have to ensure that the vehicle behaves equally to metal counterparts [20,21]. This sounds straightforward; however, the behaviour of fibre reinforced materials, when subjected to crash loading, is very different with respect to metals. While metal materials are characterised by plastic failure, enabling them to bend and fold, composites are characterised by brittle failure, leading to abrupt failure. The type of material failure plays a key role in the structure's behaviour and performance in the event of a crash.

When an aircraft is subjected to crash loading, energy dissipation is key, as the vehicle's kinetic energy needs to be dispersed. This task lies upon the fuselage structure, as this is the main structure coming into contact with the impacted ground. For example, it has been shown that over 40% of the crash energy of a metal aircraft is dissipated by the bending motion of the fuselage's frames [22]. Due to the brittle nature of the newly introduced material, new designs need to be developed to account for this different behaviour. This inquiry has resulted in the creation of axially crushable tubes. These types of absorbers are taken from helicopter structures, as these types of vehicles also need to dissipate energy in a confined volume when subjected to axial crushing. It is found in research that composite specimens can have excellent energy absorption characteristics when these are designed well [9, 23]. The working principle behind such an absorber is that the component is crushed, which leads to many material failures, all of which contribute to the overall energy absorption. The crushing behaviour, due to all the simultaneous material failures, as shown in Figure 1.2, is a complex phenomenon, which leads to a difficult design process of these absorbers. Therefore, analytical and numerical methods are investigated in this research to achieve a more fundamental understanding of the crushing behaviour of such an energy absorber, which may assist during the design of an aircraft fuselage.

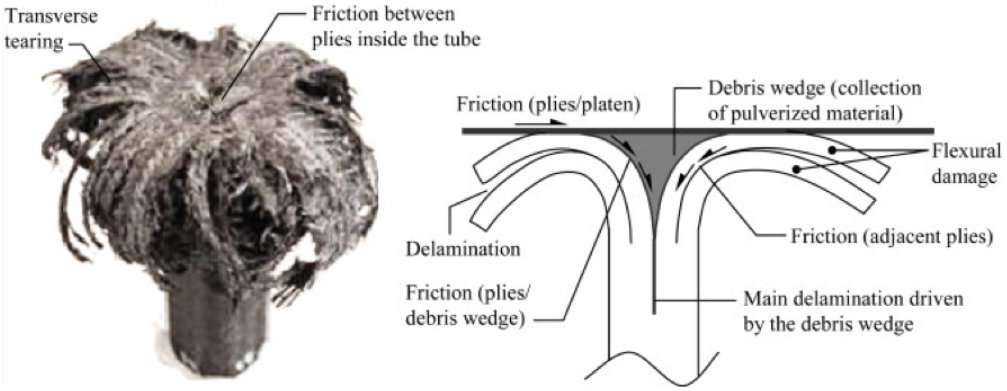

Figure 1.2: Examples of crushing behaviour of a fibre reinforce plastic [2].

When designing composite structures, the building block approach is often taken as a reference, as depicted in Figure 1.3. This pyramid indicates the level of complexity of the parts being studied. For example, the previously mentioned energy absorbers lie on the second level of the pyramid. However, to better understand the performance of the structure's crashworthiness with the newly introduced structural elements, one needs to study the behaviour at the component level. Therefore, this step is also performed in this study by analysing the keel section of an aircraft fuselage. Therefore, first, the crush elements are studied separately to examine their behaviour, which are subsequently introduced into the fuselage section, to investigate the element's behaviour in a more realistic situation. For this, the Next Generation Multifunctional Fuselage Demonstrator, as developed by the STUNNING project, is taken as the test case structure.

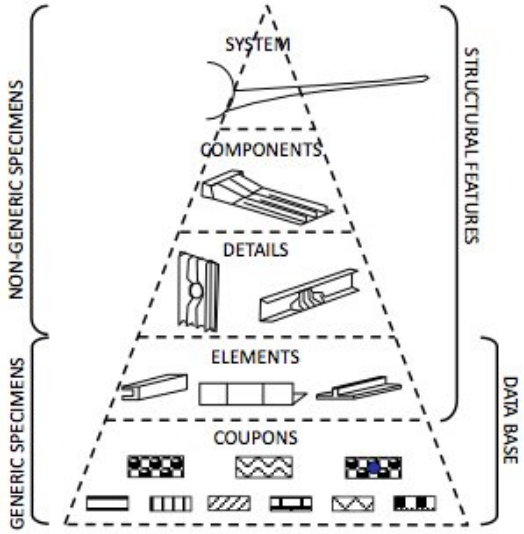

Figure 1.3: Building block pyramid for composite aircraft structures [3].

1.1 Thesis Goal

An aircraft's crashworthiness is commonly examined in the last stages of the vehicle's design process. This analyses mainly consists of digital and physical testing, which leads to insights into the structure's behaviour when subjected to crash loading. By doing so, the structure is adjusted to meet the crashworthy requirements. This process is not optimal, as it requires matured designs to be altered, leading to a sub-optimal design. Theoretically, when one takes the crashworthiness requirements into account during the first designs stages of the aircraft, a more synergistic, thus optimal design can be achieved. This leads to an overall improvement of the structure, which in turn has a positive snowball effect on the rest of the aircraft. An example of how concurrent design can be achieved is depicted in Figure

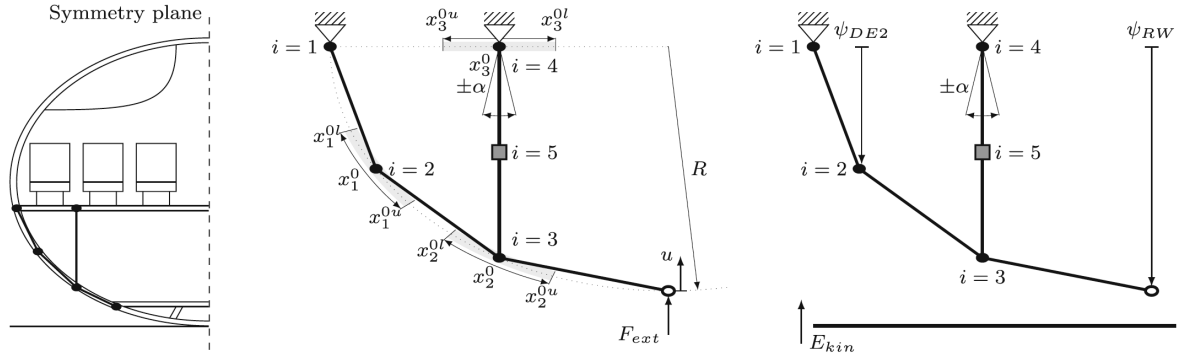

Figure 1.4: Simplified beam and spring model of an aircraft fuselage [4].

1.4. Here one can see how the lower section of a fuselage can be simplified using a series of beams and springs to reduce the complexity of the structure to promote ease of analysis. Therefore, beam and spring simplifications can be implemented to determine the element's behaviour analytically, which can be used to assemble the (semi-)analytical model of the global structure. The aspect withholding this is the limited analytical knowledge available to estimate the element's behaviour when subjected to crush loading, to simplify these with springs and beams.

Consequently, this thesis aims to gain more insight into the isolated crushing behaviour of composite energy absorbers. Subsequently, the absorber's behaviour is studied when integrated into a fuselage structure subjected to crash loading. The structural elements are studied numerically as analytically, while the fuselage section is only studied using finite element models.

To accurately perform the desired simulations, inspiration is taken from the building block approach, reported in Figure 1.3. Thus, before studying the element's behaviour, one needs to understand the material's behaviour at a coupon level. This is especially important as the structural elements are subjected to crash loading and are therefore loaded beyond the material's failure stress, meaning that understanding the material's post-failure behaviour is of paramount importance. Hence, the first step of this research revolves around analysing the different material models that finite element software have to offer. More specifically, Abaqus' and LS-Dyna's finite element tools are investigated as potential candidates to model the crash behaviour of the fuselage section. In Abaqus, the built-in Hashin material model is used, while in LS-Dyna, the MAT054, MAT08, and MAT262 material models are studied. To understand the material model's and the influence the parameters have on the material's behaviour, coupon simulations are performed for a series of laminates, with both tensile, as compression loading.

One remarkable aspect of this thesis is that the polymer used in the fibre reinforced material is thermoplastic rather than the more commonly used thermoset material. Therefore, this research provides insight into how this material behaves when implemented in an aircraft fuselage subjected to crash loading.

Once the material models have been studied, the crushing behaviour of composite energy absorbers is analysed. One key aspect of this research is to understand further what variables play a role in the crushing behaviour of these structural elements. Therefore, this study is

not limited to a numerical analysis but is accompanied by an analytical investigation. In doing so, insight is gained regarding which geometric and material properties play a key role in the energy-absorbing behaviour of the structural component. The analytical model is based upon the model derived by Hussein et al., which is solely implementable on straight, square tubes [13]; therefore, this model is generalised to study other shapes of absorbers. Subsequently, one can estimate the mean crushing load of a wider variety of composite energy absorbers, solely using material and geometric properties. Furthermore, numerical models are created to verify the analytical model and study the performance of finite element tools in predicting the complex crushing behaviour. The numerical models are first calibrated using test data and subsequently altered to study different sizes of absorbers. The numerical models are also used to investigate which finite element software and material model can accurately reproduce the crushing behaviour of the composite element with the simplified modelling technique. This way, the aforementioned material models can be studied when implemented in a complex environment where these need to capture various failure modes, such as delamination and crack formations. Consequently, the knowledge gained from the isolated simulations can be implemented during the creation of the digital twin of the fuselage section.

The analysis of the fuselage section consists of two stages. First, the isolated absorbers are studied, after which these are integrated into the section's structure. When performing the design of the isolated absorbers, their specific energy absorption is taken into account to maximise the element's effectiveness. An important aspect of this study is the stability and reliability of the absorber, which is found to depend on how the absorber is integrated into the structure. Therefore a study is performed such that the maximum amount of energy is absorbed by the structure. Furthermore, to study the efficacy of the introduced absorbers, a baseline run is performed. In this simulation, no energy absorbers are installed to analyse the improvement that has been achieved with the design alterations.

As stated at the beginning of this section, ideally, one can determine the crashworthiness of an aircraft structure using a semi-analytical method; however, this requires more research to study the behaviour of the other structural elements. Nevertheless, as a final step, the suggested analytical-numerical method is used to estimate the fuselage section's energy absorption. By implementing the suggested analytical method, the crash absorber's behaviour can be estimated without complex numerical models, which speeds up the design process, as design iterations can be performed more quickly. Furthermore, when, in the future, the baseline behaviour of the fuselage section can be determined analytically, the frame design can also be altered efficiently. However, to achieve this, more research is required, as this lies outside the scope of this thesis.

1.2 Thesis Outline

In Chapter 2, an overview is provided regarding the crashworthiness of aircraft structures. This entails research concerning the requirements that aircraft have to fulfil and how state of the art methods are used to meet these requirements. Afterwards, the reader is guided from the base of the building block pyramid to its tip by going from the material tests to the analysis of structural elements and concluding with the study of the components. Therefore, in Chapter 3, the coupon simulations are performed, accompanied by a thorough description

of the implemented material models. After this, the isolated crush absorbers are studied. As stated before, these are both studied numerically and analytically, which is described in chapter 4 and 5, respectively. Subsequently, the knowledge gained from the crush absorbers' analysis is implemented during a case study, where an absorber is designed for a fuselage section, which can be found in Chapter 7. Finally, all the conclusions are gathered into one chapter, wrapping up the research in Chapter 8.

Chapter 2

Literature Research

This chapter investigates the requirements for an aircraft under crash conditions and what parameters are used to quantify the structure's performance. Once those two aspects have been clarified, it is investigated how an aircraft behaves in crash conditions. First, the behaviour of the global structure is studied by looking into which phenomena play a key role in the performance of the structure. From this, it becomes clear that due to the introduction of composite materials the behaviour, or more importantly, the performance, of the structure changes. To gain more insight into where this difference originates, a more detailed analysis is performed on the behaviour of single structural components when these are subjected to crash loading. Finally, some conclusions are drawn summarising the key aspects that are taken to advance this research further.

2.1 Aircraft Crashworthiness Regulations

In the aerospace sector, safety is of paramount importance. Thanks to the implemented measures, the standard of the air transport industry is appraised. This standard is achieved thanks to a combination of the requirements being set by the authorities, for example, the Federal Aviation Association (FAA) and the European Aviation Safety Agency (EASA). The qualifications set by the airworthiness authorities regarding crashworthiness can be found in the Code of Federal Regulation (CFR). All these regulations essentially boil down to safeguard four characteristics that an aircraft needs to fulfil in the event of a crash. These properties can be found in 14 CFR Part 25 Subpart C [24], and are reported below.

- **1 - The Retention of Items of Mass** - All the objects that are situated in the cabin should remain in place in the event of a crash.
- **2 - Maintenance of Acceptable Loads Experienced by the Occupants** - The structure and seats should be designed in such a manner that these absorb the energy and transfer the loads to the passengers such that these do not sustain head or spinal injuries caused by excessive accelerations.

- **3 - Maintenance of a Survivable Volume** - The fuselage may not deform in such a manner that there is no sufficient volume for the occupants to be able to move.
- **4 - Maintenance of the Occupant Egress Paths** - All the emergency paths need to remain free and undamaged in the case of a crash.

The specifications reported above are all qualitative. In other sections of the regulations, more quantitative details are listed, which are analysed in the following subsections.

Impact Velocity Requirements

Perhaps one of the most important requirements when designing for crashworthiness is the required impact speed an aircraft must sustain. When an elevated impact speed is required, it might be impossible to create a feasible design, due to the excessive weight such a design might require. Therefore, to set a viable limit for this requirement, the Transport Aircraft Crashworthiness and Ditching Working Group studied the survivability of different crash situations [5]. In the research, Figure 2.1 is reported, where the suggested impact speed is given as a function of the Maximum Take-Off Weight (MTOW). Based on this research, in 4 CFR Part 25 code, the minimum impact velocity for which an aircraft should be designed is listed, which is given to be 30 ft/s (9.14 m/s) [24].

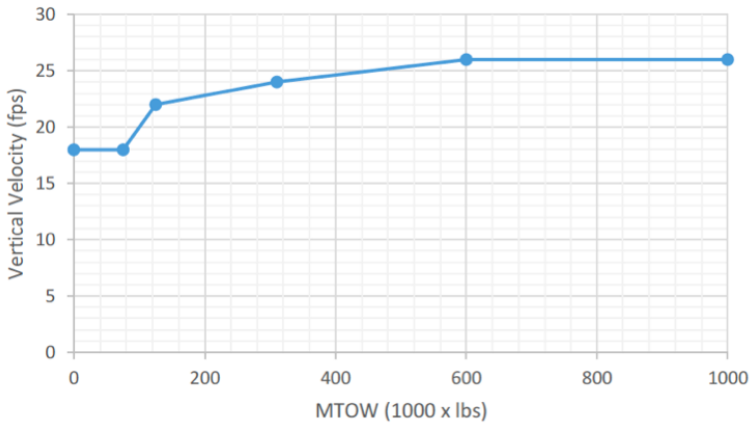

Figure 2.1: Suggested design impact speed versus aircraft MTOW [5].

Passenger Acceleration Requirements

In the requirements listed above, points one, three and four, dictate the requirement for the cabin. The keel section naturally influences the behaviour of the upper part of the fuselage, however, to a lesser extent. Therefore, these points are of minor importance in this study. On the other hand, point two is dictated largely by the occupants' seats; however, the behaviour of the lower part of the fuselage dictates which loads the seats need to transfer to its occupants. Accordingly, for completeness, the loads which the passenger may experience as provided in 4 CFR Part 25.561 [25], are reported below.

- **Upward** - 3.0g
- **Downward** - 6.0g
- **Forward** - 9.0g
- **Rearward** - 1.5g
- **Sideward** - 4.0g

Ideally, the keel section of the aircraft absorbs a large amount of energy. To achieve this, it needs to sustain high loads, which is not desired for the passengers. Hence, a good balance is required between the energy absorption of the lower section of the fuselage and the transferred load to the surrounding structure.

Head Injury Criterion Requirements

Next to the accelerations that the passengers may experience, more details are provided, which are set in place to avoid head or spinal injury, as reported in 14 CFR Part 25.562 [26]. Here it is stated that the compressive load measured between the pelvis and the lumbar column of the occupants may not exceed 1500 pounds (680.4 kg) and that the maximum acceptable Head Injury Criterion (HIC) is 1000 units [26]. The HIC can be calculated using Equation 2.1. In the equation t_1 and t_2 represent the initial and final integration times respectively, while $a(t)$ represents the acceleration as a function of time.

$$\mathrm{HIC} = \left\{ (t_2 - t_1) \left[\frac{1}{(t_2 - t_1)} \int_{t_1}^{t_2} a(t)\mathrm{dt} \right]^{2.5} \right\}_{\max} \tag{2.1}$$

2.2 Crashworthiness Performance Parameters

In the previous section, the requirements set by the FAA are reported, which entail a combination of both qualitative and quantitative guidelines, such as the maintenance of volume or requirements dictating the loads that the passengers may experience. Furthermore, while designing, engineers also use parameters to evaluate a structure's performance, as other aspects need to be considered. An example may be the total amount of energy that the structure can absorb. However, in aerospace applications, where weight is of predominant importance, the Specific Energy Absorption (SEA), which represents the amount of energy the structure can absorb per unit of mass, is more commonly used. To compute the SEA, the amount of energy the structure can absorb needs to be computed, which can be done using Equation 2.2. In the equation, P indicates the load on the structural element, which is subsequently integrated over the crushable length of the component (L_c).

$$E_{total} = \int_0^{L_c} P\mathrm{d}s \tag{2.2}$$

The obtained energy is subsequently divided by the mass (M_c) of the structural element, as depicted in Equation 2.3. A proposed formula for the mass is also suggested in the equation. The applicability of this equation naturally depends on the shape of the structural component. In this case, a tube-like element is assumed, with material density ρ and cross-sectional area A.

$$SEA = \frac{E_{total}}{M_c} = \frac{\int_0^{L_c} P \mathrm{d}s}{\rho A L_c} \tag{2.3}$$

The final indicator used to study the crashworthiness of structural elements is called the Crushing Load Efficiency (CLE). The CLE is given as the ratio between the mean crushing load (F_{mean}) and the peak load (F_{max}) a structural components experiences when subjected to crush loading, as depicted in Equation 2.4.

$$CLE = \frac{F_{mean}}{F_{max}} \tag{2.4}$$

The objective of the Crush Load Efficiency is to minimise the peak load. This factor is important when looking at the survivability of a vehicle's occupants. A structure can have optimal energy-absorbing behaviour; however, if the occupants experience excessive accelerations during the crash phase, the energy-absorbing structure is of no use. Under ideal conditions, the CLE value is equal to one, minimising excessive loads.

2.3 Crash Behaviour of a Fuselage

Now that it is clear what is required from an aircraft under crash conditions, and which means are used to measure its performance, it is important to study how an aircraft behaves under these loading conditions. During a crash, the fuselage is the main structure that ensures the passengers' survival by absorbing the energy of the crash. Therefore, this study focusses on this structure or a section of this structure. The fuselage's behaviour and the absorbed energy depend on the structure's failure modes and the material the fuselage is made from. Therefore, first, the structure's crash kinematics is analysed; subsequently, it is examined how the material selection influences the fuselage's behaviour.

2.3.1 Crash Kinematics

The first tests for crashworthiness stem back to the 1950s, which the National Advisory Committee for Aeronautics (NACA) performed. These tests were followed by a campaign performed by the FAA, sponsored by the National Aeronautics and Space Administration (NASA) in the 1980s. More recent experiments have been conducted on fuselage sections of a B737 and an A320, performed in the 1900s and beginning of the 2000s. A few examples of the latest test campaign results can be found in the upper part of Figure 2.2. In the displayed tests, two different scenarios can be observed, a graphical representation of which can be found in the lower part of the figures. Both scenarios revolve around the formation of hinge points in different locations in the fuselage's frame. Prior to the formation of these hinge points, the lower section of the fuselage is crushed, entailing the first stage of the crash scenarios. The second stage differs per scenario. In Scenario A, three hinge points are formed, one in the middle of the lower section, while the other two are formed symmetrically, along the fuselage's circumference. The location of the hinge points along the circumference of the fuselage is generally in the proximity of the struts supporting the cabin's floor, as indicated by location three in Figure 2.2a. In Scenario B, on the other hand, multiple hinge points are

formed, such that the keel section can be flattened out, as depicted in Figure 2.2b. Finally, depending on the remaining crash energy, in both idealised kinematics models, the struts supporting the passenger floor are crushed.

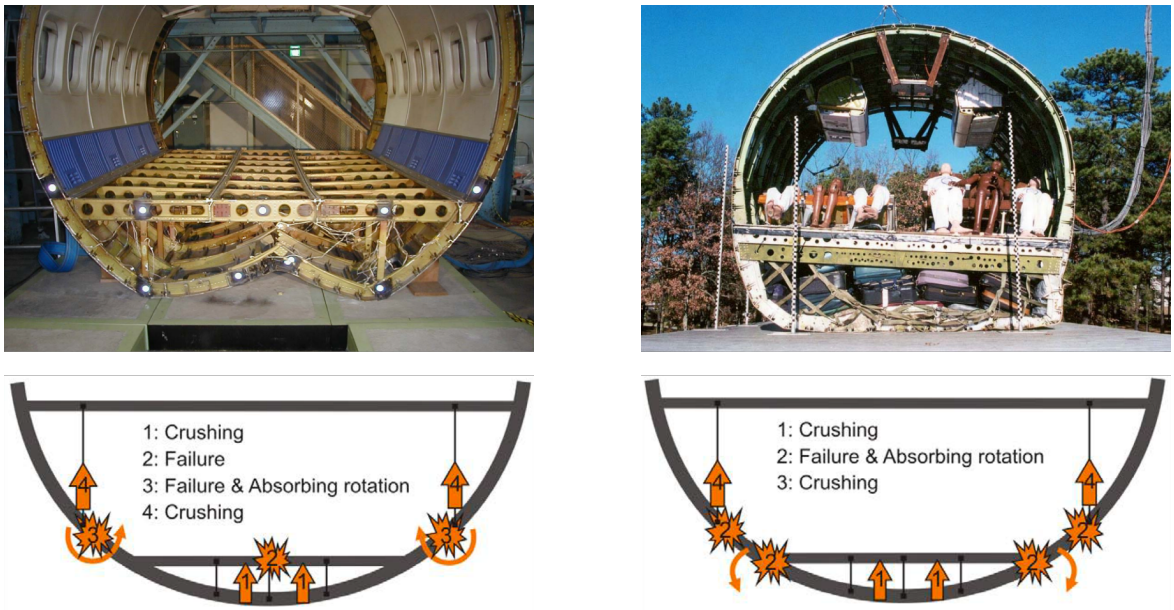

(a) Scenario A [7, 27] **(b)** Scenario B [7, 28]

Figure 2.2: Drop test of actual fuselage sections and corresponding idealised kinematics.

The kinematics described above are representatives for cases where no roll angle is present in the crash event. In research performed by H. Mou in 2015, the effect of the roll angle at impact is studied [29]. In the research, one can see how the three hinge points of Scenario A change in location as the roll angle is altered. Next to the shift in the hinge points' location, one can note that the roll angle affects the behaviour of the struts supporting the passenger floor. When the roll angle is increased, the load is introduced more directly into the strut, leading to its failure. Next to the change in behaviour of the struts supporting the cabin floor, it is found that the energy absorption effectiveness of the sub-cargo area is reduced, as the impact location changes. There are no requirements regarding the roll angle that an aircraft has to sustain in the event of a crash. Based on data provided by the National Transportation Safety Board (NTSB), it was concluded that a roll angle of ± 30 degrees is a reasonable design range when designing for crashworthiness [29]. It was found that this entails 65% of all crashes which are considered to be in the survivable range. In the future, the airworthiness authorities or the aircraft manufacturers themselves may implement these design requirements and therefore be taken into account when designing for crashworthiness.

2.3.2 Difference Between Metal and Composite Fuselages

The kinematics of the fuselage, described in the previous subsection, is exhibited in both metal, as composite designs. The way the various phases absorb the energy is, however, different. These differences are, therefore, investigated.

First, it must be stated that there are no specific requirements set for composite aircraft. Nevertheless, by looking at the special conditions published for the B787-8 and the A350-900, published in 72 FR 54531 and 79 FR 43237, respectively, it can be found that the composite designs shall have at least the same behaviour as similar metal aircraft [20, 21]. This means that these need to absorb the same amount of energy and transfer the same loads.

Due to the different behaviour of the two materials, the failure modes the two exhibit are also different, which in turn yields different energy absorption mechanisms. For example, in the research performed by Ren et al. in 2016, it is found that the hinges formed in the frame of a metal aircraft entail around 43% of the energy absorption of the fuselage [22]. This different behaviour of composite materials poses a new challenge for engineers, which have to produce new designs that can absorb equal amounts of energy.

When designed well, composite structural elements have excellent energy-absorbing behaviour. For example, in research performed by Bisagni in 2009, it is found that composite absorbers can deliver an increase in SEA of 47% compared to aluminium counterparts [9]. This increase in SEA can be achieved when the failure of the structural component is such that the material fails in a controlled manner. More details about the failure of composite structural elements are reported in Section 2.4.

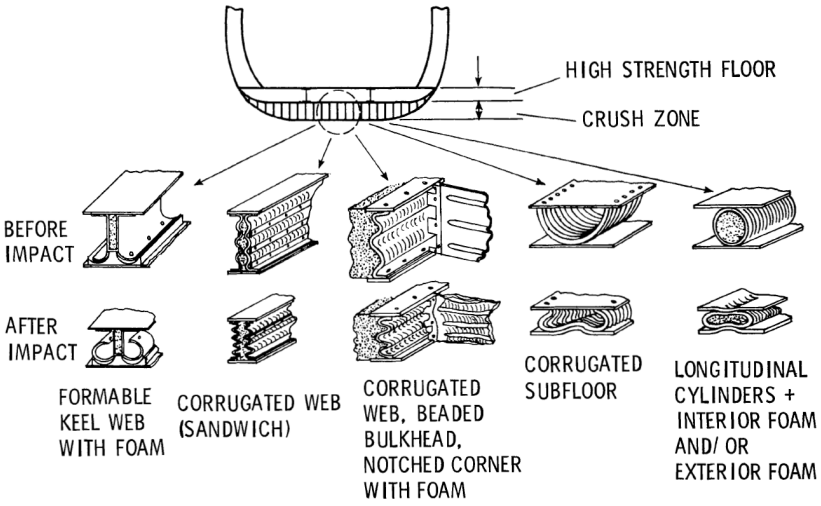

Figure 2.3: Energy absorbing concepts for lower sections of fuselages [6].

At this stage, a distinction has to be made between narrow and wide-body aircraft, as this influences the opportunities that the structure offers to absorb energy. In narrow-body fuselages, a large part of the energy needs to be absorbed by the keel section of the fuselage, entailing the sub-cargo floor section due to their smaller size. Wide-body aircraft dispose of more volume in the cargo area, which can be utilised to absorb energy. In this research, a narrow-body aircraft is studied. Therefore only solutions which can be implemented in this type of aircraft are reported. The options investigated to meet the frames' different behaviour to absorb energy have been based on designs developed for helicopters, as these vehicles also have limited space to house an energy-absorbing structure. Some of these examples can be found in Figure 2.3.

The further development of the structures used in helicopters has led to the introduction of energy absorber into the sub-cargo-floor section of the aircraft. The shapes that have

been studied range from simple c-shaped absorbers to more complex corrugated beams, some examples of which can be found in Figure 2.4. Most studies revolve around the implementation of these tube-like absorbers. Other studies investigate more complex types of absorbers, such as the tension absorber, under development by Waimer et al. [30]. This type of absorber still requires large amounts of research and is therefore not further considered in this study. Another attempt to meet the energy absorption requirements is the use of hybrid materials. This way, one can use the properties of the composite material during nominal operation, while the plastic properties of the metal material are used in crash loading [30]. At a coupon level, this new system showed an improvement; however, when the hybrid material is incorporated into a frame-like structure, this behaviour is not observed anymore.

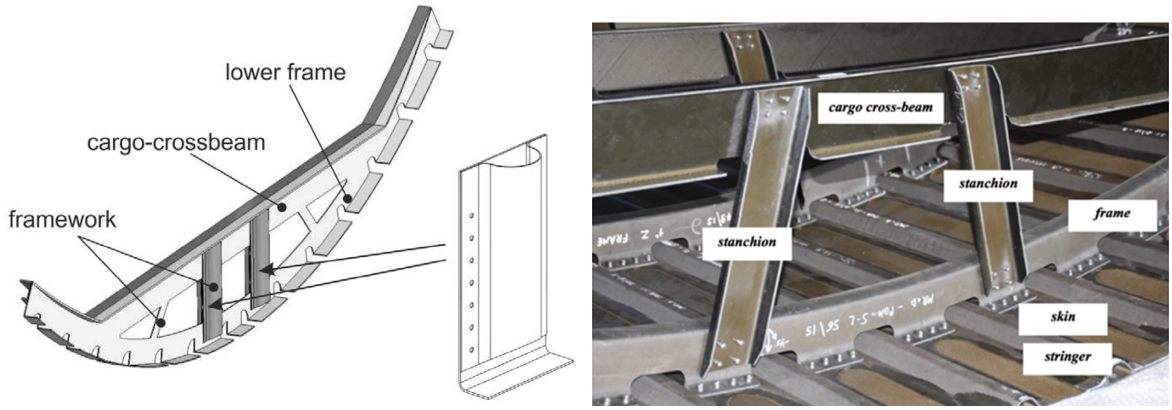

(a) (b)

Figure 2.4: Shock absorber as suggested by Waimer [7] (a), and Guida et al. [8] (b).

2.3.3 Modeling the Crash Behaviour of a Fuselage

In Subsection 2.3.1, it has been shown how in the past physical tests have aided engineers to analyse a fuselage section's behaviour subjected to crash loading. Currently, physical testing is being accompanied more and more by computer models, which simulate the performed tests. By doing so, costs can be reduced, while a larger variety of loading conditions can be tested more easily. Also during crashworthy analyses, finite element tools are used to predict the structure's behaviour more and more.

The oldest simulations for crashworthiness entail a simplification of the structure using Lumped Parameter Models (LPM). These models are mostly used in the automotive industry to predict the acceleration of different bodies [31]. This modelling technique is accomplished by simplifying the main components with rigid masses connected with springs. Subsequently, given an input loading, the acceleration of the different bodies, including passengers, can be computed. Over the years, these models have become more detailed by including volumes, leading to the creation of Multi-Body Models (MB). The further development of these models has led to the creation of finite element software, which is considered the modern standard.

Some examples of finite element modelling for aircraft crashworthiness can be found in work published by Gransden and Alderliesten in 2019 [32], where a comparative study is performed between a metal and a composite aircraft fuselage section. On the other hand, in research

published by Song et al. in 2018 [33], a full-scale model is created for aircraft certification. From these papers, it becomes clear that simulating the crash behaviour of an aircraft, or even only a fuselage section, is a complex task, which requires a large amount of time to both set up as to run. Therefore, research published by Waimer in 2013 aims to reduce the complexity of these models [7]. This is achieved by simplifying the complex behaviour of some locations in the structure, such as the hinge locations described in Subsection 2.3.1, by a series of axial and rotational springs, as depicted in Figure 2.5. By doing so, the complex behaviour of structural components can be studied in an isolated manner, while the overall structure can be modelled more efficiently.

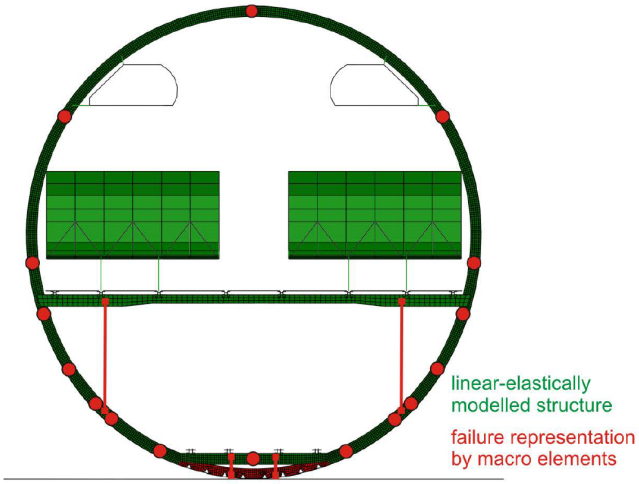

Figure 2.5: Kinematics model as suggested by Waimer [7].

2.4 Crash Behaviour of Structural Elements

In the previous section, it has been shown that structural elements are required in the sub-cargo floor section to serve as an energy absorber. It has been seen that these may assume different shapes, such as C-struts or corrugated beams. To further understand the behaviour of these structural components, more detailed research is performed concerning these components.

It is first investigated how composite tubes behave when subjected to crush loading. Here it will be seen that there are different failure modes, which are accompanied by various phenomena. From this, it will become clear that some failure modes are more beneficial with respect to others when considering energy absorption. After this, it is investigated what factors influence the occurrence of the failure modes. Finally, it is examined how the crush behaviour of composite structures can be modelled, where first, analytical methods are investigated, after which finite element techniques are studied.

2.4.1 Crush Behaviour of Composite Tube-Like Structures

Composite materials have different behaviour with respect to metal materials; because of this, their crushing behaviour is also very different. While metal materials are characterised

by ductile failure, composite materials are defined by brittle failure. This contrast leads to different crushing behaviour of energy absorbers. On the left-hand side of Figure 2.6 one can see an example of how a metal tube is crushed, while on the right-hand side, a crushed composite counterpart is represented. Here it can be seen that the metal tube is characterised by recurrent folding, with each fold roughly equal. On the right-hand side, one can observe the formation of the composite tube's splaying layers, which embodies the more brittle nature. Note that the figure presented on the right-hand side represents one failure mode for composite energy absorbers. Later it will be seen that these structural components may exhibit different failure modes when crushed.

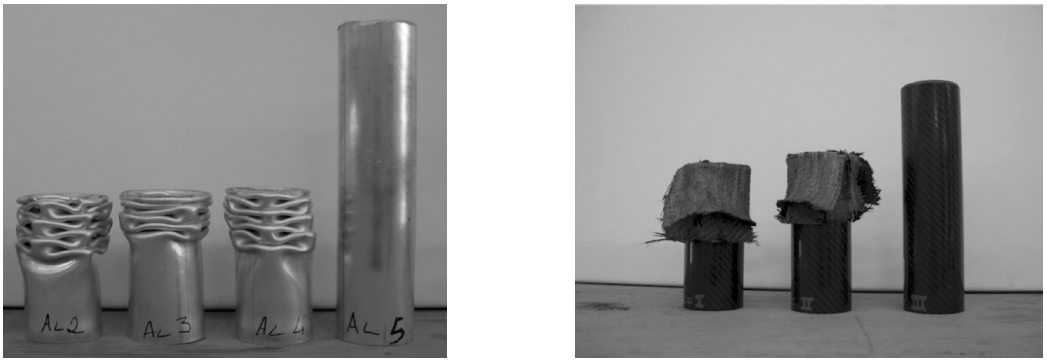

(a) Metal **(b)** Composite

Figure 2.6: Comparison between metal and composite crushing [9].

The different nature of the failure modes leads to a dissimilar load curve when crush specimens are tested. Figure 2.7 shows qualitative examples of how the load-displacement curves may be. In the figures, one can see three zones. The first zone represents the linear elastic regime of the crush specimens, where no permanent deformation occurs. Once the specimen is loaded beyond its maximum load, one enters Zone II, where the stable crushing load is achieved. It must be stated that not all specimens may achieve a mean load, while the magnitude of the mean crushing load also varies from specimen to specimen. The value and length of this stable crush regime greatly influences the energy that the structural component can absorb, as the area under the load-displacement curve gives the energy incorporated by the system. Finally, once the whole specimen has been crushed, the final compaction phase is obtained, depicted in Phase III, where the remaining material is further compacted. In Figure 2.7a, which represents the behaviour of a metal specimen, one can see that the mean crushing regime is characterised by a periodic behaviour, which originates from the intermittent folding behaviour of the specimen's sidewalls. In Figure 2.7b, which represents the load curve for a composite crush specimen, one can see that Zone II is not characterised by this periodic behaviour; it is more random, which originates from the accidental failures in the crush frond.

As stated before, the value of the mean crushing load is of great importance, as this influences the amount of energy that the specimen can absorber. One aspect that greatly influences the mean crushing load is the failure mode of the structural component. One of the first researches performed on the crushing of fibre reinforced polymers is performed by Hull in 1991, who classified the failure modes of composites in four categories [34]. The first failure mode entails global buckling of the specimen, which corresponds to Euler's buckling of beams. However, this represents the geometric failure of the specimen, while in this case, to absorb

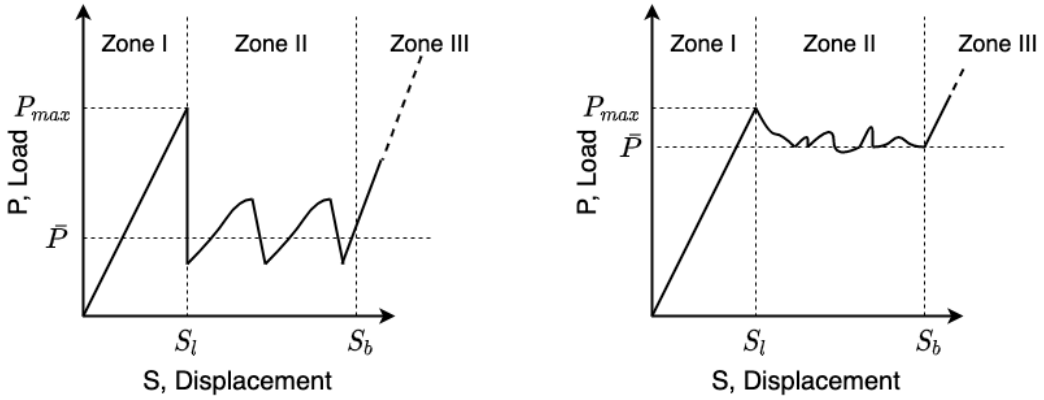

(a) Metal **(b)** Composite

Figure 2.7: Load curve comparison between metal and composite crushing.

more energy, material failure modes are desired. In Figure 2.8, one can see the different failure modes that a composite specimen may exhibit. In Figure 2.8a the folding failure mode is depicted, which is similar to the metal failure mode, that occurs when the composite material is flexible. As flexible materials are generally not used in aerospace structures, along with the fact that this failure mode does not absorb large amounts of energy, this failure mode is not further investigated. The other material failure mode is characterised by progressive crushing, which can be further categorised in two modes: progressive splaying and progressive fragmentation, represented in figures 2.8c and 2.8b, respectively. Generally, a combination of the two failure modes occurs, depending on the type of absorber. The progressive crushing failure modes entail a large number of material failures. These single failures may not dissipate large amounts of energy due to the stiff and brittle nature of composite materials. However, when all the single failures are combined, a large amount of energy can be absorbed. As Bisagni showed in 2005, fibre-reinforced composites have excellent specific energy absorption characteristics, by studying some applications in Formula One cars [23].

2.4.2 Influencing Factors on the Crush Behaviour

The previous subsection clarifies that the failure mode of fibre-reinforced composite structural components greatly influences the mean crushing load and energy absorption. However, it has not been discussed what influences the failure modes. There are namely various aspects that affect the failure modes and the stability of these crush specimens. This aspect is important as a failure mode needs to be assumed to derive the analytical equation.

Influence of the Material on the Crushing Performance

As stated before, the goal during the design of the energy absorber is to achieve the highest specific energy absorption. It has been described how the idealised failure mode is characterised by many failures; this way, the sum of the single failure leads to high energy absorption. Therefore, the ideal material promotes this type of failure while providing a large amount of energy per single failure.

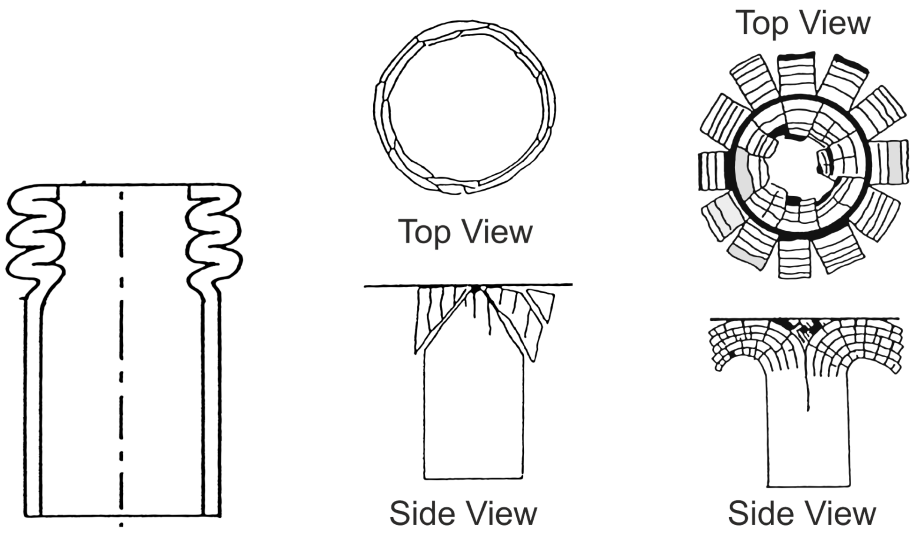

(a) Folding **(b)** Fragmentation **(c)** Splaying

Figure 2.8: Composite energy absorber failure modes [10].

A good example of good material selection can be found in the research performed by Hamada et al. in 1995 [35]. In the referenced paper, a SEA of 180 kJ/kg is achieved using thermoplastic material, which is almost double the value of what is achieved using carbon/epoxy counterparts. The higher SEA value can be attributed to the superior performance of thermoplastic materials regarding crack propagation. The material's molecular structure delays the final failure, enabling higher mean crushing loads and thus energy absorption, increasing the overall performance of the part [35].

Influence of the Layup on the Crushing Performance

The specimen's layup has a considerable influence on the crush specimen's stability. It is known that when laminates are designed, ideally, one has all the fibres in the load direction, such that a strong laminate is obtained. Therefore, one might think that this is also the case for energy absorbers, which is indeed the case, as shown by Chambe et al. in 2020 [36]. However, as with laminates, where one needs to account for multiple load cases and ensure the good behaviour of the laminate, also in crash absorbers, more orientations are required to stabilise the crush component. In fact, in the research published by Chamber et al., it is shown how using solely plies aligned with the specimen's loading axes leads to the formation of long vertical cracks, which causes the specimen to collapse. Using solely plies oriented horizontally with respect to the vertical loading-axes leads to circumferential cracks, risking the collapse of the structural component. Based on this, it is found that to have a stable crush regime, the laminate's orientations need to be such that it avoids the formation of long cracks, which is achieved by having multiple orientations in the laminate. Most importantly, it is found that the external layers of the specimen help bundle the inner layers, adding stability to the specimen.

Influence of Triggers on the Crushing Performance

To promote the formation of a stable crush regime and lower the crush specimens' initial peak load, triggers are used to initiate the crush frond. The first research papers regarding the use of triggers stem back to the 1980s. One of these papers is published by Hanagus [37], where the effect of a trigger is studied in a corrugated beam. Three different triggers were analysed: chamfer, ply drops, and notches. The study showed a clear correlation between the initiator's size and the mean crushing load, stating that a smaller initiator has a good impact on the mean crushing load. This change in behaviour can be attributed to the fact that a larger trigger requires more displacement until the steady crushing load is achieved. It is also stated that the trigger influences the peak load which the structure experiences. The trigger, therefore, has a large influence on the Crush Load Efficiency, defined in Section 2.2.

Other studies have confirmed that the most efficient trigger is a 45° bevel, as this provides a stable crushing load and lowers the peak load, enabling a higher Crushing Load Efficiency. More recent research developed more articulated triggers, such as Huang's research published in 2010 [38], where a crown trigger is suggested. With this shape, a 21.2% increase in crushing load efficiency is achieved compared to the traditional bevel trigger. Next to failure promoters fabricated within the specimen, external initiators have also been studied. These range from simple designs as presented by Y. Tong in 2018 [39], to more complex shapes as suggested by Heumbs in 2010 [11]. The trigger, as developed by Tong, is based on a semi circular-cavity, which bends the composite material outwards, driving it to failure. Due to the relatively closed section, the fibres are forced to break into smaller parts, increasing the energy absorption. The amount of fibre breakage is found to be dependent on the radius of the semi-circle. Finally, it is found that both tested radii are very efficient at keeping the initial peak load low. However, the biggest achievement is that an increase of 53% in the mean crushing load is achieved when using the semi-circle trigger in combination with specimens fabricated using braided T300 carbon axial tows in 5208 epoxy resin. More complex designs have also been suggested, which study how composite energy absorber can be joined into the surrounding structure, such as the shock absorber suggested by S. Heimbs in 2010 [11]. Figure 2.9 shows a Finite Element Model of the shock absorber in different phases of its deployment.

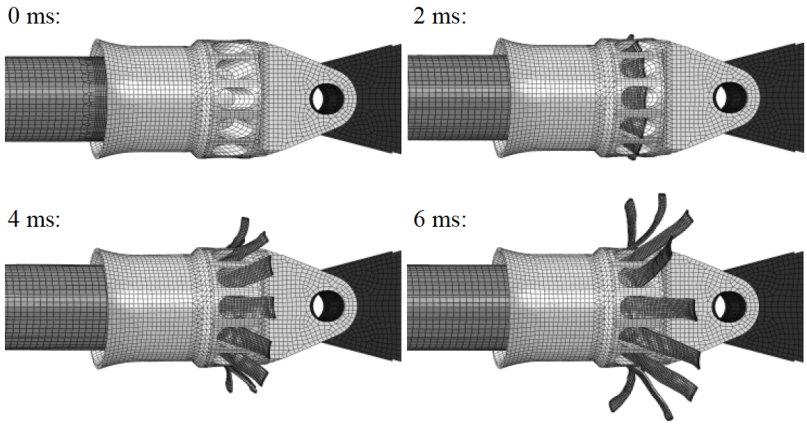

Figure 2.9: Different time steps of the finite element model on the deployment of Heimbs' shock absorber [11].

Influence of Manufacturing Methods on the Crushing Performance

The last two considered influencing factors are the impact of the specimen's manufacturing process and the loading rate. These have a minor influence on the energy absorption of the specimens. However, to provide a complete overview, these are reported swiftly.

One research that thoroughly investigates the influence of manufacturing regarding the mean crushing loads of fibre-reinforced composite specimens is published by Esnaola et al. in 2018 [40]. In this research, it is found that the inter-laminar shear strength (ILSS) has a large influence on the mean crushing load of the specimen. Therefore, manufacturing techniques that have a positive influence on this value also promote higher energy absorption. It was found that the distribution of fibres and matrix material, and void content have a large influence on the ILSS. For example, the compaction of the fibres is important to ensure good matrix material distribution. On the other hand, the voids act as crack initiators, which lead to lower crushing loads. It is found that by implementing the right manufacturing technique, an increase of 100% in SEA can be achieved.

Finally, it is found that an increase in material property homogeneity reduces the amount of fluctuation in the mean crushing regime.

Influence of the Loading Rate on the Crushing Performance

When inquiring about the influence of the loading rate regarding the properties of fibre reinforced materials, one obtains contradicting results. It is known that carbon fibres' material properties are independent of load rate, while the matrix materials generally are loading rate sensitive. Based on this knowledge, in the research performed by Farley et al. in 1987 [41], a conclusion is provided keeping these properties in mind. In the paper, it is stated that the energy absorption is indeed loading rate dependent. However, the degree of influence regarding the loading rate depends on the failure modes that characterise the failure of the composite specimen. In other words, when the failure of the specimen is matrix dominated, one can expect a large dependency regarding the loading rate. On the other hand, when the failure is fibre dominated, the influence of the loading rate is of a lesser influence.

Generally, when the loading rate increases, materials become more brittle, along with an increment in its failure stress. An example of this behaviour can be found in the paper published by Ploeckl et al. in 2017, where an increase in compressive strength of 60% is achieved [42].

With increasing loading rate and thus increasing the brittleness of the material, one needs to take into account that this may alter the failure mode of the structural component. The increased loading rate may, for example, lead to global buckling of the structure, which prevents it from absorbing large amounts of energy.

2.4.3 Analytical Models to Estimate the Crush Behaviour

In the previous section, it has become clear that the crushing behaviour and performance of a fibre-reinforced composite specimen depends on a multitude of variables, and it is therefore difficult to predict the value of the energy absorption and mean crushing load. However, when

designing a composite absorber, one desires to have direct insight into which parameters influence the aforementioned properties. Therefore, to meet this desire, studies have been performed to determine the absorbers' mean crushing load analytically. Some of the developed methods are presented in this subsection, while in Chapter 5 one of the referenced models is further expanded such that the mean crushing load of a wider variety of shapes can be predicted.

To determine the mean crushing load, two different approaches can be found in references. Older techniques rely on determining the buckling or failure of the splaying layers formed during the crushing process. On the other hand, more recent models consider the amount of energy dissipated by the failing material, which is balanced with the work being inserted into the system. With this equilibrium, the mean crushing load can be determined.

Two examples of the methods that consider the failure of the splaying layers can be found in work presented by Zhou in 1991 and Wolff in 1994 [12, 43]. Zhou's model considers all the delaminations present in the crush frond as beams, which, for the crush frond to propagate, need to buckle. Therefore, to determine the crushing load, one needs to determine the buckling loads of all the splits in the crush frond. As one can imagine, this method is rather complicated, as buckling of composites beams is an eigenvalue problem. Moreover, one can not determine how many and where the splaying layers are formed. Zhou does propose a simplification for this last problem, suggesting that statistical data can be used. However, as later will be seen, energy methods provide more manageable and accurate estimations of the mean crushing load. The method presented by Wolff also treats the formed splits as beams. However, in this case, the crushing load is determined by determining the bending load required to bend the splaying layers outwards, as depicted in Figure 2.10. This method is useful as it uses direct insight into the laminate properties, such as the A, B, and D matrix entries obtained from classical laminate theory. One big drawback of this method is that it requires empirical values to degrade the material properties in the crush zone.

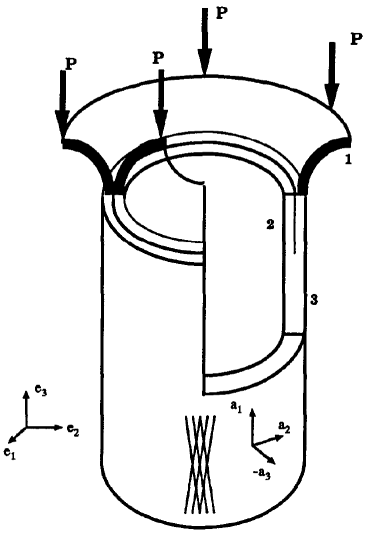

Figure 2.10: Beam bending model as depicted by Wolff et al. [12].

The first energy-based model was introduced in 1996 by Mamalis et al. [44], which studied the crushing of fibreglass tubes. In the energy-based methods, the crush frond geometry is of paramount importance, as by studying the frond, one can determine which failure modes need to be taken into account. Figure 2.11 shows how the analysis of the crush frond can lead to an idealised crush frond geometry. On the left-hand side, one can see the crush frond of the tested specimen, while on the right-hand side, one can see the idealised geometry.

The method developed by Mamalis is further developed in 1997 by the same author to study specimens with taper [45]. The method analyses the different sources of energy dissipation, which in this case are: friction, bending of the fronds, causing material failure, crack propagation between the splaying fronds, and the splits forming in the outwards bent material. By applying the energy method, and accuracy of around 15% is achieved. Also this method requires the calibration of empirical parameters, such as the characteristic crush stroke.

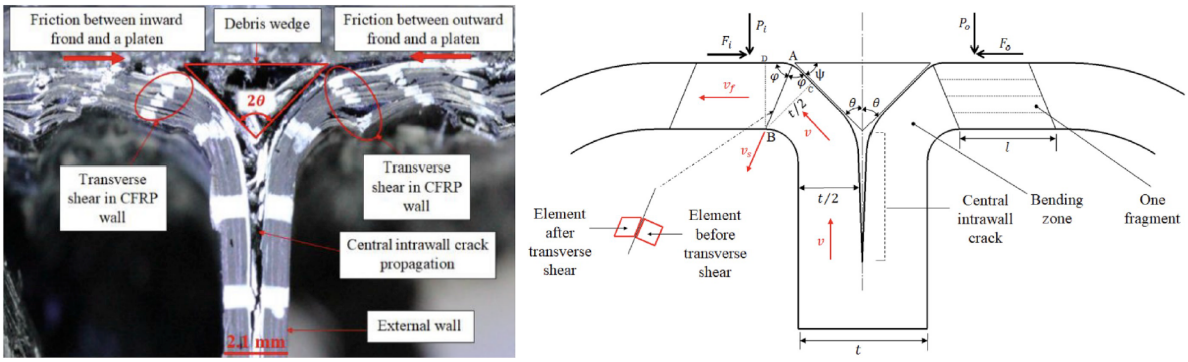

(a) (b)

Figure 2.11: Crush frond idealisation, with left a test specimen and right the corresponding idealisation [13].

To reduce the required empirical parameters, Boria et al. further developed this method by providing an equation for the crushing stroke [46]. The equation that Boria et al. obtained for the mean crushing load of a composite specimen can be found in Equation 2.5. In the equation, h represents the stroke length, which can be determined by applying a minimisation requirement on the crushing load, while f and g are a function of the specimen's properties, which can be obtained as depicted in Equation 2.6. The specimen properties, in this case, are t_1 and α, which are the thickness of the internal splaying layer and the angle of the external splaying layer, respectively.

$$P = \frac{\pi f\left(h, t_1, \alpha\right)}{2hg\left(t_1, \alpha\right)} \tag{2.5}$$

In Equation 2.6, T represents the laminate's thickness, α represents the external bending angle of the outward bending splaying layers, while ϕ is the taper angle of the specimen. Finally, t_1 represents the thickness of the inward splaying layer. The two λ terms, on the other hand, can be determined using Equation 2.7.

$$\begin{aligned} f =& 2hT\lambda_2 \sin(\alpha - \phi) + \left(\alpha - 2\phi \frac{t_1^2}{(T - t_1)^2 + t_1^2}\right)\lambda_1 + 2h \sin\phi\lambda_2 \left(T - 2t_1\right) \\ g =& -\cos(\alpha - \phi) - \mu \sin(\alpha - \phi) + \cos\phi + \mu \frac{2t_1 - T}{T} \sin\phi \end{aligned} \tag{2.6}$$

In Equation 2.7, σ_0 represents the laminate's ultimate failure stress, R indicates the specimen's radius, while σ_m denotes the ultimate out of plane shear strength of the laminate. Finally, T, and t_1, are as defined before, the thickness of the laminate and the inward bending splaying layer, while ϕ is the taper angle of the specimen. This leaves the stroke length h undetermined, which, as stated before, can be determined by applying the minimisation of the mean crushing load, as introduced by Boria et al.. This yields Equation 2.8.

$$\begin{aligned} \lambda_1 &= \sigma_0(R + h\sin\phi)\left((T - t_1)^2 + t_1^2\right) > 0 \\ \lambda_2 &= h\sigma_0 + 2R\sigma_m + h\sigma_m \sin\phi > 0 \end{aligned} \tag{2.7}$$

In Equation 2.8, once again, θ_0 and θ_m indicate the ultimate in-plane tensile and out of plane strengths of the laminate, respectively. While T and t_1 indicate the laminate's and the inward splaying layer's thicknesses. Finally, R and ϕ indicate the specimen's radius and taper angle, respectively.

$$h = \sqrt{R\sigma_0 \frac{\left((T - t_1)^2 + t_1^2\right)\pi/2 - 2t_1^2\phi}{2\left(T\cos\phi - (2t_1 - T)\sin\phi\right)(\sigma_0 + \sigma_m \sin\phi)}} \tag{2.8}$$

With this equation and the data taken from the research of Gupta et al. [47], Boria et al. achieved an accuracy of 20%, which given the complex nature of the failure modes is acceptable.

This method's limitation is that it requires determining the stroke length of the crushing cycle, which is achieved; however, this method can be questioned. Therefore, in more recent work published by Hussein et al. in 2018, the use of energy has been converted into the use of energy rate, which makes the use of a loading stroke obsolete by utilising the loading velocity [13]. The method presented by Hussein et al. is, however, only applicable to straight and square tubes. Therefore, in Chapter 5, some assumptions are altered, such that a wider variety of structural components can be studied. Hussein's method also entails the study of the failure modes, along with the friction and the external work. The failure modes considered in this method are the formation of the central wall delamination, which is required to form the splaying layers. Furthermore, the splitting energy is taken into account, which originates from the vertical cracks formed in the loading direction. It is assumed that these form at the corners of the loaded specimen. Finally, the shearing energy rate is considered, which is required to push the splaying layers downwards. By combining and rearranging all the energy rates, one obtains the final form of the equation for the mean crushing load, as presented in Equation 2.9. In the equation, b represents the side length of the square specimen, G_{IC} represents the mode I fracture toughness of the material. σ_u and τ_s indicate the ultimate stresses for the specimen's material, loaded transversally in tension and out of plane in shear, respectively. ε represents the failure strain of the laminate when loaded transversally in tension. t indicates the specimen's thickness, while μ indicates the friction coefficient. Finally, θ indicates the angle the debris wedge forms between the slaying layers with the specimen's vertical axis.

$$P = \frac{4bG_{IC} + \frac{\pi}{2}\sigma_u\varepsilon_f t^2 + \tau_s \frac{4b\cdot t}{\sin^2\varphi}\cos\theta}{1 - \mu\frac{\cos\left(\frac{\pi}{4} - \frac{\theta}{2}\right)}{\sin\left(\frac{\pi}{4} + \frac{\theta}{2}\right)}} \tag{2.9}$$

Using the equation depicted above, Hussein et al. can estimate the mean crushing load with the discrepancy going up to only 7% [13].

2.4.4 Finite Element Modeling of Crushing Behaviour

To determine the mean crushing load of a composite structural component, rather than using the analytical equations, one can simulate the components' behaviour using finite element tools. Therefore, some techniques used to model the complex failure of composite crush specimens are described in this subsection.

When performing finite element analysis, one needs to make a trade-off between computational effort and accuracy. One commonly known problem with this is the mesh size. By reducing the mesh size, one generally increases the accuracy of the solution; by doing so, however, the size of the problem also increases, leading to additional computational time. This is naturally also the case for the crushing of fibre reinforced composites; however, one additional aspect needs to be included in this case. The failure mode of this type of structural components entails the formation of delaminations. Therefore, to accurately predict this phenomenon, the model should be able to capture these failure modes. To achieve this, multi-layer models have been created [17, 48, 49]. Frequently, composite laminates are modelled using a single shell approach, which incorporates all the lamina layers of the laminate. This approach, however, is not able to accurately predict delaminations. In the multi-layer models, every lamina is modelled using a shell element, which are subsequently stacked to obtain the laminate. The interaction between the laminas is modelled using tie constraints with failure or, more commonly, using cohesive elements. This method enables the estimation of the formation of delaminations; however, this drastically increases the degrees of freedom of the problem, and thus the computational effort.

Next to the modelling of the part, material behaviour is of importance. Most finite element tools have built-in material models, which dictate the material's linear elastic behaviour, but in this case, more importantly, the failure and post-failure behaviour of the material. In this study, two finite element tools are considered, Abaqus and LS-Dyna. Both offer different opportunities when defining material. The previously cited papers all implement user-defined material subroutines for Abaqus. This is rather complex and therefore lies outside the scope of this study. Abaqus, however, also offers built-in composite material models, which are used in this study. The built-in material model in Abaqus is based upon Hashin's failure criterion, which implements energy dissipation in its post-failure regime [50]. LS-Dyna, on the other hand, offers a multitude of material cards. More importantly, these material cards offer the possibility to degrade material properties in the crush frond, mimicking the behaviour of delaminations and cracks [51]. In reference research, it is found that this parameter enables the user to accurately recreate the crush behaviour of fibre reinforced composite structural elements [14, 52]. One downside of this parameter is that it requires calibration with test data, preventing engineers from performing predictive analysis.

Because of these differences, the two finite element tools are compared, to study which can be used effectively in future research. More details about the material models are provided in Chapter 3, where the material cards are selected and described.

2.5 Literature Study Conclusions

In this chapter, it has been studied what aspects are of importance when studying the crash-worthiness of an aircraft fuselage.

First, research has been performed regarding the requirements that have been set for an aircraft under crash conditions. The most important takeaway is that the required impact speed is 30 ft/s, which is based on reference data, by studying what is considered a survivable impact velocity. Along with the given impact speed, maximum accelerations which the passengers may experience are reported.

Afterwards, it has been investigated what parameters are used by engineers when evaluating the design of an aircraft structure for crashworthiness. Energy dissipation is crucial during a crash event, as the aircraft's kinetic energy needs to be dissipated. Therefore, these parameters mainly focus on the energy absorption of a structural element and the specific energy absorption, which considers the component's mass.

Once all the parameters and requirements have been gathered, the behaviour of the fuselage has been studied. Here it is found that when these types of structures are subjected to crash loading, these exhibit two types of characteristic deformation kinematics. Both revolve around the formation of hinge points in the frames along the circumference of the fuselage. These hinge points enable the deformation of the structure, so to absorb the energy. It is found that in a metal aircraft, more than 40% of the energy is absorbed by the frames. Due to the different behaviour of composite materials when subjected to crash loading, the way these materials absorb energy is also different, requiring re-evaluating designs. Furthermore, little knowledge is available regarding the crashworthiness of thermoplastic composites. Nevertheless, it has been found that due to the different molecular structure, thermoplastic materials may lead to an increase in energy absorption with respect to their thermoset counterparts.

To further study the crashworthiness of an aircraft fuselage, composite energy absorbers have been researched. Here it is found that these type of structural components may exhibit different crushing behaviours, depending on a multitude of variables. The most important aspects are found to be the material properties, to sustain fragmentation crushing, and a trigger to ensure the desired crush frond and promote the crush initiation. Finally, some analytical models have been studied to predict the crushing behaviour of composite energy absorbers. The most accurate and implementable models were found to be energy-based models, with accuracies that vary between 7 and 20%. However, these models are restricted to a limited amount of structural components.

From the study, it becomes clear that research is required, which predicts the crash behaviour of structural components analytically. This way, the behaviour of isolated structural components can be assembled using the simplified global models, such as the kinematic model suggested by Waimer. By doing so, the crash behaviour of an aircraft fuselage can be predicted without the need for complex and lengthy finite element simulations, enabling designers to obtain fast results in the initial design stages.

Chapter 3

Material Test Simulations

To perform the verification of the analytical model, finite element simulations are performed to acquire reference data. Therefore, the simulations need to capture the complex behaviour of the composite material subjected to crush loading as described in Chapter 2. Different material models are available in different finite element software to capture the failure behaviour of composite materials. Therefore, before modelling the complex crushing behaviour of composites, one needs to understand the material's behaviour in a more controlled situation; hence, material tests are simulated to gain more insight into the material models.

The first section describes how physical material tests are performed, such that these standards can be adopted when modelling the tests. Afterwards, the different material models are described in Section 3.3, followed by the description of the simulated specimens' material properties. Subsequently, in Section 3.4 the results of the simulations are described, and the differences between the different material models are pointed out, the conclusions of which are reported in Section 3.6

3.1 Material Test Standards

To ensure a good quality of the material test simulations, the testings standards here considered are those provided by the American Society of Testing Materials (ASTM). The material is tested both in tension and compression to study the behaviour in both load cases. Furthermore, three different types of layups are studied, one with all the fibres aligned in the loading direction ($[0]_8$), one with all the fibres normal to the loading direction ($[90]_8$), and finally a quasi-isotropic layup ($[0/\pm 45/90]_s$). In the tests standards, recommended widths, lengths, and thicknesses are provided, along with the clamping region's length, called tabs, required to introduce the specimen's load. Finally, recommendations for the loading speed are provided. All these specifications are presented in the following subsections.

Tension

For the tensile simulations, the D3039/3039M - 08 standard is adopted [53]. The recommended dimensions for the tensile coupons can be found in Table 3.1.

Another important aspect is the specimen's loading speed, as too high loading rates may lead to premature failure of the specimen, caused by inertial effects. In contrast, low loading rates may lead to an unacceptable simulation time. According to the D3039 - 09 testing manual, the testing speed can be controlled in two manners, strain or head-speed controlled. For the former, a maximum speed of 0.01 min^{-1} is prescribed, while for the latter, a loading rate of 2 mm/min is suggested [53].

Compression

The standard adopted for the compression simulations is the D3410/D3410M - 16 standard [54]. The dimensions for the coupons prescribed by the standard can be found in Table 3.1.

As with the tensile tests, the loading speed is reported in the standard, which is given to be 1.3 mm/min.

Table 3.1: Dimensions and layups of material test specimens for different loading cases.

Loading Case	Layup	Length [mm]	Width [mm]	Thickness [mm]	Tab Length [mm]
Tension	$[0]_8$	250	15	1	55
Tension	$[90]_8$	175	25	2	25
Tension	$[0_2/\pm 45/90_2]_s$	250	25	2.5	55
Compression	$[0]_8$	155	10	2.5	65
Compression	$[90]_8$	155	25	2.5	65
Compression	$[0_2/\pm 45/90_2]_s$	155	25	2.5	65

3.2 Material Coupon Modelling

Two different finite element tools are used for the material tests simulations and for the tubes crushing, as both software offer different material models. This way, the performance of the different material models can be studied in the crushing simulations. Even though the material models change, the overall modelling technique between the material models and Finite Element (FE) software is equal, as far as the software allows, to have a valid comparison. Therefore, the modelling technique is first described, which applies to both FE software, while afterwards, the different material models are presented.

There are different aspects of importance during the modelling procedure, all of which are described in the following subsections.

Meshing and Element Type

All the material coupons are modelled as rectangles, with the dimensions provided by Table 3.1. All the specimens are meshed with 5 mm by 5 mm shell elements. In Abaqus, the 4-node doubly curved shell, reduced integration, hourglass control, small membrane strains shell elements are used (S4RS). Note that in general aerospace applications, similar elements are used, however, with no membrane strains. It is found that the addition of the small membrane strain in the element improves the compression behaviour of the shell elements. In LS-Dyna, a similar element type is chosen, known as the Belytschko-Tsay elements, with Reissner-Mindlin kinematics, which can be achieved by setting ELFORM to 2 in the CONTROL_SHELL card.

Loading and Boundary Conditions

Tabs need to be modelled to introduce the load into the test specimens. The tabs' behaviour is achieved by controlling the displacement of the nodes situated in the tab area utilising a reference point. Therefore, two reference points are created, one at each side of the specimen, one of which is fully clamped to represent the fixed-end of the testing fixture. In contrast, the other side is restricted in all but one degree of freedom, to load the specimen. The loading of the specimen is controlled by altering the displacement at one end of the coupon. The rate at which this displacement is introduced depends on the loading type. The ASTM standards prescribe a speed of 0.03 mm/s and 0.02mm/s for tensile and compressive tests, respectively. For the performed compression tests, this rate has been implemented, while for the tensile tests, the speed has been increased to reduce the simulation time. Hence an increment of 0.15 mm/s is adopted. By changing the loading, one needs to ensure that no premature failure occurs in the specimen. This can be done by verifying the lamina's failure stresses. As later will be seen in the results, the adopted rate does not cause the test specimens' premature failure.

Simulation Type

All the material tests are performed using the FE software's explicit solver; this is done because the crushing simulations are also performed with this solver; therefore, the results obtained from the material tests are more inherent to later steps of this research.

Composite Modelling

Finally, the layup of the specimens needs to be assigned to the coupons. In both programs, this can be achieved with different methods. For the case at hand, the lamina material is defined separately, and are subsequently stacked to obtain the full laminate. Also, the orientation of the laminate can be defined using various techniques. In both FE codes, the layup is defined based on the coordinate system of the shell element. This method is chosen as it is found that this type of orientation definition is most accurate when element undergo large deformations [55]. This may not be important during the material test; however, the shell elements may undergo large deformation during the crushing simulations, leading to this method's necessity. Using the orientation of the shell elements, the connectivity of the nodes

of the element dictates the orientation of the material. Figure 3.1 shows how the orientation of a shell element is determined. Here, one can see that the x-axis of the shell element is determined by going from node one to two, while the y-axis is formed by going from node one to four. Finally, the z-axis is formed by completing the right hand based coordinate system. The laminate's coordinate system is based upon the orientation of the element, to which, when desired, an additional rotation can be given depicted by β in Figure 3.1, leading to the a, b, and c coordinate system of the laminate. Finally, each layer's orientation can then be determined separately, based upon the laminate's coordinate system, where a represents the zero direction, while b represents the traverse direction. Finally, the normal direction (c) can be determined by completing the right hand based coordinate system.

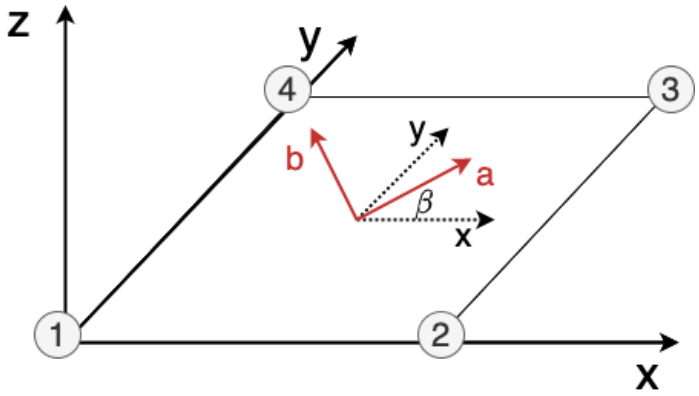

Figure 3.1: Shell element connectivity and material orientation.

The number of integration points per node differs between the FE codes. Abaqus automatically assigns three integration points per layer, while LS-Dyna only assigns a single integration point per layer. Figure 3.2 shows how the different lamina layers are stacked with respect to the shell elements and how the integration points are subsequently defined. In the example, a single integration point per layer is taken. When more integration points per layer are considered, these are distributed over the thickness of the lamina. In Abaqus, the number of integration points can be changed by altering the composite layup definition's entry. In LS-Dyna, the number of integration points is controlled by the MAXINT entry in the DATABASE_EXTENT_BINARY card. Furthermore, to account for the different strains that the different layers of the composite layup may experience, lamination theory needs to be activated in LS-Dyna in the CONTROL_SHELL card by setting the LAMSHT flag equal to one. The definition of the lamina material, especially the damage onset and its propagation, is where the FE codes differ; therefore, these are treated separately in the following section.

Figure 3.2: Laminate integration points per lamina layer.

3.3 Finite Element Software Material Models

The above-mentioned modelling techniques are, to a certain extent, equal in the two finite element tools. The material models, on the other hand, is where the software differ. Therefore, these are treated separately in this section to shed light on the different models, how they behave under different loading conditions, and which variables dictate their behaviour.

3.3.1 Abaqus Material Models

In Abaqus, there are three built-in methods to model damage in composite materials, stress-based, strain-based, or by implementing Hashin's failure criterion. The first two methods are very effective in simulations where it is only required to determine whether a material has failed or not, while Hashin's method also enables the user to study the material's behaviour beyond its failure load. In this study, the material's post-failure behaviour is of paramount importance; hence, this failure mode is adopted. It must be stated that Abaqus also offers the possibility to implement personalised material model subroutines, called VUMATs; however, these are not considered in this study and therefore lie outside the scope of this study.

Hashin

Hashin's failure criterion considers four different failure criteria, distinguishing between fibre and matrix failure, and tension and compression. The failure criteria are evaluated for every integration point through the thickness of the laminate. Subsequently, all the integration points through the laminate's thickness need to fail for the node to fail.

The equation for the failure index for fibres loaded in tension, indicated by F_f^t, can be found in Equation 3.1. In the equation, the $\hat{\sigma}_{11}$ term indicates the effective tensile stress at the integration point in the fibre direction. At the same time, X^T represents the lamina's tensile strength in the fibre direction. Similarly, $\hat{\tau}_{12}$ and S^L represent the effective shear stress and strength respectively at the integration point. The α term represents the contribution of the shear stress to the failure of the integration point, which in Hashin's original model has a value of 1 [50].

$$F_f^t = \left(\frac{\widehat{\sigma}_{11}}{X^T}\right)^2 + \alpha\left(\frac{\hat{\tau}_{12}}{S^L}\right)^2 \tag{3.1}$$

For fibres loaded in compression, Equation 3.2 can be used to determine the failure index, which is denoted with F_f^c. As before, $\hat{\sigma}_{11}$ represents the effective stress value in the fibre direction, while X^C represents the compressive strength of the lamina in the fibre direction.

$$F_f^c = \left(\frac{\widehat{\sigma}_{11}}{X^C}\right)^2 \tag{3.2}$$

The tensile traverse failure index, denoted with F_m^t, can be obtained similarly to the tensile fibre failure index, as can be seen in Equation 3.3. However, in this case, the values of for the effective stress ($\hat{\sigma}_{22}$ and $\hat{\tau}_{12}$) and the strengths (Y^T and S^L) are those of the traverse

and longitudinal direction, respectively. Note that in this case, the α factor is not taken into account.

$$F_m^t = \left(\frac{\widehat{\sigma}_{22}}{Y^T}\right)^2 + \left(\frac{\hat{\tau}_{12}}{S^L}\right)^2 \tag{3.3}$$

Finally, the failure index for traverse compression loading (F_m^c), can be computed using Equation 3.4. In the equation, all the terms have been defined before, while S^T represents the lamina's shear strength in the traverse direction.

$$F_m^c = \left(\frac{\widehat{\sigma}_{22}}{2S^T}\right)^2 + \left[\left(\frac{Y^C}{2S^T}\right)^2 - 1\right]\frac{\widehat{\sigma}_{22}}{Y^C} + \left(\frac{\hat{\tau}_{12}}{S^L}\right)^2 \tag{3.4}$$

In the equations for the failure indices, the effective stresses have been introduced. The effective stress can be obtained by converting the true stress of the integration point with the damage variable as depicted in Equation 3.5. In Equation 3.5 σ represents the true stress at the integration point, while M is the damage operator, populated by the d terms, which represent the internal damage variables. As with the failure indices, the internal damage variables have a fibre and a traverse direction, depicted with subscripts f and m, respectively, with both directions having values for tension and compression, with superscripts t and c, respectively. Other than the failure indices, the internal damage variable also has a shear direction, denoted with the subscript s. The definition of the internal damage variables can be found in Equation 3.6.

$$\widehat{\sigma} = \mathbf{M}\sigma, \text{ where } \mathbf{M} = \begin{bmatrix} \frac{1}{(1-d_f)} & 0 & 0 \\ 0 & \frac{1}{(1-d_m)} & 0 \\ 0 & 0 & \frac{1}{(1-d_s)} \end{bmatrix} \tag{3.5}$$

In the equation, the f, m, and s subscripts indicate the fibre, matrix, and shear directions, respectively, while the t and c superscripts indicate the loading case, tension, or compression. As the term suggests, the damage variable is important once damage has occurred; in fact, before the onset of damage, the damage operator $\mathbf{M}$ corresponds to the identity matrix.

$$d_f = \begin{cases} d_f^t \text{ if } & \widehat{\sigma}_{11} \geq 0 \\ d_f^c \text{ if } & \widehat{\sigma}_{11} < 0 \\ d_m^t \text{ if } & \widehat{\sigma}_{22} \geq 0 \\ d_m^c \text{ if } & \widehat{\sigma}_{22} < 0 \end{cases} \tag{3.6}$$

$$d_s = 1 - \left(1 - d_f^t\right)\left(1 - d_f^c\right)\left(1 - d_m^t\right)\left(1 - d_m^c\right)$$

Once damage has occurred, the damage operator influences the propagation of the damage and the material's final failure. Different criteria can be implemented to describe the material's behaviour beyond its failure point, where a commonly used method is the energy dissipation method. According to this method, the damage variable can be computed as depicted in Equation 3.7. In the equation, δ_{eq}^f represents the final failure displacement, while

δ_{eq} represents the equivalent displacement, and δ^0_{eq} represents the displacement at the onset of damage.

$$d = \frac{\delta^f_{eq}\left(\delta_{eq} - \delta^0_{eq}\right)}{\delta_{eq}\left(\delta^f_{eq} - \delta^0_{eq}\right)} \tag{3.7}$$

For a better understanding of the displacements, one can refer to Figure 3.3, where on the x-axis, the equivalent displacements are depicted, while on the y-axis, the equivalent stress can be found. The upward-sloping line in Figure 3.3 represents the material's linear elastic behaviour, which is valid until the material's failure stress is achieved. While the downward-sloping line represents the post-damage behaviour of the material

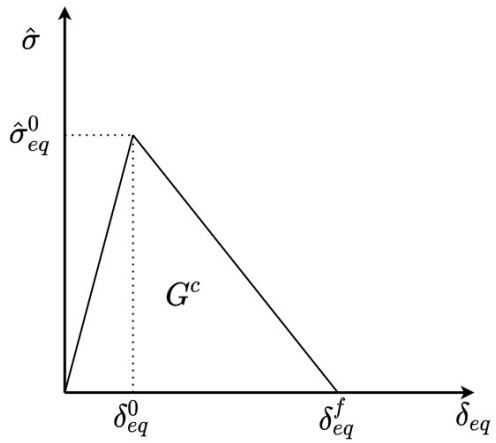

Figure 3.3: Qualitative tress-displacement curve for Abaqus' failure model.

The failure displacement depends on the failure strain and length of the element. The equation for the different failure strains for the different loading conditions and directions, can be found in Equation 3.8. Note that here the loading direction and loading state for the displacement terms (δ^{xx}_{eq}) are grouped into a single superscript, with ft and fc representing the fibre direction loaded in tension and compression, respectively, while mt and mc represent the corresponding loading cases in the traverse direction. In the equations, L^c represents the element length. The different ε terms represent the lamina's failure strains in the direction indicated by the subscripts, with 11 indicating the fibre direction, 22 in the traverse direction, and 12. the shear direction. Finally, α is, as defined before, the shear term's contribution leading to failure. Note that the $\langle\rangle$ is the Macaulay operator, which is defined such that $\alpha \in \mathfrak{Re}$ as $\langle\alpha\rangle = (\alpha + |\alpha|)/2$.

$$\begin{aligned}
\delta_{eq}^{ft} &= L^c \sqrt{\langle \varepsilon_{11} \rangle^2 + \alpha \varepsilon_{12}^2} \\
\delta_{eq}^{fc} &= L^c \langle -\varepsilon_{11} \rangle \\
\delta_{eq}^{mt} &= L^c \sqrt{\langle \varepsilon_{22} \rangle^2 + \varepsilon_{12}^2} \\
\delta_{eq}^{mc} &= L^c \sqrt{\langle -\varepsilon_{22} \rangle^2 + \varepsilon_{12}^2}
\end{aligned} \tag{3.8}$$

The failure strains are not given as an input into the program; in fact, the failure energy dissipation is given as an input in the FE program, denoted with G^c in Figure 3.3. This variable alters per failure direction and loading case, and is determined by computing the area under the curve depicted in Figure 3.3.

Along with determining whether damage occurs in the material, one needs the means to characterise its propagation, which is achieved using the damage variable. This depends on the type of simulation and the user's input. For example, the default maximum value for the damage variable is given as one; however, the user can lower this value. A qualitative example of how the damage variable evolves can be found in Figure 3.4. Once the maximum damage variable has been reached, the behaviour of the integration point depends on the simulation type. In Abaqus/Standard, the integration point fails once the material has failed in all directions. In Abaqus/Explicit, this occurs once the integration point has failed in the fibre direction. Note that all the integration points through the thickness of the specimen need to have failed in order for the entire node to be degraded.

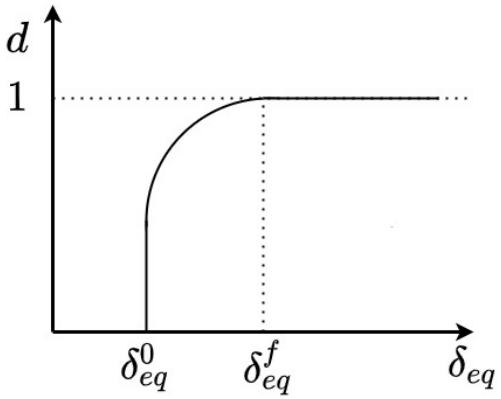

Figure 3.4: Qualitative example curve for the internal damage variable.

3.3.2 LS-Dyna Material Models

LS-Dyna offers different material cards to model composite materials. Therefore a few selection criteria need to be set up when selecting the adequate material card. First, the selected material cards need to offer the ability to define a lamina material, which can be used to

construct a laminate. Moreover, the material cards need to capture the behaviour of thermoplastic and thermoset materials with continuous fibres. Finally, the material cards need to be implementable with shell elements, as these are the most commonly used element types in the crash simulation industry [14]. Based on these requirements, the following material cards have been selected:

- MAT_ENHANCED_COMPOSITE_DAMAGE (MAT054)
- MAT_LAMINATED_COMPOSITE_FABRIC (MAT058)
- MAT_LAMINATED_FRACTURE_DAIMLER_CAMANHO (MAT262)

The three material models differ in both pre-failure behaviour as post-failure behaviour. An example of the material's behaviour loaded in compression in the fibre direction can be found in Figure 3.5, where on the x-axis, the strain in the material is depicted while on the y-axis, the stress is represented. The figure shows that the material models have a series of variables that need to be provided. These variables can be divided into two groups, mechanical properties and non-physical parameters. The mechanical properties are characteristics of the material that can be obtained during material testing. At the same time, non-physical parameters are variables that can be tuned in order to stabilise or tune a simulation. Examples of the material's mechanical properties are the Young moduli or the failure stresses, while non-physical variables can be softening parameters. The mechanical properties are commonly known material properties. These are reported in Section 3.4. The non-physical properties are proprietary to the specific material models, and are therefore described separately in the following subsections.

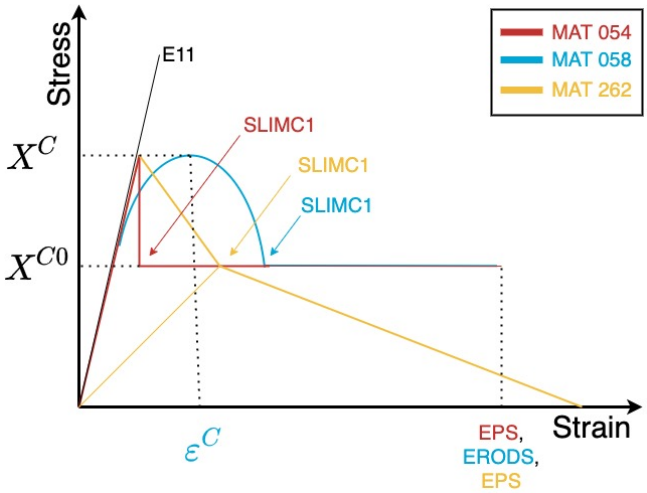

Figure 3.5: LS-Dyna's failure models (Image based on [14]).

MAT054

The Material Enhanced Composite Damage model, depicted in red in Figure 3.5, has a linear elastic behaviour until the material's failure stress is reached. Once damage has occurred, the

stress is limited to the stress limit value, the value of which is obtained with the SLIMXX variable, where the first X indicates the loading case, compression (C), or tension (T), while the second X indicates the fibre direction (1), or the traverse direction (2). Taking the example depicted in Figure 3.5, where the fibres are loading in compression yields the following form: SLIMC1. The stress level is sustained until the element is eroded. The erosion of the element can be controlled by three different variables: the effective failure strain of the material, the time-step, and the different failure strains of the material, for its various loading conditions. The failure strain and time-step element erosion control parameters are common to all studied material cards. When using the time-step for element erosion, a minimum threshold is given for the time-step to reach. When the time-step for the integration points becomes smaller than the provided minimum, the integration point is degraded. When using the strain limits, the maximum strain of the material needs to be provided, and when the provided value is reached, the integration point is degraded. Finally, the EPS parameter is similar to the failure strain; the strains in the different directions of the material are grouped into a single parameter. When the grouped strain value is higher than the provided EPS value, the integration point is degraded.

In order to determine the failure of an integration point, the MAT054 material model implements the Chang-Chang failure criterion [56], as depicted in Equation 3.9.

$$\begin{aligned} F_f^T &= \sqrt{\left(\frac{\sigma_{11}}{X^T}\right)^2 + \beta\left(\frac{\tau_{12}}{S^L}\right)^2} \\ F_f^C &= \sqrt{\left(\frac{\sigma_{11}}{X^C}\right)^2} \\ F_m^T &= \sqrt{\left(\frac{\sigma_{22}}{Y^T}\right)^2 + \left(\frac{\tau_{12}}{S^L}\right)^2} \\ F_m^C &= \sqrt{\left(\frac{\sigma_{22}}{2S^L}\right)^2 + \left[\left(\frac{Y^C}{2S^L}\right)^2 - 1\right]\left(\frac{\sigma_{22}}{Y^C}\right) + \left(\frac{\tau_{12}}{S^L}\right)^2} \end{aligned} \tag{3.9}$$

In the equation, the F symbols indicate the failure indices, in the fibre (f) and matrix direction (m), and in tension (T) and compression (C). The σ variable, with subscript 11, indicates the stress in the fibre direction, while the traverse direction is denoted with the 22 subscripts. τ_{12} represents the shear stress. The X, Y, and S^L terms indicate the maximum stress the material can sustain in the fibre, traverse, and shear direction, respectively. When the material is loaded in compression, this is depicted with the C superscript, while tension is depicted with T. Finally, the β symbol depicts the influence the shear stress has on the failure of the material.

Next to the failure and the degradation of the integration points, the MAT054 model offers the possibility to reduce the strength of the material when loaded in compression in the fibre direction once the matrix material has failed, leading to fibre buckling. The strength reduction can be achieved by adjusting the YCFAC variable, which computes the compressive failure stress in the fibre direction as a function of the compressive failure in the traverse direction as follows X^C =YCFAC·Y^C. Finally, another variable that is important in the post-failure regime is the SOFT variable, which reduces the strength of the neighbouring nodes of a failed

node. This non-physical parameter is of importance during crash simulations of composites, as this incorporates the formation of a crush-frond by replicating the formation of cracks and delaminations. Different studies have shown the influence of this parameter in crush simulations. It is found that this variable has a big effect on the stability and the value of the mean crushing regime [14, 52].

MAT058

The Material Laminated Composite Fabric material card, as depicted by the blue line in Figure 3.5, is characterised by non-linear behaviour around the failure of the material. This means that both in the pre-failure and post-failure regime, the material is characterised by material softening. As later will be seen, this has a positive influence on the solution's stability and the formation of a stable crush frond. The failure criteria used in this material card, which are based upon an alternate form of Hashin's failure criterion, are presented in Equation 3.10,

$$\begin{aligned} F_f^T &= \frac{\hat{\sigma}_{11}}{X_T} \\ F_f^C &= \frac{\hat{\sigma}_{11}}{X_C} \\ F_m^T &= \sqrt{\left(\frac{\hat{\sigma}_{22}}{Y_T}\right)^2 + \left(\frac{\hat{\tau}_{12}}{S_L}\right)^2} \\ F_m^C &= \sqrt{\left(\frac{\hat{\sigma}_{22}}{Y_C}\right)^2 + \left(\frac{\hat{\tau}_{12}}{S_L}\right)^2} \end{aligned} \tag{3.10}$$

All the terms in the equation are equal to the ones presented for the MAT054 model. However, the effective stress states are used as implemented for the Hashin failure criterion applied in Abaqus, which can be computed with Equation 3.5. Furthermore, in the MAT058 model, the internal damage variables are obtained as depicted in Equation 3.11. In the equation, m represents the parameter controlling the shape of the stress-strain response, while ε represents the actual strain, and ε_f indicates the failure strain of the material.

$$d_{ij} = 1 - \exp\left[-\frac{1}{m\varepsilon} \cdot \left(\frac{\varepsilon}{\varepsilon_f}\right)^m\right] \tag{3.11}$$

As shown in Figure 3.5, this material model avoids abrupt removal or changes in stress by having a non-linear behaviour pre and post-failure until reaching the post-failure stress limit. Like the MAT054 material card, the integration points are eroded depending on the time-step, and on the ERODS value, which has a similar meaning as the previously described effective failure strain. Finally, the MAT058 model, as with the MAT054 model, offers the possibility to degrade the properties of the neighbouring nodes of a failed node by altering the SOFT parameter, which can aid in forming a stable crush regime.

MAT262

The MAT262 material model is based upon the model developed by Maimí, Camanho, Mayugo, and Dávila [57], which is based upon a linearisation of the material's behaviour.

For failure in the fibre direction, a linear behaviour until failure is assumed, while a bi-linear behaviour post-failure is assumed (see Figure 3.6a). The material's behaviour in the traverse direction is dictated by both linear behaviour pre-failure as post-failure, see Figure 3.6b. Finally, the complex non-linear shear failure behaviour is approximated using a three-step linearisation as depicted in Figure 3.6c.

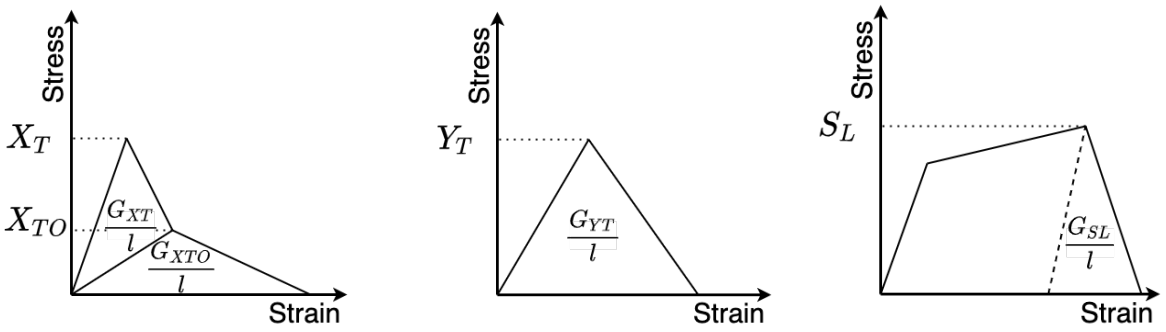

(a) Fibre **(b)** Traverse **(c)** Shear

Figure 3.6: Comparison of damage evolution law in the MAT262 material card for different loading directions.

The failure indices in the MAT262 material model consider the formation of fracture surfaces when the composite material is loaded in compression and the subsequent frictional forces that may arise, depending on the inclination of the fracture surfaces. The equation for the failure indices for the fibre direction can be found in equations 3.12 and 3.13.

$$\phi_{1+} = \frac{\sigma_{11} - \nu_{12}\sigma_{22}}{X_T} \tag{3.12}$$

$$\phi_{1-} = \frac{\langle |\sigma_{12}^m| + \mu_L \sigma_{22}^m \rangle}{S_L} \tag{3.13}$$

Equation 3.12 computed the failure index in the fibre direction when loaded in tension, depicted by the symbol ϕ_{1+}. In the equation σ_{11} and σ_{12} indicate the stress in the fibre and shear direction respectively, while ν_{12} indicates the Poisson ratio and X_T indicates the strength of the material in the fibre direction subjected to tensile loads. In Equation 3.13 S_L represents the shear strength of the material. In the same equation, σ_{12}^m, σ_{22}^m, and μ_L, can be found by implementing equations 3.14, 3.15, and 3.16 respectively. From these equations it can be seen how the formation of cracks influences the behaviour of the material.

$$\sigma_{12}^m = (\sigma_{22} - \sigma_{11}) \sin(\varphi^c) \cos(\varphi^c) + |\sigma_{12}| \left(\cos^2(\varphi^c) - \sin^2(\varphi^c) \right) \tag{3.14}$$

$$\sigma_{12}^m = (\sigma_{22} - \sigma_{11}) \sin(\varphi^c) \cos(\varphi^c) + |\sigma_{12}| \left(\cos^2(\varphi^c) - \sin^2(\varphi^c) \right) \tag{3.15}$$

$$\mu_L = -\frac{S_L \cos(2\phi_0)}{Y_C \cos^2(\phi_0)} \tag{3.16}$$

In the equations, S_L once again indicates the in-plane shear strength of the material, while Y_C indicates the strength of the material loaded in compression traverse. The σ terms indicate the material's stress state, with 11 indicating the fibre direction, 22 the traverse direction, and 12 the shear direction. ϕ_0 indicates the fracture angle for material loaded in pure traverse compression, the default value of which is 53°. Finally, the ϕ^c value can be computed as shown in Equation 3.17.

$$\varphi^c = \arctan\left(\frac{1-\sqrt{1-4\left(\frac{S_L}{X_C}+\mu_L\right)\frac{S_L}{X_C}}}{2\left(\frac{S_L}{X_C}+\mu_L\right)}\right) \tag{3.17}$$

In the above-depicted equation, the X_C andS_L terms indicate the stress limits of the material loaded in compression in the fibre direction, and in shear, respectively, while μ_L is as defined in Equation 3.16.

The traverse failure index of the material is computed using Equation 3.18. There is a distinction between the laminate loaded in compression or tension in the equation, leading to the two cases for the failure index. In the equation, S_L and Y_T represent the material's stress limit when loaded in shear or transversely in tension. In the equation, the σ terms indicate the stress states in the various directions of the material. Once again, the μ_L is introduced in the equation, which can be determined with Equation 3.16. Finally, a new term is introduced, g, which depicts the fracture toughness ratio, which is defined as G_{Ic}/G_{IIc}, where G_{Ic} is the mode one fracture toughness, while G_{IIc} represents for the mode two fracture toughness.

$$\phi_{2+} = \begin{cases} \sqrt{(1-g)\frac{\sigma_{22}}{Y_T} + g\left(\frac{\sigma_{22}}{Y_T}\right)^2 + \left(\frac{\sigma_{12}}{S_L}\right)^2} & \text{if} \quad \sigma_{22} \geq 0 \\ \frac{\langle|\sigma_{12}|+\mu_L\sigma_{22}\rangle}{S_L} & \text{if} \quad \sigma_{22} < 0 \end{cases} \tag{3.18}$$

The MAT262 material model also possesses a failure index for combined loading with compression in the traverse direction and shear loading. The equation for this failure index can be found in Equation 3.19.

$$\phi_{2-} = \sqrt{\left(\frac{\tau_T}{S_T}\right)^2 + \left(\frac{\tau_L}{S_L}\right)^2} \tag{3.19}$$

In the equation, the shear strength is defined by S_L, while there is also a corrected traverse strength, denoted with S_T, which can be computed using Equation 3.20. In the equation, Y_C represents the compressive strength in the traverse direction, while ϕ_0 is the fracture angle under pure traverse compression, the default value of which is 53°.

$$S_T = Y_C \cos(\phi_0)\left[\sin(\phi_0) + \frac{\cos(\phi_0)}{\tan(2\phi_0)}\right] \tag{3.20}$$

Finally, the τ_T and τ_L terms in Equation 3.19 can be determined as depicted below.

$$\begin{aligned} \tau_T &= \langle -\sigma_{22}\cos(\phi_0)\left[\sin(\phi_0) - \mu_T\cos(\phi_0)\cos(\theta)\right]\rangle \\ \tau_L &= \langle \cos(\phi_0)\left[|\sigma_{12}| + \mu_L\sigma_{22}\cos(\phi_0)\sin(\theta)\right]\rangle \end{aligned} \tag{3.21}$$

In Equation 3.21, the σ terms indicate the stress state of the material, with the directions denoted by the subscripts, while ϕ_0, is as before the fracture angle under pure compression. In contrast, θ can be determined using Equation 3.22. The σ terms indicate the stress states, and ϕ_0 represents the fracture angle under pure compression.

$$\theta = \arctan\left(\frac{-|\sigma_{12}|}{\sigma_{22}\sin(\phi_0)}\right) \tag{3.22}$$

Until failure is reached, the material behaves linear-elastically, while once failure has occurred, its behaviour is dictated by the compliance tensor represented in Equation 3.23.

$$\begin{bmatrix} \frac{1}{(1-d_1)E_1} & -\frac{v_{21}}{E_2} & 0 \\ -\frac{v_{12}}{E_1} & \frac{1}{(1-d_2)E_2} & 0 \\ 0 & 0 & \frac{1}{(1-d_6)G_{12}} \end{bmatrix} \tag{3.23}$$

In the tensor E_1 and E_2 represent the Young moduli in the fibre and traverse direction respectively, while ν_{12} and ν_{21} are Poisson ratios, and G_{12} is the shear modulus. The different d terms represent the damage variables, which depend upon the damage models described above.

3.3.3 Material Models Comparison

The presented material models present both similarities as large differences. Naturally, there are some differences regarding the failure indices, which are analytically defined, and therefore difficult to interpret qualitatively. Some clear differences can be noted, such as the MAT262, which considers crack formation and sliding interfaces, which the other material models do not include. On the other hand, by looking at the qualitative stress-strain relations of the material models, one can get a more intuitive understanding of the material's behaviour. All material models naturally present a linear elastic relation before failure. In the post-failure regime, the material models distinguish themselves. One commonality can be found between Hashin's material model in Abaqus and the MAT262 model in LS-Dyna. Both material models rely on energy dissipation in the post-failure regime. However, while all failure modes present in Abaqus are characterised by a bi-linear simplification as depicted in Figure 3.3, the MAT262 model distinguishes between the different failure modes, enabling tri-linear behaviour of the material, as depicted in Figure 3.6. The MAT054 and MAT058 material models, on the other hand, are characterised by stress and strain limits. The main difference between the two models is the brittleness of the model. While the MAT058 allows material softening in the failure regime, enabling non-linear behaviour, the MAT054 model presents an abrupt drop in the material's load-carrying capability. This behaviour can be clearly seen in Figure 3.5.

3.4 Material Properties

Now that the different variables dictating the material's behaviour in the various material models have been described, the actual values attributed to the variables can be presented. As before, the variables are separated into two groups, namely the mechanical properties,

which are variables common to all the material models, while the non-physical parameters are proprietary to the different material models. First off, the mechanical material parameters are defined, which are followed by the non-physical parameters. Once all material variables are provided, the coupon simulations are presented, from which the conclusions regarding the material models can be drawn, which are depicted in Section 3.6

Mechanical Properties

The material utilised in the coupon simulations is the unidirectional IM7/8552 prepreg from the world wide failure exercise [58], the mechanical properties of which can be found in Table 3.2.

Table 3.2: Mechanical material properties of IM7/8552 unidirectional composite lamina.

Variable	Symbol	Value	Unit
Mass density	ρ	1.58E-06	kg/mm^3
Young's modulus - Fibre direction	E_{11}	165000	MPa
Young's modulus - Traverse direction	E_{22}	9000	MPa
Shear modulus	G_{12}, G_{31}	5600	MPa
Shear modulus	G_{23}	2800	MPa
Poisson ratio	ν_{12}	0.0185	-
Tensile strength fibre direction	X^T	2560	MPa
Compressive strength fibre direction	X^C	1590	MPa
Tensile strength traverse direction	Y^T	73	MPa
Compressive strength traverse direction	Y^C	185	MPa
Shear strength	S^L	90	MPa
Tensile failure strain fibre direction	ε_{11}^T	0.01551	mm/mm
Compressive failure strain fibre direction	ε_{11}^C	0.011	mm/mm
Tensile failure strain traverse direction	ε_{22}^T	0.0081	mm/mm
Compressive failure strain traverse direction	ε_{22}^C	0.032	mm/mm
Engineering failure shear strain	γ_{12}	0.05	mm/mm

Non-Physical Properties for LS-Dyna

The non-physical material properties, which are required for LS-Dyna's material cards, are primarily based upon reference recommendations. At the same time, some are tuned to obtain a good correlation with test results. It must be noted that the non-physical parameters have a more extensive influence on the crushing behaviour of the material, which will be treated later in this report, as these have a minor influence on the coupon simulation results. Therefore, the values obtained during the calibration of the model for the crushing simulation, are discussed in Section 4.2.3. The non-physical variables used for the MAT054 can be found in Table 3.3. Note that more values can be altered into the material card; however, when these are not reported in Table 3.3, these variables are left unchanged with respect to the default value; this also holds for the other material cards. The non-physical material properties used in the

MAT058 card can be found in Table 3.4, while the ones used for the MAT262 card can be found in Table 3.5.

Table 3.3: Non-physical MAT054 card entries.

Variable	Symbol	Value	Units	Source
Stress limit fibres tension	SLIMT1	0.01	MPa/MPa	[51]
Stress limit fibres compression	SLIMC1	0.375	MPa/MPa	[14]
Stress limit matrix tension	SLIMT2	0.1	MPa/MPa	[51]
Stress limit matrix compression	SLIMC2	1.0	MPa/MPa	[51]
Shear stress limit	SLIMCS	1.0	MPa/MPa	[51]
Element time-step limit	TFAIL	1.0E-07	s	[14]
Crush frond softening factor	SOFT	0.8	-	[14]

Table 3.4: Non-physical MAT058 card entries.

Variable	Symbol	Value	Unit	Source
Tensile failure strain fibre direction	E11C	0.01551	mm/mm	[58]
Compressive failure strain fibre direction	E11T	0.011	mm/mm	[58]
Tensile failure strain traverse direction	E22C	0.0081	mm/mm	[58]
Compressive failure strain traverse direction	E22T	0.032	mm/mm	[58]
Maximum effective strain for element failure	ERODS	-0.55	mm/mm	[14]
Stress limit fibres tension	SLIMT1	0.01	MPa/MPa	[51]
Stress limit fibres compression	SLIMC1	0.375	MPa/MPa	[14]
Stress limit matrix tension	SLIMT2	0.1	MPa/MPa	[51]
Stress limit matrix compression	SLIMC2	1.0	MPa/MPa	[51]
Stress shear	SLIMCS	1.0	MPa/MPa	[51]
Element time-step limit	TSIZE	1.0E-07	s	[14]
Crush frond softening factor	SOFT	0.57	-	[14]

Table 3.5: Non-physical MAT262 card entries.

Variable	Symbol	Value	Units	Soucre
Effective failure strain	EFS	-0.55	mm/mm	[14]
Crush frond softening factor	SOFT	0.4	-	[14]
Fracture angle in transverse compression	FIO	55	deg	[51]
Fracture toughness for fibre compression	GXCO	1491.1	MPa	Computed
Fracture toughness for fibre tension	GXTO	957.2	MPa	Computed
Longitudinal compressive strength at inflection point	XCO	1367.4	MPa	Computed
Longitudinal tensile strength at inflection point	XTO	2124.8	MPa	Computed

3.5 Material Simulation Results

The different material models have been described in the previous sections, and the material parameters have been provided. In this section, the influence of these parameters is studied by performing simulations of material tests according to the D3039/3039M - 08 standard for tensile specimens, and the D3410/D3410M - 16 for compression specimens.

The material simulation results are all depicted using the same figure style, an example of which can be found in Figure 3.7. Two plots characterise each figure. The plot on the left-hand side represents the data as would be collected from the load-cell of a test set-up, while the plot on the right-hand side depicts the data as would be collected by a strain gauge. From the load cell, one obtains the load applied to the specimen and the corresponding displacement, which are depicted on the y-axis on the left side of the plot, and the lower x-axis. The obtained load and displacement can then be converted into the stress and strain using the equations depicted in 3.24. In the equation, F represents the load applied to the specimen, while A represents the cross-sectional area of the specimen obtained from the product between the specimen's thickness and width. The ratio between the load and the area gives the stress σ in the axial loading direction of the specimen x. The strain ε in the axial loading direction of the specimen is given by the ratio between the displacement in the loading direction, depicted by $u1$, and the initial length of the specimen l_0. Note that only the free length is intended by the specimen's initial length, determined by the difference between the total length and the total tab length.

$$\sigma_x = \frac{F}{A} \text{ and, } \varepsilon_x = \frac{u1}{l_0} \tag{3.24}$$

The load-displacement and stress-strain relations obtained from the load-cell are depicted in one plot, depicted on the figure's left-hand side. Therefore, two pairs of axis are obtained. The y-axis on the left-hand side and the lower x-axis can be used to read the load-displacement relation. While on the y-axis on the right-hand side and the upper x-axis, the stress-strain relation can be interpreted. The plot on the right-hand side of the figure represents the values extracted from a central node in the simulated specimen. In the simulations with a single orientation, the values of the fourth layer are depicted. In contrast, for the quasi-isotropic layup, the zero layer values are provided, as this layer leads to the specimen's final failure. The legend of the figure houses the line and marker styles of the performed simulations. Here, the ABQEla abbreviation indicates a simulation that has been performed in Abaqus, which does not include a failure model. ABQDam, on the other hand, indicates the simulation performed in Abaqus with Hashin's damage model. The remaining entries represent the simulations performed in LS-Dyna with the different material cards and are self-explanatory. Finally, in each figure, a horizontal dotted line indicates the expected material stress limit.

First off, in Subsection 3.5.1 the results from the tensile simulations are presented, which are followed by the results of the compression simulation, depicted in Subsection 3.5.2.

3.5.1 Tension Results

As stated before, different tensile tests are performed. First, an all 0 layup is simulated in order to verify the properties in the fibre direction. Subsequently, an all 90 laminate

is simulated in order to verify the traverse properties. Once these have been performed, a quasi-isotropic layup is simulated. All the laminates are constructed using eight layers.

$[0]_8$ Specimen

In Figure 3.7, one can find the results obtained from the tensile test of the $[0]_8$ specimen. As can be seen, all the material models reach the expected maximum strength of the lamina in the fibre direction. This means that the adapted loading rate is satisfactory for this simulation. Moreover, all the materials behave equally in the linear elastic phase, both for the load cell and strain gauge data. The material models differ however when the stress in the material is in the proximity of the failure stress, where the primary phenomenon that stands out is the non-linear behaviour of the MAT058 model, before failure, enabling it to achieve higher strain values at a similar stress level. The behaviour between the load-cell and the strain gauge is equal until failure. However, once failure has occurred, it is interesting to note that bot stress values go to zero, as expected; however, the final displacement values are different. As the load cell advances its displacement, these values grow. For the strain gauge, on the other hand, the node has failed, which means that the strain goes back to zero. In future simulations, it will be seen that this leads to noise in the results of the strain gauge data.

All the data supporting these conclusions, such as obtained Young moduli, failure stresses, and strains, can be found in Table A.1 in Appendix A.

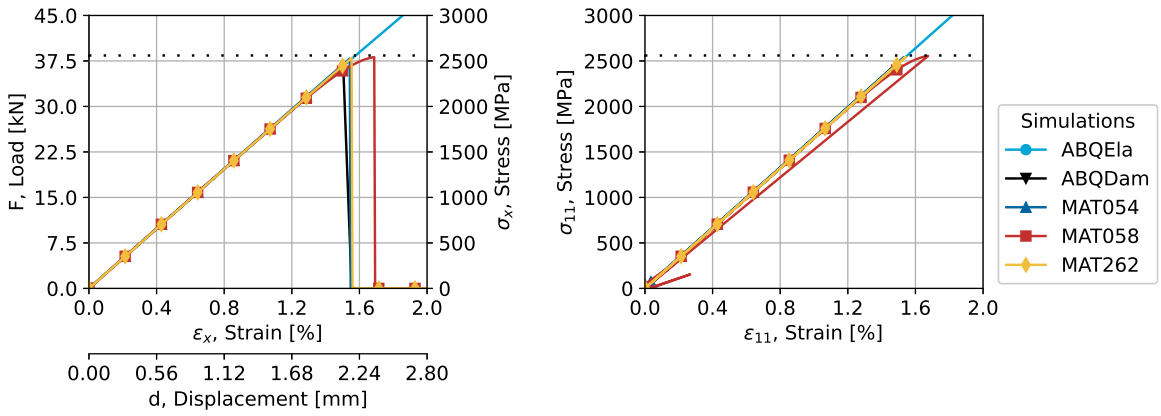

Figure 3.7: $[0]_8$ tensile specimen simulation results.

$[90]_8$ Specimen

In Figure 3.8 one can see the results of the simulation for the tensile test $[90]_8$ specimen, while in Table A.2 in Appendix A one can find the actual values for the ultimate stress and strain, accompanied by the obtained material moduli. As before, the material models behave equally in the linear elastic regime of the material, while MAT058 differentiates itself in the section leading up to failure, with its non-linear behaviour. It must be noted that the noisy behaviour of the material models is originated in the post-failure regime of the specimens, which are not of interest in this stage of the research.

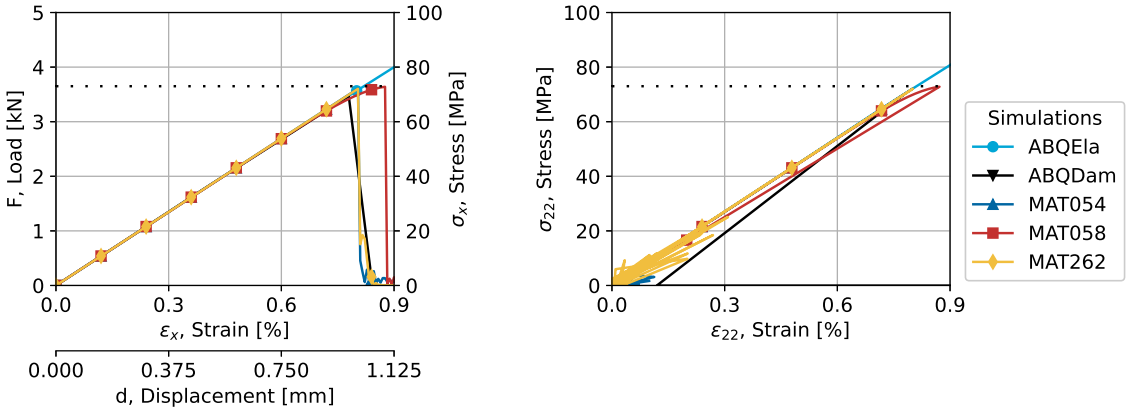

Figure 3.8: $[90]_8$ tensile specimen simulation results.

$[0/\pm45/90]_s$ Specimen

The last results for the tensile simulations can be found in Figure 3.9, which depicts the quasi-isotropic laminate results. It must be noted again that in this case, the right-hand side plot depicts the stress-strain relation for the zero degrees layer, as this layer is the last one to fail, controlling the final failure of the laminate. From these figures, it becomes clear how the laminate stress state differs from the lamina's stress state, as do the elastic moduli. Finally, it is interesting to note how the laminate fails gradually. It can be seen that first ply failure occurs at a displacement of approximately one millimetre, while last ply failure differs clearly from material model to material model. The main difference that can be noted is the extensive plateau that the MAT262 material model can sustain. The actual values of the final failure stress and strain and the moduli of the specimens can be found in Table A.3 in Appendix A

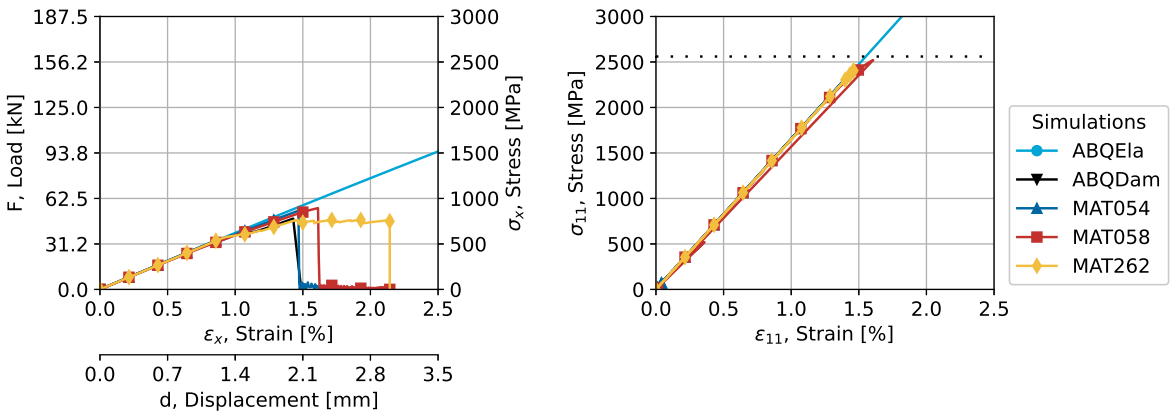

Figure 3.9: $[0/\pm45/90]_s$ tensile specimen simulation results.

3.5.2 Compression Resusults

The compression test results are presented in the same fashion as the tensile test results have been presented. It must be pointed out that compressive stress states and contractions are normally given as negative values according to the sign convention; however, all the values are given as positive values for convenience.

In the compression specimens' strain gauge results, the post-failure values are characterised by much noise caused by the failed specimen, which is loaded beyond its failure load.

$[0]_8$ Specimen

As with the tensile tests, the first specimen tested in compression is the specimen with solely zero layers. While during the tensile tests, there are only small differences regarding the results, the only one being the non-linearity of the MAT262, in the compression case, the difference between the different models can be seen as the stress limits dictate the post-failure behaviour of the specimens. The results of the simulations can be found in Figure 3.10. First, it must be noted that the specimens modelled in Abaqus fail prematurely in buckling. This leads to load eccentricities in the specimen, causing the specimen to fail. Finally, in the post-failure regime, one can see how the different stress limits for LS-Dyna's different material models lead to different stress plateaus until the final failure strain is achieved. Here already a large difference between the Abaqus and LS-Dyna material models can be found. The LS-Dyna's failure models can sustain post-failure loads by tuning the non-physical parameters. Abaqus' material model leads to abrupt failure, as the nodes and elements are removed from the simulation, due to the failure in the fibre direction. The failure values and the obtained moduli for this material test can be found in Table A.4 in Appendix A.

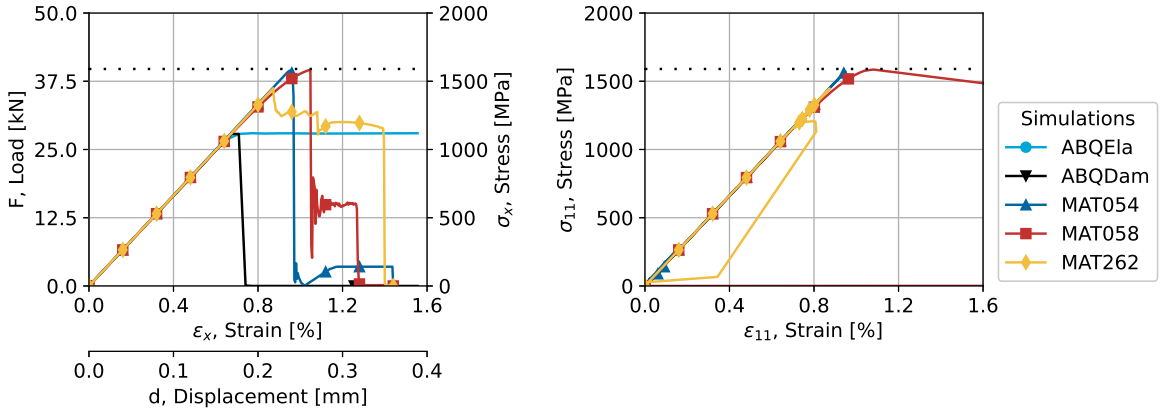

Figure 3.10: $[0]_8$ compression specimen simulation results.

$[90]_8$ Specimen

In the compression test of the $[90]_8$ specimen, the non-linear behaviour of the MAT058 material card can be seen in the region leading up to failure. It is interesting to note how

the non-linear behaviour already influences the behaviour early in the loading phase due to the material's lower modulus and failure strength. Moreover, the similarity between the two energy-based materials can be seen, which are characterised by brittle failure. The MAT054 and MAT058 specimens behave as expected, characterised by the stress limit sustained until the final failure strain is reached. Also here the difference between the loading cell and strain gauge data can be noted, where the MAT054 and MAT058 material models can sustain some load and displacement after failure. In contrast, both stress and strain values go to zero in the node data, taking into account the noise. The failure values and the obtained moduli for this material test can be found in Table A.5 in Appendix A.

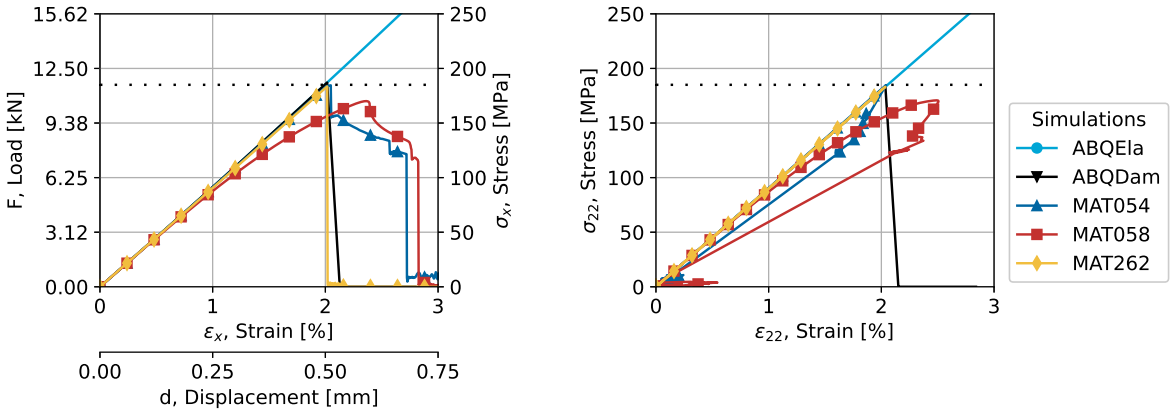

Figure 3.11: $[90]_8$ compression specimen simulation results.

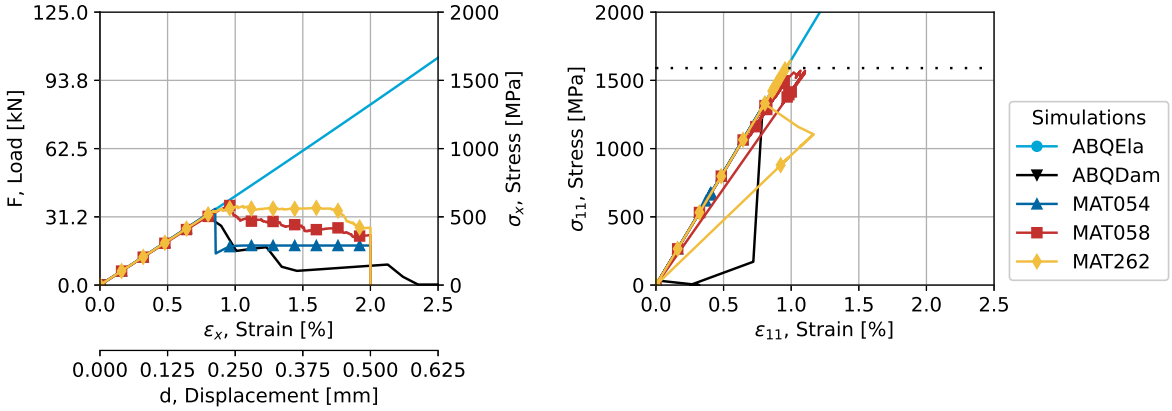

Figure 3.12: $[0/\pm45/90]_s$ compression specimen simulation results.

$[0/\pm45/90]_s$ Specimen

The final specimen to be examined is the quasi-isotropic specimen loaded under compression. The results of this simulation can be found in Figure 3.12. An essential aspect of this failure progression is the fluency of the failures, and it can be seen how a few abrupt failures

characterise the MAT054 card and the material model in Abaqus. In contrast, the remaining material cards have a relatively gradual failure mechanism until the final failure strain is achieved. As it will later be seen, this greatly influences the performance of the crush simulations. The failure values and the obtained moduli for this material simulation can be found in Table A.6 in Appendix A.

3.6 Material Simulation Conclusions

There are different takeaways for the material simulations. First off, the different models can depict the material's behaviour until failure, with differences arising in the post-failure regime originating from the different value of the non-physical parameters. From this, a large difference that has been noted is the brittleness of the different material cards. Later, it will be seen in the crushing of the composite specimens that this greatly influences the stability and, thus, the simulation's quality. Moreover, it has been observed how the different stress and strain limits influence the specimens' post-failure regime. This difference is especially noticeable in the compression of the quasi-isotropic specimen loaded under compression.

It is found that the tensile loading rate can be increased with respect to the prescribed material test speed provided by ASTM. The change from 0.03 mm/s to 0.15 mm/s is necessary for the tensile tests to obtain reasonable simulation times. This way, the obtained simulation times are in the order of five to ten minutes.

Chapter 4

Finite Element Modelling of Composite Tube Crushing

In Chapter 2 it has been described how composite tubes can act as a good energy absorber. Thus, the behaviour of these structural components is studied in this research to gain more insight into which parameters influence the mean crushing load and the energy absorbance of the aforementioned components. In order to develop the analytical model, reference data is required to validate the models. Therefore, finite element models are developed to sustain the verification of the analytical study.

This chapter describes these finite element models and discusses the challenges that arise when modelling these phenomena. In the literature research presented before, light has been shed on the complex behaviour of the crushing of composites; as one can imagine, this poses a challenge when modelling these complex phenomena. Therefore, to be sure that the adopted modelling is adequate, test data is used to validate the FE models. The test used as a reference to validate the models is described in Section 4.1. Subsequently, a comprehensive introduction is given on how the test is modelled in the finite element software, after which more details are given regarding the different finite element software used and the selected material models. From the different FE models, conclusions are drawn, after which a potential method to improve the results is described in Section 4.2.5.

4.1 Test Description

As stated before, finite element models are used to verify the derived analytical model. However, the finite element models themselves also need validation; therefore, these are validated using real test data. The data is taken from the results of the tests performed by Oak Ridge National Laboratory (ORNL) [59]. The tubes that are taken as a reference from this testing campaign are the 46b and 47B specimens, which are square tubes, fabricated from Hexcel IM7/8552 with a quasi-isotropic layup $[0_2/\pm45/90_2]_s$, and a bevel trigger. The tube's length is 200 mm, with a side length of 50 mm, a corner radius of 6.4 mm, while the tube's average

cured thickness is 2.16 mm. The specimens are tested in a 500 kN servo-hydraulic test machine, with a speed of 6 m/s [59,60]. The actual crushing speed envelope of the specimen can be found in Figure 4.1.

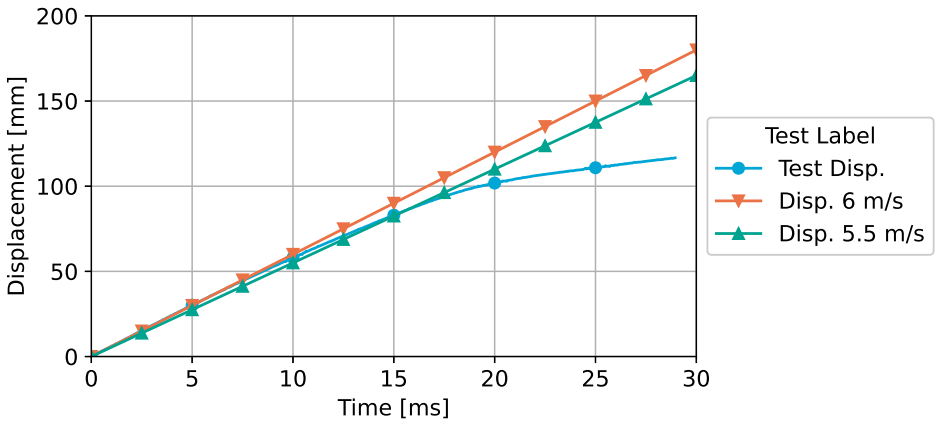

Figure 4.1: Crushing speed of the composite specimens.

In the figure, two ideal profiles are also depicted: one with a speed of six metres per second and one with a speed of 5.5 m/s. By studying the figure, one can see that a loading rate of five metres per second is more accurate than the provided six metres per second loading speed; therefore, this speed is taken as the tube's loading speed. From the same figure, it can be seen that the speed is almost constant up to a time of 15 ms; therefore, this time is taken as the total simulation time. To the selected time of 15 ms, a small buffer is added to account for the initial plate displacement, which leads to a simulation time of 16 ms. The obtained load as a function of displacement gathered from the tests can be found in Figure 4.2.

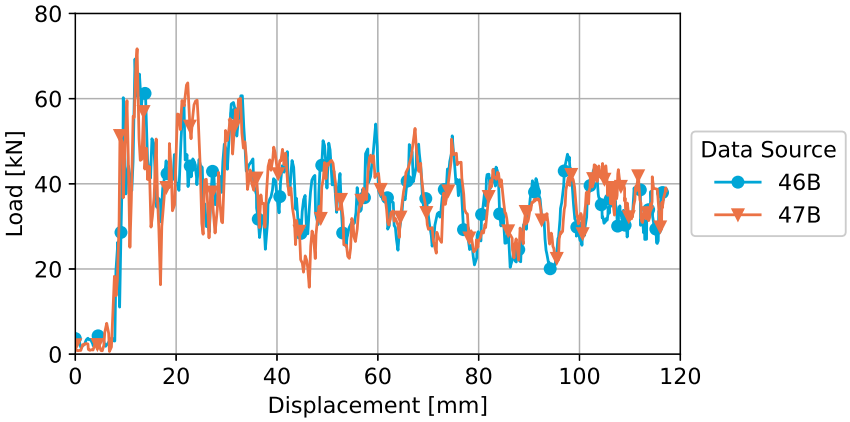

Figure 4.2: Square tube crush specimen test load results.

Figure 4.2 shows that the mean crushing regime of the tube starts at 3.6 ms (displacement of 20 mm). With this, the energy absorbed in the mean crushing regime corresponds to 2551 J, while the obtained mean crushing load is found to be 38.6 kN.

Figure 4.3: Square tube crush specimen test results pictures.

4.2 Finite Element Modelling

The test data depicted above can be useful to validate the analytical model for the studied absorber; however, this would limit the flexibility in verifying different shapes and sizes of absorbers. To test different geometries or materials, these finite element models are developed, which can verify the analytical model and study the absorber's behaviour in the global structure. Therefore, first finite element models are created that simulate the test performed described above, which can subsequently be altered to aid during the verification of the analytical model. As with the material tests, both Abaqus and LS-Dyna are used to study the performance of the different material models that can be implemented in the finite element software. During the modelling of the tubes' crushing phenomena, one needs to ensure the similarity between the two finite element software to have a valid comparison between the two. Therefore, the modelling technique is described in the following subsections, where the similarities and differences are pointed out.

4.2.1 Overall Models Properties

The modelling process of the different material models in LS-Dyna is straightforward, as the material cards can be interchanged; however, one also needs to ensure the similarity between the LS-Dyna and Abaqus models. Figure 4.4 shows an example of the FE model set up in LS-Dyna.

The part model is based on the reference test. This means that a square tube is modelled with a side length of 50 mm, and a length of 200 mm. The corners have a radius of 6.4 mm, and a bevel trigger is included in the upper part of the specimen to ensure the desired crushing frond. The material used in the model is the one studied during the material tests, namely the IM7/8552 unidirectional composite lamina material, the properties of which can be found in Table 3.2. Finally, the layup used to manufacture the tube is as follows: $[0_2/\pm 45_2/90_2]_s$.

Part Modelling

In both FE software, the tubes are modelled using shell elements. The composite laminates are defined by specifying the lamina material separately. Subsequently, the laminate is generated by stacking the lamina according to the layup. Using this laminate definition means that a single shell is used through the laminate's thickness. This modelling technique is not

ideal, given the nature of the problem, where delaminations occur in the specimen's crush zone. Other modelling techniques include the representation of every single ply by a shell element, which are subsequently connected using cohesive elements [15,17,48]. However, this method increases the degrees of freedom of the problem, which leads to an unacceptable simulation time for this application. The simulation time could be acceptable for a single crush absorber; however, this is not deemed possible when implementing the absorber into the global structure. Therefore the single element modelling technique is chosen. In Abaqus, the S4RS element is used again. In LS-Dyna, the corresponding elements are used, which is achieved by setting ELFORM equal to 2. In most aerospace applications, the S4R shell element suffices, which does not include the small membrane strain. However, it is found that this causes problems with the onset of the crushing. Square shell elements are used with a side length of 2 mm. In LS-Dyna, four elements define the corners' curvature, while in Abaqus, this curvature is omitted. In reference research, where a tube-like specimen with similar dimensions is studied, a mesh sensitivity study is performed where it is found that a mesh size of 5 mm is satisfactory [61], therefore a mesh size of 2 mm is deemed adequate. By doing so, 9200 elements are obtained.

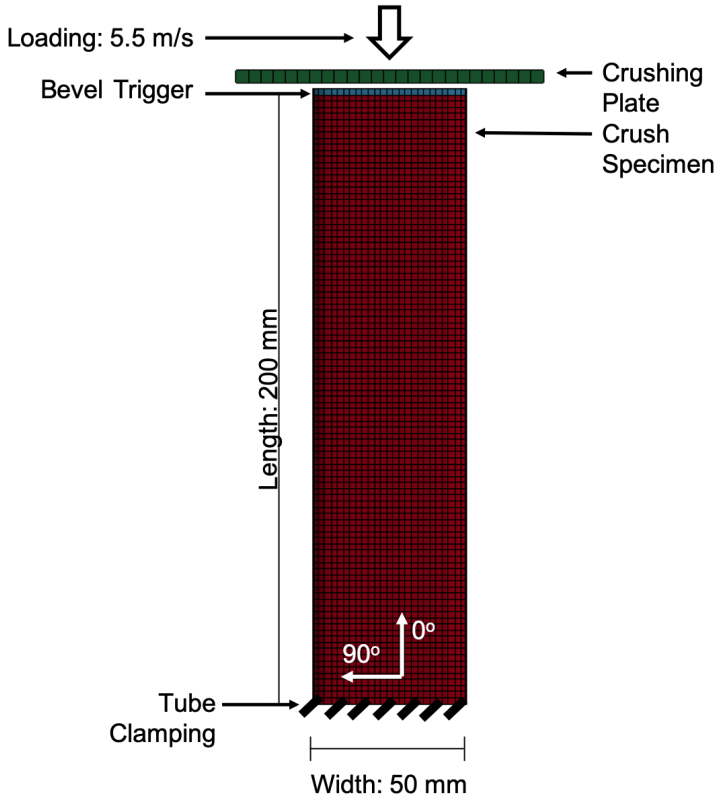

Figure 4.4: Example of a finite element model of the crush tube.

When crushing simulations are performed, it is essential that the laminate's orientation is determined by the orientation of the shell elements, as other material orientation techniques may cause errors when elements are distorted excessively [55]. Therefore, during the modelling of the specimens, one needs to ensure that the elements' connectivity is constant. An example

of how the orientation of square shell elements is defined can be found in Figure 3.1, for further information, the reader can refer to Section 3.2 or the Abaqus and LS-Dyna user manuals [51, 62].

Next to the tube itself, a crushing plate is also modelled, representing the servo-hydraulic test machine. In LS-Dyna, the crushing plate is a 100 by 100 mm, 4 mm thick rigid plate, while in Abaqus, this is achieved by modelling a 100 by 100 mm thin plate, with its nodes constrained using the rigid body constraint.

Boundary Conditions

There are two boundary conditions to be applied in the model, namely the tube's fixture and the loading of the tube, which is controlled by the rigid plate. The tube's lower edge is fixed by clamping the nodes situated on the lower edge of the tube. By doing so, these nodes are restricted in all degrees of freedom (translation and rotation). A roller support defines the displacement of the crushing plate; this means that all the degrees of freedom of the crushing plate are constrained, excluding the motion in the tube's axial direction. In the axial direction, the loading plate is given a constant speed of 5.5 m/s. According to the test manual, the specimens are loaded with a rate of 6 m/s [59]. Figure 4.1 shows the obtained displacement over time of the crushing head. In the same figure, two idealised displacements are also reported, one with a constant speed of 6 m/s, the other with a rate of 5.5 m/s. By studying the figure, it can be seen that the lower rate of 5.5 m/s is more accurate for longer simulation times. Hence, this loading rate is implemented in the model.

Part Interaction and Contact

To increase the reality of the simulation, friction is added to the model. In both simulations, the friction surfaces are defined ass all with self, which is the standard option in Abaqus, while it is the suggested method in LS-Dyna for crash simulations [51]. This means that the finite element software automatically detects whether two parts come into contact or a part comes into contact with itself, as may occur during crash or crush simulations. This way, one does not need to specify all the interactions separately. The friction coefficient is set equal to 0.2 with a viscous damping factor of 20% in order to stabilise the results. It is found that the inclusion of friction into the model does increase the stability and accuracy of the crushing load. In the reported references, friction coefficients range from 0.1 to 0.2 [48, 63]. In work presented by A. Cherniaev et al., a similar tube is modelled, where a friction coefficient of 0.2 is used [14], therefore this value is also implemented in the current study.

Load Extraction and Filtering

Due to the nature of the model, the extracted crushing load contains large fluctuations. This peak-like behaviour of the load is obtained due to the elimination of entire rows of elements in the crush frond. The removal of entire rows causes the tube to temporarily detach from the loading plate until a new row of elements is loaded till failure. This process is repeated over the entire stroke length of the crushing process. When extracting the load from the FE simulation, one can extract the load from the tube's clamping region. This, however, increases

the fluctuation even further due to the inertial effects of the tube, leading to pulling loads after the removal of the row of shell elements. Therefore the load needs to be extracted from a different location. In Abaqus, the load is extracted from the reaction force of the crushing plate. In LS-Dyna, the CONTACT_FORCE_TRANSDUCER_PENALTY_ID card is used to extract the contact force from the crushing plate. However, the collected loads still present large fluctuations; therefore, it is common-use in crash simulations to filter the load using a low-pass digital filter (SAE) [64]. The load curve's characteristic shape needs to be maintained during the filtering process, such as the initial peak; therefore, only high frequencies can be filtered. In this case, it is found that 1000 Hz is the right cutoff frequency. When applying the filter, one needs to ensure a small time-delta between the beginning of the simulation and the specimen's loading to have good initial behaviour of the filtered load curve. To account for this time delta, the test results have been shifted along the x-axis to have a better comparison. All the presented load curves in this chapter have been filtered using the SAE filter; in Appendix B.2, the numerical and filtered results for the different simulations can be found.

Bevel Trigger Modelling

An important aspect of the models is the crushing trigger. In the literature research in Chapter 2 is has been shown that a trigger is crucial in the achievement of a stable crush regime. The tested specimens are manufactured with a bevel shaped trigger; therefore, this is included in the FE model. The bevelled shape is achieved by omitting the laminate's symmetry of the first row of shell elements in the tube. This way, the specimen's thickness is halved, mimicking the bevel of the test specimens. A graphical representation of the bevel trigger modelled in FE can be found in Figure 4.5.

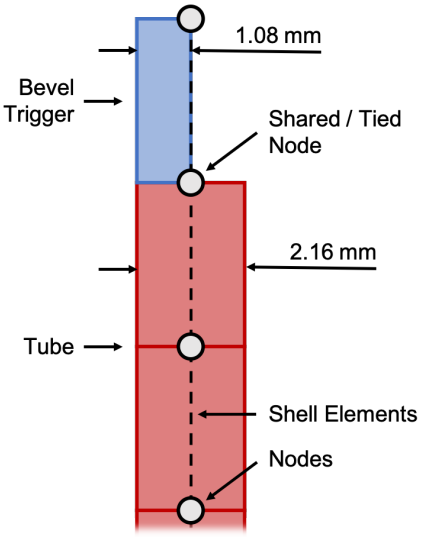

Figure 4.5: Modelling of the bevel trigger.

Two separate parts need to be created to reduce the thickness of the first row of shell elements. Subsequently, these parts are coupled by their adjacent nodes, as depicted in Figure 4.5. In Abaqus, the nodes are attached using a tie constraint. In LS-Dyna, on the other hand, as the nodes are defined separately from the parts, the two parts can share the same node.

With this, the common elements and differences between the two FE software tools have been analysed. In the following subsections, some final details are explained, which are proprietary to the specific FE tool, after which the results of the simulations are presented.

4.2.2 Abaqus Model and Results

The crushing of the square tube specimen has been modelled with different settings in Abaqus to obtain results that reflect the test data. These settings are described in this subsection.

During the modelling of the tube, the element size of the shell elements has been changed with respect to the material tests. Therefore, the energy dissipations need to be recomputed as described in Section 3.3.1 to account for this change. The computed energy release values can be found in Table 4.1.

Table 4.1: Material energy release values for tube crushing in Abaqus.

Failure Mode	Value	Units
Fibre Tension	235	Nmm
Fibre Compression	31	Nmm
Matrix Tension	6	Nmm
Matrix Compression	16	Nmm

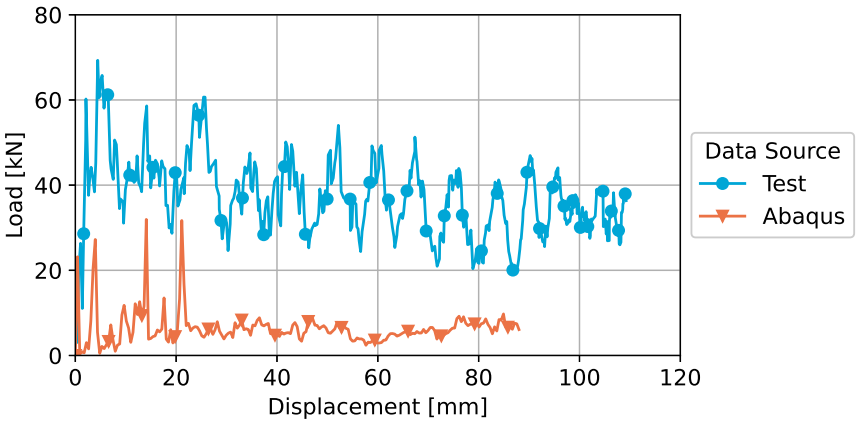

Figure 4.6: Abaqus crush simulation results.

The load results obtained from the simulation performed in Abaqus using the built-in Hashin failure criterion be found in Figure 4.6, while the deformation of the crush specimen can be seen in Figure 4.7. In the figure, one can see the load obtained from the simulation and the test load. Here, the mean crushing regime is lower than the one obtained in the test. The tested specimen has a mean crushing load of 38.6 kN, while the simulation only achieves a mean crushing load of 5.9 kN. The reported results represent the most accurate results that have been obtained using the applied modelling technique in Abaqus. From this, it can be seen that the FE model is unable to represent the crushing phenomena accurately. This is confirmed by the deformation shown in Figure 4.7, where it can be seen that the tube exhibits more collapse-like behaviour, rather than forming a crush frond. The crush frond is formed at the beginning of the simulation, where the element rows are removed every stroke. This leads to high load fluctuations, which eventually cause the tube to fail.

Other attempts have been made to improve the simulation; however, these have not been successful. One study is performed on the influence of the number of integration points per ply to better capture the laminate's outward bending motion. By increasing the number of integration points with respect to the standard value of three, the results improve by some degree; however, the obtained mean crushing load is still lower than the tested load. The

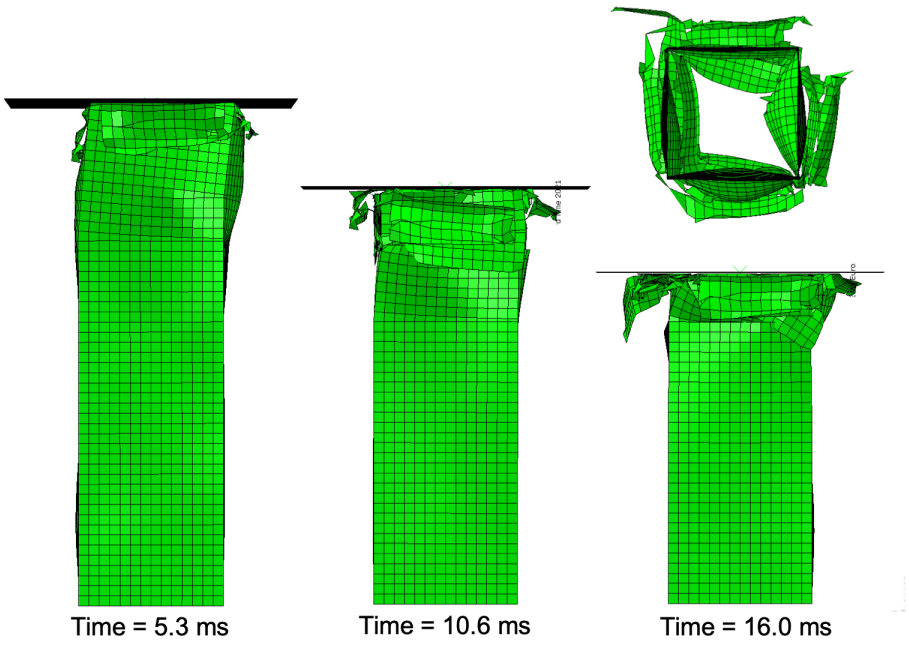

Figure 4.7: Deformed states of the square tube modelled in Abaqus.

results depicted in Figure 4.6 has nine integration points per lamina, while the default value is three. In Figure B.1 in Appendix B.1 one can find the results obtained from the simulations with the varying number of integration points. An alternative method to improve the results is by introducing mass scaling into the model. It is found that this does improve the results, as the obtained peaks in the numerical results are higher. However, as the actual behaviour of the simulations does not improve, this method is not deemed feasible. More importantly, due to the danger of generating non-realistic results, this method has not been implemented. The results of the simulation with mass scaling implemented can be found in Figure B.2 in Appendix B.1. Finally, an inclined mesh has been implemented to reduce the fluctuation in the mean crushing load by controlling the element erosion, to prevent the elimination of entire rows, as suggested by Waimer et al. in 2017 [65]. However, it is found that this introduces other instabilities into the model, causing the entire tube to collapse.

Based on the performed simulation, one can conclude that the mean crushing load error using the built-in material models in Abaqus is very large. Research has shown that it is possible to simulate composite crushing using a single shell model [48, 49, 66]. However, in the cited papers, user-specified material subroutines are used, which lie outside this study's scope. In literature, other modelling techniques are investigated, which use multiple shell layers to model the laminate. This method is indeed very accurate when modelling the crushing of composite specimens. The drawback of this methodology is that it is not applicable when modelling the behaviour of the global structure, as this would increase the complexity and the degrees of freedom of the global model. Due to the inability of the selected modelling technique in Abaqus to accurately represent the crushing of composite specimens, the same experiment is recreated using a different finite element tool, namely LS-Dyna. The modelling of the crushing of the tube using this FE software is described in the following section.

4.2.3 LS-Dyna Models and Results

It is investigated whether LS-Dyna can accurately represent the crushing process of the tested composite specimen. The study is mainly centred around the opportunities that the different material models offer during the modelling of the crushing of the composite specimens, as described in Chapter 3, and whether these can achieve a stable crush frond, leading to more accurate results.

When modelling the crushing of the tube in LS-Dyna, other cards are included to improve the simulation results. Below one can find the most critical parameters that have been altered from their default values in the corresponding cards.

- CONTROL_TIMESTEP: To limit the step size of the simulation, the TSSFAC value has been set equal to 0.5. This way, the simulation does not make large time-steps, increasing the accuracy of the simulation. One needs to consider that this slows down the simulation, as the number of required time-steps is increased.
- CONTROL_HOURGLASS: In order to control the hourglass modes, IHQ is set equal to 4. This effectively stiffens the elements in order to avoid element hourglassing. When doing so, one needs to ensure that the amount of hourglass energy is lower than 10% than the total energy.
- CONTROL_ENERGY: To control the hourglass energy, HGEN is set equal to 2, enabling the calculation of hourglassing energy, such that this can be monitored.
- CONTROL_ACCURACY: During the degradation of elements, the orientation of the material may become an issue, as the orientation is based upon the numbering of the nodes of the shell elements. Therefore, to reduce this problem, the invariant mode variable INN is set equal to 4.

As with the material tests presented in Chapter 3, one needs to take into account the number of integration points for the different lamina layers by altering the MAXINT variable in the DATABASE_EXTEND_BINARY card, and account for the different strains in the lamina layers by activating the LAMSHT flag in the CONTROL_SHELL card. For more detailed information about the different cards, the reader is referred to the LS-Dyna User's Manual [51]. With this, the cards used to model the crushing of the composite tubes have been completed.

Above, the hourglass energy has been mentioned. Hourglass energy is an essential factor that must be taken into account when performing finite element analysis using rectangular shell or parallelepiped elements. Therefore at the end of each simulation, it needs to be verified whether the hourglass energy of a part is less than ten percent of the total energy within the same part [51]. Next to the hourglass energy, the energy ratio can be taken to estimate the quality of the simulation. This ratio is given by dividing the total energy by the sum of initial energy and the external work. Ideally, this ratio needs to be equal to one [51]. When these criteria are not met, the mesh needs to be altered, or there are unexpected energy instabilities that harm the quality of the simulation.

One crucial aspect that still has to be treated is the material model. The behaviour of the material models have already been described in Chapter 3; however, as stated in the previous

chapter, the non-physical parameters provided for the material test simulations are based upon the calibration for the crush simulations. The parameters that have been calibrated for the crushing simulations influence the element erosion parameters. As the element removal criteria vary per material model, these are treated separately in the following subsections. Overall, a very effective method during the determination of the values for these non-physical parameters is the bisection method; this way, the interval within which the values may lie is reduced effectively. The actual value of the different non-physical parameters and how these are determined is described in the following subsections.

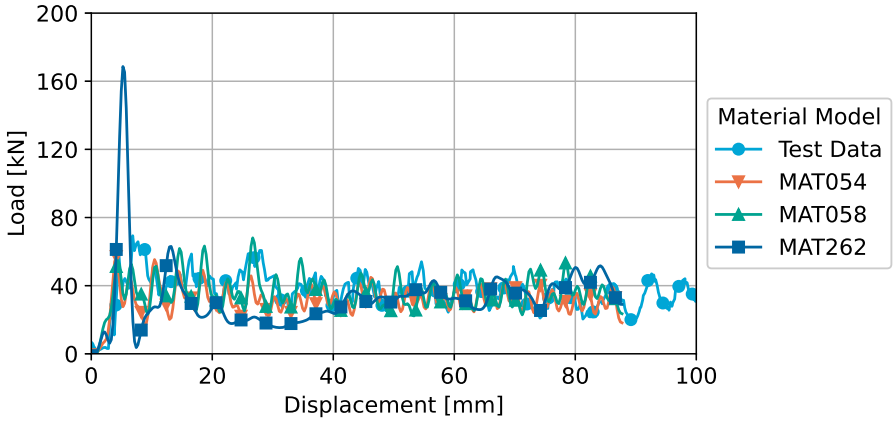

Figure 4.8: Crushing load simulations for square tubes with varying material models.

Table 4.2: LS-Dyna simulation results compared to test data.

Material Model	Mean Crushing Time [ms]	Mean Crushing Load [kN]	Absorbed Energy [J]
Test Results	2.00	38.6	2551
MAT054	1.75	32.4 (-16.1%)	2333 (-12.5%)
MAT058	1.75	36.2 (-6.2%)	2349 (-7.9%)
MAT262	1.75	31.7 (-17.9%)	1579 (-38.1%)

MAT054

In the MAT_ENHANCED_COMPOSITE_DAMAGE material card, there are multiple options to control the element removal. The most used method entails the removal using a minimum time-step size or the use of effective strain. Element removal can also be controlled by providing the maximum strains the material can sustain. The standard method implemented for this material card is solely using the time step and the Effective Strain (EFS); therefore, this is first implemented into the model. It is found, however, that elements that are detached from the tube harm the overall simulation. When these separated elements do not interact with the other parts of the simulation, these do not influence the result of the simulation; however, it is found that these elements increase in size, causing them to collide with the crushing specimen and plate. The interaction between the detached element and the

tube inflicts damage to the tube itself, leading to its premature failure. Therefore, to limit the growth of these detached elements, maximum failure strains have been added to the material card. These strains need to be sufficiently large not to influence the crush-frond's behaviour, while being small enough to limit the growth of the separated elements. The values used for the failure strains can be found in Table 4.3.

Table 4.3: Failure strains implemented in the MAT054 card to control element erosion.

Failure Type	Symbol	Value	Units
Tensile failure strain fibre direction	DFAILT	0.6	mm/mm
Compressive failure strain fibre direction	DFAILC	-1.0	mm/mm
Matrix failure strain	DFAILM	0.12	mm/mm
Shear failure strain	DFAILS	0.4	mm/mm
Effective Strain	EFS	1.0	mm/mm

The results obtained from the crushing simulation can be found in Figure 4.8, depicted by the light blue line. Note that the data presented in the figure has been filtered using the LS-Dyna built-in SAE filter, with a cutoff frequency of 1000 Hz. The simulation's numerical results and their comparison to the filtered results can be found in Appendix B.2. From Figure 4.8, it can be seen that the obtained results are acceptable. However, to further investigate the quality of the simulation, one can study the mean crushing load and the absorbed energy. In Table 4.2, one can see the obtained mean crushing load and energy absorbed by the specimen in the mean crushing regime. It is important to note that pinpointing the time at which the mean crushing load begins is difficult due to the result's fluctuating nature. The time at which the mean crushing load initiates influences the mean crushing load itself and, subsequently, the amount of absorbed energy. The selected times at which the mean crushing load is deemed to begin are also reported in Table 4.2. In the table, the errors are additionally reported. These are considered acceptable for this simulation, given the high degree of simplification implemented during the modelling process, using the single shell layer model.

Next to the obtained load and energy data, the actual deformation of the simulated specimen is also of importance; therefore, in Figure 4.9 one can see the deformed state of the crush specimen in different phases of the crushing loading. In the figure, it can be seen that a large number of shell elements have been removed from the simulation, which is due to the implementation of the failure strains reported in Table 4.3. Even though the elements have been degraded, with the risk of changing the geometry of the crush zone, the simulation provides good results for both the mean crushing load as the absorbed energy in the mean crushing regime. Therefore, the non-physical strain limit values are accepted.

MAT058

The MAT_LAMINATED_COMPOSITE_FABRIC (MAT058) material card offers similar element erosion opportunities as the MAT054 material card, including the time step limitation and the Effective Failure Strain, this time represented by the ERODS variable. In this material model, however, it is more common to include the material's failure strains; therefore, the failure strains as depicted in Table 3.2 are implemented in this model. For the time step

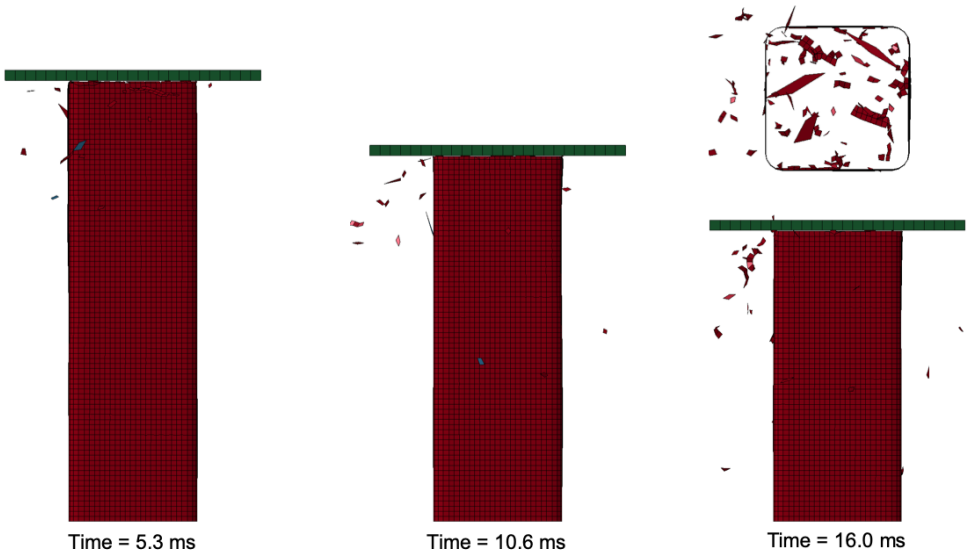

Figure 4.9: Deformed states of the square tube with the MAT054 model.

and Effective Failure Strain variable, the values of 1.0E-7 s and -0.55 mm/mm are used, respectively [14].

The load vs displacement curve for the MAT058 model can be found in Figure 4.8, where the green curve with triangular markers represents the results for the currently described material model. As with the MAT054 material model, the load values reported in Figure 4.8 are the filtered values. In Appendix B.2, one can compare the numerical and the filtered results for this simulation. The mean crushing load and energy can be found as before in Table 4.2, along with the selected time at which the mean crushing regime begins. When looking at Table 4.2 and Figure 4.8, one can see that the simulation is able to recreate the test data very well. The mean crushing regime's behaviour is very accurate, as are the values for the mean crushing load and the absorbed energy.

Finally, in Figure 4.10, one can find the crush tube's deformed state in different phases of the crushing process. In the figure, one can see the more plastic-like behaviour of the material, as less element have been degraded. The deformation difference is apparent when comparing the bottom view of the tube at its final crushed state, situated in the upper right corners of figures 4.9 and 4.10. In the MAT054 simulation, one can see the elements that have detached from the tube, while in the MAT058 simulation, one can see that the elements are still in the simulation but have been folded inwards, mimicking the behaviour of the splaying layers.

MAT262

The third and final material card that has been used for the simulation of the crushing of the tube is the MAT_LAMINATED_FRACTURE_DAIMLER_CAMANHO (MAT262) material card. As described in Subsection 3.3.2, the behaviour of this material is dictated by the energy released during the failure progression of the material. The energies have

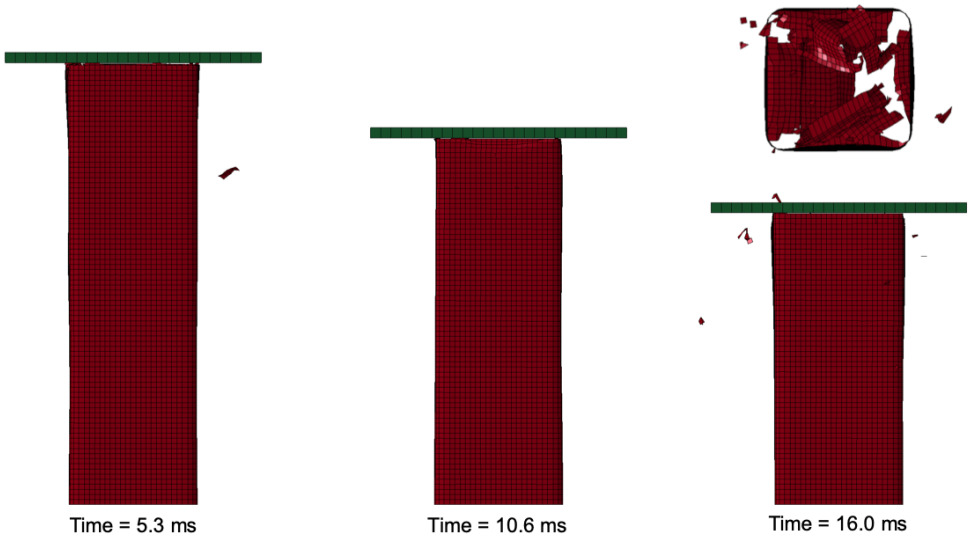

Figure 4.10: Deformed states of the square tube with the MAT058 model.

been computed earlier; however, as these values are mesh-size dependent, these need to be recomputed. The values used in the simulation of the crushing of the tube can be found in Table 4.4. The fracture toughness only dictates the material's erosion in the fibre direction; hence the effective failure strain is implemented once again with a value of -0.55 mm/mm, to control the element erosion in the traverse direction.

Table 4.4: MAT262 critical energy release rates for the simulation of the square tube crush specimen.

Failure Mode	Symbol	Value	Units
Fibre Tension	GXTO	1491.1	MPa
Fibre Compression	GXCO	957.2	MPa

As for the other material models, in Figure 4.8 the filtered load results can be found, depicted by the green line, while in Appendix B.2 one can find the comparison between the numerical and the filtered loads. In Table 4.2 one can find the summary regarding the initiation of the mean crushing regime, the value of the mean crushing load and the absorbed energy. When looking at the provided data in the load vs displacement plot, and the values reported in the table, one can see that this material has the lowest performance of the three material models studied in LS-Dyna. The mean crushing regime is represented reasonably well; however, a large peak precedes the stable plateau, which is not present in the reference data.

Finally, in Figure 4.11, one can find the square tube's deformed state in different phases of the crushing process. This process is more similar to that of the MAT058 model. However, in this material model, an even smaller amount of shell elements have been degraded.

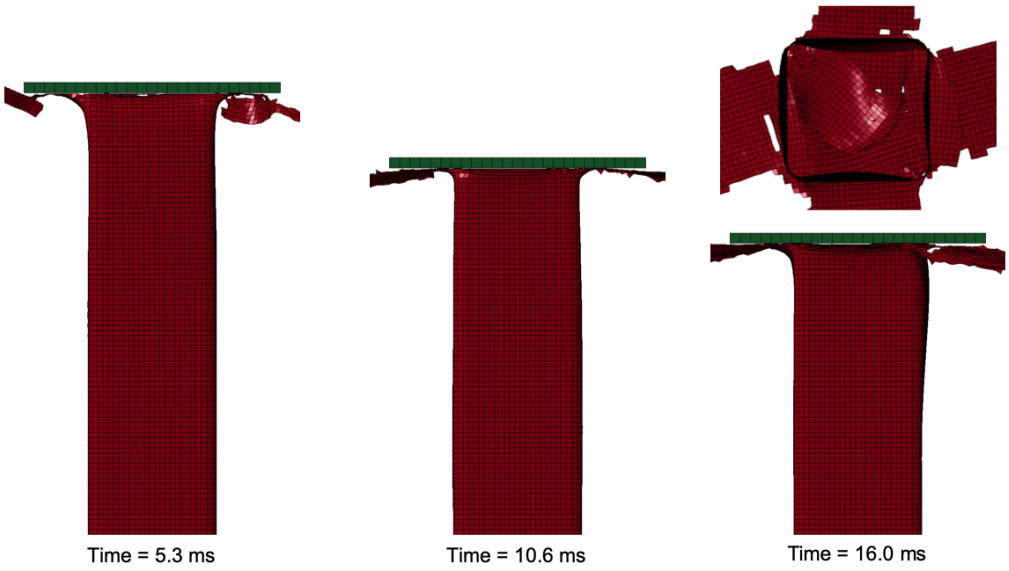

Figure 4.11: Deformed states of the square tube with the MAT262 model.

4.2.4 Computation Time Comparison

Next to the results regarding the load behaviour and the absorbed energy, a simulation's computational effort can also be of importance. As stated in the introduction, simulations are a useful tool during the design of structures. However, the development of these FE models and the run-times can be time-consuming; therefore, the simulation times for the different finite element software and material models are presented. The CPU times can be found in Table 4.5. All the simulations have been run on the same machine with an Intel i5-4670 core, running at 3.40 GHz and a RAM of 8.00 GB. In the table, it can be seen that Abaqus is faster than LS-Dyna; however, yielding inaccurate results. The MAT058 and MAT262 material models require a similar amount of computational time, while the MAT054 material model requires around 33% more with respect to the other to LS-Dyna based material models, which is interesting as the material model is relatively more simple than the other two. The increase in computational effort may arise from the more brittle nature of the problem, leading to a higher amount of element erosion, which requires additional computation with respect to the degradation of material properties.

Table 4.5: Simulation times for the crushing of the square tube, for the different software and material models.

FE Software	Material Model	CPU Time [s]
Abaqus	Hashin	2426 (42 minutes, 1 second)
LS-Dyna	MAT054	16639 (4 hours, 37 minutes, 19 seconds)
LS-Dyna	MAT058	13685 (3 hours, 48 minutes, 5 seconds)
LS-Dyna	MAT262	12627 (3 hours, 30 minutes, 27 seconds)

4.2.5 Model with Imperfections

In the previous section, the results for the mean crushing simulations of composite tubes have been depicted. However, from the results, especially the unfiltered results, it can be seen that the results fluctuate with large amplitudes around the mean crushing load, a phenomenon that during the real test does not occur. It has been stated that this originates from the way the tube is meshed, as entire rows of elements are degenerated or bent inwards, leading to the drop in load. In Abaqus, an attempt was made to reduce this effect by mapping the mesh with an inclination with respect to the crushing plane, as suggested by Waimer et al. [65]. However, it is found that this led to other problems, such as the instability of the entire tube. Another option to suppress these fluctuating values is suggested in the papers published by Waimer et al. and Cherniaev et al. [14, 65], where it is suggested to model manufacturing imperfection into the tube. By introducing manufacturing imperfections in the simulation, the representation of the tube is more realistic, as, in the original model, the tube and the tube's material are perfectly straight and aligned. However, during manufacturing, this level of perfection can not be achieved, as there are always some miss-alignments of the lamina layers. Therefore Cherniaev et al. suggested introducing a small out of plane displacement for the nodes of the tube's walls, while Waimer also includes in-plane imperfections. In the paper published by Cherniaev et al., the imperfections are determined by a random number between zero and five percent of the specimens' thickness. By doing so, Cherniaev et al. found that the fluctuation in the load is reduced.

Implementing this material imperfection could be beneficial during the modelling of the global structure, as the load peaks may have a negative effect on the behaviour of the global structure. Therefore, this method is studied for the square tube at hand. Moreover, next to the out of plane imperfection, an in-plane imperfection is integrated to account for material miss-alignment. The values for the imperfection offsets have been taken from the interval as suggested by Cherniaev et al., of zero to five percent of the specimen's thickness. For the imperfect tubes, the model is taken from the MAT058 tube simulation, the only difference being the nodal coordinates as described above. In Figure 4.12 one can see a comparison between the filtered results of the perfect tube with the MAT08 card, and the filtered results of the four simulations of the imperfect tubes. While for completeness, the final energy values of the simulations can be found in Table B.3 in Appendix B.3.

Table 4.6: Mean crushing loads and variance for the imperfect tube simulations.

Specimen	Simulated Load [kN]	Load Variance [kN^2]
Perfect Specimen	36.2	613.5
Imperfect 1	34.1	404.6
Imperfect 2	36.1	527.1
Imperfect 3	33.5	440.4
Imperfect 4	33.2	419.1

In Figure 4.12 hardly any difference can be seen between the results of the simulations. Therefore, to have a more quantitative comparison, the mean crushing loads are determined along with the variance of the raw loads in the mean crushing, the values of which can be found in Table 4.6.

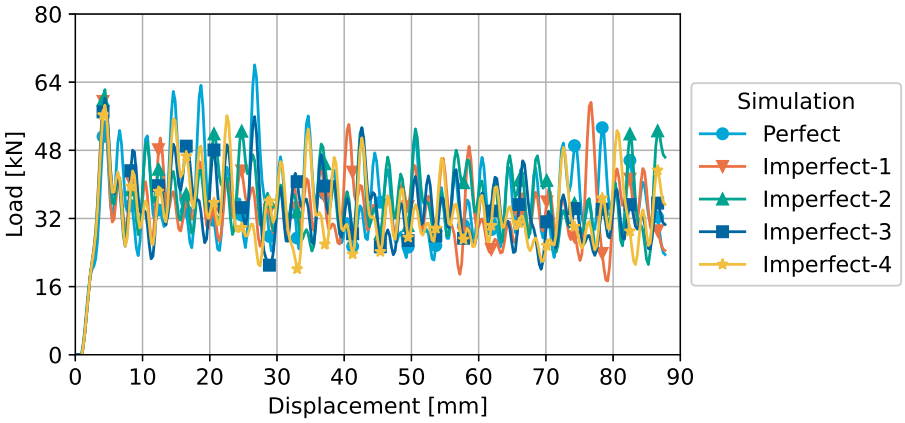

Figure 4.12: Comparison between the simulation of a tube with and without imperfections.

In the Table 4.6 it can be seen that overall the obtained mean crushing load is lower than the load obtained from the perfect tube, which is as expected, as the initial coordinates of the nodes have already some displacement, which promotes further displacement due to load eccentricities. More importantly, it can be seen that the variance is indeed reduced, however, not to a large extent. Due to the limited variance reduction, the gain from this method is minimal when a more stable crushing load is desired. Therefore this method is not deemed useful for further simulations.

4.3 Finite Element Modeling of Composite Tube Crushing Conclusions

In this chapter, the different modelling techniques have been investigated, used to model the behaviour of a square composite tube subjected to crushing loading, with the main focus lying on two finite element software, Abaqus and LS-Dyna, with special attention given to the available material models.

Abaqus implements the most simple material model, characterised by the bi-linear model. However, it is found that this simple model is not able to recreate the complex behaviour observed in the reference test nor recreate the obtained load. This inability is deemed to originate from the brittle nature of the implemented material model, which is not able to represent the formation of the crushing frond. The brittle nature leads to large instability in the numerical load, and a subsequent low mean crushing regime obtained when filtering the numerical load. The MAT054, MAT058, and MAT262, used in LS-Dyna, are, on the other hand, able to represent the crush phenomenon more accurately. The obtained filtered load curves are very similar to the obtained test load, with the largest error for the mean crushing load being smaller than 18%. Next to the mean crushing load value, the energy absorbance is an essential aspect in evaluating the effectiveness of composite crushing specimen. It is found that both the MAT054 and MAT058 have the most accurate predictions regarding energy absorbance, with their error being below 13 % with respect to the test data. The MAT262 material model, while being energy-based, has the least accurate prediction, with an error of

38.1% with respect to the data. This error is mainly attributed to the lower mean crushing load and the lower degree of damage, as in the other models a large amount of the energy contribution originates from the damage of the material. The energy analysis of the results obtained in Abaqus is not performed as this would not yield any valuable insights.

The difference in material models can also be observed in the deformation of the simulated tubes. Both the Hashin and the MAT054 model present a more brittle like nature, wherein Abaqus the element are removed entirely from the simulation, leading to the fluctuating nature, while in the MAT054 model different shell elements are detached from the tube and are scattered, which can also be seen in the physical test. The MAT058 and MAT262 material models show a more ductile behaviour. In the MAT058 material model, this is expected, owing to its non-linear softening around the material's failure stress. Interestingly, the MAT262, which is the LS-Dyna material card, which is most similar to the Abaqus material model, shows this ductile behaviour, enabling the formation of large splaying layers.

Even though the LS-Dyna material models provide satisfactory results, these material models require non-physical parameters to be calibrated, which is a time-consuming task. During the calibration of the material parameters, it is found that the bisection method proves to be a very effective method to determine the correct values for the material cards; this way, an initial interval is chosen for the parameters, which by every iteration is halved, yielding a fast convergence to the calibrated value.

The numerical results provided by the different material models are characterised by a large degree of fluctuation; therefore, it is common practice to filter these results. As the highly irregular load behaviour may trouble the fuselage section simulations, methods are analysed to reduce this fluctuating nature. Therefore, the effect of imperfections is studied to reduce the variance in the obtained load. It is found that the introduction of imperfections does have a positive effect on the stability of the load. However, this improvement is minimal and is, therefore, not considered a feasible solution.

Chapter 5

Analytical Approach for Composite Absorber Crushing

In the previous chapter, it has been described how a finite element model for the crushing of a composite specimen can be created. From that chapter, it has become clear that it is not easy to construct a reliable model; for example, the material models require non-physical parameters that need to be calibrated. This leads to a time-consuming process that is not desired in initial design phases, where quick solutions are required. Therefore, analytical equations that give insight into the energy absorption and crushing load would help engineers in preliminary design phases. Not only can these analytical models provide fast results, but more importantly, show which parameters influence the energy absorption and mean crushing load and to what extent. Therefore, this chapter investigates whether a reliable analytical equation can be derived for the mean crushing load of composite crush absorbers, which can also be used to determine the energy absorption.

The derived model is not completely novel, as this based upon the analytical model as derived by Hussein et al. [13]. The limitation of Hussein's model is that its application is limited to straight, square specimens. Therefore, some assumptions are altered, while other aspects are altered, such that the mean crushing load of a wider variety of crush absorbers can be determined, entailing different shapes and taper. Therefore, to obtain the mean crushing load for the crash absorbers, the derivation similar to the one performed by Hussein et al., taking into account the variability in the specimens' cross-section and taper.

5.1 Model Assumptions

When deriving an analytical equation for some phenomenon, assumptions need to be put in place to confine the applicability of the model. Without assumptions, the model might be too general, which may lead to inaccuracy. A good example for the case at hand may be the failure mode of the specimen. In the literature research chapter, it has been shown that composites can fail in multiple ways when subjected to crushing loads. Therefore, an important

assumption, in this case, would be the failure mode of the absorber. This assumption will be a fundamental building stone in the derivation of the analytical equation for the crushing load of a composite energy absorber. One other aspect pointed out in the literature research is the theoretical basis for the analytical model. Some models have used buckling equations, while others are based on energy dissipations. Due to the promising results, and the simplicity of the energy models, this theoretical basis is adopted in the current analytical model. Accordingly, the current model being developed generalises the energy rate model suggested by Hussein et al. [13].

In this section, the applied assumptions are investigated, starting with the failure mode and the crush frond geometry. This is followed by a description of the assumptions that have been made regarding the energy contributions during the failure of the specimen.

5.1.1 Crush Frond Geometry

To study the different failure modes in the crush frond and how the structure behaves under crushing loads, it is necessary to study close-by which phenomena occur in the crush frond. This investigation is important because one can study how much material is failing, at what rate, and which forces play a role in this process. In the literature study chapter, it has been shown that the combination of splaying and splitting is the failure mode that leads to the highest specific energy absorbance. Therefore this failure type is studied as this leads to the most optimal design. Furthermore, based on previous studies and the assumptions mentioned above, an idealised geometry of the crush zone can be created, represented in Figure 5.1.

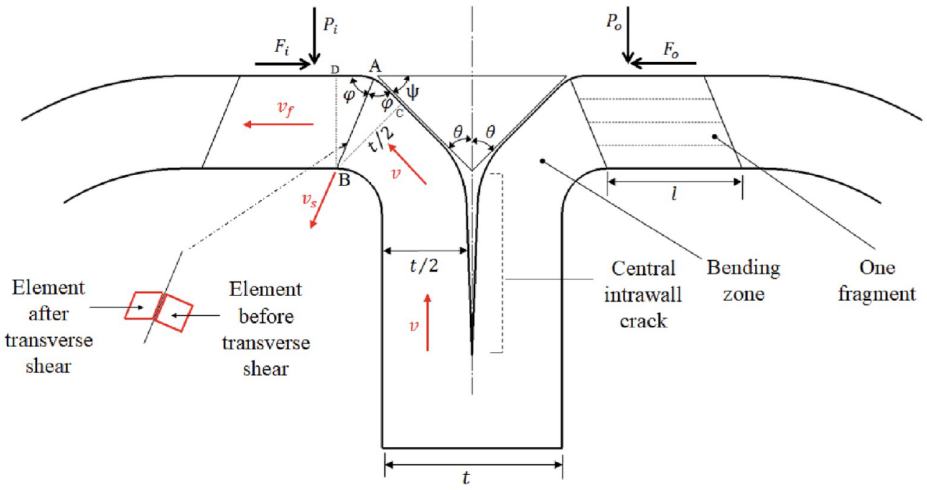

Figure 5.1: Assumed crush frond geometry [13].

In the figure, one can see how the debris wedge causes the formation of the two splaying layers and how these layers are pushed downward, causing them to fail under shear. Note that in the figure a straight specimen is represented. In the case a tapered specimen is considered, the two splaying layers can be denoted with the subscripts o (outer) and i (inner). Moreover, in the figure, one can see all the relevant angles. The inclination angle of the specimen θ is not reported in the figure. The value of the two wedge angles, depicted with θ depends on the specimen's inclination, while the sum of the two angles, the total wedge angle, is assumed

to be approximately 90°. Therefore, for specimens with no inclination angle, θ is taken to be of 45°, while for specimens with an inclination angle, it is assumed that the splaying layers form a 45° angle with the vertical axis. This way, the wedge angle is kept at a value of 90°, as was found experimentally [13,44]. Other essential angles in the given geometry are formed between the wedge, the crushing frond, and the splaying layers. The wedge's angle formed with the crushing-plane is given by ψ while the angle the splaying layers form while being sheared downward is given by φ.

One aspect that needs to be considered is that the implemented modelling technique in the finite element tools cannot represent this splaying phenomenon, owing to the single shell modelling technique. In LS-Dyna, this is partially incorporated in the SOFT parameter, while in Abaqus, this failure type is not taken into account. In a later stage, it will be seen that the splaying failure has little to no influence on the mean crushing load, according to the analytical model. Therefore, the inability of the finite element software to represent this behaviour, given the selected failure mode, does not have a large influence on the validity of the simulations.

In future calculations, to have a better overview of the implications of the assumptions, the angles are converted such that these are a function of a single variable, namely the wedge angle θ. There are two values for every angle, namely for the inward and the outward bending fronds; however, as the derivations for the angles are equal, the subscripts are omitted.

As the sum of the internal angles of a triangle needs to be equal to 180°, the value for ψ can be computed as a function of the angle θ, as depicted in Equation 5.1, note that the units in the equation are in radians.

$$\frac{\pi}{2} + \psi + \theta = \pi \quad \rightarrow \quad \psi = \frac{\pi}{2} - \theta \tag{5.1}$$

Subsequently, as the sum of two times the shear angle φ and the wedge angle ψ also need to be equal to 180°, as these form the flat crushing plane, in combination with the previously derived value for ψ, the value for the shear angle φ can be obtained, as depicted in Equation 5.2, also here the units are in radians.

$$2\varphi + \psi = \pi \quad \rightarrow \quad 2\varphi + \frac{\pi}{2} - \theta = \pi \quad \rightarrow \quad \varphi = \frac{\pi}{4} + \frac{\theta}{2} \tag{5.2}$$

This way, all the angles of interest are expressed dependent on a single variable, namely the wedge angle θ.

Other essential aspects of the geometry are the loading velocities. Energy rates are used in the analytical model; hence loading velocities or fracture rates are required. The crush loading velocity is denoted as v, while the velocity that the specimen's sidewall experiences is denoted with v_c. Finally, the frictional velocity and shearing velocity are depicted by v_f and v_s, respectively. Also here the two splaying layers have their respective values denoted by the previously mentioned subscripts. To have a better overview, the different velocities are derived as a function of the loading velocity and the previously derived angles. First, the specimen sidewall velocity can be determined using Equation 5.3

$$v_c = \frac{v}{\cos\phi} \tag{5.3}$$

Afterwards, to determine the other velocities, the sine rule can be applied to the triangle that the velocities form as depicted in Figure 5.2.

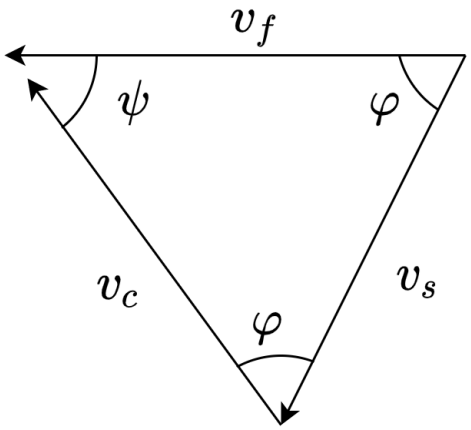

Figure 5.2: Relation between the loading velocities.

By applying the sine rule to the triangle, the relation as depicted in Equation 5.4 is obtained.

$$\frac{v_c}{\sin\varphi} = \frac{v_f}{\sin\varphi} = \frac{v_s}{\sin\psi} \tag{5.4}$$

From the equation, it becomes clear that the friction and the cone sidewall velocity are equal. While the shear velocity can be determined as depicted below, where the values for the angles and specimen velocity are plugged in as previously derived.

$$v_s = \frac{\sin\psi}{\sin\varphi} v_c = \frac{\sin\left(\frac{\pi}{2} - \theta\right)}{\sin\left(\frac{\pi}{4} + \frac{\theta}{2}\right)} v_c = \frac{\cos\theta}{\cos\phi \sin\left(\frac{\pi}{4} + \frac{\theta}{2}\right)} v \tag{5.5}$$

With this, all the necessary knowledge about the crush frond geometry is collected, hence in the following subsection, the different energy contributions are studied.

5.1.2 Energy Contributions

To derive an analytical model for the mean crushing load, a series of assumptions need to be made to point out the phenomena considered important and simplify there where possible. One of the important assumptions in this model are the failure modes that occur and the energy dissipations that these failure modes exhibit.

First, two different crack propagation energies are considered, namely the central wall delamination and the vertical splits forming the petals. It is assumed that a single delamination is formed, which for straight specimens is situated in the mid-plane of the laminate [44, 45], while for inclined specimens, research has shown that the thickness ratio between the inward and outward bending layers lies between 0.5 and 0.7 [47], with the thicker layer bending inwards. The number of vertical splits depends on the specimen's configuration. For polygonal specimens, the number of splits is assumed to be equal to the number of angles of the sections, as stress concentrations at the angles cause the splits to form in their proximity [48]. On the

other hand, for circular cross-sections, these stress concentrations do not occur; therefore, it is not possible to determine the number of splits. However, as later will be seen, the number of splits has a small influence on the final value of the mean crushing load; therefore, this does not have a considerable influence on the performance of the model.

The second phenomenon taken into account is the shear failure of the material caused by the crushing plate's downward motion. This failure is assumed to occur over the whole perimeter of the specimen. During the shearing process, the two fronds bent in and outwards can be considered to be two different laminates; however, as this process is dictated by the out of plane properties of the laminate, which are dictated by the matrix material, it can be assumed that the out of plane material properties of the inward and outward bending sections are equal.

The final phenomenon being considered is friction energy. It is assumed that the friction acts continuously along the whole perimeter of the specimen. As later will be seen, the amount of energy being dissipated by the frictional forces is a function of the friction coefficient and the mean crushing load itself.

Now that the assumptions have been stated, the actual derivation of the analytical equation can be performed utilising the tools and knowledge gained from the assumptions.

5.2 Analytical Derivation

As stated before, to determine the mean crushing load analytically, all the energies need to be determined, which are subsequently equated to the loading energy. Finally, with the energy balance in place, the crushing load can be determined; how this is done is captured by Equation 5.6. In the equation, $\dot{W}_e$ is the external work rate, which is the rate at which the load is putting energy into the system. $\dot{W}_c$ is the crack propagation energy rate, which, as described before, is composed out of two contributing factors, namely the central wall delamination, denoted with $\dot{W}_{c1}$, and the vertical splitting energy rate, denoted with $\dot{W}_{c2}$. Finally $\dot{W}_s$ and $\dot{W}_f$ represent the shearing and friction energy rates. When one is able to determine all the single energy rates, one can rearrange the equation to obtain the mean crushing load. Therefore, in order to do so, the energy rates are determined in the following subsections.

$$\dot{W}_e = \dot{W}_c + \dot{W}_s + \dot{W}_f \tag{5.6}$$

Central Internal Wall Delamination Energy Rate

The internal wall delamination energy rate is determined by the product between the Mode I interlaminar fracture toughness of the specimen's material, denoted with (G_{IC}), and the area rate at which the delamination is propagating, denoted with $\dot{A}$. The crack area rate is given by the product between the perimeter (p) of the specimen and the specimen loading rate v_c, which, as derived before, can be related to the loading rate. By implementing the various steps, the equation for the central internal wall delamination energy rate can be obtained as depicted in Equation 5.7

$$\dot{W_{c1}} = G_{IC}\dot{A} = G_{IC}pv_c = \frac{G_{IC}p}{\cos\phi}v \tag{5.7}$$

Vertical Splitting Energy Rate

During the failure of a material, the released energy is determined by the volumetric integral of the product between the stress and the strain of the material. This can be simplified by multiplying the energy released by the material, per unit of volume, by the volume rate at which the material fails. Therefore, the area under the material's stress-strain curve is required along with the failing material volume. Exploiting that composite material usually has a linear elastic behaviour till brittle failure, the area of the triangular curve is taken. By implementing these first simplifications, Equation 5.8 is obtained. In the equation, $\sigma_{u,22}$ and $\varepsilon_{f,22}$ indicate the ultimate stress and failure strain of the specimen's material, respectively. Note that the traverse 22 direction of the laminate is given as the failure direction, as this is the direction along which the splits are formed. $\dot{V}$ represents the volume rate at which the material fails.

$$\dot{W_{c2}} = \frac{1}{2}\sigma_{u,22}\varepsilon_{f,22}\dot{V} \tag{5.8}$$

As stated before, the determination of the splitting volume varies per specimen. For polygonal specimens, this can be determined by multiplying the failure volume rate of one single split by the number of edges, while for a circular cross-section, the number of splits can not be determined. This leads to the final equation for the splitting energy rate as depicted in Equation 5.8, where t represents the specimen's thickness, n represents the number of splits, while l represents the split size along the perimeter direction. Once again, the specimen's load velocity can be substituted with the global load velocity.

$$\dot{W_{c2}} = \frac{1}{2}\sigma_{u,22}\varepsilon_{f,22}tlv_c = \frac{n\sigma_{u,22}\varepsilon_{f,22}tl}{2\cos\phi}v \tag{5.9}$$

Traverse Shearing Energy Rate

The traverse shearing energy is given by the product between the required shear force and the shearing velocity. The shearing velocity v_s has been determined in the assumptions section, which leaves the shear force F_s undetermined. The shear force can be determined using the out of plane shear strength of the material and the shearing surface area. The shearing surface area can be split into two, namely the inward and outward splaying sections, while as stated before, the out of plane shear strength is assumed to be equal for both splaying layers. All the preformed steps can be found in Equation 5.10.

$$\dot{W_s} = F_s v_s = A\tau_s v_s = \left(A_{s,i}v_{s,i} + A_{s,o}v_{s,o}\right)\tau_s \tag{5.10}$$

The two areas in Equation 5.10 are given by the product between the perimeter and the splaying layers' thickness. The perimeter shortens for the inward bending splay, while it becomes larger for the outer bending layer. However, it is assumed that the change in the perimeter is negligible, meaning that the original perimeter is used. Finally, the thickness of the splaying layer needs to be corrected for the inclination under which the section fails. By implementing the assumptions, the following equation is obtained.

$$\dot{W}_s = \left(\frac{t_i v_{s,i}}{\sin \varphi_i} + \frac{t_o v_{s,o}}{\sin \varphi_o} \right) p\tau_s = \left(\frac{\cos \theta_i}{\sin^2 \varphi_i} t_i + \frac{\cos \theta_o}{\sin^2 \varphi_o} t_o \right) p\tau_s v_c \tag{5.11}$$

Finally, by substituting the values for the various angles as functions of the wedge angles and the shear velocity as a function of the global loading velocity, the final equation for the traverse shearing energy rate is obtained, as depicted in Equation 5.12.

$$\dot{W}_s = \left[\frac{\cos \theta_i}{\sin^2 \left(\frac{\pi}{4} + \frac{\theta_i}{2} \right)} t_i + \frac{\cos \theta_o}{\sin^2 \left(\frac{\pi}{4} + \frac{\theta_o}{2} \right)} t_o \right] \frac{p\tau_s}{\cos \phi} v \tag{5.12}$$

Frictional Energy Rate

The derivation of the frictional energy rate is relatively straight forward. The initial equation for this energy rate can be found in Equation 5.13.

$$\dot{W}_f = P_i \mu_i v_{f,i} + P_o \mu_o v_{f,o} \tag{5.13}$$

First, it is assumed that the friction coefficient (μ) is equal for the two slaying sections, as the material and crush plate interfaces are equal, while it is proven is Subsection 5.1.1 that the frictional velocity is equal to the specimen loading velocity, and is therefore equal for the two splaying sections. The common factors can be collected, which multiply the sum of the inner and outer load, which is equal to the total load acting on the specimen. Performing all the steps yields the final form of the frictional energy rate equation, depicted in Equation 5.14.

$$\dot{W}_f = P\mu v_c = \frac{P\mu}{\cos \phi} v \tag{5.14}$$

External Work Rate

The external work rate is given by the product of the system's loading rate (v) and the applied load (P).

$$\dot{W}_e = Pv \tag{5.15}$$

Final Equation

With this, all the elements required for the energy balance are derived as depicted in Equation 5.16, which is obtained by filling in the energy contributions into Equation 5.6.

$$Pv = \frac{G_{IC} p}{\cos \phi} v + \frac{n \sigma_{u,22} \varepsilon_{f,22} tl}{2 \cos \phi} v + \left[\frac{\cos \theta_i}{\sin^2 \left(\frac{\pi}{4} + \frac{\theta_i}{2} \right)} t_i + \frac{\cos \theta_o}{\sin^2 \left(\frac{\pi}{4} + \frac{\theta_o}{2} \right)} t_o \right] \frac{p\tau_s}{\cos \phi} v + \frac{P\mu}{\cos \phi} v \tag{5.16}$$

Rearranging the above-depicted equation for the mean crushing load P, and noting that all the terms contain the loading rate v, which thus can be eliminated from the equation, leads to the final form of the equation for the mean crushing load as depicted in Equation 5.17.

$$P = \frac{\frac{G_{IC}p}{\cos\phi} + \frac{n\sigma_{u,22}\varepsilon_{f,22}tl}{2\cos\phi} + \left[\frac{\cos\theta_i}{\sin^2\left(\frac{\pi}{4}+\frac{\theta_i}{2}\right)}t_i + \frac{\cos\theta_o}{\sin^2\left(\frac{\pi}{4}+\frac{\theta_o}{2}\right)}t_o\right]\frac{p\tau_s}{\cos\phi}}{1-\frac{\mu}{\cos\phi}} \tag{5.17}$$

5.3 Model Verification and Validation

To determine whether the derived analytical model is accurate, one needs to validate or verify it with test or simulation data. This is where the finite element models are required, set up in Chapter 4. The actual test data can be used to validate the analytical model. However, the upside of using the finite element models is that these offer the opportunity to study the energies in the simulation and a wider variety of specimens. Therefore, first, the result of the actual test data is compared to the mean crushing load obtained from the analytical equation; subsequently, the loads and energies obtained from the FE simulation are compared. Once the energies and loads have been analysed, the influence of the most unfounded assumptions is studied. Finally, to study the specimen's performance regarding different parameters and shapes, the results of other FE models are compared to the results computed analytically. Once the analytical model has been fully validated, the conclusions are drawn in Section 5.4.

5.3.1 Validation with Test Data

One part of the validation of the analytical model is based on test data. As before, the data used to validate the model is the data obtained by the Oak Ridge National Laboratory [59]. The specimen taken into consideration is the same as the specimen studied during the creation of the finite element models. The obtained data provides the basis for validating the analytical model with a rather simple case, namely that of a straight square tube. The shape of the tube at hand enables to perform some simplifications to the analytical equation, namely the inclination angle ϕ can be set equal to zero degrees, which means that all the $\cos\phi$ values become one, while the number of corner splits can be set to four. Finally, research has shown that when straight specimens are subjected to crushing loads, and these manifest the assumed failure mode, the inner and outer splaying layers are equal [44,45]. This implies that the last term in the numerator of Equation 5.17 can be grouped into a single term. By implementing these modifications, the equation for the mean crushing load, as depicted in Equation 5.17, can be transformed into Equation 5.18.

$$P = \frac{G_{IC}p + 2\sigma_{u,22}\varepsilon_{f,22}tl + \frac{\cos\theta}{\sin^2\left(\frac{\pi}{4}+\frac{\theta}{2}\right)}tp\tau_s}{1-\mu} \tag{5.18}$$

The remaining terms in the equation are mostly material and geometric properties, the values of which are given in Table 5.1. The geometric properties are obtained from the test data. The remaining material data is computed using classical laminate theory, implementing a

maximum stress criterion and first ply failure for the in-plane properties of the laminate. For the out of plane shear strength, on the other hand, as this property is dominated by the matrix material, it is independent of the layup, which implies that the value for the out of plane properties of the ply material can be taken. This leaves a few parameters that ought to be determined, one of which is the splitting length l, which is set equal to the tube's thickness. Next to the splitting length, the splaying angle θ is left undetermined. Research has shown that the value of θ lies between 40 and 50 degrees [45]; therefore, a value of 45 degrees is taken. Finally, the friction coefficient needs to be determined. The references reported during the finite element modelling have shown that a value 0.2 provides good results for the finite element models; hence this value is adopted. For convenience, the assumed values are also reported in Table 5.1

Table 5.1: Material and geometric values used in the equation for the mean crushing load determination.

Variable	Symbol	Value	Units
Mode I Interlaminar Fracture Toughness	G_{IC}	0.2	N/mm
Laminate Traverse Ultimate Failure Stress	$\sigma_{u,22}$	1269.0	MPa
Laminate Traverse Ultimate Failure Strain	$\varepsilon_{u,22}$	0.001	mm/mm
Out of Plane Shear Strength	τ_s	90	MPa
Cross-Sectional Length	p	189.0	mm
Tube Thickness	t	2.16	mm
Splaying Angle	θ	45	°
Friction Coefficient	μ	0.2	-

Using the provided values, one obtains a mean crushing load of 38.2 kN. As the mean crushing load obtained from the test is equal to 38.6 kN, the analytically determined load underestimates the tested mean crushing load by only 1%. Next to the validation of the analytical model using the value of the mean crushing load, the different energy contributions obtained from the crush simulation can be used to examine the validity of the analytical model. In the test, the tube absorbs 2551 J of energy in the mean crushing regime. Using the analytical equation, a value of 3121 is obtained. In Table 5.2, one can find the energy contributions of the different phenomena occurring during the crushing of the composite specimen as computed with the analytical model. In the table, it can be seen that, according to the analytical model, the main contributing factors to the energy absorbance of the tube are the shearing and the friction energies. The splitting and delimitation failure modes have little to almost no influence. A sensitivity study is performed in the following section to further determine the influence of the splitting and the delamination energies. Furthermore, a more in-depth energy analysis is performed in Section 5.3.2, where various crush specimen simulations are studied.

Sensitivity Study of Assumptions

In the derivation of the analytical equation for the mean crushing load and its verification, assumptions have been made regarding both material properties and failure geometry. It is assumed that the Mode I fracture toughness of the material is 0.5 N/mm, which is a

Table 5.2: Energy contributions in crushing of square tube according to analytical model.

Energy Source	Value [J]	Percentage of Total [%]
Total	3059	-
Delamination	8	0.3
Corner Splits	4	0.1
Shearing	2436	79.6
Friction	612	20.0

reasonable assumption for this material [13]. Moreover, it is assumed that the circumferential length of the splitting corner is equal to the thickness of the tube itself, while it is assumed that the splaying layer angle θ is equal to 45 degrees. From the energies reported in table 5.2, it already becomes clear that the splitting and delaminating energies have a small influence on the overall energy dissipation; therefore, one can assume that these values also have a small influence on the value of the mean crushing load. However, to study the effect of these assumptions regarding the mean crushing loads, the mean crushing load is determined for a given interval of these values. Subsequently, the difference with respect to the base value for the mean crushing load is computed. The splitting length is varied between a null length and twice the assumed value, thus twice the specimen's thickness. The fracture energy is varied between a null value and a value of four; note that values of 2 N/mm are already considered to be high [13]. Finally, the same procedure is performed for the splaying angle θ. As research has shown, the interval for θ lies between 40° and 50° [44, 45], this interval is studied. The results of this study can be found in Figure 5.3. The different plots indicate the influence the different variables have on the mean crushing load; on each y-axis, the percentage difference with respect to the assumed values is depicted. Note that each y-axis has a different scale to accentuate the differences better.

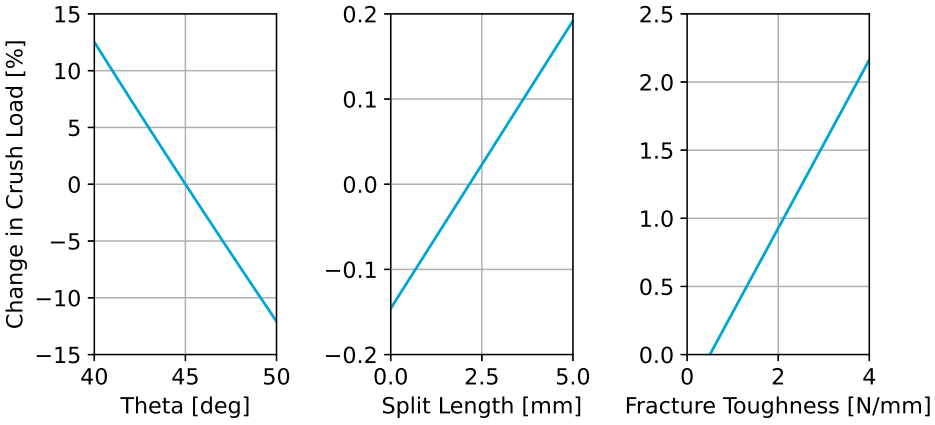

Figure 5.3: Sensitivity study of the assumed geometric and material properties.

As expected, the split length and fracture toughness have little influence on the mean crushing load value. On the other hand, the splaying angle does have a more considerable influence on the mean crushing load value, with the difference going up to 12.5%. This discrepancy is acceptable, given the nature of the problem.

5.3.2 Verification with Finite Element Data

Although the analytical model results are in excellent agreement with the test results, a single confirmation does not suffice to validate the analytical model. Therefore, to study the model's performance, other test and simulation data is gathered to verify the model further.

From the results of the previous section, it becomes clear that the cross-sectional length and the thickness of the crush-specimen have a considerable influence on the mean crushing load of the absorber, provided that the material needs to be kept constant. Therefore, the influence of these parameters is studied by performing a series of finite element simulations where these variables are altered. The finite element models are based upon the MAT058 crush tube model, as presented in the previous chapter. The length variable can be altered by adjusting the side length of the specimen. The thickness variation, on the other hand, is less straight forward. In a realistic case, one has a fixed ply thickness, which means that the number of plies determines the tube's thickness. However, as the number of plies, especially their orientation, may influence the tube's failure behaviour, the layup is kept constant. Therefore, in order to alter the thickness of the tube, the ply thickness is altered. By altering the plies' thickness, the case study is less realistic; however, this can provide useful insight regarding the performance of the analytical model regarding thickness variations. The side lengths studied are 25, 35, 50, 65, and 75, all in mm, while the thickness values are 1.08, 1.62, 2.16, 2.70, 3.24, and 3.78, also in mm.

In order to thoroughly verify the analytical model, two aspects are investigated. First, the mean crushing load is studied to see whether the obtained load from the crushing simulations is within a tolerable error of the analytical load. Subsequently, to further investigate the performance of the analytical model, the different energy sources are studied.

Mean Crushing Load

The results of the two studies can be found in Figure 5.4. In the figure, the dashed line represents the mean crushing load one obtains with the analytical model, while the blue squares represent the mean crushing loads obtained from the finite element simulations. For the actual load-displacement curves, the reader is referred to Appendix C.1.

In the figure, it can be seen that the analytical equation is able to represent the behaviour of the simulation quite well. In the results, there are, however, some data points that do not match the analytical trend. Namely, the point for the largest side length variation corresponding to a side length of 75 mm. While the smallest thickness, of 1.08 mm, has a lower value than the expected analytical load. The reason for these inaccuracies are geometric instabilities. In the side length study, the tube's sidewall becomes too long, which causes it to collapse, leading to the collapse of the tube. In the thinnest tube, similar behaviour is observed where all the walls collapse at once.

The actual values for the mean crushing load obtained from the analytical equation and the FE simulation are depicted in Tables 5.3. In the table, one can see that, when the unstable cases are not considered, the error between the analytical model's and FE mean crushing loads are small, especially for the side length variation, which is a more realistic analysis as stated before. Nevertheless, the thickness variation also provides satisfactory results, with the largest error being 35%.

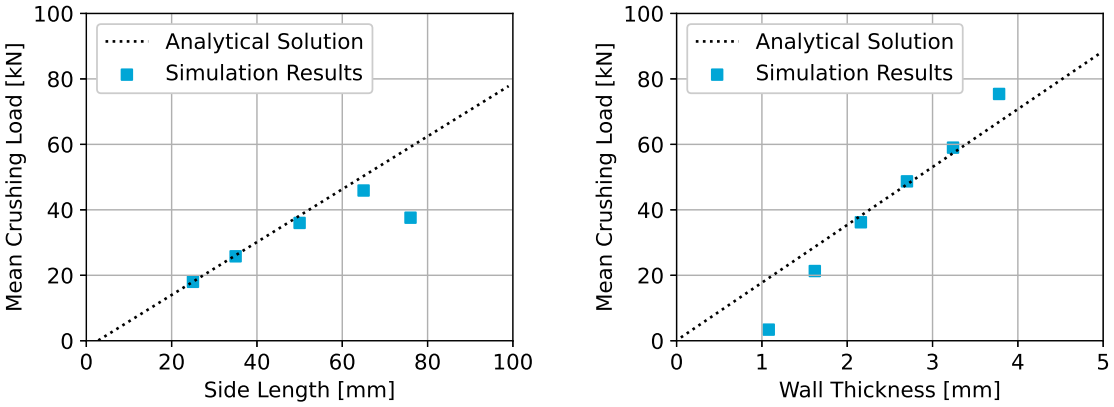

(a) (b)

Figure 5.4: Comparison between analytical model and simulation results for varying side length (left) and specimen thickness (right).

Table 5.3: Mean crushing load study for varying geometric parameters of a square tube.

(a) Varying side length.

Specimen Side Length	Mean Crushing Load Sim. [kN]	An. [kN]
25	18.0	18.0 (0.0%)
35	25.8	26.1 (1.2%)
50	36.2	38.2 (5.5%)
65	45.9	50.3 (9.6%)
75	37.6	58.4 (55.3%)

(b) Varying thickness.

Specimen Thickness	Mean Crushing Load Sim. [kN]	An. [kN]
1.08	3.4	19.2 (464.7%)
1.62	21.3	28.7 (34.7%)
2.16	36.2	38.2 (5.5%)
2.70	48.7	47.7 (-2.0%)
3.24	59.0	57.3 (-2.3%)
3.78	75.4	66.8 (-16.4%)

Energy Contributions

In the previous section, it has been seen that the analytical model can represent the mean crushing behaviour of the simulated and tested specimens. However, it is essential that the various energy contributions, which form the basis for the derivation of the analytical equation, are also within an acceptable error range. In the finite element software, it is not possible to distinguish between the various material damage modes, as these are grouped into a single value called Eroded Internal Energy. From the comparison between the analytical model and the test data, it is found that the delamination and the splitting energies represent a minimal contribution to the overall energy dissipation, the values of which fall within the error of the obtained values. The energy contributions obtained from the side length variation can be found in Table 5.4, while the energy contributions for the thickness variation can be found in Table 5.5. In the tables, it can be seen for the cases where a stable crushing regime is achieved, the total energy absorbance corresponds very well, as do the energies absorbed by material damage. The values obtained from the friction, on the other hand, show larger

discrepancies. The actual source of the discrepancy is not clear. One source of difference between the simulation and the analytical model may be the erosion of the elements in the simulation. The analytical model assumes that the two splaying fronds come into contact with the crushing plate, leading to friction energy dissipation. In the simulation, many elements are removed from the simulation, limiting their interaction with the crushing plate, leading to lower friction energy values from the simulations.

Table 5.4: Main energy contributions in the crushing of square tubes with varying side length.

Side Length	Total Energy [J] Sim.	Total Energy [J] An.	Fracture Energy [J] Sim.	Fracture Energy [J] An.	Friction Energy [J] Sim.	Friction Energy [J] An.
25 mm	1350	1564 (15.9%)	1188	1177 (-0.9%)	162	294 (81.5%)
35 mm	1949	2114 (8.5%)	1730	1722 (-0.5%)	219	431 (96.8%)
50 mm	2307	3059 (32.6%)	1891	2447 (29.4%)	416	612 (47.1%)
65 mm	2944	3821 (29.8%)	2427	3311 (36.4%)	517	828 (60.2%)
75 mm	2142	4569 (113.3%)	1655	3662 (121.3%)	487	915 (87.9%)

In the current study, the energies reported in the tables represent the energies relevant to the verification of the analytical model. The finite element simulation also produces other energies relevant for the verification of the simulations themselves, such as hourglass energy. For a complete overview of the energies, the reader is referred to Appendix C.2, where tables can be found with the final values of all the energy sources in the simulation, which can be used to verify the hourglass energy of the models.

Table 5.5: Main energy contributions in the crushing of square tubes with varying thickness.

Specimen Thickness	Total Energy [J] Sim.	Total Energy [J] An.	Fracture Energy [J] Sim.	Fracture Energy [J] An.	Friction Energy [J] Sim.	Friction Energy [J] An.
1.08 mm	296	1564 (428.4%)	214	1252 (485.0%)	82	313 (281.7%)
1.62 mm	1044	2114 (102.5%)	722	1691 (134.2%)	322	423 (31.4%)
2.16 mm	2307	3059 (32.6%)	1891	2447 (29.4%)	416	612 (47.1%)
2.70 mm	3587	3821 (6.5%)	3278	3057 (-6.7%)	309	764 (147.2%)
3.24 mm	4768	4569 (-4.2%)	4363	3655 (-16.2%)	405	914 (125.7%)
3.78 mm	5875	5496 (-6.5%)	5334	4397 (-17.6%)	541	1099 (103.1%)

5.3.3 Corrugated Beam

The goal of altering Hussein's analytical mode is to study a wider variety of composite energy absorbers, as the model derived in the referenced paper is only applicable to square absorbers. The results from the square tube absorber are promising; however, different shapes of absorbers are being investigated, as seen in the literature research chapter, an example of which is the corrugated beam. Therefore, to study the newly derived analytical model's applicability on different shapes of absorbers, a corrugated beam is analysed in this subsection. The selected beam is of a shape that is being widely used in different research papers for this type of absorber [15, 17, 52], a graphical representation of which can be found in Figure 5.5.

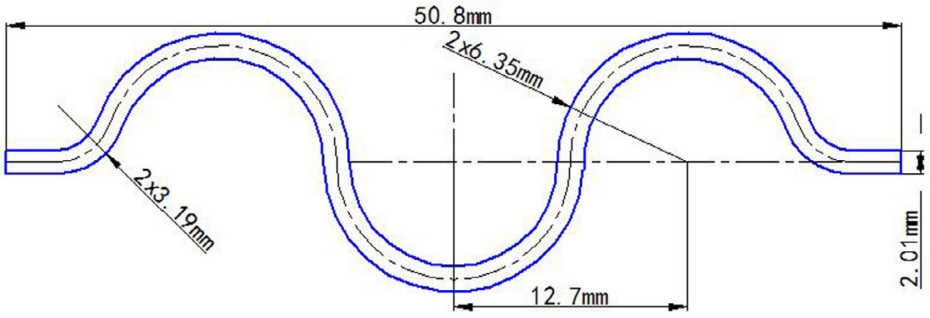

Figure 5.5: Geometry of the corrugated beam absorber [15].

The tube analysed in this study is based on the work presented by Sokolinsky et al. and H. Jiang et al. [15, 17]. The material used in this study is the TROYCA T700/2510 composite fabric material, the properties of which can be found in Table 5.6. A $[0/90]_{2s}$ layup is used with a cured thickness of 2 mm. The total width of the specimen is 50.8 mm, while the length is 76.2 mm. The sinusoidal pattern is composed of three semi-circles of a radius of 6.35 mm, while the transition to the final straight parts of the specimen is characterised by a quarter circle of radius 3.19 mm. The original specimen has three repetitions of the semi-circle; once the finite element model has been calibrated, the number of repetitions is increased to study the performance of the analytical model.

Table 5.6: Mechanical material properties TROYCA T700/2510 composite fabric [17].

Variable	Symbol	Value	Unit
Mass Density	ρ	1.5E-06	kg/mm^3
Young's modulus - Fibre direction	E_{11}	55900	MPa
Young's modulus - Traverse direction	E_{22}	54400	MPa
Shear modulus	G_{12}, G_{31}, G_{23}	4200	MPa
Poisson ratio	ν_{12}	0.042	-
Tensile strength fibre direction	X^T	911.3	MPa
Compressive strength fibre direction	X^C	704.0	MPa
Tensile strength traverse direction	Y^T	770.1	MPa
Compressive strength traverse direction	Y^C	698.2	MPa
Shear strength	S^L	131.6	MPa

The modelling of the specimen is based upon the lessons learned from the crushing of the square tubes as described in Chapter 4. Therefore the cards implemented in the modelling of the crush tube are also implemented in the current finite element model. The MAT058 material card is used, which requires the strains to be implemented. However, as these are not provided in the reference paper, these are estimated using the linear elastic relation between stress and strain and the provided failure stresses. The corrugated beam is meshed with square elements of size 2.54 mm, based upon the work published Feraboli et al., where an equally sized corrugated beam is modelled in LS-Dyna [52]. In the reference specimen, a bevel trigger is used to achieve a stable crushing regime; therefore, the same modelling technique as in the crush tube is implemented.

The non-physical material parameters are calibrated using the bisection method. For the time-step limitation, a value of 1E-7 s has been found, while the ERODS value is set equal to -0.4. Finally, the SOFT parameter has been set equal to 0.65. The actual loading speed of the test specimen is 0.4 mm/s. However, to reduce the simulation time and increase the similarity with the previous simulations, this is set equal to 5.5 m/s. The change in loading speed entails a big increase; therefore, one needs to ensure the validity of the simulation. In the work presented by Feraboli, it has already been shown that the loading speed has a negligible influence on the obtained load [52]. The beam is simulated for a duration of 8 ms, leading to a displacement of 44 mm.

The obtained mean crushing load of the test is 17.0 kN, while the obtained mean crushing load from the simulation is 11.1 kN. More interestingly, the load obtained from the analytical model is 13.9 kN, which is an error of 18.2%.

The specimens' analytical loads are determined using a simplification of Equation 5.17. The vertical splitting energy, which can not be determined when round specimens are used, is omitted during the determination of the analytical mean crushing load. This can be done as in the previous section it has been found that the contribution of this failure mode is minimal. Furthermore, as the corrugated beams are straight in the loading direction, the $\cos\phi$ terms are all equal to one. As the specimens are straight, it is assumed that the two splaying layers are equal, which means that these can be grouped into a single term. By implementing the aforementioned assumptions, the equation for the mean crushing load of the corrugated beams can be obtained, as depicted in Equation 5.19. In the equation, the G_{IC} and τ_s terms indicate the material's Mode I Interlaminar Fracture Toughness and out of plane shear strength, respectively. θ is as defined before the angle the debris wedge forms with the crushing axis, which is assumed to be 45°, while μ is the friction coefficient. Finally, p and t indicates the specimen's section length and thickness, respectively.

$$P = \frac{G_{IC}p + \frac{\cos\theta}{\sin^2\left(\frac{\pi}{4}+\frac{\theta}{2}\right)} tp\tau_s}{1-\mu} \tag{5.19}$$

With the calibration of the finite element model in place, multiple specimens are simulated, where the number of semi-circle repetitions is altered. In table 5.7, one can find the mean crushing load of the specimens and the corresponding analytical loads. In the table, it can be seen that the analytical model is able to predict the mean crushing load reasonably well, which means that the analytical model is indeed applicable to other shapes than square tubes, which is the goal of this chapter.

Table 5.7: Crushing load results of the corrugated beams.

Specimen	Repetitions	Load [kN]		Error
		Sim.	An.	
Beam 1	3	11.1	13.9	25.2%
Beam 2	5	18.4	20.9	13.6%
Beam 3	7	24.6	27.9	13.5%
Beam 4	9	32.0	34.9	9.1%

In Appendix C.3, one can find the actual load-displacement curves that have been obtained from the simulations, the energies that have been extracted, and the deformations of the simulations. This subsection aims to determine whether the analytical model is also valid for other shapes of crush specimens. Based on the obtained load results, one can say that the analytical model is indeed applicable for this type of energy absorber.

5.4 Analytical Approach for Composite Absorber Crushing Conclusions

In this chapter, an analytical equation for the mean crushing load of a composite specimen has been derived, with which, in turn, the energy absorption can be determined. The method is based upon the energy rate of the sum of the failures occurring during the crushing process of the structural component, which can be equated to the rate at which the load introduces energy into the system. Therefore, an important basis for the analytical model is selecting the failures taken into account in the crushing process. To do so, a crush frond geometry is assumed as depicted in Figure 5.1. The delamination, splitting, friction and shearing energy have been pointed out as contributing factors to the energy dissipation. Equations for all the energy rates have been derived, which have allowed the derivation of the mean crushing load equation as depicted in Equation 5.17.

The first round of verification for the analytical model is based on reference data and the data collected in Chapter 4. The mean crushing load of the reference specimen is found very accurately, with an error of only 1%. With this first analysis, it is found that the frictional and shearing energies have a major influence regarding the energy absorbance, being responsible for around 99% of the energy absorbance. To further verify the analytical model, finite element models based upon the square crush tube have been created by varying the side length and the thickness of the specimens. Here a good correlation between the analytical and the finite element models is found, provided that the specimens are stable under the crush-loading.

Next to the verification of the obtained loads, the energy sources of the analytical model have been analysed with respect to the values obtained from the simulations. However, this research is limited regarding two aspects: the finite element models themselves have not been validated regarding the energy dissipations, and the finite element model only provides a single damage value, leading to the inability to distinguish between failures, splitting, and shearing energy. Nevertheless, the obtained fracture energy values correlate reasonably well, while the friction energy values show relatively large errors. The discrepancy in the friction energy is mainly attributed to the fact that the finite element models degrade failed elements from the simulation, which hinders them from interacting with the crushing plate, leading to lower friction energy values.

In the final section of this chapter, a corrugated beam absorber is analysed. The methodology for the validation is similar to the one of the square tube specimen. First, a finite element model is created, which is calibrated with reference test data. The calibrated model is subsequently altered by increasing the number of repetitions of the sinusoidal waves. This way, the analytical model can be verified using different sizes of specimens. Also for this type of specimen a good correlation is obtained between the finite element models and the values obtained with the analytical model, with the largest discrepancy being 25%.

Based on the presented data, one can conclude that the mean crushing load equation works well for the selected specimens. However, to further verify the analytical model, one would require more detailed insight regarding the energies being dissipated during the crushing process, as discrepancies are obtained with respect to the simulated data.

Chapter 6

Composite Energy Absorber Design

The final stage of this research comprises two parts that bring together the separate elements investigated in the previous chapters. This entails analysing an energy absorber for a composite aircraft fuselage and implementing the suggested analytical-numerical method. First, different shapes of absorbers are studied, which are subsequently integrated into a numerical model of a fuselage section. The studied fuselage is the Next Generation Multifunctional Fuselage Demonstrator developed by the STUNNING project [67]. Accordingly, in this chapter, the suggested absorbers are studied, after which, in the following chapter, these are integrated into a simplified digital twin of the fuselage structure.

The study of the isolated absorbers resembles the studies performed in the previous chapters, where the structural elements have been studied bot numerically as analytically. The goal of these last chapters is to develop further and provide an implementation case for the suggested numerical-analytical method. Accordingly, the absorbers are studied both analytically as numerically, while the fuselage section is studied only numerically. By studying the absorbers analytically, one can estimate the energy absorption characteristics, which can be beneficial during the design of the aircraft fuselage. This way, rather than simulating all the different design options, one can superimpose the behaviour of the structural element, obtained with the analytical model, with the baseline behaviour of the fuselage section, where no absorbers have been integrated.

However, before implementing the analytical model, one needs to ensure is behaviour. Therefore, the analytical model is implemented in parallel with numerical simulations of the isolated components. This way, one can further verify the analytical model and study the geometric behaviour of different shapes of absorbers. In fact, in this chapter, it will become clear that, during the design of an energy absorber, one needs to ensure the structural element's stability, preventing a premature failure, limiting its energy absorption.

The first section of this chapter investigates how the analytical model presented in Chapter 5 can contribute to the design of an energy absorber. This is achieved by further developing the model to obtain an equation for the SEA, which is essential during the design of an energy absorber with aeronautical application. Afterwards, in Section 6.2 some general properties are

presented upon which the properties of the newly introduced structural elements are based. Subsequently in sections 6.3 and 6.4 the C-strut and square tube absorbers are analysed, respectively. Finally, the chapter is wrapped, providing conclusions regarding the studied absorbers.

6.1 Analytical Specific Energy Absorption

In the previous chapters, the analytical model focuses on the mean crushing load and the simulated specimens' absorbed energy, which is done to verify the model itself. However, during the design of an actual crash absorber, especially in aerospace applications, where weight is of paramount importance, the specific energy absorption is of larger importance. As defined in Chapter 2, the SEA corresponds to the amount of energy absorbed by the specimen per unit of mass. Therefore, during this case study, more attention is given to this property of the analysed structural components. It must be noted that there are two approached to determine the weight of the SEA. Some approaches consider the crushed weight of a specimen, while the entire weight can also be considered. In this study, the total weight of each specimen is considered.

During the energy absorber design, the derived analytical model for the mean crushing load, as depicted in Equation 5.17, can be of assistance. In fact, the equation can be rewritten such that the expected SEA can be computed. To do so, it is assumed that only straight specimens are studied, which means that all the $\cos\varphi$ terms are equal to one, and the two splaying layers are equal. Furthermore, in the previous chapter, it is found that the energy contribution, due to the delamination and the vertical splits, is negligible compared to the shearing and frictional energy. These are therefore omitted from the equation. By implementing these assumptions, one obtains a simplified equation for the mean crushing load, as reported in Equation 6.1. In the equation, t represents the specimen's thickness, while p indicates the total length of the specimen's cross-section. τ_s represents the out of plane shear strength of the material, while μ represents the friction coefficient. Finally, θ depicts the angle the wedge forms with the vertical axis, along which the specimen is crushed, which is assumed to be of 45°.

$$P = \frac{tp\tau_s}{1-\mu}\frac{\cos\theta}{\sin^2\left(\frac{\pi}{4}+\frac{\theta}{2}\right)} \tag{6.1}$$

The product between the total length of the cross-section and the specimen's thickness gives the specimen's cross-sectional area, denoted with A. The energy absorbed by a specimen is given by the area under the load-displacement curve. Therefore, the absorbed energy can be estimated analytically by multiplying the mean crushing load with the crush length, which can be assumed to be equal to the specimen's total length, denoted with l. By implementing the aforementioned assumptions and simplifications, one obtains Equation 6.2, which depicts an estimation for the energy that a composite crush specimen can absorb.

$$E = \frac{Al\tau_s}{1-\mu}\frac{\cos\theta}{\sin^2\left(\frac{\pi}{4}+\frac{\theta}{2}\right)} \tag{6.2}$$

As stated above, specific energy absorption is of more importance in aerospace applications. Therefore, the mass of the absorber needs to be determined, which is given by the product between the volume of the specimen, denoted with V and the density of the specimen's material, denoted with ρ, as follows $m = V\rho$, where the volume can be written as the product of the cross-sectional area and length of the specimen, as follows $V = Al$. With this, the specific energy absorption can be determined as presented in Equation 6.3.

$$SEA = \frac{E}{m} = \frac{\frac{Al\tau_s}{1-\mu}\frac{\cos\theta}{\sin^2\left(\frac{\pi}{4}+\frac{\theta}{2}\right)}}{Al\rho} = \frac{1}{1-\mu}\frac{\cos\theta}{\sin^2\left(\frac{\pi}{4}+\frac{\theta}{2}\right)}\frac{\tau_s}{\rho} \tag{6.3}$$

In Equation 6.3, a series of simplifications can be carried out, after which one finds that the specific energy absorption is independent of the specimen's geometry. Instead, the specific shear strength of the material, which is given by the ratio between the out of plane shear strength and the density of the material, dictates the absorber's SEA, as can be seen by the ratio $\frac{\tau_s}{\rho}$ in Equation 6.3.

The obtained result for the SEA is valid under ideal conditions. This means that the specimen needs to fail under the assumed failure mode and that no other geometric instabilities occur during the loading of the specimen. In the following sections, this hypothesis is further analysed, and it will be seen that this hypothesis holds rather well.

6.2 General Absorber Properties

Although the shape of the suggested absorbers may be different, some parameters are kept constant to have a valid comparison between the studied structural elements. The common parameters are based upon the C-strut, which is present in the original design of the fuselage. Therefore, in this section, the common aspect that the different absorbers share are described. First, the geometry of the original C-strut absorbers is described, and the implications that this has, are described, after which the material properties of the lamina material used to create the laminate is described along with the specimen's layup. Finally, some comments regarding the crushing rate are provided.

6.2.1 Geometry

In the original design of the fuselage developed by the STUNNING project, C-shaped struts have been placed between the cargo floor and the frames. This strut has a length of 378 mm, with a flange width of 26 mm and a web height of 90 mm. These dimensions are of importance as this dictates the absorber's mass, which is essential for the component's specific energy absorption.

All the newly suggested structural elements have the same length as the original C-strut, such that these can bridge the same gap between the fuselage's frame and cargo cross-beam, such that these can be installed in the original location. Moreover, to ensure the same crushing frond behaviour, the specimens' layup is kept constant, which means that the thickness is also constant. The cross-section of the absorbers varies per specimen. When studying the

C-strut absorbers, the section's lengths are kept constant, such that the mass is constant as well. This means that the web and flange lengths are balanced accordingly. During the study of the square absorbers, the absorbers' cross-sections are altered, as this offers a good opportunity to study the influence on the SEA. One absorber, called Tube 3, has a similar mass as the reference C-strut to compare the behaviour of the two types of sections. More details about the specific absorbers are provided in the dedicated sections.

6.2.2 Material Properties

One novel aspect of this study is the implementation of an analytical model for the design of an energy absorber for an aircraft fuselage. However, one other innovative aspect is the use of thermoplastic material in both the fuselage section, as the energy absorber. One big advantage of thermoplastic material is the gain one achieves during the manufacturing and assembly phase of the aircraft, as one can implement welding techniques, which may enable a higher production rate. However, when looking at the crashworthiness of aircraft, one can also achieve an increase in performance. As pointed out in Chapter 2, thermoplastic materials may achieve higher SEA values, owing to their different molecular structure with respect to more traditional thermoset materials [35].

The material that is used to manufacture the fuselage is the Toray Cetex TC1225 Peak laminate material. The physical material properties can be found in Table 6.1. The failure strains are also reported; however, as these values are not available, these have been calculated using the linear relation between the material's failures stress and stiffness.

Table 6.1: Toray Cetex TC1225 mechanical material properties [18].

Variable	Symbol	Value	Unit
Mass density	ρ	1.59E-06	kg/mm^3
Ply thickness	t_{ply}	0.184	mm
Young's modulus - Fibre direction	E_{11}	143000	MPa
Young's modulus - Traverse direction	E_{22}	8800	MPa
Shear modulus	G_{12}, G_{31}	4300	MPa
Shear modulus	G_{23}	3400	MPa
Poisson ratio	ν_{12}	0.0185	-
Tensile strength fibre direction	X^T	2755	MPa
Compressive strength fibre direction	X^C	1089	MPa
Tensile strength traverse direction	Y^T	78	MPa
Compressive strength traverse direction	Y^C	248	MPa
Shear strength	S^L	48	MPa
Tensile failure strain fibre direction	ε_{11}^T	0.019	mm/mm
Compressive failure strain fibre direction	ε_{11}^C	0.008	mm/mm
Tensile failure strain traverse direction	ε_{22}^T	0.009	mm/mm
Compressive failure strain traverse direction	ε_{22}^C	0.028	mm/mm
Engineering failure shear strain	γ_{12}	0.05	mm/mm

Based on the study performed in Chapter 4, it is chosen to use the MAT058 material card when modelling the composite material. This means that non-physical parameters are re-

quired to complete the material card, including stress limits, material erosion and softening parameters. In previous studies in this research, reference tests are used to calibrate these values. However, in this case, no reference data is available for this material; hence other methods need to be implemented. The stress limit factors, except for the compressive stress factor in the fibre direction, are taken as suggested by the LS-Dyna user manual [51], the values of which can be found in Table 6.2. The TSIZE and ERODS values are taken equal to the values of the previously performed simulations. This leaves the values of SLIMC1 and SOFT undetermined, representing the stress limit in compression for the material loaded in the fibre direction and the material degradation factor, respectively. Ideally, these values are determined by correlating to test data; however, as test data is not available, these values need to be estimated. The value assumed for the SLIMC1 parameter is 0.6, equal to the value used in previous simulations. The SOFT parameter a value of 0.22 is implemented. In a later stage, the influence of the SOFT parameter on the crush behaviour of the absorbers is studied. With this, all the non-physical variables are determined, required to complete the material card. An overview of the chosen variables is reported in Table 6.2

Table 6.2: Toray Cetex TC1225 non-physical material properties.

Variable	Symbol	Value	Unit
Stress limit fibres tension	SLIMT1	0.01	MPa/MPa
Stress limit fibres compression	SLIMC1	0.6	MPa/MPa
Stress limit matrix tension	SLIMT2	0.1	MPa/MPa
Stress limit matrix compression	SLIMC2	1.0	MPa/MPa
Stress shear	SLIMCS	1.0	MPa/MPa
Element time-step limit	TSIZE	1.0E-07	s
Effective failure strain	ERODS	-0.55	mm/mm

The layup implemented in all the specimens is based upon the original layup of the C-strut and is as follows: $[\pm 45/0_2/90/\pm 45/90/0_2/\pm 45]$. With this, a specimen thickness of 2.208 mm is obtained.

6.2.3 Absorbers Loading Rate

The mean crushing load is independent of the loading rate according to the analytical model. However, to ensure the crushing simulations' validity, the alterations with respect to the models presented in Chapter 5 are kept to a minimum. Accordingly, the specimens are fixed on the lower end while these are crushed on the opposite side by a rigid crush plate. The motion of the crushing plate is set at a constant rate of 5.5 m/s. The impact speed of the fuselage is set to 10 m/s. Therefore, to gain insight into the influence of the crushing rate, a comparative study is performed to investigate eventual differences in the specimens' crush behaviour.

6.3 C-Strut Absorbers

In the original design of the fuselage, C-struts are placed under the cargo floor to support the cargo floor itself. To further investigate this shape's behaviour when subjected to crush loading, some variations are studied in this section.

6.3.1 Strut Geometry

The variations of the C-struts are such that the absorbers' mass is kept constants with respect to the baseline absorber, such that a valid comparison for the SEA can be made, as described in Subsection 6.2.1. The dimensions of the simulated absorbers can be found in Table 6.3.

Table 6.3: C-Strut dimensions.

Specimen	Web Length [mm]	Flange Length [mm]
Original Strut	90	26
C-Strut 1	116	13
C-Strut 2	164	39
C-Strut 3	38	52

The length of the absorbers is as defined in Subsection 6.2.1, which is 378 mm, while the layup and material are as defined in Subsection 6.2.2.

6.3.2 Strut Mean Crushing Load and Energy Absorption

By keeping the cross-section's length and thickness constant, the value that one obtains from the analytical equation for the mean crushing load is the same, which is found to be 15.8 kN. Also the specific energy absorption of the studied C-struts is found to be constant. When looking at the values obtained from the simulations, reported in Table 6.4, one can see that the obtained mean crushing load, energy absorption, and specific energy absorption are of similar values. In Figure D.1, in Appendix D.1 one can find the load-displacement curves of the simulations. In figures D.4 to D.7 in Appendix D.3 one can find the deformations of the simulated specimens. Finally, in Table D.1 in Appendix D.2 one can find the final energy values of the simulations to study the hourglass energy.

6.3.3 Strut Flange Buckling and Crippling Analysis

First, it can be noticed that the analytical load is higher than the simulated loads. This discrepancy may originate from two phenomena, one of which is the instability of the flanges that is not taken into account in the analytical model, while the other reason may be the incorrect assumption of the non-physical parameters of the material. As a reminder, the main non-physical parameter that influences the value of the mean crushing load is the SOFT parameter. The first phenomenon can be studied by computing the buckling and crippling loads of the flanges and comparing these to the obtained crushing loads. The influence of the

Table 6.4: C-strut crush load and energy absorption results.

Specimen	Mean Crushing Load [kN]	Absorbed Energy [J]	Specific Energy Absorption [kJ/kg]
Analytical	15.8	1338	7.1
Original	13.4	983	5.2
C-Strut 1	12.3	902	4.8
C-Strut 2	12.8	969	5.1
C-Strut 3	12.7	939	5.0

SOFT parameter is studied later with square specimens, where the influence of the geometric instability is of lesser influence.

When looking at the deformation of the C-struts, an example of which can be found in Figure 6.1, one can see that the flanges indeed undergo buckling-like deformation. In the figure, the y-displacement is shown, which is the out of plane deflection of the flanges. By the red and blue values, one can see that the flanges have an out of plane displacement of almost ±4 mm, indicating that these indeed undergo buckling-like deformation.

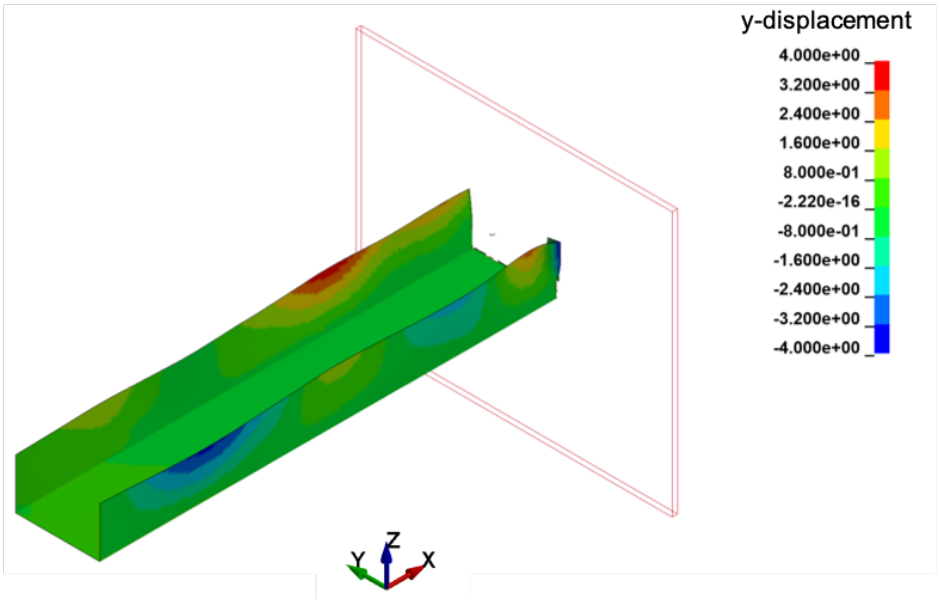

Figure 6.1: Buckling of the flanges. Fringe levels show the, y displacements of the strut, in the out of plane deflection of the flanges, in units of mm.

The buckling and crippling loads of the flanges can be computed. The buckling equation of the flanges is given by the one edge free buckling equation for composite plates, reported in Equation 6.4 [68]. In the equation, N_o represents the distributed load on the flange required for it to buckle, while b and a are the flange's width and length, respectively. Finally, the different D terms indicate the entries of the laminate's flexural matrix, which can be obtained with classical laminate theory. From this, it can be seen that the buckling load is actually a function of the strut's length, which depends upon the crush location. To compute the buckling loads, the initial length of the specimen is taken.

$$N_o = \frac{\pi^2}{b^2}\sqrt{D_{11}D_{22}}(K), \text{ where } K = \frac{12}{\pi^2}\frac{D_{66}}{\sqrt{D_{11}D_{22}}} + \frac{1}{\lambda^2}, \text{ and } \lambda = \frac{a}{b}\left(\frac{D_{22}}{D_{11}}\right)^{1/4} \tag{6.4}$$

To determine the crippling load, two different equations can be used. First, one can use the one edge free buckling equation, reported in Equation 6.4, and compute the limit for flange's length that goes to infinity, which holds Equation 6.5. In the equation, b is the width of the flange, while D_{66} is the entry of the flexural matrix, obtained with classical laminate theory. Finally, N_{crip} indicates the distributed load on the flange required for it to cripple.

$$N_{crip} = \frac{12D_{66}}{b^2} \tag{6.5}$$

However, from the Composite Material Handbook [69], where a series of tests have been performed, it is found that irrespective of layup, when at least 25% of the layers are of 0, 25% of the layers are of 45 degrees, and the flange width over thickness ratio is greater than 2.9, which is the case for the studied flanges, Equation 6.6 can be used. In the equation, σ_{crip} indicates the crippling stress, while σ_c^u indicates the laminates ultimate compressive stress, while b and t represent the flange's width and thickness, respectively.

$$\frac{\sigma_{crip}}{\sigma_c^u} = \frac{1.63}{\left(\frac{b}{t}\right)^{0.717}} \tag{6.6}$$

With the provided equations, the buckling and crippling loads for the flanges can be computed. First, to compute the actual values, the laminate's flexural matrix needs to be determined, along with the ultimate failure stress under compression. The flexural matrix is determined using classical laminate theory, while the ultimate stress is determined using a first ply failure maximum stress criterion, to avoid the use of complex failure criteria. The values obtained from this are reported in Table 6.5.

Table 6.5: C-struts laminate properties

Variable	Value	Units
D_{11}	60412.0	Nmm
D_{22}	33102.2	Nmm
D_{66}	25187.6	Nmm
σ_u^c	389.3	MPa

With the provided values in tables 6.3 and 6.5, and knowing that the C-strut's thickness is 2.208 mm, one can determine the buckling and crippling loads. Note that the distributed load and the crippling stress are converted into total loads on the strut, such that the obtained values can be compared to the crushing loads. The calculated values are reported in Table 6.6. For convenience, the mean crushing loads obtained from the simulations are also reported in the table.

In the table, one can see that the buckling and crippling loads are larger than the mean crushing loads. It must be noted though that, the mean crushing regimes are characterised

Table 6.6: C-strut buckling and crippling loads.

Specimen	Mean Crushing Load [kN]	Buckling Load [kN]	Cripple Load [kN]
Original	13.4	64.1	34.0
Strut 1	12.3	254.5	55.8
Strut 2	12.8	28.8	25.4
Strut 3	12.7	16.5	20.7

by large fluctuations, especially the unfiltered loads. The temporary loads exceed the buckling and/or crippling loads of the flanges, causing them to buckle or cripple. This behaviour may yield a lower crushing load, but more importantly, leads to a higher irregularity of the load in the mean crushing regime.

6.3.4 Strut Loading Rate Analysis

As stated in the introduction, the struts are simulated with a crushing rate of 5.5 m/s, which is done to reduce the changes with respect to the validated models of Chapter 4. As the actual fuselage is loaded at a speed of 10 m/s, one needs to study the influence the loading speed has on the absorber. In the finite element model, no strain rate dependent properties are included in the material card; therefore, one should not have any discrepancy regarding the material properties. One difference that may arise, though, is the inertial effect of the structural component.

When looking at the deformation of the absorber loaded at the higher rate, one can see that the amount of buckling waves increase. To visualise this, as a single figure would not capture the behaviour, in Figure 6.2 one can see the out of plane displacement of all the nodes situated at the outer edge of the specimen's flanges. On the left-hand side of the figure, one can see the displacement of the specimen loaded at 5.5 m/s, while on the right-hand side, the displacements of the strut loaded at 10 m/s can be seen. Here it can be seen that the amplitude of the displacement increases when the loading rate is raised.

The buckling waves that are formed cause the lower clamped edge of the specimen to fail. As the lower edge of the specimen fails, the whole absorber loses its ability to sustain a crushing load, and therefore also the ability to absorb energy. In Figure 6.3 one can find the comparison between the load-displacement curves of the specimens loaded at 5.5 m/s and 10 m/s. Here one can see that the crushing load of the specimen with the higher loading rate indeed collapses.

6.4 Square and Rectangular Tube Absorbers

In the previous section, it has become clear that the C-shaped absorber is not an ideal shape for crush loading, mainly due to its open section, which may lead to instabilities. Therefore, to have a more reliable energy absorber, a component with a square cross-section in studied.

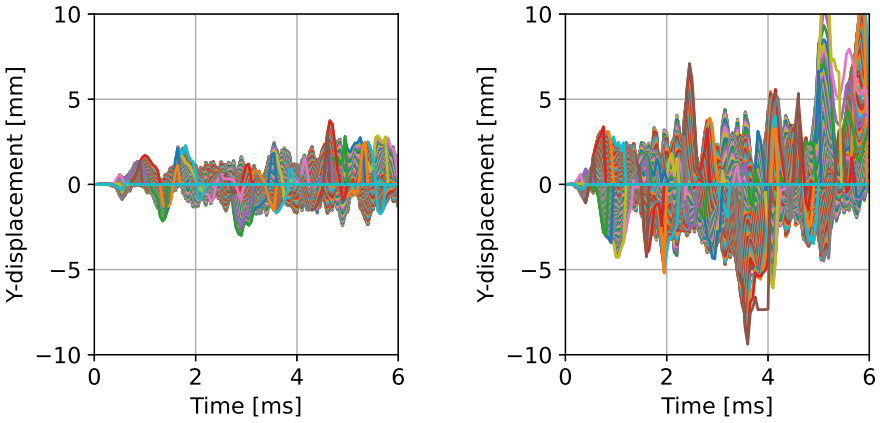

Figure 6.2: Out-of-plane displacement of the outer nodes of the strut's flanges for the two loading rates, with 5.5m/s left and 10 m/s right.

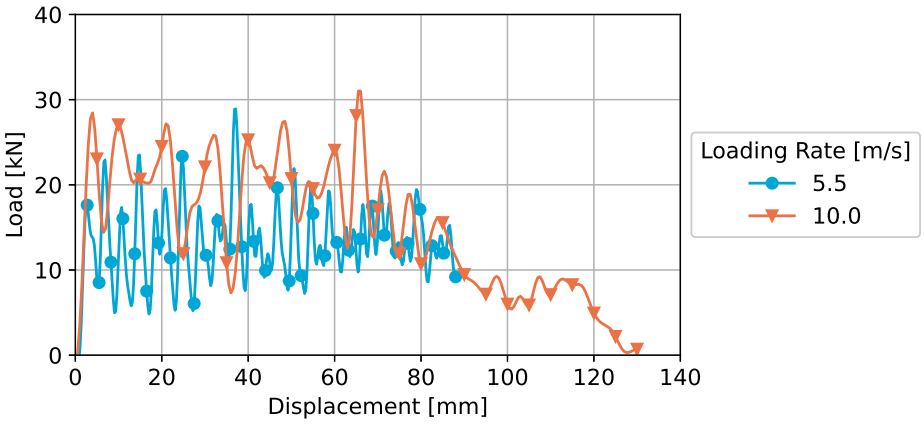

Figure 6.3: C-Strut loading speed analysis.

6.4.1 Tubes Geometry

The geometry of the square absorbers is based upon the geometry of the absorbers studied in Chapter 4. Therefore, the absorbers possess a corner radius of 6.4 mm, while the length is equal to the absorbers studied above, of 378 mm. Finally, the side-length is varied between the different specimens. An overview of the geometry of the simulated absorbers can be found in Table 6.7. Note that the layup and the material used in the square absorbers are equal to the C-strut absorbers studied in the previous subsection to ensure the same crush frond behaviour. When looking at the considered tubes, Tube 3 is the specimen whose weight is most similar to the original C-strut absorber. Therefore, this tube serves as a baseline reference for the C-strut absorbers.

Next to the square absorbers, a rectangular absorber is studied to investigate the behaviour of this type of shape. To ensure a valid comparison, the weight of the rectangular absorber is such that it is of a comparable value to the original C-strut and Tube 3. Therefore, a corner

Table 6.7: Square absorber redesign overview.

Specimen	Side Length [mm]	Total Cross-Section Length [mm]	Specimen Mass [g]
Tube 1	16.8	56.2	74.6
Tube 2	28.8	104.2	138.3
Tube 3	36.8	136.2	180.8
Tube 4	44.8	168.2	223.2
Tube 5	52.8	200.2	265.7
Tube 6	60.8	232.2	308.2

radius of 6.4 mm is used, and a rectangular cross-section of 42.8 by 32.8 mm is implemented. A total cross-section length of 140 mm is obtained by adopting these dimensions, which yields a specimen mass of 186 g.

6.4.2 Tubes Mean Crushing Load and Energy Absorption

The mean crushing loads obtained from the simulation are reported in Table 6.8, along with the absorbed energies. Moreover, in Figure 6.4, one can see the correlation between the analytical and the simulated mean crushing loads.

All the final energy values of the simulations, including the hourglass energy, for both the square as the rectangular absorbers, can be found in Table D.2 in Appendix D.2, while in Appendix D.1 one can find the extracted load-displacement curves for the square absorbers. The deformations are not reported for the tubes, as these are all very similar and comparable to the deformation reported in Chapter 4.

Table 6.8: Square tube absorber redesign crush load and energy results.

Specimen	Mean Crushing Load [kN]		Absorbed Energy [J]		Specific Energy Absorption [kJ/kg]	
	Sim.	An.	Sim.	An.	Sim.	An.
Tube 1	6.9	6.3 (-8.7%)	570	532 (-1.5%)	7.6	7.1 (-6.7%)
Tube 2	9.6	11.6 (20.8%)	805	984 (30.8%)	5.8	7.1 (-22.5%)
Tube 3	12.7	15.2 (19.7%)	1051	1285 (33.8%)	5.8	7.1 (-22.6%)
Tube 4	15.7	18.7 (19.1%)	1302	1586 (32.0%)	5.8	7.1 (-22.3%)
Tube 5	19.1	22.3 (16.8%)	1597	1887 (30.6%)	6.0	7.1 (-18.6%)
Tube 6	20.8	25.8 (24.0%)	1723	2188 (38.1%)	5.6	7.1 (-27.5%)

In Figure 6.4, and this is confirmed by the values reported in the table, it can be seen that the analytical model constantly overestimates the mean crushing load by a value of around 20%. Given the nature of the problem, a 20% error is acceptable; however, it is interesting to note that there is a constant over-estimation of the load. One source for this discrepancy may arise from the assumption of the SOFT parameter, which is known to influence the crush behaviour of the performed simulations [14]. Therefore, the influence of the soft parameter is studied later.

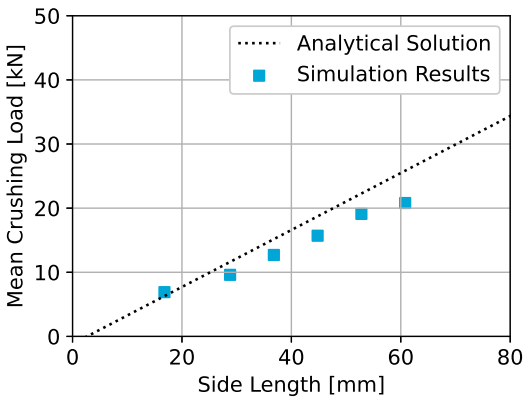

Figure 6.4: Comparison between analytical model and simulation results for the square tube absorber redesign.

It is interesting to note that the obtained data confirm the hypothesis that the specific energy absorption is independent of the cross-section's length. When looking at the values of the specific energy absorption of the simulated specimens, all the values lie around a value of six.

In the results obtained from the simulations of the rectangular absorber, no large changes in behaviour can be seen. The obtained mean crushing load is 11.9 kN (compared to the Tube 3 value of 12.7 kN), while the total absorbed energy is 955.6 J (compared to the Tube 3 value of 1051 J), which leads to a specific energy absorption of 5.6 kJ/kg, which is also close to the value of 6 kJ/kg.

6.4.3 Tube Loading Rate Analysis

As before, the loading rate effect is studied to ensure the good behaviour of the structural component. In this case, Tube 3 is simulated, as this is considered the reference for the struts. Unlike the C-struts studied in the previous section, the square tube absorber does not collapse under the higher loading rate. It is found that the mean crushing load of the specimen with the higher crushing rate is increased. The obtained value is 15.6 kN, which is a 23% increase with respect to the value obtained from Tube 3 with the lower loading rate. Due to the greater load, a higher energy absorption is obtained. With a value of 1358.4 J, this is a 25% increase with respect to the specimen loaded at the lower rate.

The change in load and energy values is interesting, as there can be no strain rate effects in the loading of the specimen, as these properties have not been included in the finite element model. Therefore, these need to arise from inertial effects or other underlying phenomena. To better understand the cause for the increase in mean crushing load, one can study the unfiltered load curve obtained from the simulations, depicted in Figure 6.5. The figure shows that for the specimen loaded at 5.5 m/s, almost all the valleys of every load cycle return to a null value, while for the specimen loaded at a higher rate, this is not the case. This difference in behaviour is suspected to be related to the element erosion of the specimens. In the specimen loaded at a lower rate, every row of elements can be removed from the simulation before the specimen is loaded once more by the crushing plate. This is not the case in the specimen with the higher loading rate, leading to a higher load build-up.

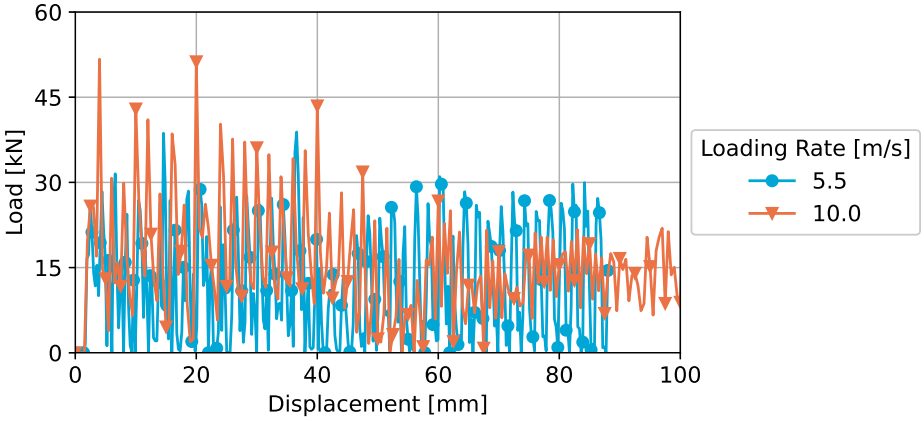

Figure 6.5: Comparison between the unfiltered load curves of the two square tubes loaded at different crush rates.

Similar behaviour can be seen in the work published by Feraboli et al. in 2011 [52], where a corrugated beam is simulated at a rate of 3.81 m/s. In the unfiltered results obtained by Feraboli, it can be seen that a perfect recurring fluctuation is achieved, suggesting that the lower loading rates enable the removal of the rows of elements in each load cycle. In real test specimens, this does not occur, as described in Subsection 2.4.1; this is, however, the nature of finite element simulation.

6.4.4 SOFT Parameter Analysis

In Subsection 7.1.2 it has been stated that the SOFT parameter of the material has been assumed to be 0.22. As a reminder for the reader, the SOFT parameter enables the formation of a crush frond in crush simulations, as this parameter incorporates the formation of delaminations and cracks by reducing the material properties. Ideally, one would obtain this parameter by calibrating the finite element model with test data. As no test data is available for this material, the value has been assumed. However, in Figure 6.4, one can notice that the analytical model constantly overestimates the mean crushing load value. One source of discrepancy may be the ill assumed value of the SOFT parameter. Therefore, the influence of this parameter is studied using Tube 3, which is considered the baseline absorber. This study is only performed for the square absorber to avoid the influence of geometric instabilities that may arise with the C-strut absorber.

In Table 6.9, one can find the results obtained from the simulations, entailing the mean crushing load, the absorbed energy and the specific energy absorption. In Appendix D.1, in Figure D.3, one can find the load-displacement curves of the different simulations. In Table 6.9, it can be seen, that as expected, all the values increase with the increasing SOFT value. Therefore, the SOFT variable may influence the discrepancy concerning the loads estimated with the analytical model. Chapter 4 shows how the SOFT variable can be calibrated to correlate with test data accurately. However, as no test data is available, the value for SOFT of 0.22 is used in future simulations, acknowledging that one should calibrate the non-physical material properties to obtain more accurate results.

Table 6.9: Load and Energy results of the SOFT analysis.

SOFT	Mean Crushing Load [kN]	Absorbed Energy [J]	Specific Energy Absorption [kJ/kg]
0.12	6.9	605.9	3.2
0.22	11.9	1036.6	5.5
0.32	17.5	1523.9	8.1
0.42	22.5	1951.6	10.4
0.52	29.1	2521.0	13.4

6.5 Composite Energy Absorber Design Conclusions

In this chapter, various aspects have been studied. First, the analytical model has been implemented for the design of an energy absorber. To support the development of the structural element, finite element simulations have been performed to investigate the parts' behaviour. In this process, various aspects have come to light, which are shortly discussed.

First, an analytical equation for the SEA of a composite energy absorber has been derived to aid during the design of such a structural element. Here it has been found that the SEA value is independent of the absorber's shape, while it largely depends upon the out of plane specific shear strength of the implemented material. By analysing the simulated specimens, one can indeed observe that for the given material, with some discrepancy, a constant SEA value is obtained.

One other aspect pointed out at the beginning of this chapter is the novelty of studying the behaviour of thermoplastic materials when subjected to crushing loads. The actual influence of this material is difficult to investigate, as solely numerical simulations have been performed, which means that the validity of the models can be questioned, which is confirmed by the SOFT parameter analysis. Nevertheless, the results obtained from the simulations and the gained knowledge regarding the SEA of the structural elements means that thermoplastic materials may be very efficient for crashworthiness structures, as found by Hamada et al. [35].

Finally, the analytical model is accurate when estimating the absorbers' crushing behaviour when these are not susceptible to geometric instabilities. It has been found that during the design of an absorber, one needs to consider the geometric instabilities that may arise when the structural element is loaded. Examples of this may entail the buckling of flanges that may occur in open sections. The buckling behaviour itself may not be problematic for energy absorption; however, excessive deformation may lead to an overall collapse of the component.

Chapter 7

Energy Absorber Implementation in a Fuselage Section

The final step of this research entails the case study of the crashworthiness of an aircraft fuselage. To do this, a section of the fuselage demonstrator as developed by the STUNNING project is taken [67], in which some of the studied absorbers in Chapter 6 are incorporated to investigate the behaviour of the composite energy absorbers in a more realistic application. This way, the suggested analytical-numerical approach can be implemented in an actual case study.

In the first section, the fuselage section is shortly introduced, after which it is described how the digital twin of the structure is created. Once this is complete, the results of the finite element simulations are presented in Section 7.3. The outcomes are then used to study the absorbers' effectiveness in contributing to the structure's energy absorption and crash load. This flows into Section 7.5, where the proposed numerical-analytical model is used to estimate the energy absorption behaviour of the fuselage section. Finally, concluding remarks are provided in Section 7.6.

7.1 Fuselage Section Description

The studied structure is a simplified form of the Next Generation Multifunctional Fuselage Demonstrator, developed by the STUNNING project as part of the Clean Sky initiative [67]. In this section, first, the fuselage's geometry is shortly introduced, after which the material properties of the fibre reinforced material used to build the fuselage are described. Finally, it is explained how the fuselage's digital twin is created in LS-Dyna's finite element software.

7.1.1 Fuselage Geometry

Figure 7.1 shows the section that is being studied. In the figure, it can be seen that a simplified version of the keel section is taken, with the cut made just above the cargo-floor.

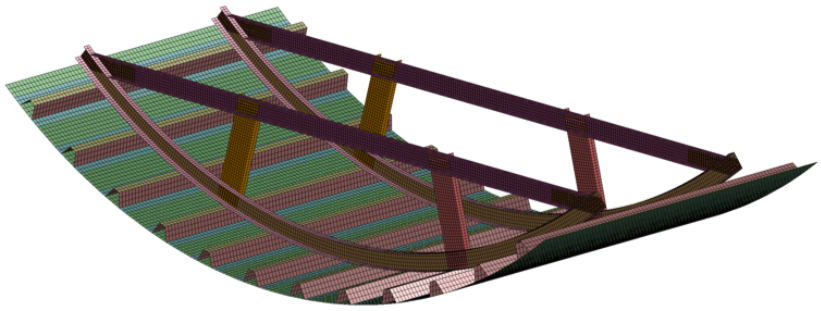

Figure 7.1: Fuselage demonstrator section.

The sub-cargo section is the part of interest when studying the crashworthiness of a narrow-body aircraft, as this structure has the task to absorb the energy of the impact. Furthermore, two frame sections are taken. This leads to a size of 1270 mm in the lengthwise direction and 2664 in the diameter direction. The fuselage is characterised by a typical stringer frame configuration, with a frame spacing of 635 mm and a stringer spacing of 212 mm. The fuselage section is adopted with two diagonally placed C-struts connecting the frame and the cargo cross-beam to strengthen the cargo floor. More details about the single parts can be found in Appendix E.1.

The assembly of the parts making up the structure of the fuselage is based upon composite welding. Next to the welds, a series of clips and brackets are used to provide extra strength to the structure. These brackets and clips are not included in the presented figure, nor are these included in the FE model. In Figure 7.1, it can be seen that the frames are placed on top of the upper flange of the hat stringers. The stringers themselves are attached to the skin of the fuselage section. The cargo-crossbeam, on the other hand, is connected to the frames using metal plates. Finally, the C-struts form a connection between the frames and the cargo-crossbeam and provide support for the cargo cross-beam, but more importantly, they are in this study considered to be the energy absorbers in case of a crash. In the original design, the struts are placed under a small inclination, while in many simulations, the newly introduced absorbers are placed vertically to promote the crushing behaviour. As later will be seen, both configurations are investigated.

7.1.2 Fuselage Section Material Properties

The entire fuselage is made using the same thermoplastic material which has been utilised in the previous chapter. As most crash analyses have been performed for thermoset aircraft fuselages, this study is also valuable to gain more insight into the behaviour of thermoplastic materials in an aircraft fuselage subjected to crash loading.

All the physical material properties can be found in Table 6.1, while the non-physical material parameters are reported in Table 6.2. In the previous chapter, the influence of the SOFT parameter has been studied and found to have a large influence on the material's crushing properties. Therefore, to limit the influence of this parameter in the fuselage's behaviour, the crushing softening is disabled for all parts but the energy absorber. Accordingly, the SOFT value for the energy absorbers is thus kept equal to 0.22 to ensure correlation between

the isolated and integrated simulations; simultaneously, for the remainder of the parts, the softening subroutine is disabled by setting the SOFT variable equal to one.

As stated in the previous subsection, the fuselage also has metal parts. These plates are made from AA6111-T4 aluminium, the material properties of which can be found in Table 7.1. The post yielding behaviour of the metal is controlled by defining a post-yield behaviour curve and assigning this to the material.

Table 7.1: AA6111-T4 material properties.

Variable	Symbol	Value	Unit
Mass Density	ρ	2.89E-06	kg/mm^3
Young's modulus	E	70500	MPa
Poisson ratio	ν_{12}	0.34	-
Yield stress	σ_y	192.1	MPa

7.2 Fuselage Section Finite Element Model

The modelling of the fuselage is done in LS-Dyna and is based upon the experience gained from the simulations performed for the isolated crush components. Accordingly, many cards that have been implemented to simulate the crushing of the composite specimens are implemented in the global structure's simulation. To have a clear overview of the included cards, these are described separately to highlight the reason for their inclusion or alteration.

Mesh and Element Types

The fuselage section is modelled with square elements, which have a size of approximately 10 mm. The absorbers are modelled with a more fine mesh to capture their crushing behaviour better. In the isolated simulations of the absorbers, a mesh of 2 mm is used, which is deemed too fine for the global simulation, which would lead to long simulation times. Therefore, the mesh size of the energy absorbers is increased to 4 mm. In the research published by Boria et al., a mesh sensitivity study is performed on similarly sized absorbers, where it is found that a mesh size of 5 mm suffices [61]. Therefore it assumed that a mesh size of 4 mm is also satisfactory.

The applied element type for all the parts is equal to the isolated absorbers, namely the Belytschko-Tsay elements, with Reissner-Mindlin kinematics, which is achieved by setting ELFORM to 2 in the CONTROL_SHELL card.

By implementing shell elements, the fuselage section is highly simplified. This means that not all details, such as part edge fillets or corner rounding, are taken into account in this simulation, as these are not deemed to influence the crash behaviour of the structure.

Loading and Boundary Conditions

To simulate the fuselage section's crash, a rigid part is created, which crushes the fuselage section, similarly to the simulations performed for the crushing of the isolated absorbers in

Chapter 4. By controlling the crushing with the plate, the simulation's behaviour is more controlled than simulating an actual drop test, which is beneficial for comparing the different simulations.

The fuselage is fixed by applying a clamping boundary condition at the ends of the frames and the skin. By doing so, all the degrees of freedom are constrained at the cutting plane where the rest of the fuselage would be attached. Ideally, one would include a fixture that provides a reaction moment for a given rotation. This complicates the model, along with the fact that it is unknown what the function for the reaction moment should be. Therefore, the clamping condition is deemed sufficient for the current simulation.

The plate's displacement is controlled by a roller support, much like the crushing plate of the isolated energy absorbers simulation. The plate's displacement is restricted in all degrees of freedom except the loading direction of the fuselage. The movement of the plate is set at a constant loading velocity of 10 m/s. This rate is based upon the required impact velocity, as found in Chapter 2.

Next to the fixture and loading of the fuselage, symmetry constraints need to be applied. These control the motion of the nodes where the cut is made along the circumference of the fuselage to obtain the two-frame section. This means that the nodes of the stringers and the skin situated along this cutting plane have applied symmetry, with the cutting plane being the plane of symmetry.

Figure 7.2 shows a summary of the boundary conditions and where these are applied. The orange dashed ellipses indicate the symmetry section, while the light-blue ellipses indicate the clamped regions; finally, the blue arrow indicates the plate's loading rate.

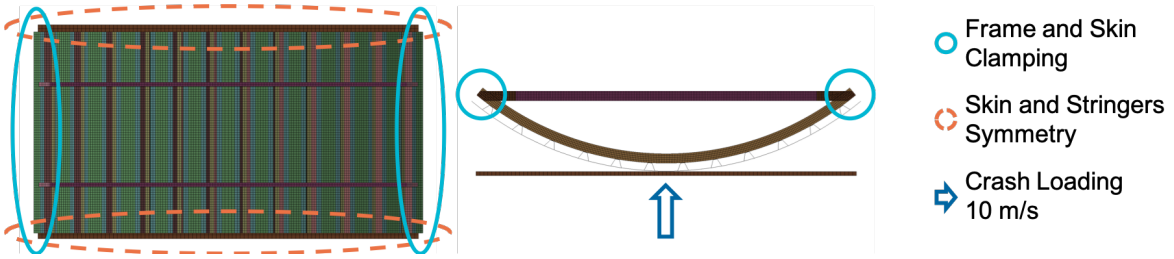

Figure 7.2: Fuselage section boundary conditions

Contact

In the introduction, the use of thermoplastic materials has been introduced, and how this material enables composite parts to be welded together, which may have an advantage during the assembly of an aircraft. Ideally, this type of connection is also modelled during the crash simulation of the fuselage section. However, the behaviour of these types of connections can be self-standing research, and therefore lie outside the scope of this research. Hence, the behaviour of these connections is simplified using the CONTACT_TIED_SHELL_EDGE_TO_SURFACE card. By doing so, the two parts are joined by attaching the slave nodes to the surface of the master part. As later will be seen, this connection creates some complications during the simulation of the fuselage, as this type of contact does not allow for failure in the connection, leading to an unrealistically rigid joint.

During crush simulations, one needs to define the CONTACT_AUTOMATIC_GENERAL card to define the interaction between parts, in case these come into contact during the simulation [51]. Therefore, this card is included in the contact definition, including all the parts of the simulation.

Control

The control cards are based upon the lessons learned from the simulations of the crushing of the composite tube. This means that the Accuracy, Bulk Viscosity, Hourglass, and Shell cards have been implemented, as defined for the crushing simulations. The CONTROL_CONTACT and CONTROL_TIMESTEP cards have been altered with respect to the crushing simulations. The friction coefficient has been set equal to 0.15, while a dynamic friction coefficient has been added with a value of 0.08. The friction coefficient has been reduced with respect to the previously used value of 0.2, as for crush simulations values between 0.1 and 0.2 have been used [14, 48]; therefore, an average of these values has been chosen. The small dynamic friction coefficient has been added to stabilise the model. Moreover, as the model has more degrees of freedom than the simulation of the isolated components, the time scaling factor has been increased from 0.5 to 0.75 to reduce the computational effort. Finally, the termination time is set to 30 ms when the rigid plate reaches the cargo crossbeam.

Parts

All the parts, except for the metal plate, which has been modelled with the PART card, have been modelled using the PART_COMPOSITE cards and by defining the layups using lamina material defined in Table 6.1. To account for the thicknesses of the shell elements in the contact definitions, the NLOC flags have been used to shift the parts' central lines.

7.3 Fuselage Section Simulation Results

To study the performance of the various absorbers, multiple simulations are performed. While performing these simulations, it is found that there are some limitations due to the applied part connections. These limitations are thus described, and alterations are made to improve the effectiveness of the absorbers. The various steps are described below to guide the reader through the process.

7.3.1 Performed Fuselage Section Simulations

As will be seen in the following subsections, different simulations of the fuselage segments have been performed. These simulations not only entail the integration of different energy absorber; in fact, these also entail the alteration of joints and the implementation of a simplified payload mass.

Two different absorbers are studied: the original C-strut absorber and a square tube absorber with comparable mass, which corresponds to Tube 3 of the previous chapter. However, when integrating the aforementioned absorbers, some limitations are found regarding the behaviour

of the absorbers. Ideally, the absorbers are crushed similarly as performed in the isolated simulations to maximise the energy absorption. As later will be seen, two aspects hinder this behaviour, namely the strength of the cargo crossbeam and the connection between the frame and the absorber. Due to the stiffness of the absorber, the cargo crossbeam is pushed upwards. To limit this movement, a simplified payload mass is included in the model to limit the cargo cross-beam's upward motion, as the inertial effect of the payload causes a reaction force on the beam. Consequently, simulations are referred to as 'with Payload' when the simplified payload mass is implemented. One other phenomenon that impedes the crash kinematics is the rigid connection between the frame and the absorber. Therefore in some simulations, this connection has been removed to promote the crushing of the energy absorbers. It is assumed that this connection fails during the first impact of the fuselage section. When the contact between the absorbers and the frame is omitted, these simulations are referred to as 'Free Ends', indicating the absorbers' free ends.

The final simulations that are performed are the ones of the full original STUNNING design. In the proposed designs, the absorbers are placed vertically to stimulate the crushing. In the original design, the struts are placed under a slight inclination. Therefore, to study this behaviour, this geometry is also studied to provide a complete comparison.

7.3.2 Baseline Results

First, a baseline fuselage section is simulated, with no energy absorbers, to study the effectiveness of the introduced absorbers later. This means that the baseline is used to obtain the crash load and, more importantly, the energy absorbed by the fuselage section, without the presence of any absorbers. Figure 7.3a shows the baseline configuration in its undeformed state. The deformed states at three different time instances of the simulation can be found in figures 7.3b to 7.3d. On the bottom of every figure, one can observe a front view of the deformation, while in the upper part of every figure, one can see an isometric view of the deformation.

In the various stages of the deformation, it can be noticed how the frames are slowly flattened as these come into contact with the crushing plate. Similarly, as found in Chapter 2, the frame forms hinge points that enable the deformation. As with the reference fuselage sections, these hinge points are formed at the lower midpoint of the fuselage, while two are formed along the frames' circumference. Interestingly, there is no material damage in the first part of the simulation, not until excessive rotation at the hinge points is achieved. In fact, the only damage that can be visually inspected is located at the hinge points.

Next, to study the fuselage section's baseline performance, the results can be used to verify the finite element model. In the previous sections, it has been shown how the energy sources can assist during the verification of the finite element model. As there is no test data to validate the models, the model's verification phase is key. The tools used to verify the model are the energy ratio, the hourglass energy and ensure that there are no large instantaneous changes in the energy values. The energy ratio has been found to deviate only slightly from the value of one, and therefore meets the requirements. On the other hand, as multiple parts are present in the model, the single parts' hourglassing energy is studied to ensure that these are below the required 10% [51]. In Table E.5 in Appendix E.2.1, one can find an overview

of the energies in the different parts. Here one can see that the hourglass energy of each part is indeed lower than the required 10%.

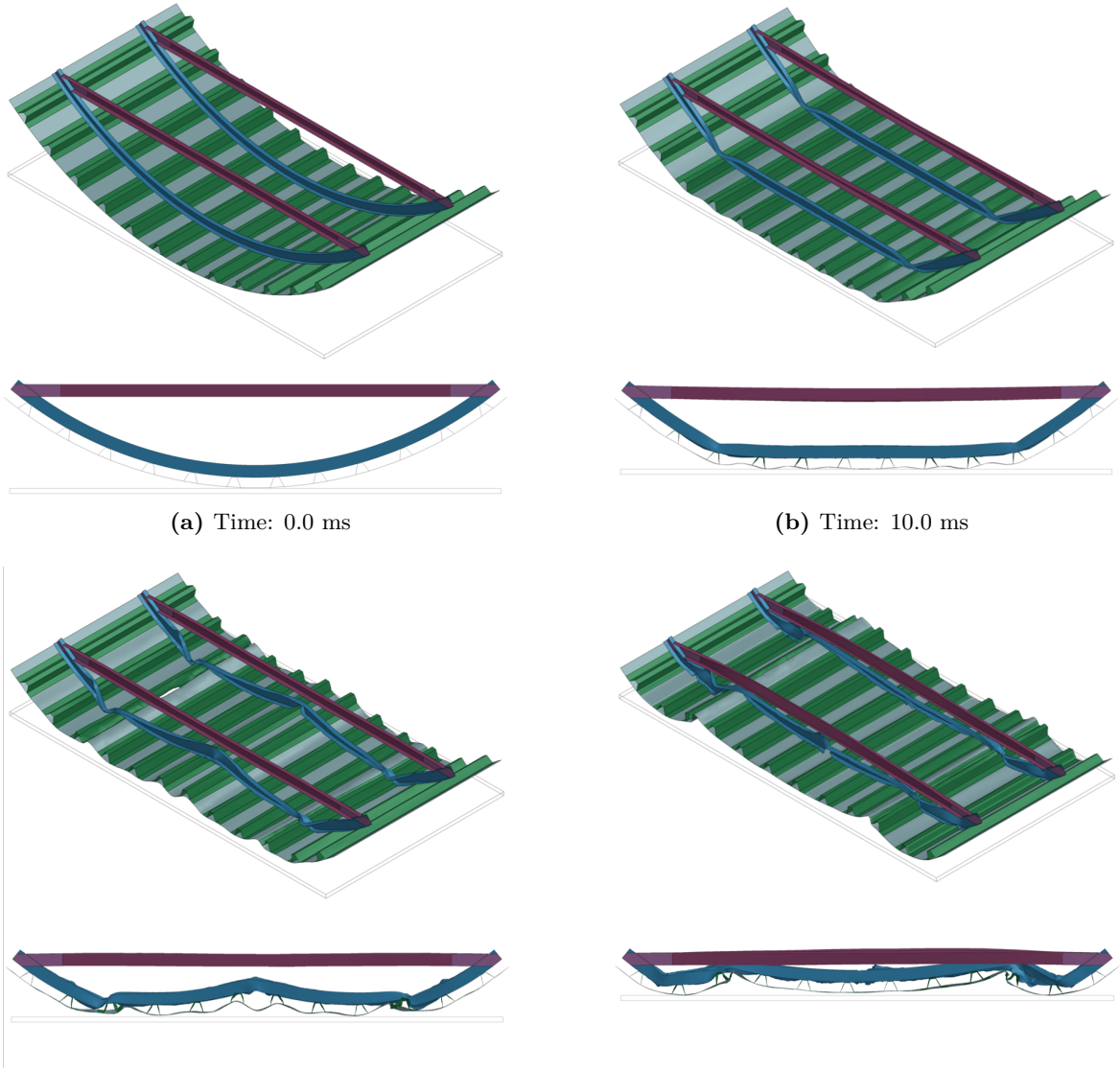

(a) Time: 0.0 ms

(b) Time: 10.0 ms

(c) Time: 20.0 ms

(d) Time: 30.0 ms

Figure 7.3: Simulation deformation at various time-steps of the baseline fuselage.

When looking at the part energy results, an example of which is presented in Figure 7.4, one can notice strange behaviour in the part's internal energy and the sliding energy of the entire model. This behaviour is characterised by negative friction energies, accompanied by a large increase in the part's internal energy. This behaviour is manifested in the skin and stringers of the fuselage section. The LS-Dyna user manual states that this behaviour can be isolated and originates from node penetration during contact [51]. In the manual, it is also stated that when the internal and friction energies are mirrored, as is the case, this isolated behaviour does not have a large influence on the validity of the overall simulation. To study this isolated behaviour, one can study the energy density of the shell elements. In Figure 7.4,

the blue line with the round markers and orange line with triangular markers represent the internal and frictional energy of the part, respectively, while the green dashed line represents the energy density of a probed shell element. The part values with the continuous lines can be read on the left-hand axis, while the energy density, depicted by the dashed line, can be read on the right-hand vertical axis. By studying the simulation's energy density values, it is found that there are indeed small areas with a large increase, especially in the skin and stringer regions, where contact with the crushing plate occurs. Based on the obtained results, and the suggestions of the LS-Dyna user manual regarding energy density, it is assumed that this local effect does not have a large influence on the validity of the simulation. It must be stated that other simulations show similar behaviour; these have been verified according to the aforementioned criteria and are deemed valid.

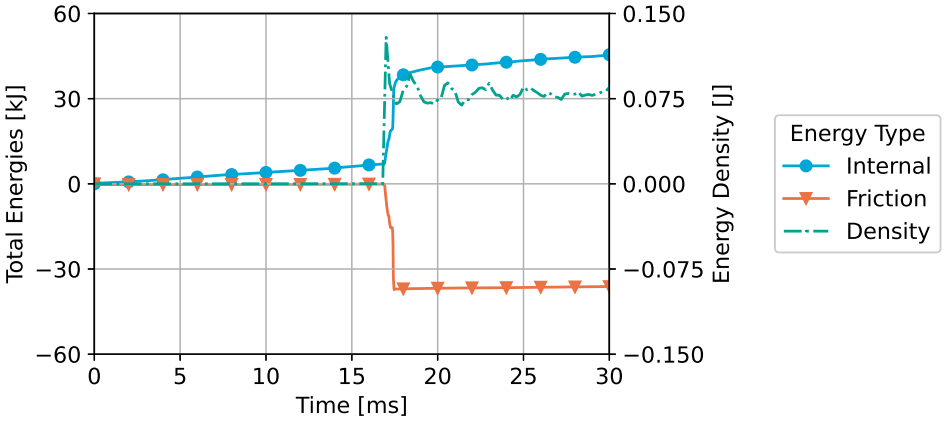

Figure 7.4: Baseline skin internal energy, friction energy and energy density of probed shell.

When looking at the structure's deformation, it is interesting to note that the skin and stringers show little to no damage, while a large part of the damage occurs in the frames. In fact, the combined damage energy in the skin and stringers is only 1.6kJ. For comparison, the frame has a damage energy of 5.4kJ. This behaviour seems rather strange, as the skin and stringers are the main parts coming into contact with the crush plate. However, when looking at a reference test performed by Delsart et al. on a similar composite fuselage section, one can see similar behaviour, as shown in Figure 7.5. A similar composite fuselage section is tested in the referenced paper, with a different frame and absorber structure but similar stringers. In the figure, it can be seen that also during this test, the skin and stringers show almost no visible damage. This does not mean that there is no damage. In fact, when looking at the previously reported energies, some damage does occur.

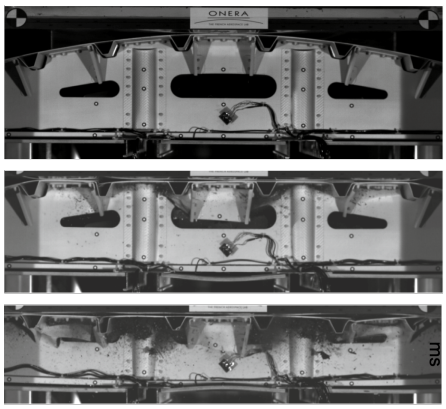

Figure 7.5: Crash results of a composite fuselage section [16].

7.3.3 Fuselage Section with C-Struts Results

The first simulation to be analysed is the fuselage section with the original strut design; however, it is placed vertically to promote the crushing behaviour. The strut is integrated into the structure by implementing a tie constraint between the strut and the cargo cross-beam, and between the strut and the frame.

The first deformation stages are similar to the deformations reported in Figure 7.3, entailing the bending motion of the frame of the keel section. Afterwards, the absorber's rigid connection with the surrounding parts leads to the cargo beam's upward bending until the absorber collapses, as shown in Figure 7.6. For a complete overview of the deformations, the reader is referred to Figure E.1 in Appendix E.2.2. Once the absorbers are collapsed, the section's frame is further deformed, similarly to Figure 7.3. The exhibited behaviour is not deemed realistic, as the absorber's tie constraint with the frame and the cargo beam forms a rigid connection. This type of connection prevents the energy absorber from being triggered into its crushing failure mode. Ideally, one would integrate a failure criterion for the connections of the absorber. However, little knowledge is available for the strength of the connection, and the modelling of this failure lies outside the scope of this research. Therefore, in a later stage, some simplifications are implemented to circumvent this behaviour. First, a simplified payload mass is included above the cargo cross-beam, limiting the beam's upward motion. Later, the tie constrained between the frame and the absorber is omitted to promote the absorber's crush behaviour further.

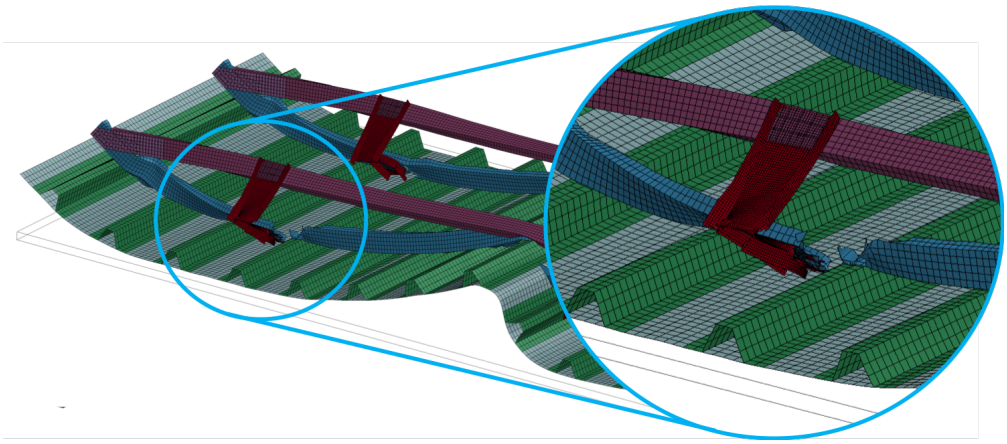

Figure 7.6: Isometric view of the failure of the C-strut absorber.

One interesting aspect of the simulation is the loss of symmetry in the results. While during the baseline simulation, the deformation is symmetric, in the fuselage section with the C-struts, this mirrored behaviour is not present. This originates from the failure of the fuselage's material. This asymmetric response is also observed in the crushing simulations of the single crush specimens, where the splaying layers do not form a perfect symmetric shape. Therefore, it can be assumed that this is reasonable for this type of simulations. Because of this, the finite element model can not be simplified by applying symmetry along the vertical axis of the fuselage section.

In Appendix E.2.1, in Table E.6, one can find the final energy values of the parts, obtained from the simulations, which can be used to verify the hourglass energy of the parts.

7.3.4 Fuselage Section with Square Absorber Results

In the previous chapter, it has been found that a square absorber is more stable when subjected to crush loading with respect to a C-shaped absorber. Therefore, the fuselage section is also simulated with this absorber type. The absorber is equal to Tube 3 of the previous chapter, which, to have a valid comparison, has a similar mass as the original C-strut.

The fuselage section with the installed square tube absorbers shows a similar behaviour as the previously simulated fuselage section with the C-struts. Accordingly, the first stages of the crash loading are similar to the baseline simulation, where the frame of the keel section is gradually pushed upwards. Once the crushing plate comes into contact with the absorber, the cargo crossbeam is pushed upwards. In this case, however, the absorber's stability is higher, which prevents it from collapsing. This leads to a failure in the cargo cross-beam, as depicted in Figure 7.7. Once the cargo crossbeam has failed, the only structure resisting the crushing plane's motion is the frame, which is further bent, similar to the baseline fuselage section.

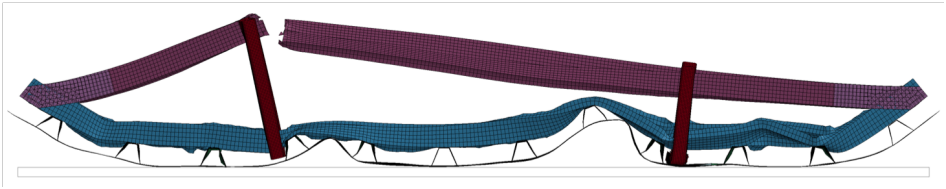

Figure 7.7: Front view of the failure of the cargo-crossbeam with the fixed square tube absorber.

In Appendix E.2.1, in Table E.7, one can find the final energy values of the parts, obtained from the simulations, while in Figure E.2 in Appendix E.2.2 one can find the deformation of the fuselage section at different time instances.

7.3.5 Fuselage Section with Simplified Payload Results

As revealed in the previous subsections, the integrated energy absorbers are not effective, withholding them from exhibiting the desired crush kinematics. This behaviour mainly originates from two sources, one being the rigidity of the connection of the absorbers with the frame, preventing these to form a stable crush frond, the other one being the upward bending motion of the cargo crossbeam, which enables the upward motion of the absorbers, preventing these from being crushed.

To improve the energy absorption, two changes are made to the model. First, a simplified payload mass is added to the model to limit the cargo beam's upward motion. By adding the payload mass, the cargo-beam is pushed against the payload, which, due to Newton's third law, causes a reaction force on the cargo-beam, limiting its motion. In a later stage, the connection between the absorbers and the frame is also omitted from the model to promote the component' crushing behaviour further. First, the model with the implemented cargo is studied, after which the model with the absorbers with the free ends are studied.

It must be stated that the model with the cargo is performed to study the idealised kinematic behaviour of the fuselage section. This is because one can not accurately estimate the amount of cargo present in the event of a crash. Hence, the cargo mass is estimated to be 20 kg per passenger. Given the length of the fuselage section, it is assumed that six passengers are

seated in this section, leading to a cargo mass of 120 kg. The payload is modelled using a rigid body of 2000 mm by 760 mm, with a thickness of 10 mm, and is placed at a small distance above the cargo cross-beam, to avoid initial penetration of the nodes.

By introducing the payload, the cargo-crossbeam is indeed restricted in its movement. However, one other aspect comes to light: the absorber's connection with the frame prevents the absorber from initialising its crushing behaviour. Instead, failure occurs in the proximity of the connection, after which the absorbers slide out under the cargo crossbeam, as depicted in Figure 7.8, preventing them from absorbing the desired amount of energy. Note that the payload has been removed from the figure's view to have better visibility of the energy absorbers.

The final energies of the parts in the simulation can be found in Appendix E.2.1, while more detailed deformations can be found in Figure E.3 in Appendix E.2.2

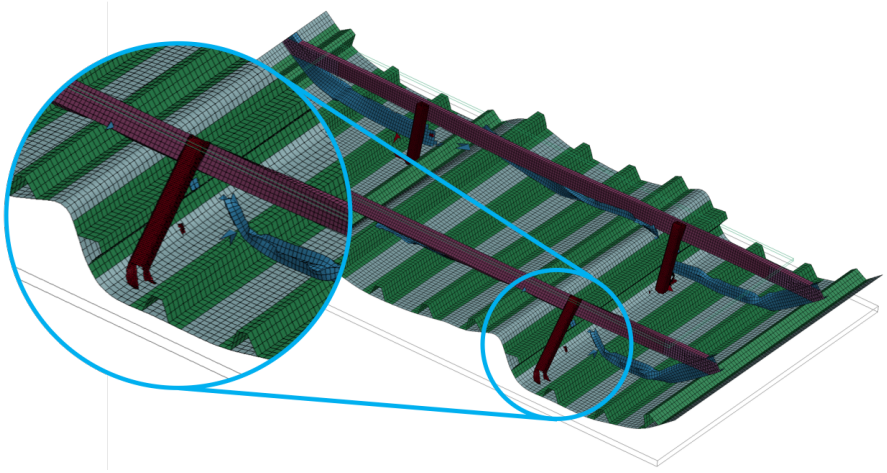

Figure 7.8: Detail of the absorber sliding out in the deformation of the fuselage section with fully fixed square tube absorber and simplified payload mass.

7.3.6 Fuselage Section with No Contact and Simplified Payload Results

To further improve the simulation and study the absorber's performance, the tie constraint between the frame and the absorber is omitted from the model. As stated before, ideally, one would model the failure of this connection; however, this lies outside the scope of this research. Furthermore, the payload mass is kept in the model, as it is found that this provides stability to the absorbers by limiting their rotating motion. This way, the conditions are ideal for the energy absorber, providing a good test case to study the absorbers' ideal behaviour. A more detailed study may be required in the future, which includes the failure of the connection between the absorber and the frame.

Figure 7.9 shows the deformation of the fuselage with the square tube absorber. Here it can be seen that the absorber is crushed as is desired. In the first stages, the frame bends to accommodate the upward motion of the crushing plane. Once the skin comes into contact with the absorbers, these form a crushing frond, as observed in the isolated simulations. More importantly, the absorbers remain straight for the entirety of the simulation, enabling them to be crushed.

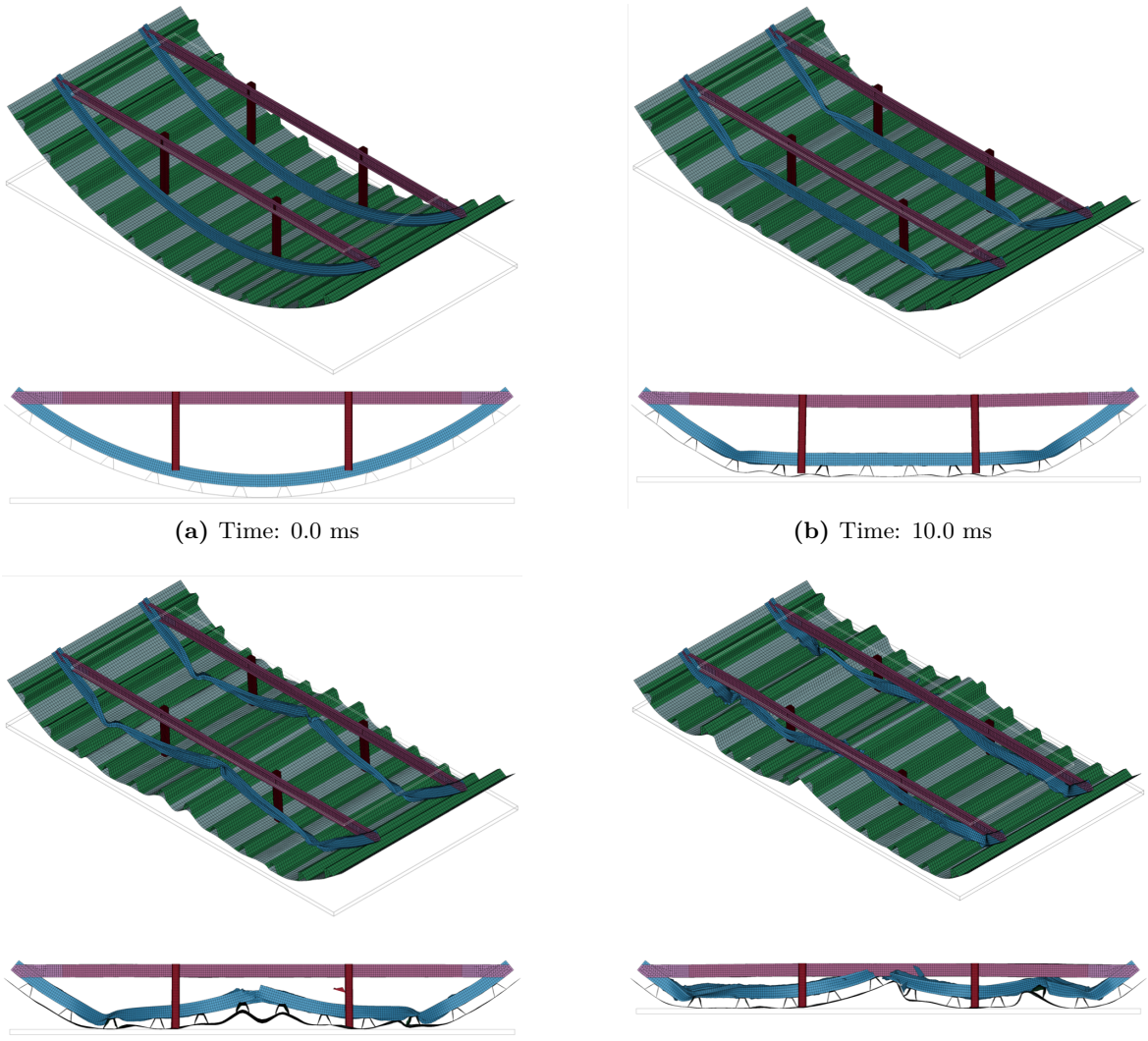

(a) Time: 0.0 ms

(b) Time: 10.0 ms

(c) Time: 20.0 ms

(d) Time: 30.0 ms

Figure 7.9: Simulation deformation at various time-steps of the fuselage section with square tube absorbers with no connection to the frames.

When the C-strut is integrated into the fuselage structure, the absorber shows unstable behaviour by sliding out under the cargo cross-beam. The first stages of the deformation are once again similar to the deformation exhibited by the baseline fuselage model. However, once the crushing plane comes into contact with the absorbers, these are rotated, which causes them to slide over the fuselage section's skin, as depicted in Figure 7.10. For more details regarding the deformation of the fuselage section with C-strut absorbers with no connection to the frames, the reader is referred to Figure E.4 in Appendix E.2.2, while the energies of the parts of both simulations can be found in tables E.10 and E.11 in Appendix E.2.1.

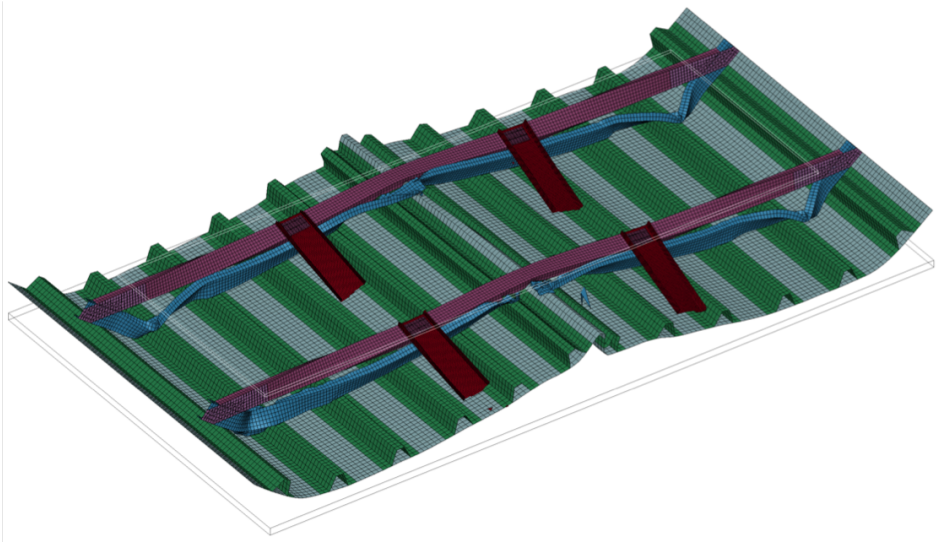

Figure 7.10: Deformation of the fuselage section with C-struts with no connection to the frames.

7.3.7 Original STUNNING Fuselage Section Results

The behaviour of the original STUNNING fuselage section is investigated in both fully-fixed configuration, as the configuration where the connection with frame is removed to stimulate the absorbers' crushing behaviour.

The obtained behaviour is similar to the previously simulated fuselage sections. First, the fuselage section with the fully fixed absorbers displays similar behaviour with respect to the fuselage section with C-shaped absorbers. This means that the absorber's instability causes it to collapse, as shown in Figure 7.11. The absorber fails in the proximity of the connection with the frame. After failure, the absorber is inclined, which causes it to slide over the fuselage skin, similarly as depicted in Figure 7.10. More detailed deformations of the structure can be found in Figure E.5 in Appendix E.2.2.

The fuselage section with the free ends has an interesting behaviour. As the lower end of the absorber is placed above a stringer, this acts as a trigger for the absorber, as shown in Figure 7.12. Once the crushing propagates, the structural element slides out under the cargo crossbeam, as observed with previous C-strut absorbers. More detailed deformations of the fuselage section can be found in Figure E.6 in Appendix E.2.2.

7.3.8 Fuselage Section Comparisons

In the previous subsections, the deformations of the structures have been discussed. The descriptions have provided a qualitative overview of the failure modes that the fuselage sections exhibit by describing the failure kinematics. To gain more quantitative insight, the absorbed energies and crush loads of the fuselage sections are reported.

First, the fuselage sections which have a fully fixed absorber are studied. As stated before, this analysis entails two aspects: absorbed energy and crash load, which are depicted in figure 7.13 and 7.14, respectively. In this case, the reported energy is the energy the fuselage section

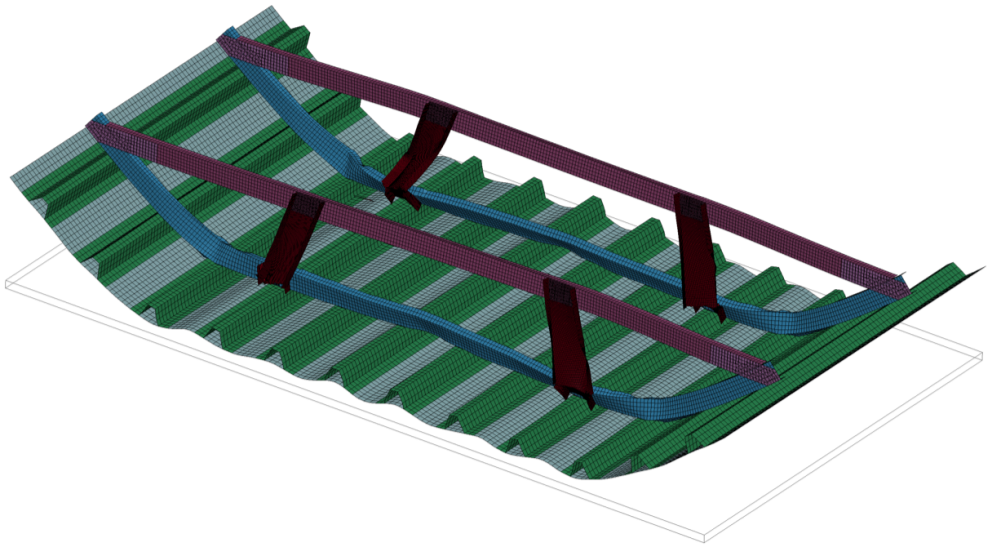

Figure 7.11: Failure of the energy absorber in proximity of its connection to the frame in the fuselage section with the original STUNNING configuration.

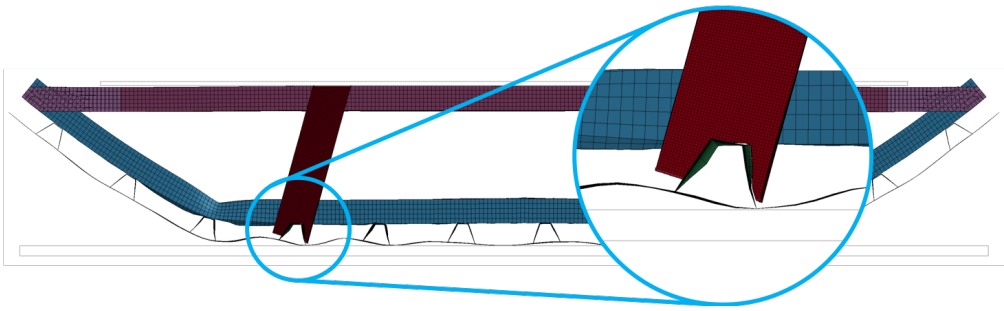

Figure 7.12: Detail of the deformation of the STUNNING fuselage section, where the stringer acts as a trigger.

can absorb, while the load is obtained from the interaction between the crushing plate and the structure. In the presented figures, two aspects stand out. One of these aspects is that it can be seen that the introduction of the energy absorbers clearly has a positive effect on the energy absorption of the fuselage section. The blue dotted line, which depicts the baseline's energy absorption, stagnates around a simulation time of approximately 17 ms. This behaviour is accompanied by a load drop, which corresponds to the snap-through like behaviour of the frame. On the other hand, all the other fuselage sections continue absorbing energy for the remainder of the simulation.

One other aspect that stands out in the simulations is the high load peak that the fuselage section with the simplified payload experiences. This peak occurs when the cargo crossbeam comes into contact with the payload crossbeam. The absorbers form a rigid connection between the crossbeam and the frame. Therefore, as the fuselage section is crushed and is limited in its upward motion, high reaction forces are generated. It must be noted that all the fuselage sections exhibit this behaviour; however, in the fuselage section with the fully fixed absorber and simplified payload mass, the peak value is considerably higher.

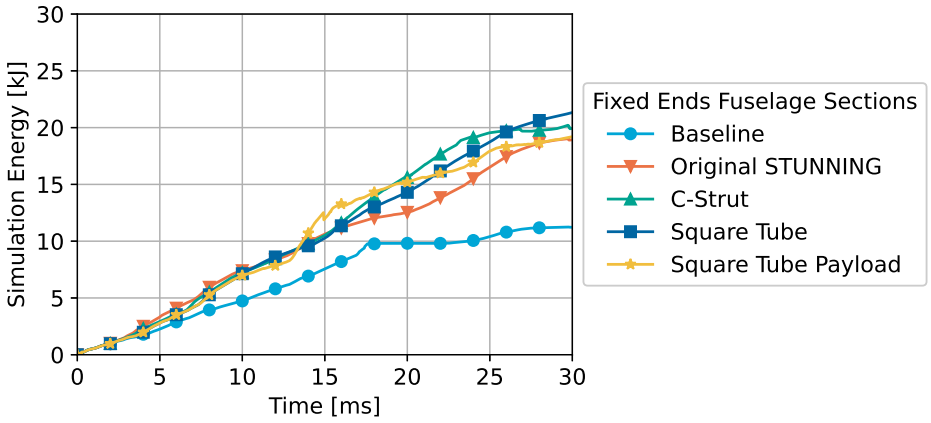

Figure 7.13: Energy absorption comparison for the fuselage section with fully connected energy absorbers.

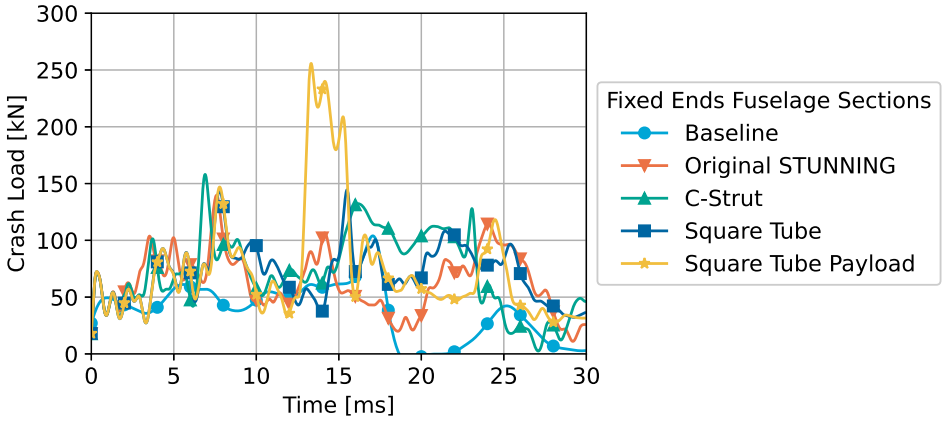

Figure 7.14: Load comparison for the fuselage section with fully connected energy absorbers.

A similar comparison can be performed for the fuselage sections whos contact is removed between the energy absorber and the frame. The energy and load results are reported in figures 7.15 and 7.16. In the figures, it can be seen that the fuselage sections are an improvement with respect to the baseline fuselage section. One other aspect that can be observed is that the peak loads experienced by the fuselage sections are lower than the fuselage section with the simplified payload and fully fixed energy absorbers. This means that by removing the absorber's contact with the frame, some improvement is achieved regarding the load experienced by the fuselage section, which translates to a lower load experienced by the passengers.

One other aspect that stands out in Figure 7.16 is the peak load that the STUNNING fuselage section experiences. Interestingly, this corresponds to the collapse of the load of the baseline fuselage section. As the absorbers are not fully carrying the crash load, due to the trigger effect of the stringer, when the frame exhibits its snap-through like behaviour, the load is instantaneously transferred to the struts, leading to the peak in the crash load.

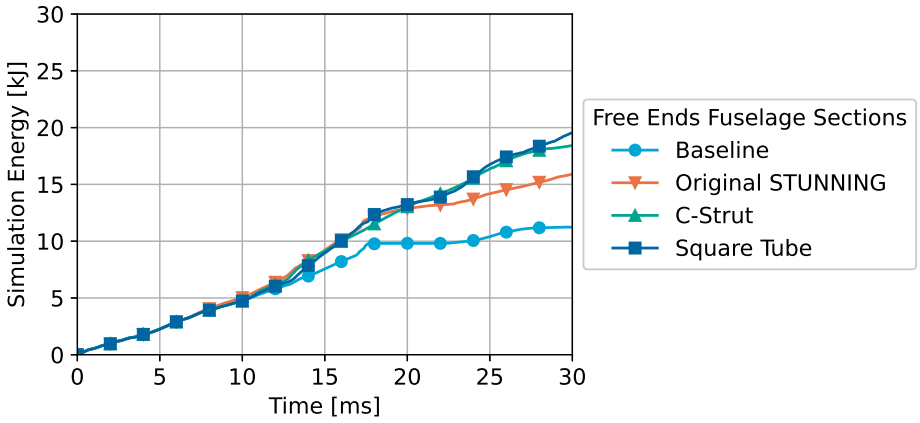

Figure 7.15: Energy absorption comparison for the fuselage section with the absorbers which have no connection to the frame.

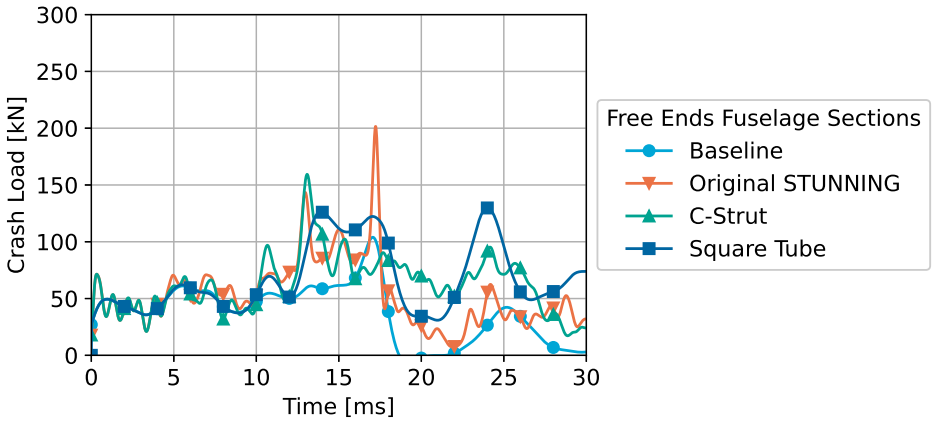

Figure 7.16: Load comparison for the fuselage section with the absorbers which have no connection to the frame.

Finally, it is interesting to note that the crash load of all the fuselage sections with fully fixed absorbers seems to converge to a value of zero. As the absorbers are fully rotated parallel to the crushing plane, they cannot provide a reaction force. From the baseline curve, it can be seen that the frame loses its load-carrying capability at approximately 17 ms; therefore, no structural elements are left to sustain a crash load. The fuselage sections which have no contact between the absorber and the frame do not exhibit this behaviour or in a lesser fashion. The fuselage section with the idealised kinematics still sustains a crash load of approximately 75 kN, meaning that the structure can absorb energy, should the simulation have continued.

To further investigate the fuselage sections' behaviour, one can refer to Table 7.2 where the absorbed energies of the fuselage sections are reported, along with the mean and peak loads. The table shows that all the fuselages achieve roughly the same increase in energy absorption, which is around 40%. The increase in energy absorption can be attributed to the higher average load, wich the fuselage sections with absorbers can sustain. Finally, it can

be seen that the peak load is almost halved by omitting the contact between the absorber and the frame in the fuselage section with the square tube absorbers. This behaviour is less accentuated in the other fuselage sections as the C-strut's instability prevents this load build-up.

Table 7.2: Fuselage section energy and load comparison.

Absorber Integration	Absorber Type	Absorber Energy Value [J]	Absorber Energy Change [%]	Mean Crash Load [kN]	Peak Crash Load [kN]
	Baseline	11225.9		37.4	104.0
Fixed Ends	STUNNING	18924.4	40.7%	63.7	139.7
	C-Strut	19927.8	43.7%	71.8	158.1
	Square Tube	21321.6	47.3%	74.8	255.8
Free Ends	STUNNING	15902.7	29.4%	54.0	201.6
	C-Strut	18416.9	39.0%	62.5	159.4
	Square Tube	19542.3	42.6%	67.4	129.8

Table 7.2 shows that all the studied fuselage sections with absorbers achieve a significant increase in energy absorption. However, the sources of the increase in energy absorption are different. Only the final design, with the square tube absorbers, with no connections to the fuselage's frame, exhibits the desired deformation, which is deemed optimal to achieve maximum energy absorption. The other observed kinematics are characterised by failures of different parts, such as the cargo crossbeam's failure, while other absorbers slide over the fuselage's skin, leading to the partial crushing of the absorber. As these types of failure are difficult to predict, only the idealised failure is further analysed in the following section to develop the analytical-numerical method further. Nevertheless, one should keep in mind that while the suggested method may improve the design process, one needs to ensure the desired failure mode to guarantee the applicability of the proposed approach.

7.4 Absorber Effectiveness Study

To examine the absorbers' performance, one can study the behaviour of the isolated absorbers, the baseline fuselage section, and the behaviour of the fuselage with the integrated absorbers. As only the final simulations have yielded the desired deformation, entailing that the absorber is crushed as hypothesised, this investigation is only performed for this fuselage section.

The analysis entails two parts, namely a load and an energy study. The methodology is equal for both, as both entail a superposition of results. Accordingly, the baseline fuselage section results are superimposed with the absorber results from the simulation of the fuselage section. Ideally, by superimposing the behaviour of the baseline fuselage section and the absorber, one obtains the fuselage section's behaviour with the installed absorber. Along with the comparisons of the fuselage sections, one can study the performance of the energy absorber in the fuselage, by comparing the extracted results of the absorber to the results of the isolated simulation. This way, one can examine how the introduction of an energy absorber influences the structure's behaviour.

7.4.1 Fuselage Section and Absorber Energy Absorption Superposition

First, the energy absorbed by the structure is analysed. Figure 7.17 shows the energy values of the studied simulations. The light-blue line, with the circle marker, represents the accumulated energy as a function of time of the baseline fuselage, while the orange line, with the upside-down triangles, represents the absorbed energy of the fuselage section with energy absorbers. From this, it is interesting to note that the baseline fuselage does not absorb any energy once the frame has collapsed, leading to the plateau starting at approximately 17 ms. The fuselage section with the absorbers, on the other hand, has an ever-increasing energy value, which originates from the absorbers. In fact, the green line in the plot, with the triangular markers, depicts the accumulated energy by the absorbers. For a large part of the simulation, the energy value is null, as the absorbers are unaltered, while once the crush plate comes into contact with the absorbers, these build up their internal energy. Finally, the dark-blue line, with the square markers, represents the superposition of the baseline fuselage section and the absorbers' energy.

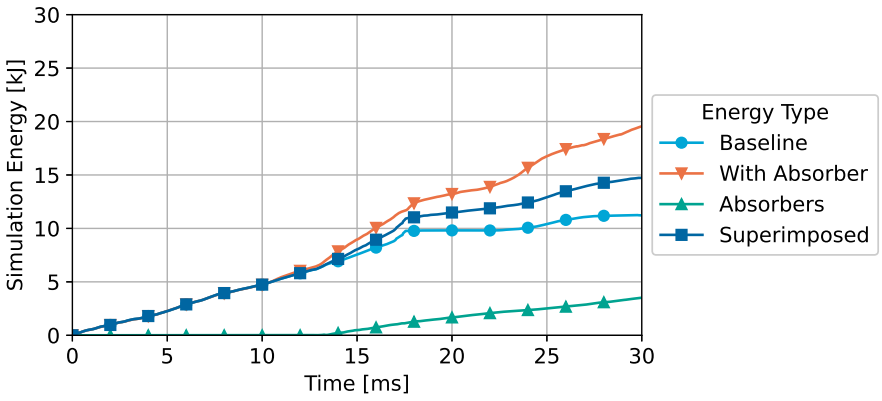

Figure 7.17: Energy comparison between the baseline fuselage, the fuselage section with square tube absorbers, and the superposition of the baseline with the energy of the energy absorbers.

By superimposing the curves, one can see that by studying the absorber's isolated behaviour and the baseline fuselage section, one can resemble the behaviour of the fuselage section with absorbers. There is some discrepancy between the superimposed and fuselage energy values, which can be expected, as other phenomena occur in the simulation. Furthermore, to have a more accurate estimation, one needs to include the sliding interface energy between the fuselage section and the absorber, which is not included here, as LS-Dyna does not allow to study this energy in an isolated manner. Furthermore, the higher energy absorption value can be attributed to more interaction between the structure's parts, which leads to higher energy dissipation.

7.4.2 Fuselage Section and Absorber Crash Load Superposition

Similarly, the fuselage sections' crash load can be studied, along with a superposition of the loads extracted from the crush absorbers and the baseline fuselage section. In Figure 7.18,

the light-blue line, with the dot marker, represents the crash load obtained from the baseline simulation, while the orange line, with the upside-down triangles as markers, represents the load obtained from the simulation of the fuselage section with the installed absorbers. From the simulation with the installed absorbers, the load in the absorbers can be extracted, which in Figure 7.18 is represented by the green line with square markers. Subsequently, the baseline and absorbers loads are combined to obtain the superimposed load curve, depicted by the dark-blue line with the square markers in Figure 7.18. Note that to remove excessive fluctuation in the results, the load data has been filtered using the SAE filter, with a cut-off frequency of 180 Hz.

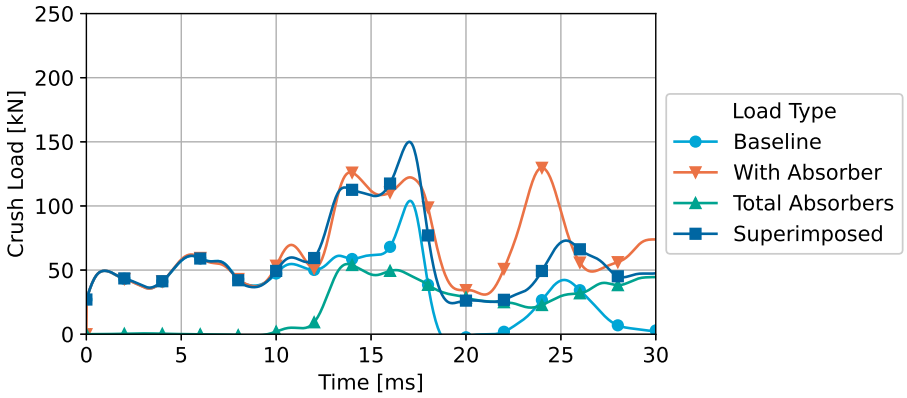

Figure 7.18: Load comparison between the baseline fuselage, the fuselage section with square tube absorbers, and the superposition of the baseline with the energy of the energy absorbers.

Similarly to the energy comparison, it can be seen that by superimposing the loads, similar behaviour is achieved as the fuselage section with the installed absorbers. There are a few aspects that can be pointed out when analysing the load curves. First, in the baseline load curve, a peak can be observed between 12 and 18 ms. This peak is obtained as the loading plate reaches the hinge points in the frames. As shown in Figure 7.3, hinge points are formed along the section's circumference, which enable the bending of the frame. This permits relatively easy upwards motion of the crush plate. However, when the plate reaches these hinge locations, these obstruct the crushing motion, leading to a higher load. Once this point has been surpassed, the baseline load collapses, as the fuselage section experiences a snap-through like motion. After the snap-through, there is no contact with the loading plate until the crushing surface has moved more upwards to come back in contact with the structure, after which it is loaded once more. In this time interval, the frames are loaded once more, leading to the central hinge point's failure, after which the load drops once more, after which the simulation is completed. Quite interestingly, the fuselage section with the absorber shows similar behaviour, with the load shifted more upwards due to the presence of the absorbers. Therefore, the curve representing the superposition of the baseline and the isolated absorbers load is similar to the fuselage section with absorbers.

7.4.3 Isolated Versus Integrated Absorber Comparison

The final comparison that is performed is centred around the performance of the absorber. Ideally, one can predict the absorber's behaviour in the overall structure by studying the absorber's behaviour in an isolated manner. This way, one does not have to study the behaviour of the absorber in the overall structure. This way, the simulation time can be reduced, as one only needs to analyse the isolated absorber rather than the whole structure. Furthermore, as a good correlation between the simulations and the analytical models has been obtained in the previous chapters, one can predict the structural component's behaviour in the global structure with an analytical equation.

This comparison is only performed for the fuselage section with the square tube absorbers, which are not connected to the fuselage's frame, as this is the only simulation that has exhibits the desired deformation kinematics.

Once again, two aspects are studied, the crushing load and the absorbed energy. On the right-hand side of Figure 7.19 the comparison between the loads obtained from the isolated and integrated simulations can be found, while on the right-hand side, the same comparison can be found but for the energy. Note that the integrated absorber results are shifted along the time axis to match the crushing behaviour of the isolated energy absorber; therefore, the x-axis in the figures is only indicative.

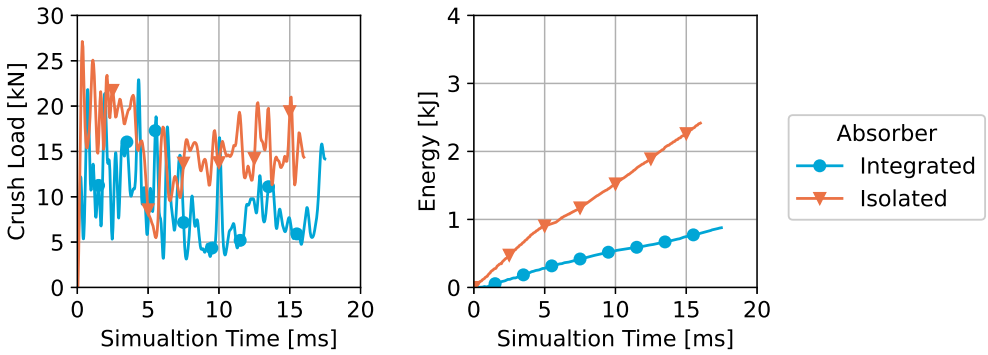

Figure 7.19: Load (left) and energy (right) comparison between the isolated and integrated absorbers.

By looking at the figure, one can see that the achieved mean crushing load of the integrated absorber is lower than the isolated one. This behaviour can be expected as the isolated absorber is simulated under ideal conditions. The lower crushing load is accompanied by lower energy absorption. Figure 7.19 shows that the energy absorption rate is also lower, as expected with a lower crushing load, which implies that the final absorption values are also lower. Hence, both curves extracted from the integrated absorbers are lower than the isolated ones. This is not surprising, as the absorbers are crushed under less than ideal conditions. Nevertheless, quite a good correlation is obtained, given the different circumstances under which the absorbers are simulated.

7.5 Fuselage Section Energy Absorption Estimation

In the previous sections, the results of the fuselage section simulations have preen presented, with the main focus being the energy absorption, failure kinematics, and crash loads. By doing so, the analytical aspect of the method has been left aside. However, during the design of the fuselage section, the analytical model is of paramount importance for the suggested methodology. In fact, using the baseline fuselage section results, combined with the analytical model, the objective is to estimate the energy absorption of a fuselage section with energy absorbers. This can be achieved by superimposing the behaviour as performed in Subsection 7.4.1. However, rather than extracting the energy incorporated by the absorber from the performed simulation, one can estimate the energy that the absorber dissipates using the analytical equation for the mean crushing load. Subsequently, by superimposing the energy of the baseline fuselage section with the absorber's analytical energy, one can estimate to final energy absorption of the improved fuselage section.

In Chapter 6, the mean crushing load obtained for Tube 3, which is the implemented absorber, is found to be 15.2 kN. Furthermore, given the absorber's location in the surrounding structure, it can be found that the absorber is crushed for a length of 165 mm. With this, the theoretical absorbed energy by the four structural elements can be found to be 10.0 kJ. The absorbed energy by the baseline fuselage section is 11.2 kJ. Therefore, the theoretical energy absorption of the structure with absorbers is 21.2 kJ, while the absorbed energy obtained from the numerical model is 19.5 kJ. This means that a discrepancy of only 9% is obtained.

To further verify the hypothesis that the energy absorption of the fuselage section can be estimated by combining the behaviour of the baseline with the proposed analytical model, one final simulation has been performed where an absorber of larger size has been integrated into the structure. The shape and integration into the fuselage section are equal to the fuselage section with square tubes, free ends at the frame side and simplified payload mass, which exhibited the desired crash kinematics. The installed tube has similar dimensions to Tube 5 studied in the previous chapter. This means that it has a side length of 52.8 mm and a length of 378 mm. This way, the same crush length at the previously studied absorbers is obtained of 165 mm. Finally, to further increase the absorber's energy absorption capabilities, the laminate has been altered slightly to achieve a wider thickness, to obtain a higher mean crushing load, and thus energy absorption. By doing so, the following layup is used: $[\pm 45_2/0_4/90/\pm 45/90/0_4/\pm 45_2]$, which leads to a specimen thickness of 3.68 mm. The deformation of the simulated fuselage section is similar to the one depicted in Figure 7.3, however, in Figure E.7 in Appendix E.2.2 one can find the deformation of the structure, while in Table E.13 in Appendix E.2.1 one can find the part energies of the simulations.

Using Equation 5.18 one can compute the expected mean crushing load of the energy absorber, which is found to be 37.1 kN. Combining the mean crushing length and the mean crushing load, one can obtain the energy absorption of the combined four absorbers of 24.6 kJ. Subsequently, combining the absorbers' energy with the baseline energy absorption of 11.2 kJ, leads to a theoretical total energy absorption of 35.8 kJ. From the simulation, the total energy absorbed by the fuselage section corresponds to 29.9 kJ. This means that the difference between the estimation and the numerical model is below 20%. One can expect an underestimation as the absorbers are not crushed under ideal conditions when integrated into the overall structure, as shown in the previous section, which leads to a lower mean crushing

load. Furthermore, the absorbers require some length to form a stable crushing frond, further reducing the idealised energy absorption.

Nevertheless, this provides a powerful tool to estimate the behaviour of the fuselage section when subjected to crash-landing. Once the baseline behaviour is determined, one can investigate different options analytically to meet the energy absorption requirements. As a comparison, once the baseline value has been obtained, which requires a simulation time of approximately 12 hours, designs can be evaluated by using the derived equation, which provides instant insights, while the simulation of the fuselage section with the absorbers requires approximately 20 hours, to run, not including preparation of the model.

7.5.1 Analytical-Numerical Method

Figure 7.20 shows a schematic overview of how the analytical-numerical can be implemented. Here one can see how the baseline behaviour of the fuselage section is determined using a numerical model. This simulation provides insight regarding the load behaviour and energy absorption of the fuselage section as a function of time. Based on this, one can design an energy absorber using the proposed analytical model, enabling one to estimate the mean crushing load and energy absorption. By combining the two components, one obtains an augmented fuselage section, of which the total energy absorption can be estimated, and some insight regarding the maximum crash load can be obtained. Subsequently, when these values are as required, a numerical model of the augmented structure can be created to study energy absorption and load over time. When these are as required, the crashworthiness analysis is complete. If not, one can alter the absorber design, or when necessary, the baseline fuselage, and repeat the process. The described methodology simplifies the actual process, as in reality, these require necessary validation and more detailed analysis, as briefly noted in Figure 7.20; however, this aspect lies outside the scope of this research.

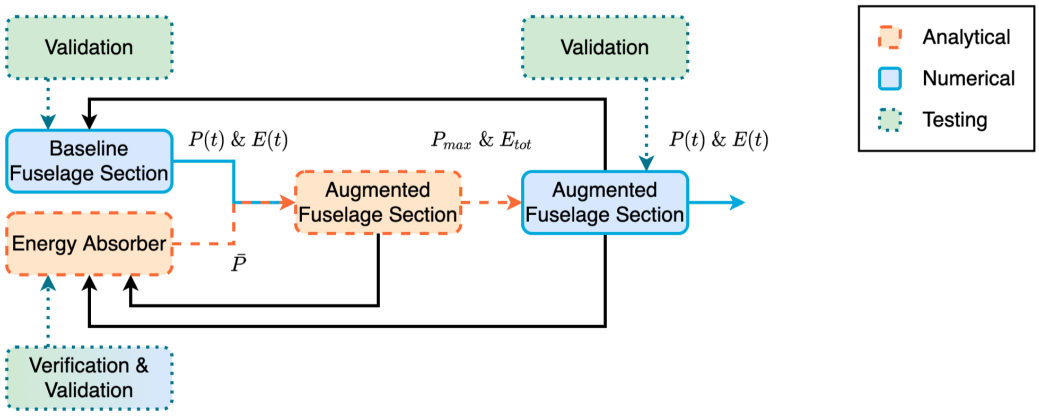

Figure 7.20: Schematic representation of the analytical-numerical method.

By using the combined analytical-numerical method, engineers can estimate the crashworthiness of an aircraft in earlier designs stages of the vehicle. This way, more optimal configurations can be achieved, as alterations can be made in an early stage of the design cycle of the aircraft. Furthermore, more insight is gained into which parameters influence the crash behaviour with respect to others. Naturally, the method has its limitations, as the analytical

method is only applicable when the desired failure mode of the shock absorber is achieved. The chosen failure mode is optimal for a composite energy absorber to maximise the specific energy absorption; however, testing is still required to ensure this. Furthermore, as seen in Chapter 6, the suggested absorbers may exhibit geometric instabilities, leading to an undesired performance; consequently, numerical models are required to study the absorber's behaviour. Finally, the way the element is integrated into the surrounding structure has a large influence on the crash kinematics, in turn, influencing its performance. Furthermore, an error of almost 20% is obtained in the energy absorption estimation, which is thought to originate from the difference in the absorber's performance in an isolated to an integrated environment. Therefore, the suggested method is not seen as a substitute for the more reliable numerical and testing methods, rather as a tool for engineers in the preliminary design of an aircraft to estimate a structure's behaviour. In fact, with the insights gained from this research, one can estimate the crash behaviour of a fuselage section in a fast manner, and one has direct insight into which parameters to change to alter the crush behaviour of a composite energy absorber which can be integrated into a fuselage structure.

7.6 Fuselage Section Test Case Conclusions

Different fuselage section configurations have been analysed in this chapter. Afterwards, the absorbers' behaviour has been compared to the behaviour observed in isolated simulations, which has led to the superposition of the behaviour of the baseline fuselage section with the behaviour of the energy absorbers. By doing so, the energy absorption of the augmented structure is determined using the suggested analytical-numerical method. Some of the key features discovered in this chapter are reported in this section.

First, the different configurations have been simulated using LS-Dyna's finite element software. Here it has been found that the shape and integration of the absorber are crucial for the structure's crash kinematics. While the first stages of all the simulations are characterised by similar behaviour, where the lower part of the frame is gradually flattened by the crushing plane, thanks to the formation of hinge points, the absorbers' failure mode differs from simulation to simulation. Generally, the C-strut absorbers, as found in Chapter 6, exhibit unstable behaviour. In this case, the instability originates from the collapse of the flanges, or the absorber fails to remain in an upright position, causing it to rotate and slide rather than being crushed axially. The square tube absorbers, on the other hand, are more stable. In fact, these are so stable that these cause failure of other parts of the structure, such as the cargo cross-beam. The elements' integration into the surrounding structure is altered to promote the crushing behaviour of the absorbers. Accordingly, at the lower end of the absorbers, the connection with the frame is removed, such that the element can develop the desired crushing frond. By doing so, the C-strut once more exhibits unstable behaviour, characterised by its rotating motion, as mentioned before. On the other hand, the square tube absorber displays the idealised crash kinematics, with the absorber's crushing behaviour resembling that of the isolated simulations. Even though not all fuselage sections match the desired kinematics, all studied structures prove to be an improvement with respect to the baseline structure. In fact, while the baseline fuselage section can absorb 11.2 kJ of energy, all the other sections absorb approximately 20 kJ, which means that the structure's energy absorption is doubled, with a mass increase of only 0.7 kg.

One other key aspect of this chapter is the investigation of the behaviour of a thermoplastic fuselage section when subjected to crash loading. One interesting aspect is that the skin and stringer show little damage when subjected to crush loading, while these structural elements are the main objects coming into contact with the crushing plate. Furthermore, it is found that the bending and failure behaviour of the frame does contribute to the energy absorption of the structure. On the other hand, thermoplastic composite energy absorbers significantly increase the energy absorbing capability of the structure.

To further sustain the development of the analytical-numerical model, the superposition of the baseline fuselage and the absorbers behaviour is analysed. It is found that by combining the behaviour of the baseline fuselage section with the absorber's behaviour, one can estimate the behaviour of the structure with energy absorbers. To achieve this, two fuselage sections are analysed with square tube absorbers, which displayed idealised kinematics. Combining the energy absorption obtained from the baseline and the analytical model presented in Chapter 5, the total energy absorption of the section is estimated with a discrepancy less than 20%. The discrepancy is expected to originate from the lower performance that one achieves from the absorber when integrated into the global structure. Nevertheless, this discrepancy is deemed acceptable, given the complex nature of the problem at hand, while this proves to be a useful approach to support the development of an aircraft fuselage for crashworthiness.

Chapter 8

Conclusions

This thesis aims to achieve a more fundamental understanding of which parameters play a key role in the crashworthiness of an aircraft fuselage. This way, during the preliminary design, engineers do not have to rely on simulations and tests to estimate the performance of an aircraft structure when subjected to crash loading. When more analytical knowledge is available regarding a structural element's behaviour, one can leverage this knowledge to alter the design variables that have a greater influence on the element's behaviour. For example, when a variable has a linear relation, when it's value is doubled, it's influence is also doubled; while when there is a quadratic relation, it's influence is quadrupled. This way designs can be altered more efficiently. Thus, one main aspect of this research is the further generalisation of an analytical model, which can predict the crushing behaviour of a composite energy absorber. To achieve this, numerical models are used to verify the model, but more importantly, the finite element models are used to study the behaviour of the energy absorbers in a test case by including them in a numerical model of a section of a fuselage structure subjected to crash loading. The results obtained from these studies are shortly summarised in this chapter.

Material Simulations

To create digital twins, a material model needs to be implemented. This is of paramount importance as this describes the material's behaviour, which is especially important for its failure and post-failure behaviour. Therefore, two finite element software have been investigated: Abaqus and LS-Dyna; moreover, different material models have been studied, Hashin in Abaqus, and MAT054, MAT058, and MAT262 in LS-Dyna. To better understand these material models, coupon simulations have been performed. In the material's linear-elastic region, the models all behave equally, while these distinguish themselves in the failure and post-failure regime, with the main difference originating from the brittleness of the material models. The energy-based models, meaning Hashin and the MAT262 card, are characterised by abrupt failure, entailing a complete loss in load-carrying capability. The MAT054 and MAT058 cards, on the other hand, thanks to the stress limit factors, can sustain some load in the post-failure regime, yielding a more gradual failure. This ability proves the be important during the crush simulations performed in a later stage.

Finite Element Modelling of Composite Crushing

As shortly mentioned before, the material's ability to sustain load after failure, and be degraded more gradually, proves to be essential when simulating the crushing behaviour of composite specimens. While LS-Dyna offers the ability the reduce material properties in the crush frond of the specimen, Abaqus removes the elements from the simulation. The load results obtained from both finite element tools are characterised by large fluctuations originating from the element erosion. Thanks to the softening parameter in LS-Dyna, this fluctuating nature is reduced, enabling the formation of a crush frond, while in Abaqus, this is not achieved, leading to an inaccurate representation of the crushing phenomena. All studied material models in LS-Dyna can accurately represent the crushing behaviour. However, to achieve this, non-physical parameters need to be calibrated, mainly influencing the material's stress limits and softening. It is found that by implementing the bisection method, the values for these variables can be estimated rapidly. All the material cards can predict the mean crushing load with a discrepancy that lays within 18%. The MAT054 and MAT058 material models have a more accurate prediction for the absorbed energy, with a maximum error of 13%, while the MAT262 model has a larger error of 38%.

Analytical Approach for Composite Crushing

The need to calibrate the material properties proves to be a limitation during the design of an energy absorber, as one can not produce predictive analysis. Therefore an analytical model is studied to predict the crushing behaviour without the need for empirical data. The analytical model is a generalisation of reference models and is able to accurately predict the mean crushing load of the studied specimen types. When comparing the analytical and the numerical mean crushing loads for square tube specimens, a maximum discrepancy of 10% is achieved. In the simulations, it has been seen that one needs to account for geometric instabilities, which may lead to the collapse of the structure. In fact, for specimens with a long side length or small thickness, geometric instabilities are observed, leading to an early collapse of the absorber.

By implementing the analytical model, it has become clear that the energy contributions originating from the vertical splits and delaminations can be omitted from the model, as these contributions are negligible with respect to the friction and shear energies. The model can thus predict the mean crushing load of other specimens than the square tube, such as the studied C-strut and corrugated beam. Accordingly, the analytical model has been implemented to predict the mean crushing load of corrugated beams, where a maximum discrepancy of 25% is obtained with respect to numerical data, which, given the fluctuating nature of the problem, is acceptable.

Energy Absorber Implementation in a Fuselage Section

By introducing the absorbers into a fuselage section, a case study is performed where the analytical model can assist during the design of such a structural component. A baseline simulation is performed to study the performance of the fuselage section with no crash absorbers. Subsequently, using the analytical model, one can estimate the fuselage section's

energy absorption by combining the absorption of the baseline structure with the estimated energy of the absorbers. Furthermore, one can estimate the crushing load that the augmented structure experiences during the crash by superimposing the load obtained from the baseline simulation with the load obtained from the analytical model.

Furthermore, to aid during the design, the analytical model is further rewritten to determine the specific energy absorption of the installed absorbers. By performing this analysis, it is found that the absorber's shape does not influence the SEA of the structural element. From this, it is found that the main property that influences the energy absorption of an energy absorber is the specific shear strength of the material. The SEA values obtained from the analytical and numerical models are compared to verify this hypothesis, where a good correlation is found, confirming the aforementioned hypothesis for the studied cases. To fully confirm this hypothesis, one needs to perform more verification and validation.

During the implementation of the absorbers, it is found that the structural component's stability is of paramount importance. The C-strut absorber, due to the buckling of the flanges, is prone to early failure caused by the component's geometric instability. Furthermore, even though the studied square tubes are more stable, it is found that the connections of the absorbers to the surrounding structure are of importance for the deployment of the absorber. The structural elements are integrated into the fuselage section using a contact constraint with the cargo cross-beam and the frame. The connection with the frame causes a rigid connection, preventing the absorber from achieving the desired crushing behaviour. Furthermore, a payload mass has been included in the model to limit the upward motion of the cargo cross-beam, while the connection with the frame has been removed, assuming that this connection fails during the initial impact of the crash. The fuselage's crash kinematics with the stable square tube absorbers are as desired by implementing these alterations, yielding a 70% increase in energy absorption.

Two fuselage sections have been obtained which exhibit the desired kinematics. Here it is found that by combining the absorbed energy of the baseline structure, with the theoretical energy absorption of the crash absorbers, one can estimate the total energy absorption with a discrepancy of 20% with respect to the numerical results. Furthermore, by superimposing the simulated and computed load, one can estimate the structure's crash load. This indicates that superposition is a useful tool during the preliminary design for the crashworthiness of an aircraft fuselage. By doing so, engineers have direct insight into which parameters influence the behaviour of a composite crash absorber, such that an efficient and compliant design can be created, reducing the need for complex simulations or physical tests.

Final Remarks and Recommendations

This thesis aims to gain more insight into which variables influence the crash behaviour of an aircraft fuselage. This has been achieved by studying the crash behaviour of a composite energy absorber. With this, different designs have been suggested to improve the crashworthiness behaviour of the provided fuselage. In this process, some assumptions have been made to ensure the analytical model's applicability and estimate the fuselage section's energy absorption. The composite energy absorber needs to fail in a combination of splaying and fragmentation for the analytical model to be applicable. However, as has been seen in reference tests, this failure mode is not always manifested. Therefore, to ensure this behaviour,

more research is required to understand further the failure origin and when each failure mode is manifested, such that this can be ensured during the design process. Furthermore, to promote the absorber's axial crushing in the global structure, alterations have been made to the numerical model to achieve the desired crash kinematics. Therefore, more research is required to study an absorber's behaviour in a structure and how this can be triggered efficiently. This way, the analytical model can be implemented to estimate the crash performance of the fuselage section.

Ideally, one can incorporate the crash requirements in an earlier design stage to reduce the necessity to alter already matured plans. This way, during the design of the fuselage for its nominal operation, the crashworthiness can be taken into account to reach a more optimal configuration for both loading cases. To achieve this, more research needs to be performed regarding the crush behaviour of the components studied in this research to predict the type of failure mode the elements exhibit. Furthermore, when the crash behaviour of other structural elements is determined analytically, such as the frames of the fuselage, one can assemble a simplified semi-analytical model of the fuselage section, consisting out of a combination of beam segments, and axial and rotational springs, as briefly described in the Introduction. By doing so, one can estimate the crashworthiness response of the structure in an analytical manner. Using the newly obtained semi-analytical methods, the fuselage can be designed concurrently for its nominal operation, as for crashworthiness. This way, all loading cases are taken into account from the aircraft's first design stages, leading to a more optimal final configuration.

References

[1] B. Alemour, O. Badran, and M. Hassan. A review of using conductive composite materials in solving lightening strike and ice accumulation problems in aviation. *Journal of Aerospace Technology and Management*, 11, 2019.

[2] C. McGregor, R. Vaziri, and X. Xiao. Finite element modelling of the progressive crushing of braided composite tubes under axial impact. *International Journal of Impact Engineering*, 37(6):662–672, 2010.

[3] Military Specifications and Standard. *Military Handbook - MIL-HDBK-17-1F: Composite Materials Handbook, Volume 1 - Polymer Matrix Composites Guidelines for Characterization of Structural Materials*, volume 1. U.S. Department of Defense, 2002.

[4] W. Lennart. A simplified model for structural stiffness and crashworthiness optimisation of composite fuselages. *Structural and Multidisciplinary Optimization*, 59:1991–2004, 2019.

[5] Transport Aircraft Crashworthiness and Ditching Working Group. Transport aircraft crashworthiness and ditching working group report to FAA, 2018.

[6] J. Cronkhite and V. Berry. Crashworthy airframe design concepts - fabbricating and testing. *NASA Contractor Report 3603*, 1982.

[7] M. Waimer. *Development of a Kinematics Model for the Assessment of Global Crash Scenarios of a Composite Transport Aircraft Fuselage*. PhD thesis, Faculty of Aerospace Engineering and Geodesy, University of Stuttgart, 2013.

[8] M. Guida, F. Marulo, and S. Abrate. Advances in crash dynamics for aircraft safety. *Progress in Aerospace Sciences*, 98:106 – 123, 2018.

[9] C. Bisagni. Experimental investigation of the collapse modes and energy absorption characteristics of composite tubes. *International Journal of Crashworthiness*, 14(4):365–378, 2009.

[10] D. Lukaszewicz. Automotive composite structures for crashworthiness. *Advanced Composite Materials for Automotive Applications: Structural Integrity and Crashworthiness*, pages 99–127, 2013.

[11] S. Heimbs, F. Strobl, P. Middendorf, and J. Guimard. Composite crash absorber for aircraft fuselage applications. *Structures Under Shock and Impact*, 11:3 – 14, 2010.

[12] C. Wolff, P. Bastid, and A. Bunsell. Relation of energy absorption of composite structures to material strength. *Composites Engineering*, 4(2):195 – 218, 1994.

[13] R. Hussein, D. Ruan, and G. Lu. An analytical model of square CFRP tubes subjected to axial compression. *Composites Science and Technology*, 168:170 – 178, 2018.

[14] A. Cherniaev, C. Butcher, and J. Montesano. Predicting the axial crush response of CFRP tubes using three damage-based constitutive models. *Thin-Walled Structures*, 129:349 – 364, 2018.

[15] H. Jiang, Y. Ren, B. Gao, and J. Xiang. Numerical investigation on links between the stacking sequence and energy absorption characteristics of fabric and unidirectional composite sinusoidal plate. *Composite Structures*, 171:382 – 402, 2017.

[16] D. Delsart, G. Portemont, and M. Waimer. Crash testing of a CFRP commercial aircraft sub-cargo fuselage section. *Procedia Structural Integrity*, 2:2198–2205, 2016. 21st European Conference on Fracture, ECF21, 20-24 June 2016, Catania, Italy.

[17] V. Sokolinsky, K. Indermuehle, and J. Hurtado. Numerical simulation of the crushing process of a corrugated composite plate. *Composites Part A: Applied Science and Manufacturing*, 42(9):1119–1126, 2011.

[18] E. Lian, R. Lovingfoss, and V. Tanoto. Medium toughness PAEK thermoplastics Toray (formerly TenCate) Cetex TC1225 (LM PAEK) T700GC 12K T1E unidirectional tape 145 gsm 34% RC qualification material property data report. *Wichita State University, National Center for Advanced Materials Performance*, 2020.

[19] A. Epstein. Aeropropulsion for commercial aviation in the twenty-first century and research directions needed. *AIAA Journal*, 52(5):901–911, 2014.

[20] Special Conditions: Boeing Model 787-8 Airplane; Crashworthiness, 72 FR 54531, (2007).

[21] Special Conditions: Airbus A350-900 Airplane; Crashworthiness, Emergency Landing Conditions, 79 FR 43237, (2014).

[22] Y. Ren, J. Xiang, J. Zheng, and Z. Luo. Crashworthiness analysis of aircraft fuselage with sine-wave beam structure. *Chinese Journal of Aeronautics*, 29(2):403 – 410, 2016.

[23] C. Bisagni, G. Di Pietro, L. Fraschini, and D. Terletti. Progressive crushing of fiber-reinforced composite structural components of a Formula One racing car. *Composite Structures*, 68(4):491–503, 2005.

[24] Airworthiness Standards: Transport Category Airplanes, 14 CFR § 25 (2011).

[25] Emergency Landing Conditions: General, 14 CFR § 25.561, (2002).

[26] Emergency Landing Conditions: Emergency landing dynamic conditions, 14 CFR § 25.562, (2002).

[27] I. Kumakura. Vertical drop test of a transport fuselage section. *SAE Technical Paper Series*, 2002.

[28] A. Abramowitz, T. Smith, T. Vu, and J. Zvanya. Vertical drop test of a narrow-body transport fuselage section with overhead stowage bins. *World Aviation Congress Exposition*, 2002.

[29] H. Mou, Y. Du, and T. Zou. Effects of different roll angles on civil aircraft fuselage crashworthiness. *Advances in Aircraft and Spacecraft Science*, 2(4):391–401, 2015.

[30] M. Waimer, T. Feser, P. Schatrow, and D. Schueler. Crash concepts for CFRP transport aircraft – comparison of the traditional bend frame concept versus the developments in a tension absorbers concept. *International Journal of Crashworthiness*, 23(2):193–218, 2018.

[31] M. Kamal. Analysis and simulation of vehicle to barrier impact. In *SAE Technical Paper*. SAE International, 1970.

[32] D. Gransden and R. Alderliesten. Development of a finite element model for comparing metal and composite fuselage section drop testing. *International Journal of Crashworthiness*, 22(4):401–414, 2017.

[33] Y. Song, B. Horton, S. Perino, A. Thurber, and J. Bayandor. A contribution to full-scale high fidelity aircraft progressive dynamic damage modelling for certification by analysis. *International Journal of Crashworthiness*, 24:1–14, 2018.

[34] D. Hull. A unified approach to progressive crushing of fibre-reinforced composite tubes. *Composites Science and Technology*, 40(4):377 – 421, 1991.

[35] H. Hamada, S. Ramakrishna, and H. Satoh. Crushing mechanism of carbon fibre/PEEK composite tubes. *Composites*, 26(11):749 – 755, 1995.

[36] J. Chambe, C. Bouvet, O. Dorival, and J. Ferrero. Energy absorption capacity of composite thin-wall circular tubes under axial crushing with different trigger initiations. *Journal of Composite Materials*, 54(10):1281–1304, 2020.

[37] S. Hanagud, J. Craig, P. Sriram, and W. Zhou. Energy absorption behavior of graphite epoxy composite sine webs. *Journal of Composite Materials*, 23(5):448–459, 1989.

[38] J. Huang and X. Wang. On a new crush trigger for energy absorption of composite tubes. *International Journal of Crashworthiness*, 15:625–634, 2010.

[39] Y. Tong and Y. Xu. Improvement of crash energy absorption of 2D braided composite tubes through an innovative chamfer external triggers. *International Journal of Impact Engineering*, 111:11 – 20, 2018.

[40] A. Esnaola, I. Tena, I. Saenz-Dominguez, J. Aurrekoetxea, I. Gallego, and I. Ulacia. Effect of the manufacturing process on the energy absorption capability of GFRP crush structures. *Composite Structures*, 187:316 – 324, 2018.

[41] G. Farley. The effects of crushing speed on the energy-absorption capability of composite material. *NASA Technical Memorandum 89122*, 1987.

[42] M. Ploeckl, P. Kuhn, J. Grosser, M. Wolfahrt, and H. Koerber. A dynamic test methodology for analyzing the strain-rate effect on the longitudinal compressive behavior of fiber-reinforced composites. *Composite Structures*, 180, 2017.

[43] W. Zhou, J. Craig, and S. Hanagud. Crashworthy behavior of graphite/epoxy composite sine wave webs. *32nd Structures, Structural Dynamics, and Materials Conference*, 1991.

[44] A. Mamalis, D. Manolakos, G. Demosthenous, and M. Ioannidis. Analysis of failure mechanisms observed in axial collapse of thin-wailed circular fibreglass composite tubes. *Thin- Walled Structures*, 24:335 – 352, 1996.

[45] A. Mamalis, D. Manolakos, G. Demosthenous, and M. Ioannidis. The static and dynamic axial crumbling of thin-walled fibreglass composite square tubes. *Composites Part B: Engineering*, 28(4):439 – 451, 1997.

[46] S. Boria, S. Pettinari, and F. Giannoni. Theoretical analysis on the collapse mechanisms of thin-walled composite tubes. *Composite Structures*, 103:43 – 49, 2013.

[47] N. Gupta and R. Velmurugan. Analysis of polyester and epoxy composite shells subjected to axial crushing. *International Journal of Crashworthiness*, 5(3):333–344, 2000.

[48] G. Zhu, G. Sun, G. Li, A. Cheng, and Q. Li. Modeling for CFRP structures subjected to quasi-static crushing. *Composite Structures*, 184:41 – 55, 2018.

[49] X. Zhao, G. Zhu, C. Zhou, and Q. Yu. Crashworthiness analysis and design of composite tapered tubes under multiple load cases. *Composite Structures*, 222:110920, 2019.

[50] Z. Hashin. Failure criteria for unidirectional fiber composites. *Journal of Applied Mechanics*, 47:329–334, 1980.

[51] LS-DYNA. *Keyword User's Manual*, volume 1. Livermore Software Technology Corporation (LSTC), 2013.

[52] P. Feraboli, B. Wade, F. Deleo, M. Rassaian, M. Higgins, and A.Byar. LS-DYNA MAT54 modeling of the axial crushing of a composite tape sinusoidal specimen. *Composites Part A: Applied Science and Manufacturing*, 42(11):1809 – 1825, 2011.

[53] ASTM International. D3039/D3039M-08, Standard test method for tensile properties of polymer matrix composite materials. *ASTM International*, 2008.

[54] ASTM International. D3410/D3410M-16, Standard test method for compressive properties of polymer matrix composite materials with unsupported gauge section by shear loading. *ASTM International*, 2016.

[55] S. Charoenphan, L. Bank, and M. Plesha. Progressive tearing failure in pultruded composite material tubes. *Composite Structures*, 63(1):45 – 52, 2004.

[56] F. Chang and K. Chang. A progressive damage model for laminated composites containing stress concentrations. *Journal of Composite Materials*, 21(9):834–855, 1987.

[57] P. Maimí, P. Camanho, J. Mayugo, and C. Dávila. A continuum damage model for composite laminates: Part I – Constitutive model. *Mechanics of Materials*, 39(10):897–908, 2007.

[58] A. Kaddour, M. Hinton, P. Smith, and S. Li. Mechanical properties and details of composite laminates for the test cases used in the third world-wide failure exercise. *Journal of Composite Materials*, 47(20-21):2427–2442, 2013.

[59] M. Courteau. *Investigating the crashworthiness characteristics of carbon fiber/epoxy tubes*. PhD thesis, Department of Mechanical Engineering, University of Utah, 2011.

[60] R. Boeman and A. Caliskan. A novel capability for crush testing crash energy management structures at intermediate rates. *SAE Technical Paper*, pages 1–1954, 2002.

[61] S. Boria, J. Obradovic, and G. Belingardi. Experimental and numerical investigations of the impact behaviour of composite frontal crash structures. *Composites Part B: Engineering*, 79:20 – 27, 2015.

[62] SIMULIA. *Abaqus/CAE User's Manual*, volume 6.11. Dassault Systèmes' Centers of Simulation Excellence, 2016.

[63] S. Pinho, P. Camanho, and M. de Moura. Numerical simulation of the crushing process of composite materials. *International Journal of Crashworthiness*, 9(3):263–276, 2004.

[64] E. Fasanella. *Best practices for crash modeling and simulation*. National Aeronautics and Space Administration, Langley Research Center, 2002.

[65] M. Waimer, M. Siemann, and T. Feser. Simulation of CFRP components subjected to dynamic crash loads. *International Journal of Impact Engineering*, 101:115 – 131, 2017.

[66] B. Zhan, L. Sun, and B. Huang. Progressive failure prediction of FRP tubes by modified damage model. *International Journal of Crashworthiness*, 23(6):593–604, 2018.

[67] S. Veldman, P. Kortbeek, P. Wölcken, R. Herrmann, J. Kos, and I. Villegas. Development of a multifunctional fuselage demonstrator. *Aerospace Europe conference*, 2020.

[68] Rockwell International and North American Aircraft Operations. *DOD/NASA Advanced Composites Design Guide*, volume 2. Air Force Wright Aeronautical Laboratories, Flight Dynamics Laboratory, Structures/Dynamics Division, 1983.

[69] Military Specifications and Standard. *Department of Defense Handbook: Composite Materials Handbook - Polymer Matrix Composite Material Usage, Design and Analysis*, volume 3. Department of Defense, 2002.

Appendix A

Simulated Material Properties

In this appendix, the supporting data for the conclusions drawn in Chapter 3 is reported. Accordingly, the results obtained from the tensile and compression simulations for the $[0]_8$, $[90]_8$, and $[0/\pm 45/90]_s$ specimens are reported. For more details regarding the specimens' dimensions, the reader is referred to Table 3.1.

The results mostly entail tables with the failure stresses and the corresponding strain. Moreover, the moduli of the simulated specimens are computed and compared to the expected values. All the results are reported form table A.1 to A.6. As with the presented plots in Chapter 3, there is a distinction made between the data extracted from the load cell and the values probed from the nodes. The values are denoted with Cell and Gauge, indicating the load cell and the strain gauge, respectively. In the tables, baseline values are reported when these are available. For the all 0 and 90 layups, the baseline values are taken from the lamina material. Only the elastic modulus is reported for the quasi-isotropic laminate, as the final failure stress and corresponding strain depend on the selected failure criterion. The elastic modulus is computed using classical laminate theory. Finally, for the quasi-isotropic layups, it is chosen only to show the values obtained from the load-cell, as each layer has its own failure stress, depending on its orientation.

Table A.1: $[0]_8$ specimen tensile simulation results.

Variable	Baseline Value	Units	Abaqus - Hashin		LS-Dyna - MAT054		LS-Dyna - MAT058		LS-Dyna - MAT262	
			Cell	Gauge	Cell	Gauge	Cell	Gauge	Cell	Gauge
Failure Stress	2560	MPa	2444	2482	2526	2540	2542	2556	2532	2545
Failure Strain	0.01551	mm/mm	0.01504	0.01504	0.01543	0.01531	0.01687	0.01675	0.01554	0.01542
Modulus	160000	MPa	164021	165000	164933	165002	164933	164999	164933	165000

Table A.2: $[90]_8$ specimen tensile simulation results.

Variable	Baseline Value	Units	Abaqus - Hashin		LS-Dyna - MAT054		LS-Dyna - MAT058		LS-Dyna - MAT262	
			Cell	Gauge	Cell	Gauge	Cell	Gauge	Cell	Gauge
Failure Stress	73	MPa	69	70	72	72	73	73	72	72
Failure Strain	0.0081	mm/mm	0.00779	0.00776	0.00804	0.00801	0.00876	0.00872	0.00804	0.00801
Modulus	9000	MPa	8923	9000	8987	9000	8987	9000	8987	9000

Table A.3: $[0/\pm45/90]_s$ specimen tensile simulation results.

Variable	Baseline Value	Units	Abaqus - Hashin	LS-Dyna - MAT054	LS-Dyna - MAT058	LS-Dyna - MAT262
			Cell	Cell	Cell	Cell
Failure Stress	n.a.	MPa	778	865	894	766
Failure Strain	n.a.	mm/mm	0.01429	0.01468	0.01613	0.01462
Modulus	62700	MPa	62439	62922	62786	62894

Table A.4: $[0]_8$ specimen compression simulation results.

Variable	Basline Value	Units	Abaqus - Hashin		LS-Dyna - MAT054		LS-Dyna - MAT058		LS-Dyna - MAT262	
			Cell	Gauge	Cell	Gauge	Cell	Gauge	Cell	Gauge
Failure Stress	1590	MPa	1114	1127	1578	1573	1583	1586	1449	1446
Failure Strain	0.011	mm/mm	0.00677	0.00683	0.00952	0.00949	0.01048	0.01082	0.00872	0.00874
Modulus	160000	MPa	165188	165006	165061	165234	165053	165213	165061	165213

Table A.5: $[90]_8$ specimen compression simulation results.

Variable	Basline Value	Units	Abaqus - Hashin		LS-Dyna - MAT054		LS-Dyna - MAT058		LS-Dyna - MAT262	
			Cell	Gauge	Cell	Gauge	Cell	Gauge	Cell	Gauge
Failure Stress	185	MPa	187	183	185	185	170	171	183	183
Failure Strain	0.032	mm/mm	0.02016	0.02036	0.02048	0.02042	0.02360	0.02490	0.02016	0.02034
Modulus	9000	MPa	9153	9000	9007	8994	9007	8994	9008	8995

Table A.6: $[0/\pm45/90]_s$ specimen compression simulation results.

Variable	Basline Value	Units	Abaqus - Hashin	LS-Dyna - MAT054	LS-Dyna - MAT058	LS-Dyna - MAT262
			Cell	Cell	Cell	Cell
Failure Stress	n.a.	MPa	509	559	583	579
Failure Strain	n.a.	mm/mm	0.0078	0.0085	0.0096	0.0106
Modulus	62700	MPa	64709	64367	64248	64335

Appendix B

Finite Element Modelling of Crushing of Composite Tubes Results

In this appendix, the numerical results obtained from the performed finite element simulations for the square tube absorber can be found. Therefore, the sections contain numerical results obtained from the simulations run in Abaqus and comparisons between numerical and filtered results obtained from LS-Dyna. Next, to load-displacement curves, tables are reported with overviews of the extracted energy from the simulations.

B.1 Abaqus Crush Simulation Results

In this section, the results obtained from the different simulations performed in Abaqus are presented. These simulations are performed to obtain better correlation with the test results, as the obtained results from the baseline Abaqus simulation are unsatisfactory. Note that to reduce the simulation time during the investigation of the different options, only a third of the total simulation time is taken, leading to 5 ms.

Layer Integration Points

The first aspect that is investigated is the number of integration points each ply layer has. The standard value in Abaqus is three; therefore, this formed the baseline for this study. In the Abaqus manual, it is stated that for non-linear simulations, going up to material failure, three integration points per lamina layer are sufficient. However, when using Simpson's rule, it states that when a higher degree of deformation is expected, as is the case in the tube crushing simulation, no more than nine integration points are required [62]. By increasing the number of integration points, the accuracy of the simulation does seem to improve; however, not sufficient to obtain results that are more similar to the test results. As shown in Figure B.1, no clear trend can be seen in the improvement. The obtained mean crushing load increases when increasing the number of integration points. However, this is most likely attributed to the more fluctuating nature of the results; therefore, this is not seen as an actual improvement.

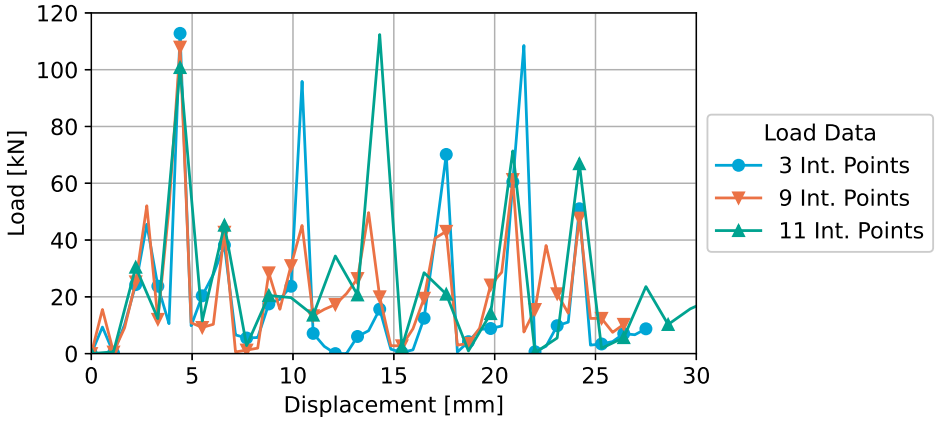

Figure B.1: Abaqus crushing results with varying integration points per lamina layer.

Mass Scaling

The second study revolves around mass scaling. In this study, mass scaling is added to the model to stabilise the extracted numerical load. In Figure B.2, one can see the results of the simulation with mass-scaling implemented, compared to the baseline simulation. In the figure, one can see that the results do improve, as the valley values are lower, while the peaks are also reduced, indicating that a more stable crushing regime is obtained. Consequently, the mean crushing load is also increased to 25.6 kN, which is still significantly smaller (-33.7%) than the mean crushing load obtained from the test of 38.6 kN. As mass scaling does not provide accurate results, and it is deemed that the increase in accuracy is not originated from a more accurate representation of the actual phenomenon, mass scaling has not been implemented in the final Abaqus model.

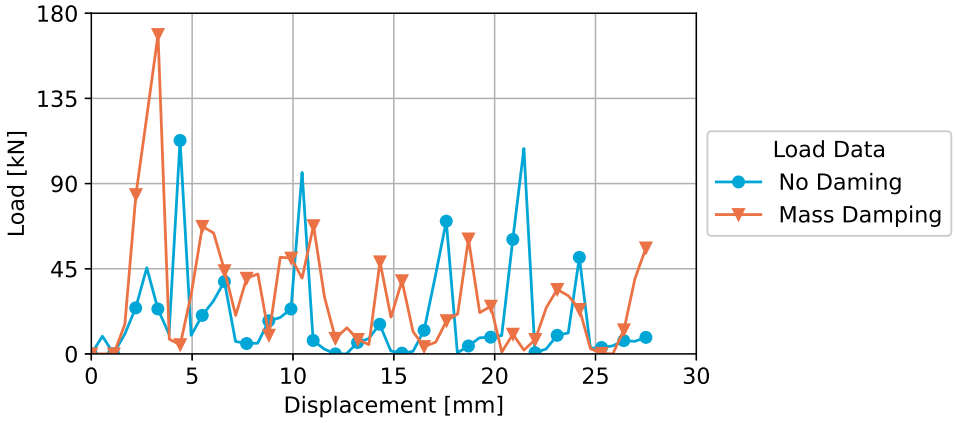

Figure B.2: Abaqus crushing results with mass scaling.

Loading Speed

The final option that is investigated is the reduction in loading speed. This method was implemented in order to see whether different boundary conditions would lead to more stable results. By reducing the loading speed, one is not representing the actual test. Therefore, this investigation is more qualitative, as one can not compare the results to the test data due to the different loading condition. In Figure B.3, one can see the results of the simulation with the reduced loading rate of 0.2 m/s, compared to the baseline loading rate of 5.5 m/s. From the figure, one can conclude that there is little to no improvement when the loading rate is decreased. The peaks in the load curve are reduced slightly, as are the valleys; however, the numerical results are still characterised by large fluctuations, while the loading rate has been decreased by more than one order of magnitude.

B.2 Numerical and Filtered Load Comparison

In this section, one can find a comparison between the numerical results obtained from the tube crushing simulations performed in LS-Dyna with the different material cards and a com-

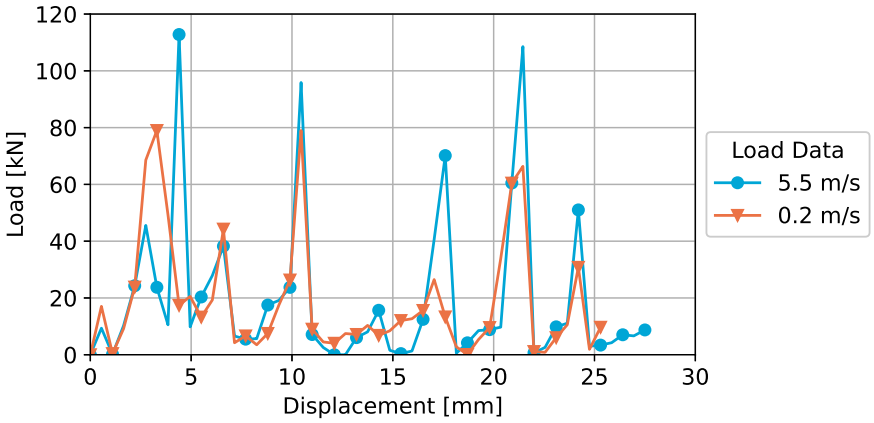

Figure B.3: Abaqus crushing results with varying loading speed.

parison with the filtered results. In this section, the load's fluctuating nature can be observed and how this may influence the absorber's behaviour in the global structure. In all the figures, the built-in SAE filter is applied to the numerical load, with a cut off frequency of 1000 Hz. With this cut off frequency, the filtered load can still represent the first peek of the load when present. When applying lower cut-off frequencies, one risks flattening the specimen's true load response; hence this frequency is deemed ideal for this loading case. In Figure B.4 one can find the load comparison for the simulation with the MAT054 material card, while in Figure B.5 one can find the comparison for the simulation with the MAT058 material card, finally, in Figure B.6 the comparison for the MAT262 material card is represented.

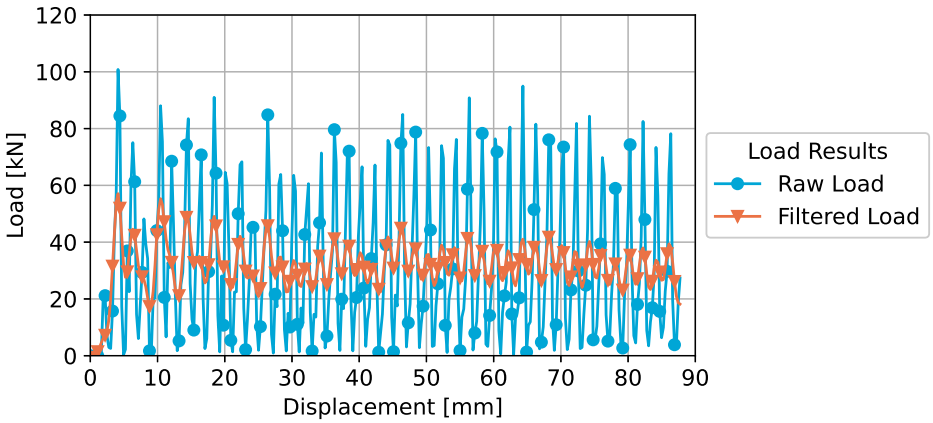

Figure B.4: Comparison between the numerical and filtered load for the square tube crushing simulation with the MAT054 material card.

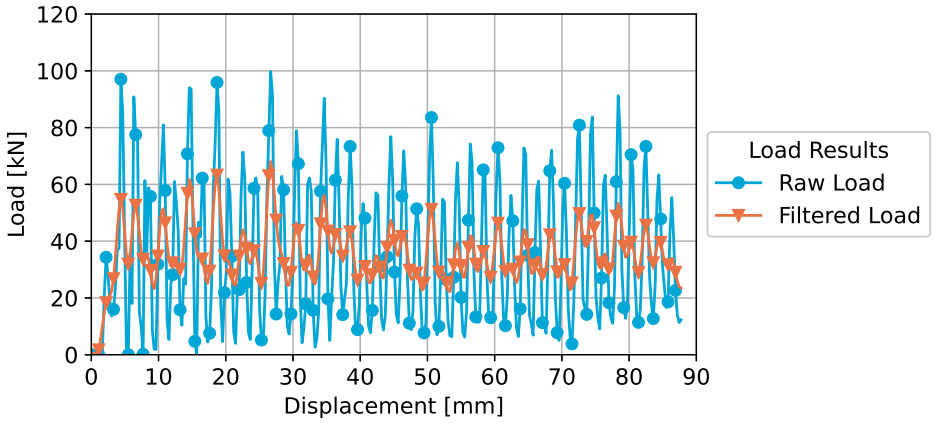

Figure B.5: Comparison between the numerical and filtered load for the square tube crushing simulation with the MAT058 material card.

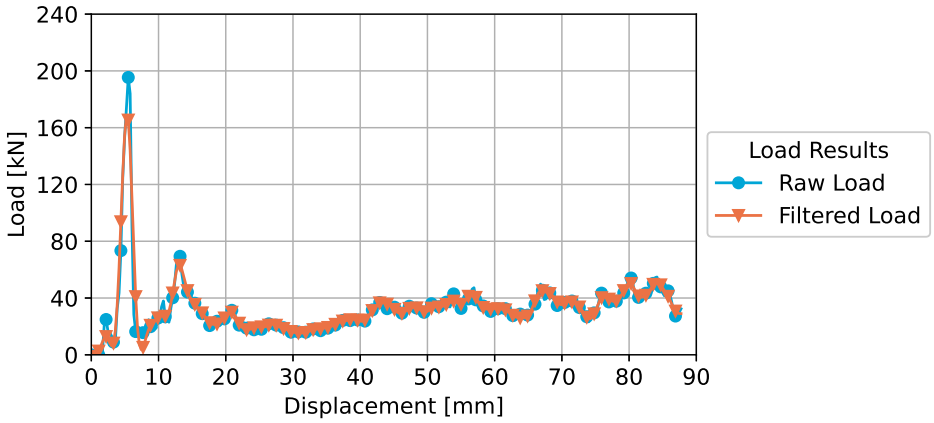

Figure B.6: Comparison between the numerical and filtered load for the square tube crushing simulation with the MAT262 material card.

B.3 Energy Overview of Finite Element Simulations

A common methodology to study the validity of a finite element model is the balance of energy. When doing so, two aspects are studied, the energy ratio and the hourglass energy. The energy ratio is the ratio between the total energy and the sum of the total initial energy and external work. The ideal value for the energy ratio is one [51]. On the other hand, the hourglass energy gives insight regarding the quality of the mesh of the model. Hourglass modes are not desired. Therefore, finite element software implement non-physical loads in order to reduce the occurrence of these modes. The implementation of these loads results in hourglass energy. As one might imagine, this energy needs to be as low as possible for the mesh to be of good quality. Therefore a common rule of thumb is to ensure that the hourglass energy value is less than 5% of the total energy. Table B.1 shows the different energy contributions obtained from the simulations of the crushing of the tubes with the

material cards. From this, one can see that the hourglass energy is indeed below the required 5%.

Table B.1: Final energies of the material card tube simulations (in units of Joule).

Specimen	Total	Internal	Hourglass	Damage	Friction	Kinetic
MAT054	2767.8	2439.9	29.6	2332.2	278.8	19.5
MAT058	3071.2	2575.5	-119.2	2043.8	432.1	182.7
MAT262	2871.3	1849.0	46.4	763.8	931.2	44.7

By studying the table's energy values, one can also see that the energy ratio is indeed one. Note that the total energy can be computed using Equation B.1. In the equation, all the subscripts describe a different energy source, an overview of which can be found in Table B.2

$$\underbrace{E_{kin} + E_{in} + E_{sl} + E_{rw} + E_{damp} + E_{hg}}_{E_{\text{total}}} = E^0_{\text{kin}} + E^0_{\text{int}} + W_{\text{ext}} \tag{B.1}$$

Table B.2: Energy sources in LS-Dyna simulations, required for energy balance.

Symbol	Variable Meaning	Symbol	Variable Meaning
E_{kin}	Kinetic Energy	E_{hg}	Hourglass Energy
E_{in}	Internal Energy	E^0_{kin}	Initial Kinetic Energy
E_{sl}	Sliding or Friction Energy	E^0_{in}	Initial Internal Energy
E_{rw}	Rigid Wall Energy	E_{ext}	External Work
E_{damp}	Damping Energy		

To verify the energy contributions of the imperfect simulations, in Table B.3, one can find the energy sources obtained from the simulations.

Table B.3: Final energies of the imperfect tube simulations (in units of Joule).

Specimen	Total	Internal	Hourglass	Damage	Friction	Kinetic
Imperfect 1	2919.2	2422.6	-175.3	1755.0	466.6	205.3
Imperfect 2	3128.6	2623.6	-92.2	2129.7	427.1	170.0
Imperfect 3	2910.8	2413.5	-120.7	1646.3	470.3	147.7
Imperfect 4	2887.0	2372.8	-126.3	1565.9	480.9	159.6

Appendix C

Analytical Model Verification Results

In this appendix, one can find the data supporting the verification of the analytical model for the crushing of composite specimens. Hence one can find the load-displacement diagrams for the specimens simulated with varying side-lengthens and thickness, accompanied by the simulations' energies. Moreover, one can find the results of the simulations of the corrugated beam, for which the deformations are also reported.

C.1 Perimeter and Thickness Study Load Results

In Section 5.3.2, the mean crushing load values are reported for the specimens with varying side length and thickness. However, to gain insight into the specimens' actual crush behaviour, load-displacement curves are reported in this section. All the loads have been filtered using the LS-Dyna's built-in SAE filter with a cutoff frequency of 1000 Hz. The filtered load-displacement curves of the simulations can be found in figures C.2 and C.1. When looking at the figure, two simulations have strange behaviour: the specimen with a side length of 75 mm, and the tube with a thickness of 1.08 mm. The reason for this different behaviour originates from geometric instabilities in the simulated specimens. The long edge and small thickness cause the tube to fail under a more buckling like failure mode rather than the desired progressive crushing mode.

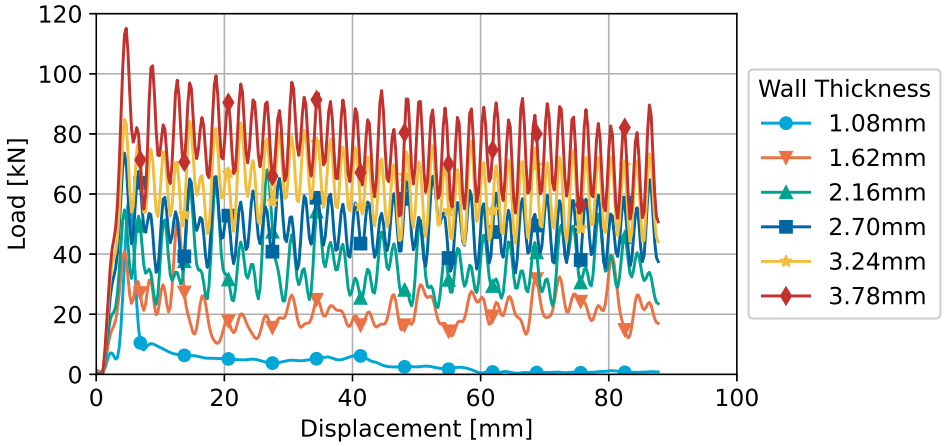

Figure C.1: Load results of the simulations for square tubes with varying thickness.

C.2 Perimeter and Thickness Study Energy Results

When performing finite element analysis, some tools can aid during the verification of the results. These tools are mainly based on the energies provided by the model. One aspect that is generally taken into consideration is the hourglass energy in the model. Hourglass modes are non-physical modes that can occur when square shell elements are used. In order to prevent this phenomenon, finite element software implements virtual forces to reduce these modes. However, as one might imagine, the amount of force has to be limited for the simulation to be realistic. Therefore a general rule of thumb is to control whether the hourglass energy

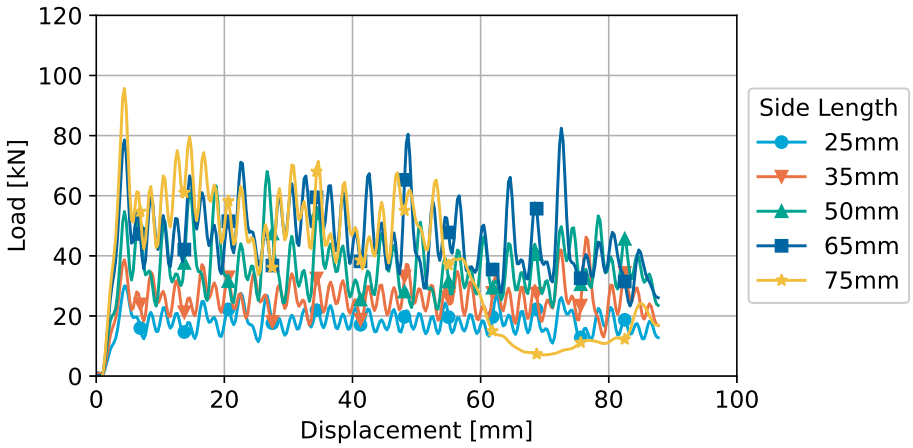

Figure C.2: Load results of the simulations for square tubes with varying side length.

is below 10% of the total energy [51]. Another method that can be easily implemented in LS-Dyna is the use of the energy ratio. The energy ratio is given by the total energy divided by the sum of the initial energy and the external energy [51]. The LS-Dyna Keyword User manual states that this ratio should not deviate from a value of one [51]. More information regarding LS-Dyna's energy balance techniques can be found in Section B.3 and the user manual itself [51].

As these value may be of importance to the reader, the final values for the different energies are depicted in table C.1 to C.2. It must be noted that the values reported in the tables are the final values obtained from the simulations. The values for the energies that have been reported in Section 5.3.2 are lower because these only report the energy of the stable crush regime, taking into account the energy that is required to form the stable crush frond, thus removing the first part of the simulation, resulting in the lower values.

Table C.1: Energy overview of the side length study for the crushing of the square composite tube (in units of Joule).

Specimen	Total	Internal	Hourglass	Damage	Friction	Kinetic
25 mm	1526.2	1292.8	-54.2	1233.3	169.2	118.4
35 mm	2191.1	1872.2	-79.4	1788.9	225.9	172.3
50 mm	3071.2	2575.5	-119.2	2043.8	432.1	182.7
65 mm	3920.2	3302.4	-141.4	2558.6	530.1	229.1
75 mm	3348.0	2753.0	-86.5	1979.9	517.7	163.8

C.3 Corrugated Beam Simulation Results

In Subsection 5.3.3, the results of the simulation of a corrugated beam crush specimens are reported. However, to remain concise to the verification of the analytical model, only the bare results of the simulation are reported. To provide the reader with more details regarding

Table C.2: Energy overview of the thickness study for the crushing of the square tube (in units of Joule).

Specimen	Total	Internal	Hourglass	Damage	Friction	Kinetic
1.08 mm	394.1	397.3	-152.6	214.5	85.2	64.2
1.62 mm	1829.4	1534.6	-172.7	937.3	353.1	114.4
2.16 mm	3071.2	2575.5	-119.2	2043.8	432.1	182.7
2.70 mm	4144.5	3574.8	85.3	3497.1	330.0	154.4
3.24 mm	5218.6	4604.1	86.9	4530.2	422.6	105.0
3.78 mm	6367.7	5625.0	87.6	5540.9	582.1	72.9

the simulation results, such as actual load diagrams, simulation energies, and deformations, these are reported in this section.

The filtered loads are depicted in Figure C.3. Note that here the filtered load is represented. For these simulations, a lower cutoff frequency is used to filter the numerical data, namely a filter of 600 Hz. This cutoff frequency is more accurate than the 1000 Hz filter due to the slightly larger mash size of the specimens, which leads to a longer crush stroke length.

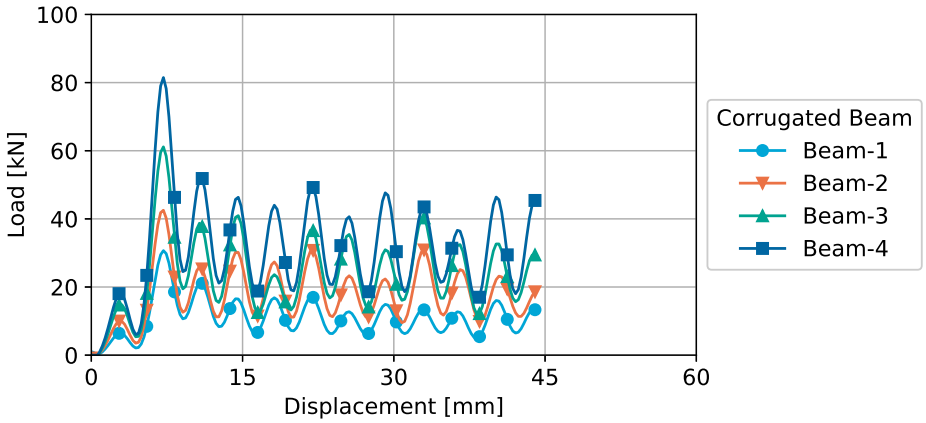

Figure C.3: Load results of the corrugated beam simulations.

As pointed out in the previous sections, the energy balance within a finite element simulation is also essential to verify the quality of the simulation. Therefore, in Table C.3, one can find the simulations' energy overview.

Finally, in figures C.4 to C.7, one can find the deformation of the different beams at various time instances of the crushing process.

Table C.3: Energy overview of the simulations of the corrugated beams (in units of Joule).

Specimen	Total	Internal	Hourglass	Damage	Friction	Kinetic
Beam 1	333.1	276.3	-7.0	236.2	41.3	22.4
Beam 2	530.1	444.6	-41.6	397.0	67.9	59.2
Beam 3	721.1	601.8	-174.9	533.5	98.2	196.0
Beam 4	938.9	785.1	-6.8	680.4	109.1	51.5

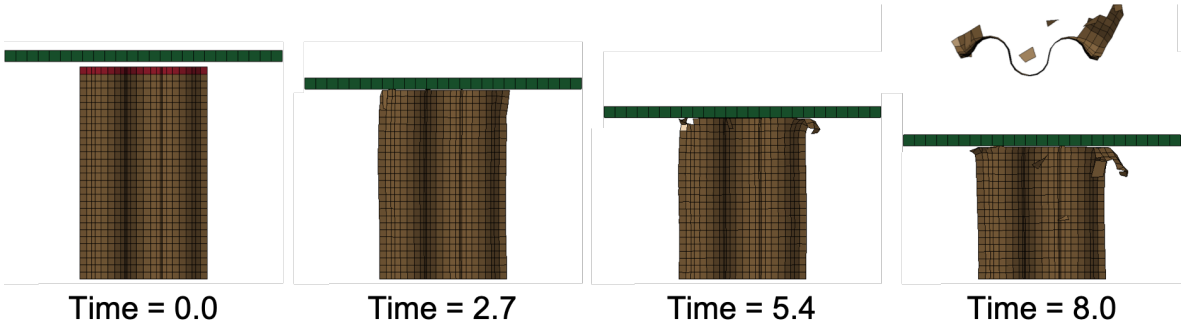

Figure C.4: Beam 1 deformation, with 3 repetitions.

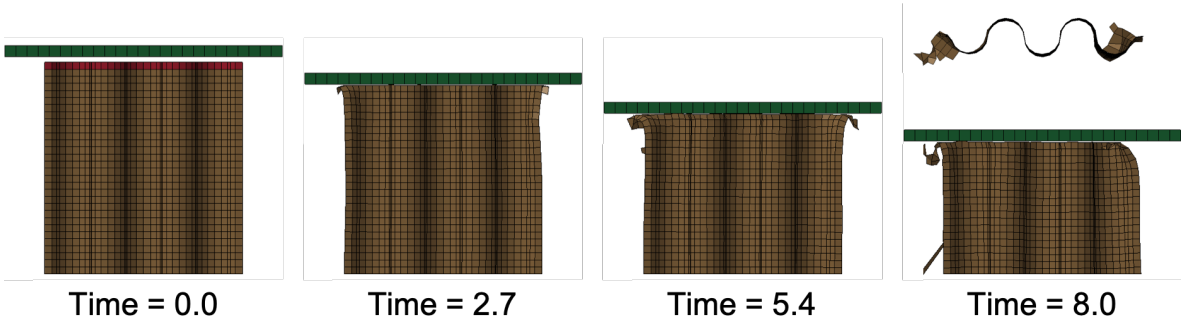

Figure C.5: Beam 2 deformation, with 5 repetitions.

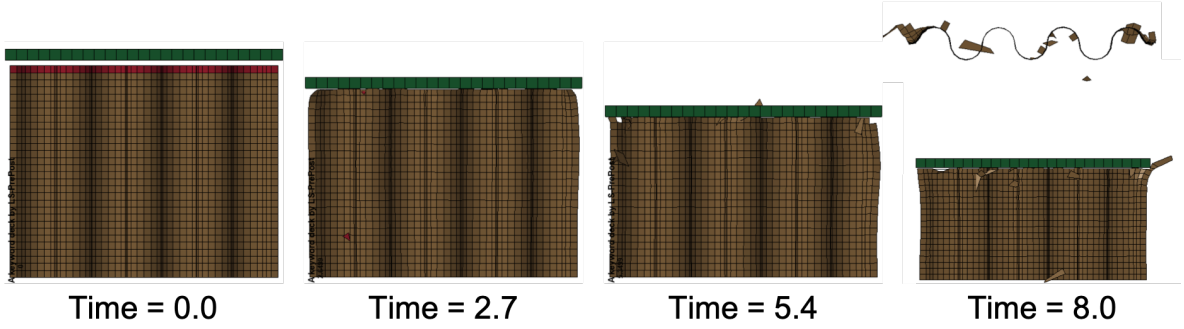

Figure C.6: Beam 3 deformation, with 7 repetitions.

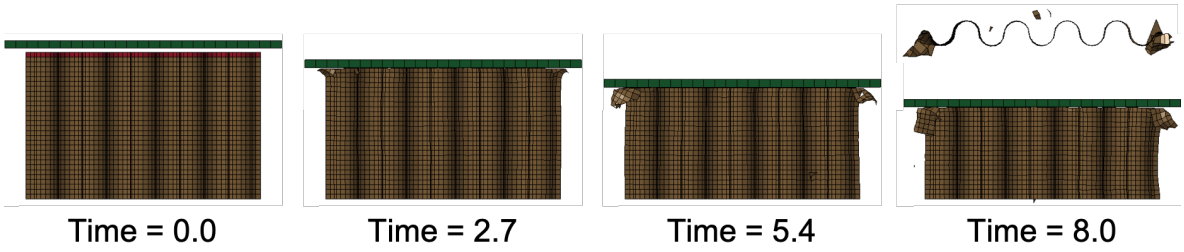

Figure C.7: Beam 4 deformation, with 9 repetitions.

Appendix D

Composite Energy Absorber Design Results

In this appendix, the results of the studied energy absorbers are presented. First, the load curves obtained from the simulations are reported. After this, tables with energy values obtained from the simulation are provided; finally, some deformations of the studied struts are provided.

D.1 Crash Absorber Load Curves

The load curves obtained from the analysis entail the loads obtained from the C-struts and square tube absorbers, along with the SOFT analysis performed for the square tube, all performed in Chapter 6. These load curves are reported as these can aid during the visualisation of the behaviour of the absorbers; as in the referenced chapter only average values are reported. All the presented results have been filtered using LS-Dyna's built-in SAE filter, with a filtering frequency of 1000 Hz, as is performed for the specimens presented in Chapter 4.

First, in Figure D.1, one can see the load curves obtained from the C-strut absorbers. As expected, due to the same cross-section length of the specimens, the load curves fluctuate roughly around the same load. As described in Subsection 6.3, the degree of fluctuation varies per absorber, as this is related to the instability of the absorber's flanges.

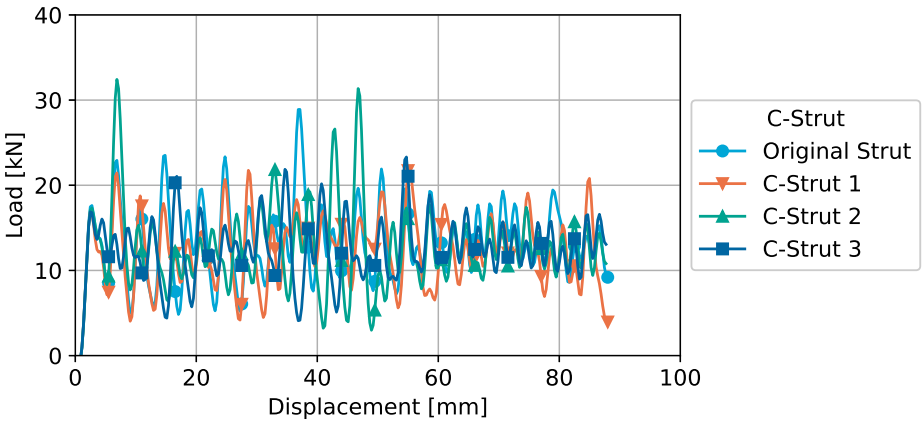

Figure D.1: Load curves for the C-strut absorbers.

In the loads obtained from the square tubes, one can see that by increasing the side length of the tube, the load increases.

The final load curves presented are obtained from the SOFT parameter study performed in Subsection 6.4.4. This study is performed to analyse the influence of the aforementioned parameter, as a constant over-estimation was obtained with the analytical model in Chapter 6, which may indicate an under-estimation of the SOFT parameter. The behaviour is as expected; with an increasing SOFT parameter, the crushing load increases.

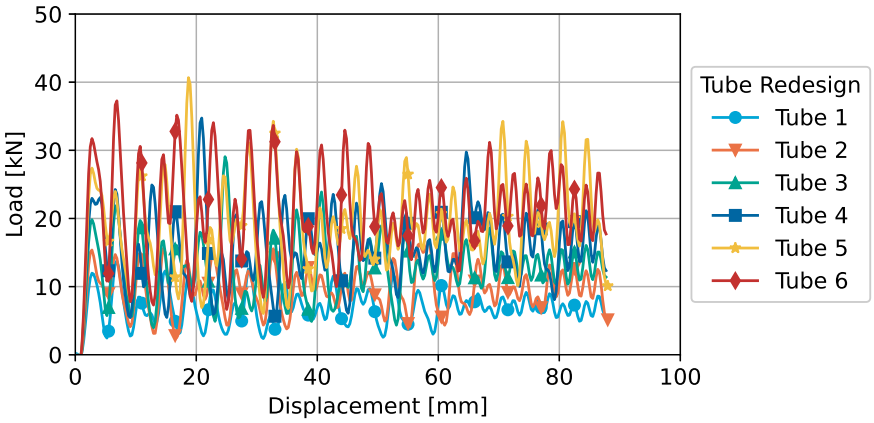

Figure D.2: Load curves of the square tube absorbers.

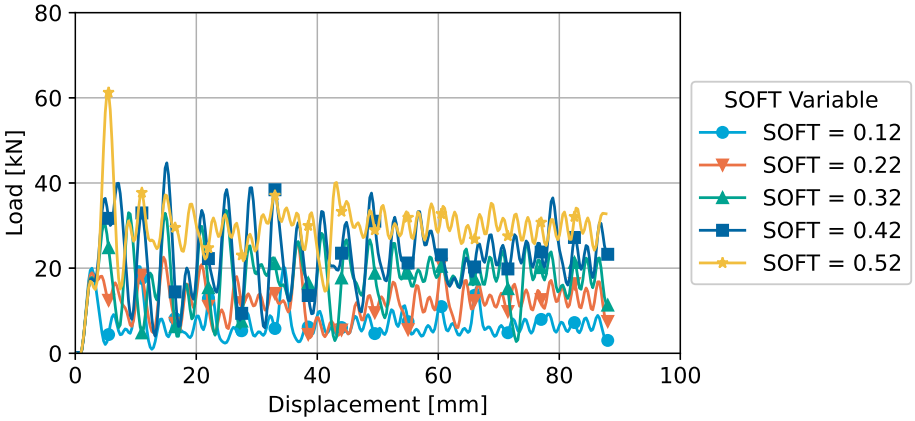

Figure D.3: SOFT analysis for the crushing of the square absorber.

D.2 Crash Absorber Energies

Next to the crushing load, one important aspect of an energy absorber is naturally the absorbed energy. While the final energy values of the studied components are reported in Chapter 6, in this section, a break down of the energy contributions are provided. The energy contributions can be found in Table D.1 and Table D.2. Table D.1 reports the energies obtained from the C-struts simulations, while Table D.2 reports those of the square and rectangle absorbers.

The energy tables are mainly of interest to study the hourglass energy to ensure that this value is lower than 10% of the total internal energy of the part [51]. By looking at the reported values, one can see that all the absorbers' hourglass energy is relatively low, indicating that the applied mesh and its deformation are acceptable.

Table D.1: Final energies of the C-strut simulations (in units of Joule).

Specimen	Total	Internal	Hourglass	Damage	Friction	Kinetic
Original	1157.5	916.4	40.7	867.1	125.2	75.2
Strut 1	1078.4	838.3	29.4	786.0	128.1	82.5
Strut 2	1107.0	898.8	25.4	868.8	109.5	73.3
Strut 3	1100.2	887.0	29.8	841.4	106.4	77.0

Table D.2: Final energies of the square tube simulations (in units of Joule).

Specimen	Total	Internal	Hourglass	Damage	Friction	Kinetic
Tube 1	592.7	503.1	14.0	493.5	50.8	24.8
Tube 2	834.1	718.3	18.0	696.9	61.7	36.1
Tube 3	1085.9	908.6	35.7	877.4	94.8	46.8
Tube 4	1348.5	1146.2	-1.9	1107.4	106.1	98.2
Tube 5	1648.6	1364.9	58.5	1312.9	144.0	81.2
Tube 6	1782.3	1510.3	54.9	1463.6	134.3	82.7
Rectangular Tube	1041.2	897	19.4	875.5	73.9	50.9

D.3 Crash Absorber Deformations

In this subsection, the deformations of the C-strut absorbers are presented. This section only reports the deformations of the C-strut absorbers, as this is of interest for the buckling of the flanges. The deformations of the tubes are not reported, as these show no particularly interesting deformation, as these are similar to the deformation as presented in Figure 4.10 for the previously simulated square tubes.

In figures D.4 to D.7 one can find the resultant deformation of the studied struts. The scales of all the reported figures are equal such that these can be compared easily. For each simulation, three different time instances are reported, 5.3, 10.5, and 16 ms. Due to the larger scale, which is required due to the higher deformation in the crush zone, the out of plane deflection of the flanges is less accentuated with respect to Figure 6.1, reported in Chapter 6. Nevertheless, some light coloured areas can be seen, indicating the buckling behaviour of the flanges.

In the deformation, one can also observe the fluctuating nature of the load caused by the element rows being degraded. For example, in Figure D.4b, there is almost no deformation in the strut, except for the damaged top side in the crush frond, indicating that there is almost no load within the strut.

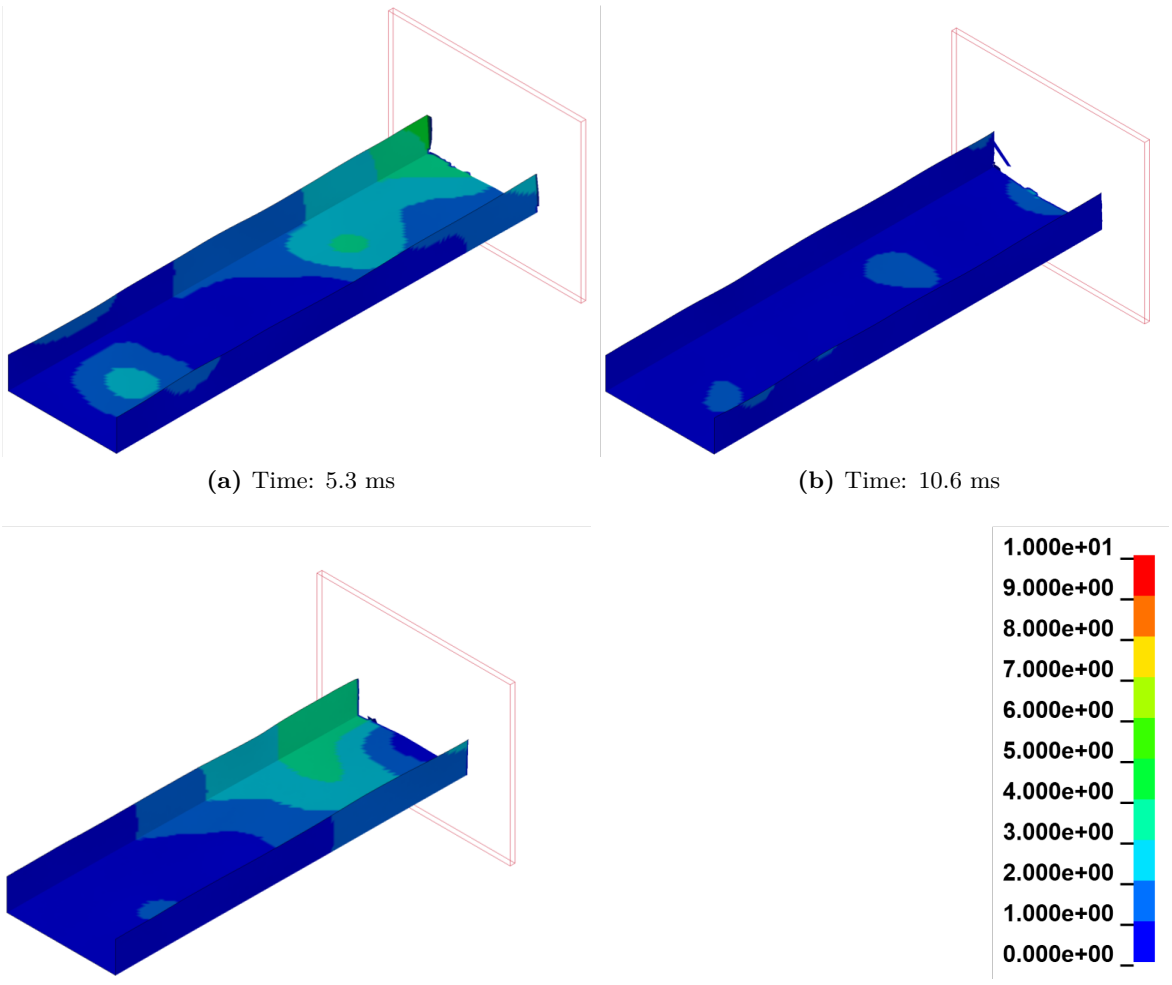

(a) Time: 5.3 ms

(b) Time: 10.6 ms

(c) Time: 16.0 ms

Figure D.4: Resultant displacement at different time instances of the crushing simulation of the original C-strut. Fringe levels depicted in the bottom right in units of mm.

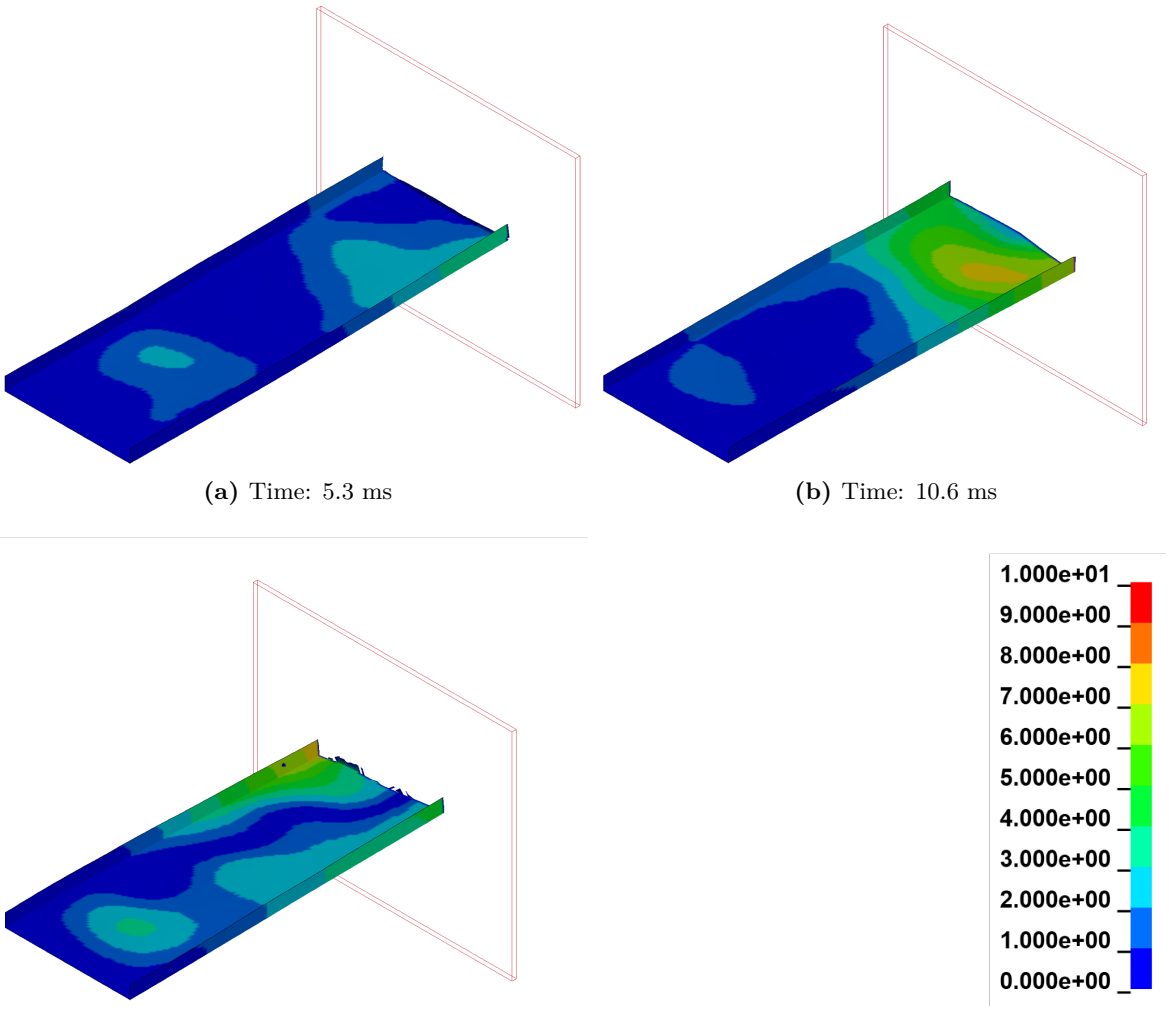

(a) Time: 5.3 ms

(b) Time: 10.6 ms

(c) Time: 16.0 ms

Figure D.5: Resultant displacement at different time instances of the crushing simulation of C-Strut 1. Fringe levels depicted in the bottom right in units of mm.

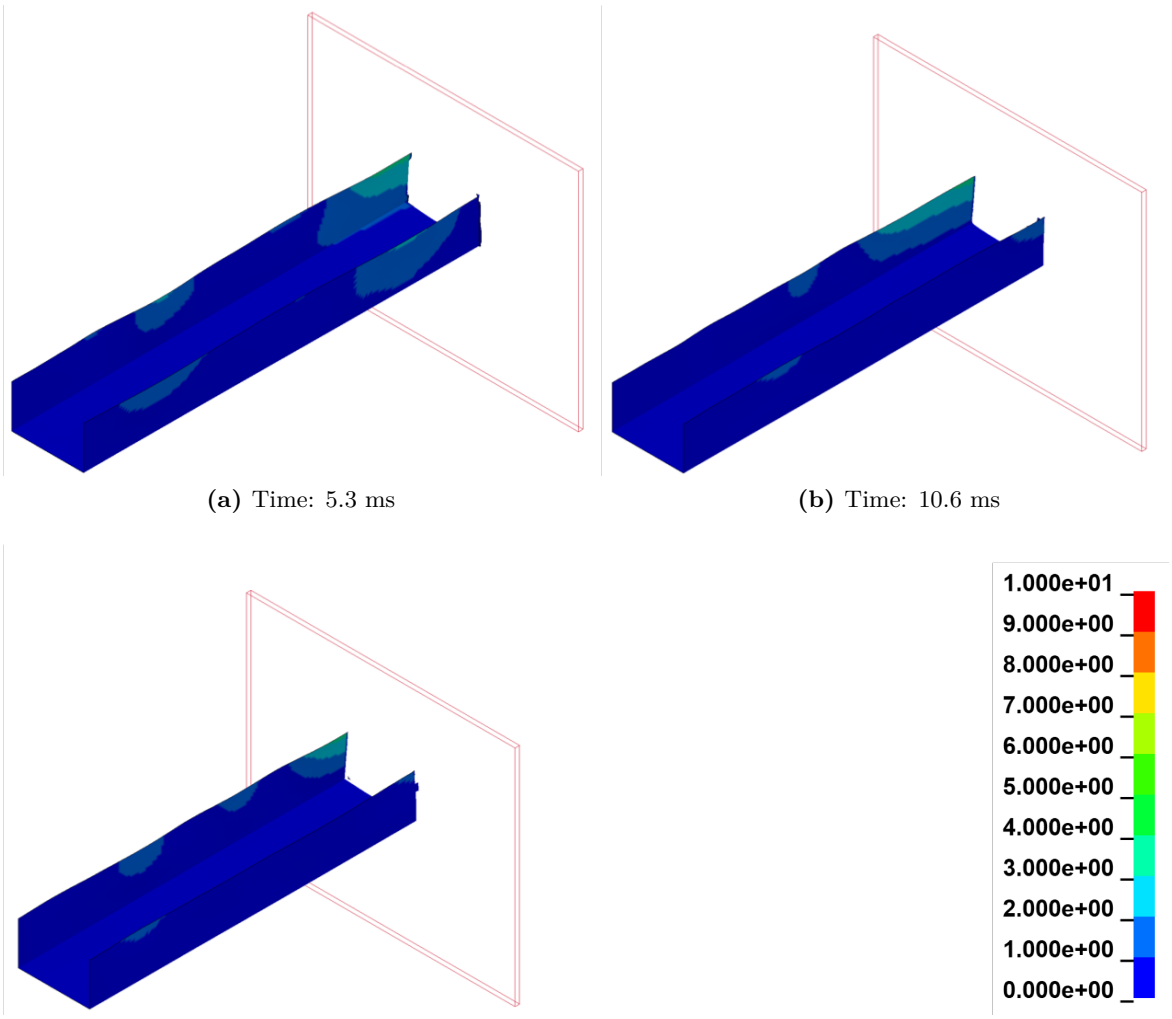

(a) Time: 5.3 ms

(b) Time: 10.6 ms

(c) Time: 16.0 ms

Figure D.6: Resultant displacement at different time instances of the crushing simulation of C-Strut 2. Fringe levels depicted in the bottom right in units of mm.

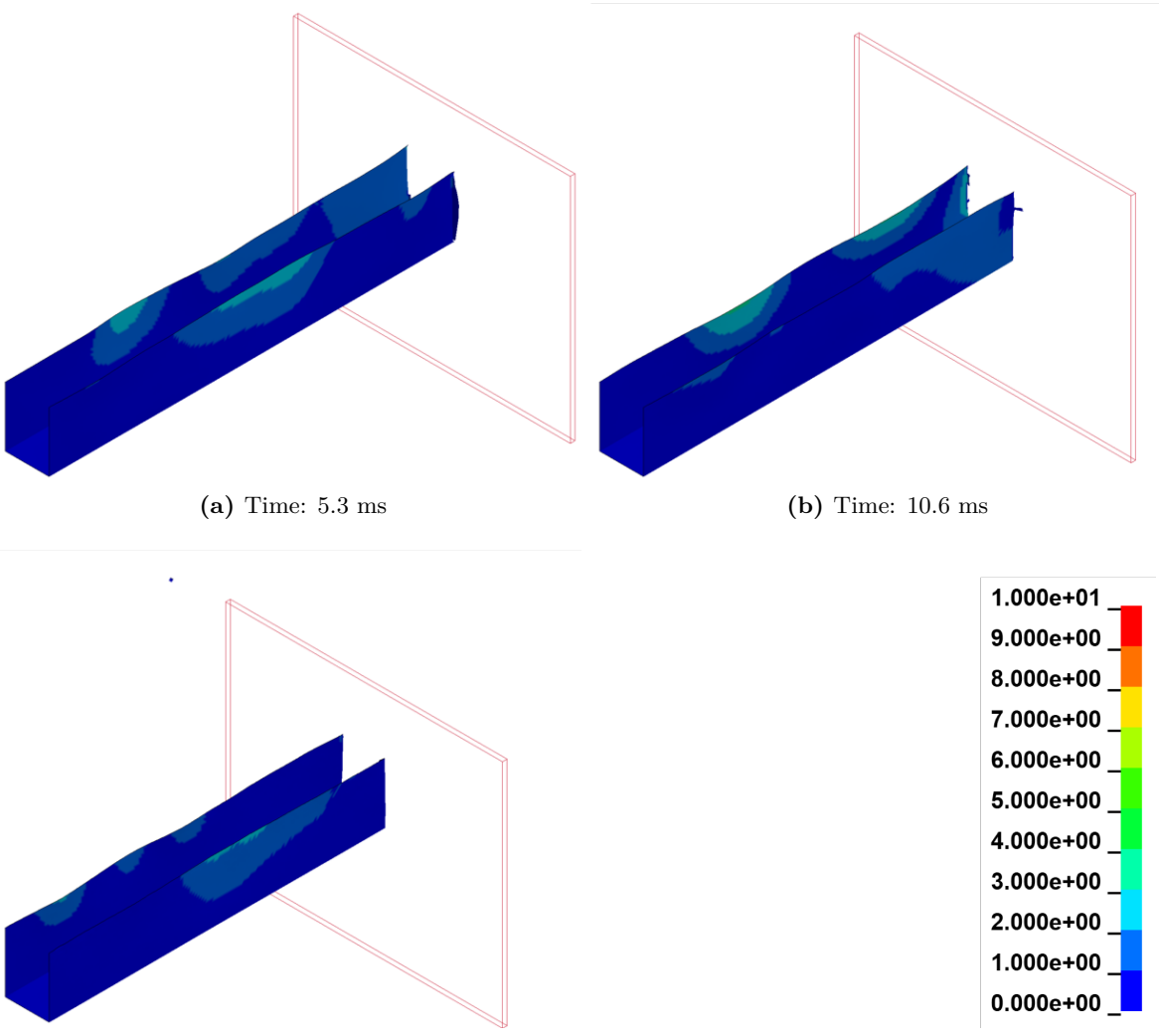

(a) Time: 5.3 ms

(b) Time: 10.6 ms

(c) Time: 16.0 ms

Figure D.7: Resultant displacement at different time instances of the crushing simulation of C-Strut 3. Fringe levels depicted in the bottom right in units of mm.

Appendix E

Fuselage Section Test Case Results

In this appendix, the supporting material for the observations and conclusion reported in Chapter 7 can be found. This entails more details about the parts, the energies of the single parts within the performed simulations, to ensure that the hourglass energies are within acceptable values, and deformation images. Accordingly, in Section E.1, one can find the geometry and layups of the fuselage section's parts. Afterwards, in Section E.2, one can find the part energies and the deformation images.

E.1 Part Overview

In this section, in table E.1 to E.4, an overview of the dimensions and layups of the fuselage parts can be found.

Table E.1: Stringer properties.

Property	Value	Units
Bottom Flange Width	28.7	mm
Top Flange Width	30.0	mm
Height	30.0	mm
Thickness	1.84	mm
Layup	$[45/0/\text{-}45/0/90]_s$	-

Table E.2: Skin properties.

Property	Value	Units
Thickness	2.208	mm
Layup	$[\pm 45/0/90/\pm 45]_s$	-

Table E.3: Frame properties.

Property	Value	Units
Flange Width	25.2	mm
Flange Thickness	2.21	mm
Flange Layup	$[\pm 45/0/90/\pm 45]_s$	-
Web Height	59.8	mm
Web Thickness	2.94	mm
Web Layup	$[\pm 45/0/90/\pm 45/0/90]_s$	-

E.2 Fuselage Section Results

In this section, the results of the performed simulations are reported. This entails two components. In the first segment, the part energies obtained from the simulations are reported, while afterwards, the deformations of the fuselage sections are provided.

Table E.4: Cargo cross-beam properties.

Property	Value	Units
Flange Width	25.2	mm
Flange Thickness	3.31	mm
Flange Layup	$[\pm 45/0/90/\pm 45/0/\pm 45]_s$	-
Web Height	60.0	mm
Web Thickness	3.31	mm
Web Layup	$[\pm 45/0/90/\pm 45/0/\pm 45]_s$	-

E.2.1 Fuselage Section Part Energies

As no reference data is available, one needs to use other tools to inspect the simulations' validity. As stated in the discussion of previous simulations, hourglassing energy can be used to examine the deformation of the mesh. Therefore, in this subsection, the energies of all the parts of the fuselage sections are reported, which can be found in tables E.5 to E.12. In the tables, it can be seen that the hourglass energies are all within the acceptable margin of 10%. More interestingly, as already pointed out in Subsection 7.3, it can be seen that the skin and stringer show little to no damage.

In the tables, the part definitions are different than described in the previous section. This is done to model the different layups and connections between the various parts in LS-Dyna. For example, the frame is modelled with two separate parts, which share coinciding nodes. This leads to the creation of the Frame Web and Frame Flanges parts. Similarly, the stringers are split into separate parts, yielding the 'Stringer Top' and 'Stringer Sides' parts, which are the upper flange and webs, respectively; finally, the lower flanges of the stringer and skin are incorporated into one part, denoted as 'Skin + Stringer'.

In Table E.5, one can find the energies of the parts of the baseline fuselage section. Here it can be seen that all the hourglass energies are withing the required 10%. Furthermore, here it can be seen that the main parts contributing to the energy absorption are the fuselage's frame and partially by the skin.

Table E.5: Final energies of the parts of the baseline fuselage section simulation (in units of Joule).

Part	Total	Internal	Kinetic	Hourglass	Damage
Frame Web	9441.7	6847.8	461.2	-541.3	2593.9
Cargo Crossbeam	425.7	425.7	187.2	17.2	0.0
Stringer Sides	8813.9	8813.9	554.0	-9.0	0.0
Skin	14041.4	13997.0	728.8	38.1	44.4
Metal Plate	511.2	511.2	10.1	1.9	0.0
Stringer Top	3461.4	3461.4	154.6	62.8	0.0
Skin + Stringer	13802.7	12214.0	413.5	-0.1	1588.7
Frame Flanges	8042.2	5227.0	329.5	-608.4	2815.2

In tables E.6 to E.13 one can find the part energies of the parts of the fuselage sections with

the absorbers. Also here one can study the hourglass energy of the parts to ensure good mesh behaviour.

One other aspect that can be noted in the part energy tables is the increase in internal energy of some parts, which is balanced by the frictional energy. This aspect is treated in Subsection 7.3.2. In the aforementioned section, it has been seen how the internal energy of a part can grow significantly, originating from node penetration during contact of two parts. Negative sliding energy balances this increase in energy. In the referenced section, it has been found that this behaviour does not influence the simulation's overall validity. One striking example of this behaviour can be found in Table E.12, where the internal energy of the absorber has a very high value, which is originated due to the aforementioned behaviour.

Table E.6: Final energies of the parts of the fuselage section simulation with fully fixed C-struts (in units of Joule).

Part	Total	Internal	Kinetic	Hourglass	Damage
Frame Web	9058.5	4144.5	425.5	-415.6	4914.0
Cargo Crossbeam	1231.4	1231.4	260.9	60.8	0.0
Stringer Sides	1178.4	1178.4	479.4	14.6	0.0
Skin	2100.9	2100.9	727.6	3.2	0.0
Metal Plate	809.6	809.6	7.8	1.1	0.0
Stringer Top	461.7	461.7	140.5	10.2	0.0
Skin + Stringer	197.1	197.1	497.5	3.4	0.0
Frame Flanges	6421.7	3668.2	351.1	-348.7	2753.5
C-Strut	3811.5	2129.2	924.5	67.1	1682.3

Table E.7: Final energies of the parts of the fuselage section simulation with fully fixed square tube absorbers (in units of Joule).

Part	Total	Internal	Kinetic	Hourglass	Damage
Frame Web	4605.9	4532.9	204.6	121.6	73.0
Cargo Crossbeam	2008.6	1393.1	328.0	58.8	615.5
Stringer Sides	2102.9	2102.9	442.3	7.3	0.0
Skin	4828.7	4828.7	684.2	7.4	0.0
Metal Plate	794.3	794.3	6.4	3.3	0.0
Stringer Top	790.4	790.4	122.2	10.7	0.0
Skin + Stringer	2456.2	2456.2	478.4	3.3	0.0
Frame Flanges	3846.6	3790.3	305.3	-121.1	56.3
Square Tube	1825.2	901.6	113.0	12.9	923.6

Table E.8: Final energies of the parts of the STUNNING fuselage section with fully fixed absorber (in units of Joule).

Part	Total	Internal	Kinetic	Hourglass	Damage
Frame Web	4365.9	3952.4	279.9	133.6	0.0
Cargo Crossbeam	499.0	373.5	106.7	18.8	0.0
Stringer Sides	1565.5	985.3	566.1	14.0	0.0
Skin	3675.9	2838.5	834.7	2.8	0.0
Metal Plate	121.3	117.6	3.6	0.1	0.0
Stringer Top	569.8	402.3	158.4	9.1	0.0
Skin + Stringer	820.5	206.5	611.6	2.4	0.0
Frame Flanges	3985.7	3624.7	322.1	38.9	1039.5
Absorber	9962.0	1299.5	8580.0	82.5	1081.8

Table E.9: Final energies of the parts of the fuselage section simulation with fully fixed square tube absorbers and simplified payload mass (in units of Joule).

Part	Total	Internal	Kinetic	Hourglass	Damage
Frame Web	13662.0	4795.5	1027.8	-756.3	8866.5
Cargo Crossbeam	562.3	562.3	84.3	10.3	0.0
Stringer Sides	2996.4	2996.4	369.0	11.6	0.0
Skin	4469.3	4469.3	484.0	12.8	0.0
Metal Plate	69.5	69.5	1.9	0.1	0.0
Stringer Top	1081.3	1081.3	109.0	15.5	0.0
Skin + Stringer	3330.9	3330.9	267.3	22.7	0.0
Frame Flanges	11159.7	3792.6	310.7	-733.6	7367.1
C-Strut	5386.5	1211.9	92417.0	-47.4	4174.6

Table E.10: Final energies of the parts of the fuselage section simulation with C-strut absorbers, simplified payload mass, and free ends at the frame side (in units of Joule).

Part	Total	Internal	Kinetic	Hourglass	Damage
Frame Web	5157.7	4379.1	247.0	-223.0	778.6
Cargo Crossbeam	940.0	940.0	84.9	24.4	0.0
Stringer Sides	1371.4	1371.4	306.4	13.4	0.0
Skin	2991.6	2991.6	393.4	6.0	0.0
Metal Plate	111.1	111.1	2.1	0.2	0.0
Stringer Top	458.2	458.2	89.8	11.4	0.0
Skin + Stringer	411.9	411.9	242.1	3.7	0.0
Frame Flanges	5198.9	3848.3	272.4	-183.6	1350.6
C-Strut	1120.6	268.6	28.7	4.8	852.0

Table E.11: Final energies of the parts of the fuselage section simulation with square tube absorbers, simplified payload mass, and free ends at the frame side (in units of Joule).

Part	Total	Internal	Kinetic	Hourglass	Damage
Frame Web	5578.5	4397.9	240.9	-16.7	1180.6
Cargo Crossbeam	618.5	357.1	78.2	1.6	261.4
Stringer Sides	4501.0	4501.0	505.4	14.0	0.0
Skin	10298.0	10298.0	698.0	30.5	0.0
Metal Plate	81.1	81.1	3.4	0.1	0.0
Stringer Top	1560.2	1560.2	137.4	13.1	0.0
Skin + Stringer	7519.7	7519.7	357.3	37.0	0.0
Frame Flanges	5625.2	4001.4	4004.2	-398.6	1623.8
Square Tube	3511.4	247.0	17.8	8.6	3264.4

Table E.12: Final energies of the parts of the original STUNNING fuselage section simulation with simplified payload mass, and free ends at the frame side (in units of Joule).

Part	Total	Internal	Kinetic	Hourglass	Damage
Frame Web	4726.5	4407.4	219.0	100.1	26.1
Cargo Crossbeam	12930.2	12739.0	177.0	14.2	0.0
Stringer Sides	4629.1	4101.0	531.8	-3.6	0.0
Skin	9669.3	8864.2	773.3	31.8	0.0
Metal Plate	167.9	165.8	1.9	0.2	0.0
Stringer Top	1518.7	1361.6	146.2	10.9	0.0
Skin + Stringer	7687.1	7179.7	499.4	8.0	773.3
Frame Flanges	4195.1	3967.7	251.8	-24.4	274.4
Absorber	52999.3	51951.0	187.5	860.8	1957.5

Table E.13: Final energies of the parts of the fuselage section simulation with larger square tube absorber, simplified payload mass, and free ends at the frame side (in units of Joule).

Part	Total	Internal	Kinetic	Hourglass	Damage
Frame Web	4262.9	3993.2	178.5	91.1	107.0
Cargo Crossbeam	346.0	284.3	57.4	4.4	0.0
Stringer Sides	2705.3	2307.4	386.4	11.5	0.0
Skin	5203.4	4659.2	536.5	7.7	0.0
Metal Plate	91.8	89.3	2.4	0.2	0.0
Stringer Top	783.1	670.1	103.9	9.1	0.0
Skin + Stringer	2637.0	2306.0	320.1	10.9	0.0
Frame Flanges	3925.6	3692.5	241.5	-8.4	199.2
Absorber	596.4	543.1	30.3	23.0	6586.3

E.2.2 Fuselage Section Deformations

Next to the energies of the different parts, the deformations are also of interest. Therefore, these are all reported in this subsection. One can find four different time instances of the

simulation in all reported figures: 0, 10, 20, and 30 ms. For each time instance, two views are reported, a front view to study the deformation of the frames, and an isometric view to have a better overview of the overall deformation of the fuselage section.

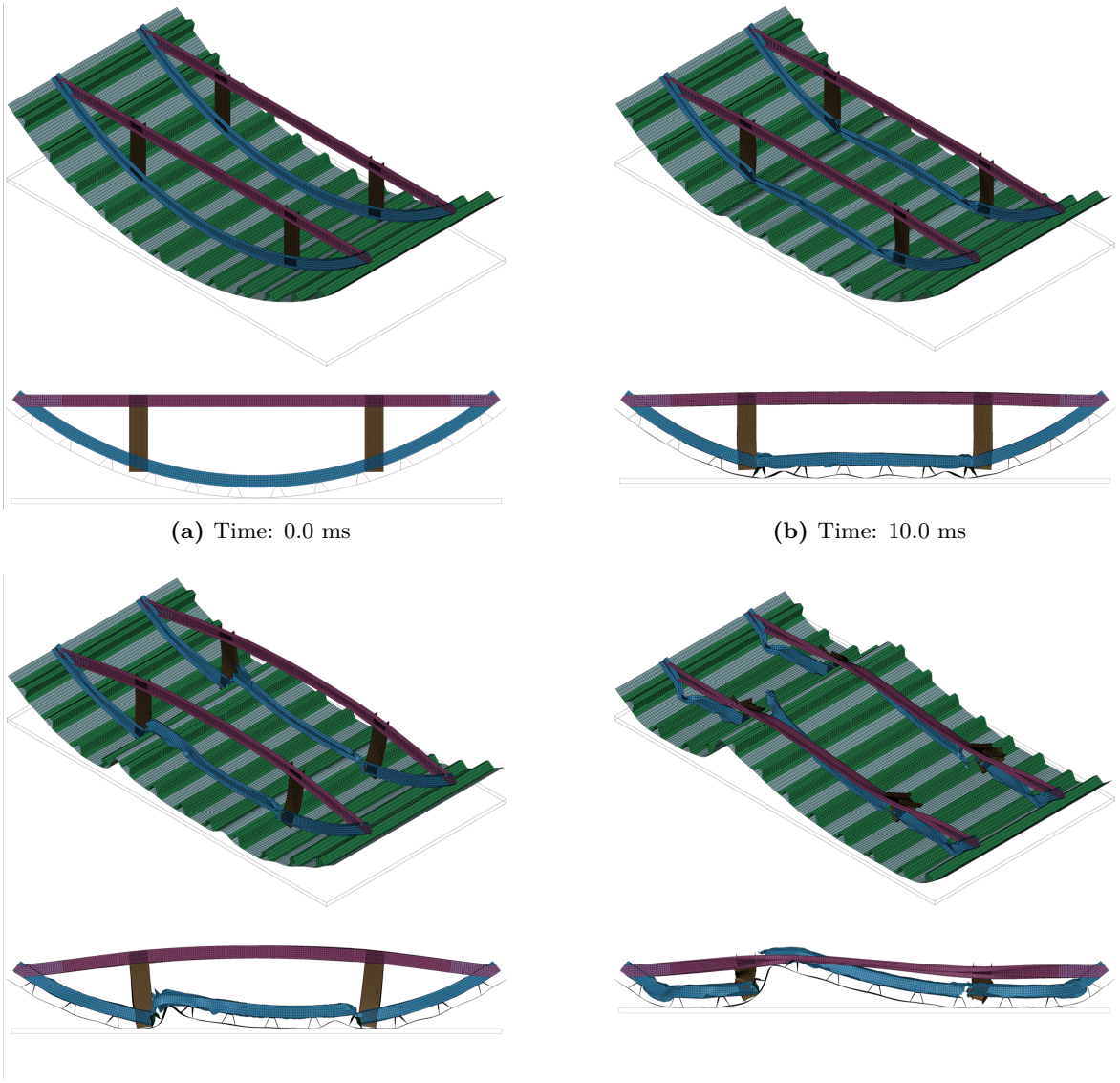

(a) Time: 0.0 ms

(b) Time: 10.0 ms

(c) Time: 20.0 ms

(d) Time: 30.0 ms

Figure E.1: Fuselage section deformation with the fully fixed C-struts.

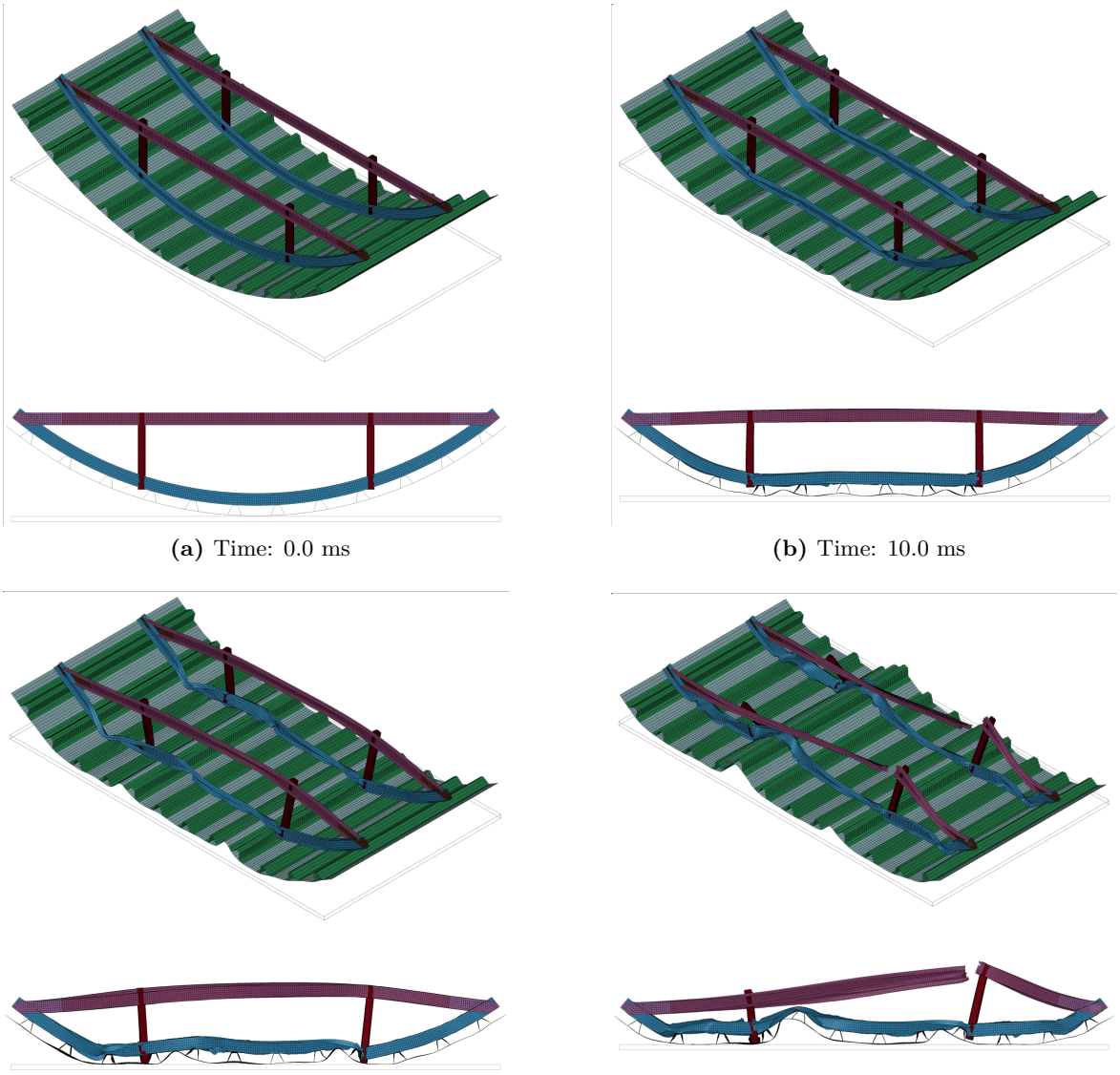

(a) Time: 0.0 ms

(b) Time: 10.0 ms

(c) Time: 20.0 ms

(d) Time: 30.0 ms

Figure E.2: Fuselage section deformation with the fully fixed square tubes.

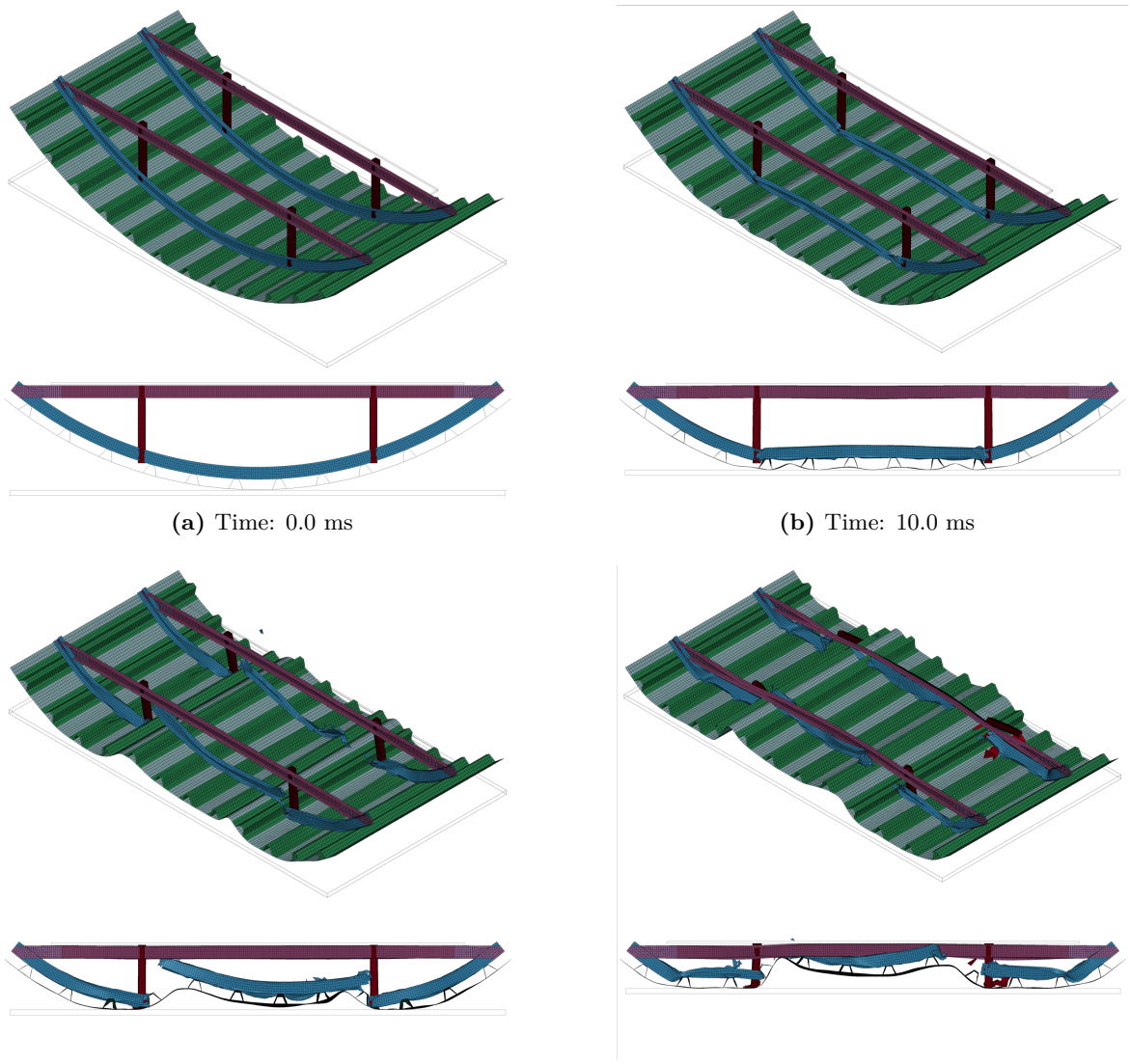

(a) Time: 0.0 ms

(b) Time: 10.0 ms

(c) Time: 20.0 ms

(d) Time: 30.0 ms

Figure E.3: Fuselage section deformation with the fully fixed square tubes and simplified payload mass.

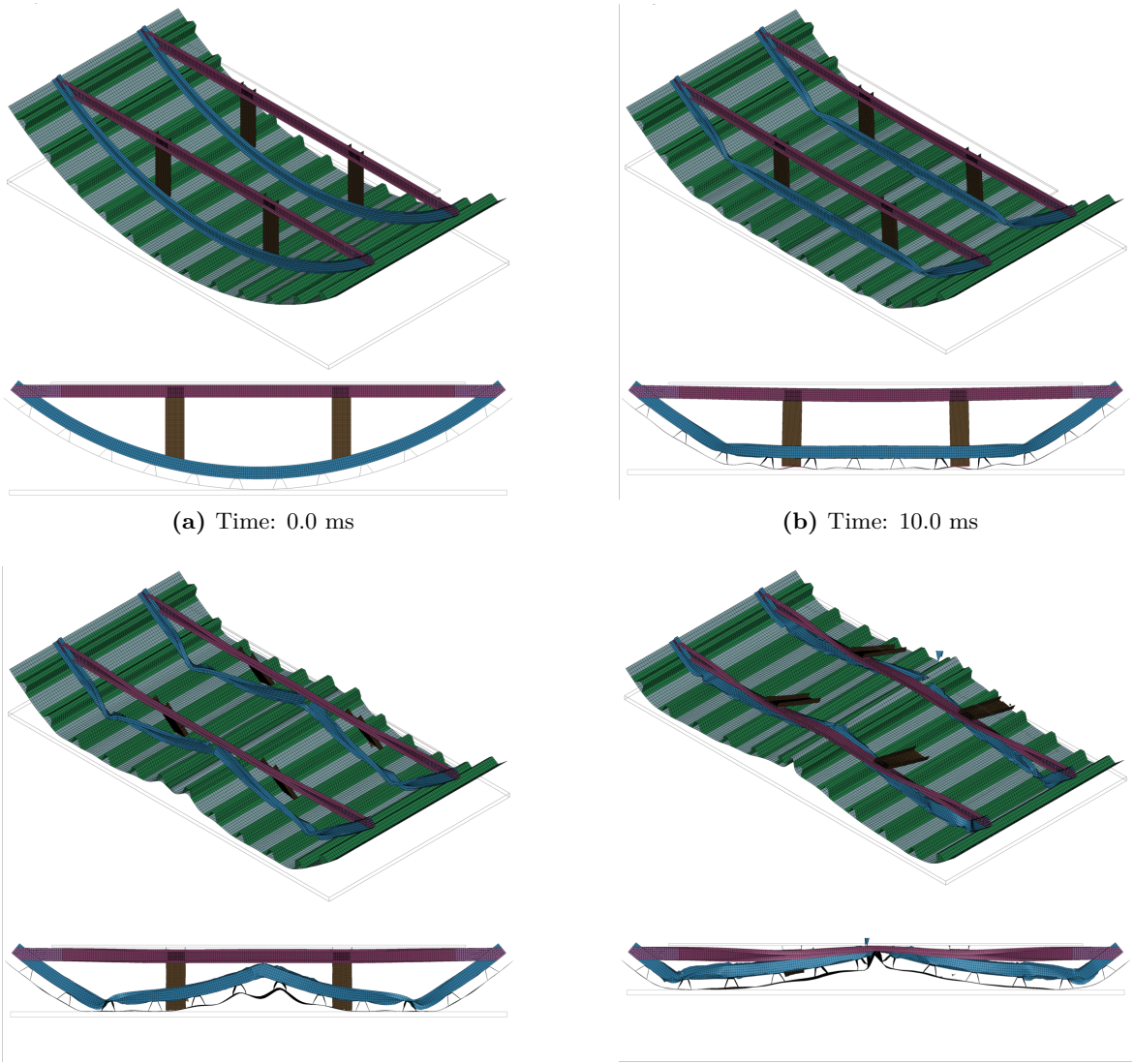

(a) Time: 0.0 ms

(b) Time: 10.0 ms

(c) Time: 20.0 ms

(d) Time: 30.0 ms

Figure E.4: Fuselage section deformation with C-struts, with no connection to the frame, and simplified payload mass.

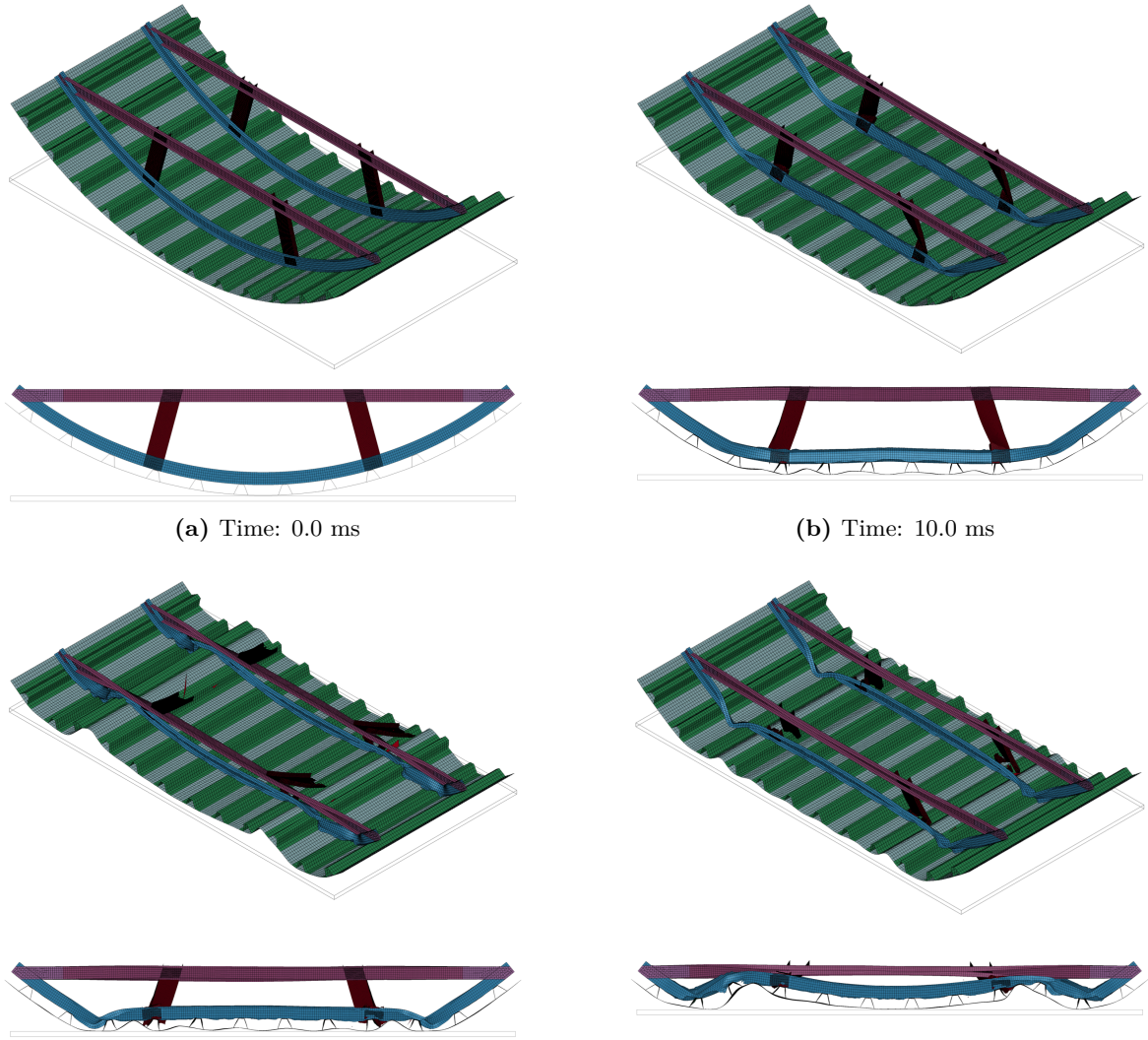

(a) Time: 0.0 ms

(b) Time: 10.0 ms

(c) Time: 20.0 ms

(d) Time: 30.0 ms

Figure E.5: Deformation of the original STUNNING fuselage with fully fixed absorbers.

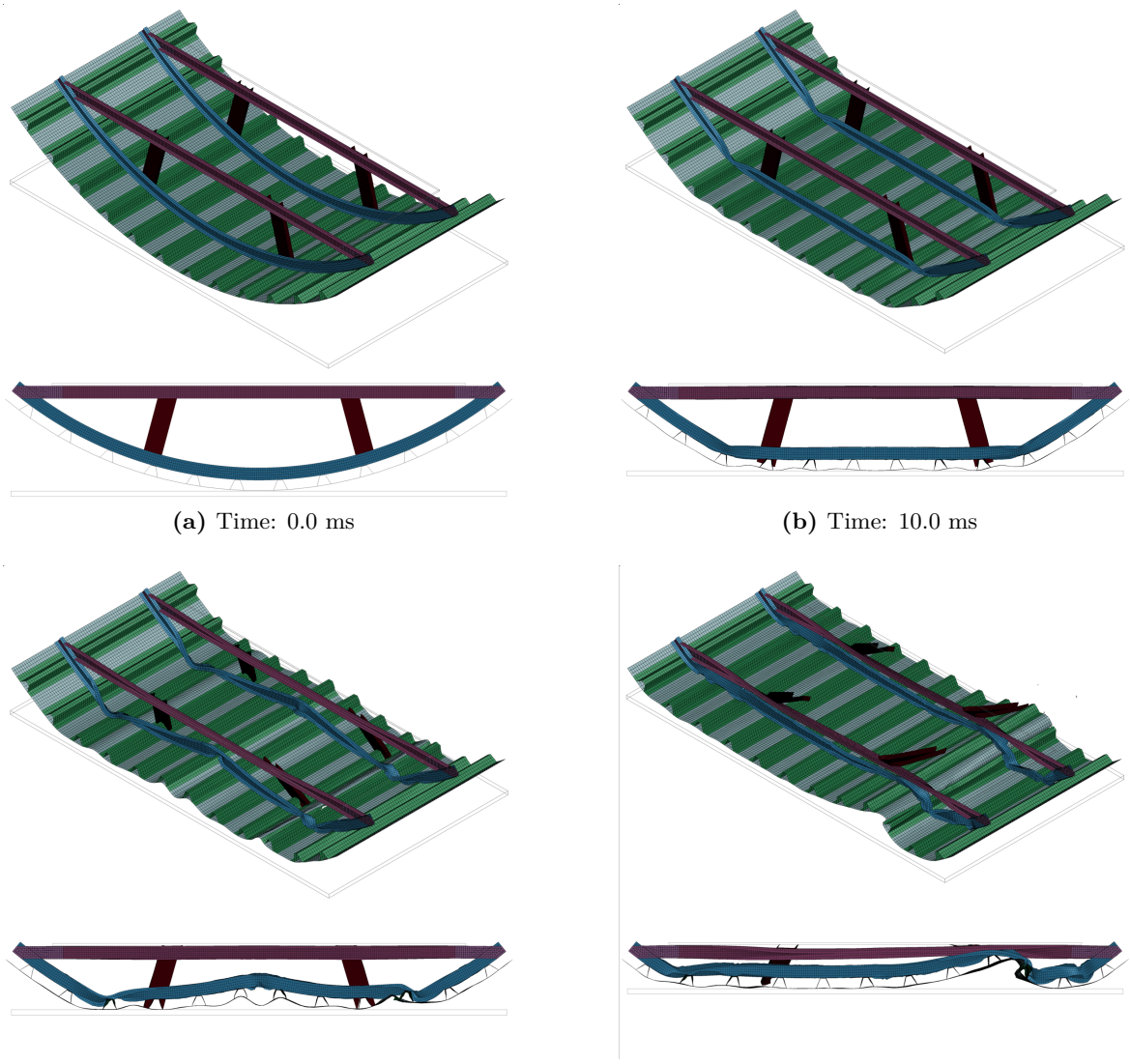

(a) Time: 0.0 ms

(b) Time: 10.0 ms

(c) Time: 20.0 ms

(d) Time: 30.0 ms

Figure E.6: Deformation of the original STUNNING fuselage with absorbers which have no connection to the frame.

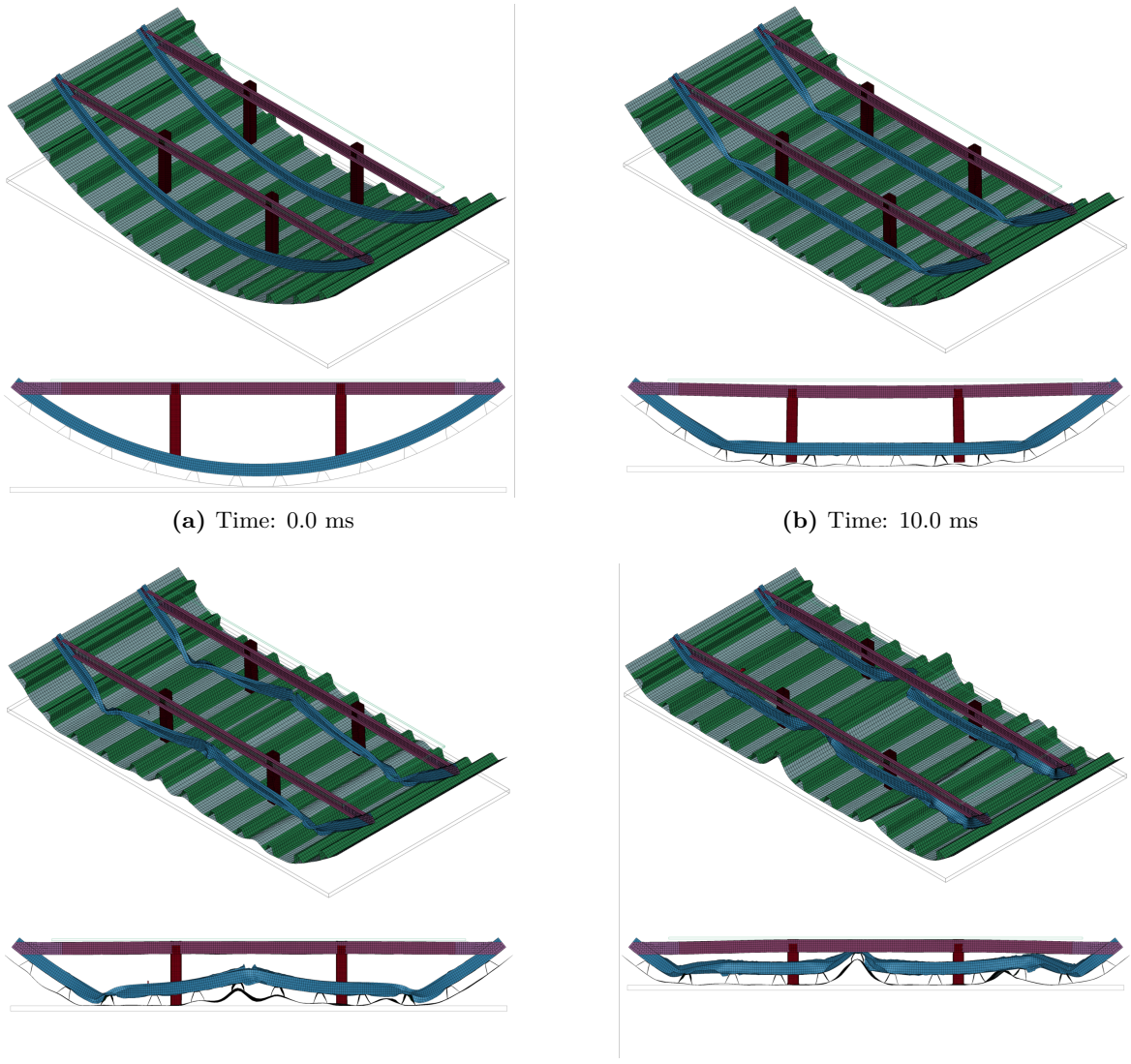

(a) Time: 0.0 ms

(b) Time: 10.0 ms

(c) Time: 20.0 ms

(d) Time: 30.0 ms

Figure E.7: Fuselage section deformation with larger square tube absorbers, with no connection to the frame, and simplified payload mass, for energy absorption estimation.